

https://dspace.org/

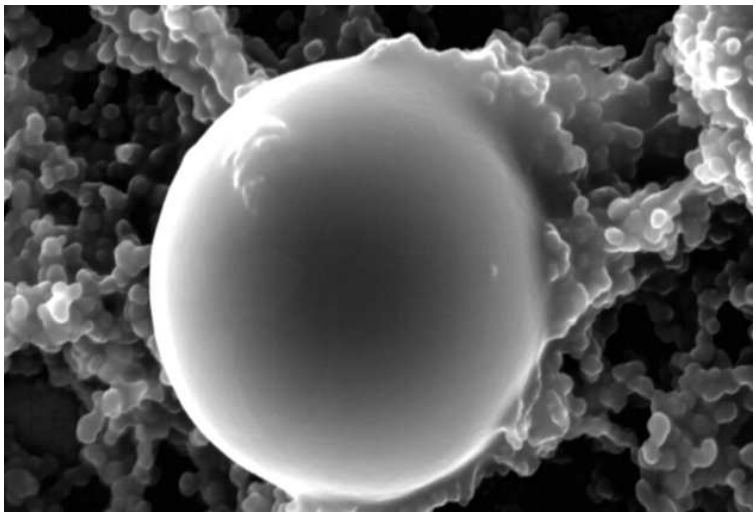
PHYSICAL AND CHEMICAL PROPERTIES OF AEROSOL PARTICLES IN THE TROPOSPHERE: AN APPROACH FROM MICROSCOPY METHODS

Gwaze, Patience

2007-02-26T13:19:17Z
http://hdl.handle.net/10539/2136

Downloaded from a DSpace repository. https://dspace.org/

PHYSICAL AND CHEMICAL PROPERTIES OF AEROSOL PARTICLES IN THE TROPOSPHERE: AN APPROACH FROM MICROSCOPY METHODS



PATIENCE GWAZE

A thesis submitted to the Faculty of Science, University of the Witwatersrand, Johannesburg, in fulfilment of the requirements for the degree of Doctor of Philosophy.

DECLARATION

I declare that this thesis is my own, unaided work, except where otherwise acknowledged. It is being submitted for the degree of Doctor of Philosophy in the University of the Witwatersrand, Johannesburg. It has not been submitted before for any degree or examination in any other university.

Signed this day ..... of ..... 20.....

.....

Patience Gwaze

Abstract

Physical and chemical properties of atmospheric particles are fundamental but not necessarily easily accessible parameters. Uncertainties in these parameters are responsible for some uncertainties associated with radiative impacts of aerosol particles in global climate models. The uncertainties pertain to limitations of sampling and measurement devices, difficulties in modelling aerosols (source strengths, spatial and temporal variability) and in understanding microphysical and optical properties of aerosol particles. Physical and chemical properties can be obtained at single-particle level by microscopy analyses of individual particles. Using refined analytical and interpretative techniques to derive some of these fundamental properties, aerosol particles collected in various field campaigns and laboratory experiments were investigated using two high resolution microscopes. The particles were collected during the LBA-EUSTACH, Large-Scale Biosphere-Atmosphere Experiment part of European Studies on Trace Gases and Atmospheric Chemistry; SMOCC campaign, Smoke Aerosols, Clouds, Rainfall and Climate; CTBH II, Cape Town Brown Haze II campaign; and a controlled combustion experiment. Microscopy techniques were compared and complemented with conventional techniques to characterise particle sizes, shapes, chemical compositions and mixing states.

Particle size distributions were compared between geometric equivalent sizes measured from microscopes and aerodynamic equivalent diameters, while taking into account particle densities. Large differences were found between the particle sizing techniques. Microscopy sizes (3D) were systematically lower than expected, and depended on the relative humidity during particle sampling. Differences were attributed to loss of mass, presumably water adsorbed on particles. Losses were high and could not be accounted for by known humidity growth factors suggesting losses of other volatile compounds adsorbed on particles as well. Findings suggest that there are inherent problems in defining particle sizes with different sizing techniques, despite accounting for humidity growth of particles and particle density. For collected particles, there are mass losses on individual particles, as opposed to particle losses to walls during sampling. These losses will inevitably bias observed mass distributions derived from collected particles and hence their number-size distributions.

Relatively young aggregated soot particles from wood combustion were investigated for particle morphology (fractality, specific mass) and dynamic properties. Based on a procedure that has been validated on modelled aggregates, several important parameters to characterise geometry and drag-to-mass relationship of aggregates were derived. Three

techniques were used to derive fractal dimension of soot aggregates. Averaged fractal dimension was found to be $D_f = 1.82 \pm 0.08$. Dynamic shape factors of soot particles were 1.7 to 2.5 and increasing with mass of aggregates. In the regime $0.2 < Kn < 0.7$ (Knudsen number, $Kn = 2\lambda/d_{mob}$) the mobility diameter d_{mob} was observed to be proportional to the radius of gyration with a ratio $d_{mob}/2R_g = 0.81 \pm 0.07$. Specific surface area of aggregates was determined to be 70 ± 10 $\mathrm{m^2 g^{-1}}$ based on SEM image analysis. These parameters can be used directly in modelling microphysical behaviour of freshly formed soot particles from biomass combustion with fractal dimension of $D_f \approx 1.80$.

Chemical composition and size distributions of particles were investigated on filter samples collected during intense winter brown haze episodes in Cape Town. The sampling technique offered the capability to characterise highly heterogeneous aerosols over a polluted urban environment. Based on morphology and elemental composition, particles were categorised into seven particle groups of: aggregated soot particles, mineral dust, sulphates ($\mathrm{SO_4^{2-}}$), sea-salt, tar balls/fly ash, rod-shaped particles associated with soot agglomerates and those that could not be attributed to any of these groups were labelled as 'others'. Apportionments of chemical species were highly variable both spatially and temporally. These variations indicate lack of lateral mixing and dependence of particle chemical compositions on localised and point sources within the Cape Town area. Sulphate and aggregated soot particles were externally mixed with fractional number concentrations of $0 - 82\%$ and $11\% - 46\%$, respectively. Aerosol complex refractive indices were derived from the chemical apportionment and particle abundance determined in microscopy analyses. The refractive indices were combined with in-situ measurements of number-size distribution to determine optical properties of aerosols. Single scattering albedo, ω_0, varied from 0.61 to 0.94 with a mean value of 0.72 ± 0.08. The ω_0 is much lower than is generally reported in literature, and this was attributed to high concentrations of highly absorbing anthropogenic soot observed in SEM analysis. The mean extinction coefficient σ_{ep} was 194 ± 195 $\mathrm{Mm^{-1}}$. σ_{ep} and ω_0 clearly demonstrated and explained quantitatively the visibility reduction due to particles in the Cape Town atmosphere, reduction observed as the brown haze phenomenon. In all the three case studies, microscopy single particle analysis played a critical role in advancing knowledge of understanding properties of aerosol particles in the atmosphere.

Preface

The thesis is divided into six chapters. Chapter 1 provides a general introduction to atmospheric aerosol particles, with emphasis on particle properties to be addressed in this study - size distributions, morphology and drag-to-mass relationship, chemical composition and optical properties of aerosols. Atomic Force Microscope (AFM) and Scanning Electron Microscope (SEM) used in the study are described in Chapter 2. In Chapter 3, a comparison of particle size distributions as measured by microscopes and several conventional instruments is given. In Chapter 4, a study on morphological and dynamic properties of soot particles is given. Chapter 5 provides a study of aerosol particles in the Cape Town brown haze. Summaries, major findings, limitations and general conclusions are given in Chapter 6.

Parts of Chapter 4 have been published in *Journal of Aerosol Science* doi:10.1016/j.jaerosci.2005.06.007. Other parts of the thesis will be submitted to *South African Journal of Science* and *Atmospheric Environment*. Parts of the thesis were presented at: Ph.D. Advisory Committee (PAC) meeting, Max Planck Institute for Chemistry (MPI), Mainz on 16 July 2003; European Aerosol Conference (EAC), Budapest, Hungary, September 6-10, 2004; 1^{st} French-German Summer School of Aerosol, Heterogeneous Chemistry and Climate, Ile d'Oleron, France, September 19 to October 1^{st}, 2004; University of Witwatersrand, Climatology Research Group Colloquia, 13 September 2005 and University of Johannesburg (UJ) Colloquia, Department of Geography, Environmental Management and Energy Studies, 14 September 2005.

Aerosol sampling and field measurements in Chapter 3 were carried out within the framework of Smoke, Aerosol, Clouds, Rainfall, and Climate (SMOCC) project, a European contribution to the Large-Scale Biosphere-Atmosphere Experiment in Amazonia (LBA). It was financially supported by the Environmental and Climate Program of the European Commission (contract No. EVK2-CT-2001-00110 SMOCC), the Max-Planck-Gesellschaft (MPG), the Fundação de Amparo à Pesquisa do Estado de São Paulo, and the Conselho Nacional de Desenvolvimento Científico (Instituto do Milênio LBA). All members of the LBA-SMOCC and LBA-RACCI Science Teams are thanked for their support during the field campaign especially A. C. Ribeiro, M. A. L. Moura and J. von Jouanne. Special thanks to P. Guyon, J. Rissler and Y. Iinuma for the cascade impactor inversion programs and humidity growth factor calculations.

The combustion experiment in Chapter 4 was carried out at the laboratory combustion facility of the Max Planck Institute for Chemistry (MPI), Mainz, with assistance from M. Welling and Dr. R. S. Parmar. This research was funded by the Max-Planck-Gesellschaft and in part by the Federal Ministry of Education and Research (BMBF) under the Atmospheric Research Programme 2000, grant 07ATF46 (EFEU).

Aerosol measurements in the Cape Town Brown Haze Project II were carried out together with the Climatology Research Group (CRG), University of Witwatersrand, with the help of Dr. L. Otter, Dr. T. Freeman and a team of MSc. students. The project was funded by the South African Petroleum Industries Association (SAPIA), Cape Town Metro and supported by British Airways and National Aeronautics and Space Administration (NASA). Data used in backward trajectory analysis were acquired from the European Centre for Medium Range Weather Forecast (ECMWF) through the Institut für Physik der Atmosphäre, Universität Mainz. Trajectory analysis was carried out with the help of Prof. H. Wernli, Universität Mainz and Dr. P. Hoor (MPI). Forward trajectories were run on-line using NOAA Air Resources Laboratory HYSPLIT model and FNL Meteorological data. Relative humidity profiles for Cape Town International Airport and daily weather bulletins for South Africa were provided by the South African Weather Service. Special acknowledgment to Dr. O. Boucher for the Mie code used in computing aerosol optical parameters.

This study was carried out with a fellowship provided by the Max-Planck-Gesellschaft in the research area 'Climatological Implications of Atmospheric Aerosol Particles' through Dr. G. Helas from January 2002 to April 2005. Microscope analyses of aerosol samples were conducted at the MPI, Mainz, with initial assistance of A. Worringen (AFM) and J. Huth (SEM). Within the framework and support of the International Max Planck Research School (IMPRS), the researcher attended the 5^{th} Summer School of Environmental Physics, *Part A Atmosphere*, Institute for Environmental Physics, Ruprecht-Karls-University, Heidelberg, July 28^{th} to August 1^{st}, 2003 and the 1^{st} French-German Summer School of Aerosol, *Heterogeneous Chemistry and Climate*, Ile d'Oleron, France, September 19 to October 1^{st}, 2004. Financial support in South Africa, including registration fees at the University of the Witwatersrand were provided with the help of Prof. H. J. Annegarn and Dr. S. Piketh, as part of an APINA Fellowship, De Beers Diamond Research Laboratories and the DTI THRIP programme.

I would like to extend my special acknowledgement to Dr. Günter Helas for inviting me to Mainz to do my Ph.D., his steadfast commitment in supervising my work and giving me the opportunity to cooperate with a wonderful scientific community. My sincere gratitude

to Prof. Harold J. Annegarn for his creative suggestions and analytical ideas. Thanks to Dr. Stuart Piketh for the persistent support in South Africa. Dr. Franz Meixner is thanked for providing the first contact to Dr. Günter Helas, for the enthusiastic discussions and encouragement, and for being part of the PAC. Special gratitude to dear friends Jane, Sandra, Sekai and so many others for their moral support. Thank you L. Frewin and J. Huth for your help in so many things. Thank you R. Burger for the initial flight data manipulations. Appreciation to Drs. P. Guyon, G. P. Frank, A. Höfer and A Worringen for the discussions. Thanks to colleagues at the MPI for all the DDGs. Sincere gratitude to the Department of Geography, Environmental Management and Energy Studies, UJ, for providing me with a place while I finished my writing. Thanks to colleagues at UJ for the friendly working environment. Finally, I would like to say thank you to my family, my parents, brothers and sisters, for the prayers and love that kept me going.

In loving memory of a special sister, mother to the girls and a friend to all

Faith - Fekede

Tinokurangarira misi yose

Contents

Abstract iii

Preface v

1 Introduction 1

1.1 Overview of atmospheric aerosol particles 1

1.2 Particle sizes and size distributions 3

1.3 Particle morphology and motion 5

1.4 Optical properties of aerosol particles 7

1.5 Single particle analysis 8

1.5.1 Aim and objectives of study 9

1.5.2 Research rationale 10

1.5.3 Research design 12

1.6 Outline of thesis 13

2 Microscopy Instrumentation - AFM and SEM 16

2.1 Atomic Force Microscope 17

2.2 Scanning Electron Microscope 19

3 Comparison of Particle Sizes Determined with Impactor, DMPS-APS, AFM and SEM 23

3.1 Introduction 24

3.2 Particle sizing techniques 25

3.2.1 Aerodynamic and electrical mobility sizing 25

3.2.2 Microscopy sizing 28

3.3 Experimental techniques 29

3.3.1 Aerosol sampling 29

3.3.2 Microscopy analysis and imaging processing 30

3.4 Data Analysis 33

3.4.1 Particle morphology 33

3.4.2 Particle size distributions 35

3.5 Discussion . . . 42
3.6 Conclusion . . . 46

4 Characterisation of Soot Aggregates from Combustion of Wood 47
4.1 Introduction . . . 48
4.2 Experimental methods . . . 50
4.2.1 Generation of soot particles and sampling procedure . . . 50
4.2.2 Electron microscopy imaging . . . 52
4.3 Data analysis . . . 53
4.3.1 Structure of soot aggregates . . . 53
4.3.2 Deriving D_f from projected surfaces . . . 55
4.3.3 Deriving D_f from primary particle counts . . . 59
4.3.4 Mobility of aggregates . . . 61
4.3.5 Dynamic shape factors . . . 65
4.3.6 Specific surface area . . . 66
4.4 Discussion . . . 67
4.5 Conclusion . . . 69

5 Physical, Chemical and Optical Properties of Aerosol Particles Collected over Cape Town During Winter Haze Episodes 71
5.1 Introduction . . . 73
5.1.1 Cape Town brown haze . . . 73
5.1.2 Objectives of this study . . . 75
5.1.3 Research rationale and design . . . 75
5.1.4 Literature review: Previous research on Cape Town brown haze . . . 77
5.2 Experiment and methodology . . . 79
5.2.1 Boundary layer structure . . . 79
5.2.2 Flight patterns . . . 80
5.2.3 Measurement techniques . . . 84
5.2.4 Meteorology conditions during campaign period . . . 90
5.2.5 Trajectory analysis . . . 92
5.2.6 Electron microscopy . . . 93
5.3 SEM single particle analysis . . . 94
5.3.1 Aerosol composition . . . 94
5.3.2 Relative abundance of particles . . . 104
5.3.3 Sizes distributions from SEM analyses . . . 108
5.3.4 Particle morphology . . . 109
5.4 Aerosol number concentrations and size distributions - PCASP . . . 111

5.4.1 Particle spatial distribution 111
5.4.2 Particle size distributions 117
5.5 Comparisons of number concentrations and size distributions - SEM and PCASP 123
5.6 Aerosol optical properties - SEM and PCASP 126
5.6.1 Aerosol refractive index 126
5.6.2 Effects of refractive index on particle size 127
5.6.3 Aerosol optical properties 130
5.6.4 Radiative forcing of aerosol particles 137
5.6.5 Sensitivity studies 139
5.7 Conclusion 141
5.8 Recommendations 145

6 Conclusions **147**
6.1 Comparisons of particle size distributions 147
6.2 Morphological and dynamic properties of soot particles 149
6.3 Characterisation of aerosol particles collected over Cape Town in winter haze episodes 151

Appendices **173**
Appendix A: Publications and conference proceedings 173
Appendix B: Analytical expressions 175
Appendix C: Other tables and figures 177

List of Figures

1.1 Schematic of sources, formation mechanisms, size ranges and sinks of atmospheric aerosol particles. The dashed line in the accumulation mode shows two peaks sometimes observed (adapted from *Finlayson-Pitts and Pitts*, 2000). 4

1.2 Sizes of atmospheric particles as defined from properties utilised in aerosol sizing instruments (adapted from *Baron and Willeke*, 2001b, pp 50). 5

2.1 Schematics of the Atomic Force Microscope. 17

2.2 SEM image of an AFM probe tip. The tip is attached to a free end of a cantilever *(imaged by J. Huth, MPI, Mainz.)* 18

2.3 5 μm x 5 μm AFM image of polystyrene latex spheres of diameter 0.356 ± 0.007 μm. The image has a colour depth of 743 nm (0 black and 743 white). 19

2.4 Scanning Electron Microscope, Leo 1530 SEM used in this study. Highlighted features are (1) Energy dispersive X-ray (EDX) detector (2) Backscatter electron detector (BSED) and (3) high vacuum sample chamber. 20

2.5 6.22 μm x 5.61 μm SEM image of polystyrene latex spheres of diameter 0.600 ± 0.005 μm. Only isolated particles which had not been deformed by neighbouring spheres were analysed. 22

3.1 Collection efficiency curves of individual impactor stages of a MOUDI. The dotted lines are artificial stages included in the inversion algorithm to recover observed mass distribution (*Roberts et al.*, 2002). 26

3.2 AFM topographic image of brochosomes collected on stage 6, Sample #1. The image size is 3 μm x 3 μm with a colour depth scale of 873 nm (0 black and 873 nm white). The image shows distinct surface structure of particles with surface diameters of 0.3 μm to 1 μm. 33

3.3 AFM topographic image of aerosol particles on collected on stage 6, Sample #1. The image size is 3.89 μm x 3.89 μm. (a) 2D image of particle silhouettes with a colour depth scale of 280 nm (0 black and 280 nm white). (b) 3D image with a shaded relief of surface topography, analogous to shining light onto a 3D surface. 34

3.4 3D image of a single particle observed on stage 4, Sample #1 with $d_a = 3$ μm. The image size is about 4 μm x 4 μm with a colour depth scale of 350 nm (0 black and 350 nm white). 35

3.5 Normalised size distribution of particles as a function of Stokes diameter $d_{1.15}$ simulated from combined distributions measured by the DMPS and APS at relative humidity = 65%. The grey area is the standard deviation from the mean, the solid line is the bimodal fit to the mean distribution, and the dotted line is the simulated fraction of the distribution collected by the MOUDI on stages 5 to 8. 37

3.6 Normalised kernel functions (dashed lines) and distributions of d_{ve} (solids) on Sample #1 for stages 8 to 5. The distributions were fitted with lognormal functions of parameters given in Table 3.3. 38

3.7 Distributions of surface diameters measured with AFM (solid dots) and SEM (open dots) on stages 5 and 6 of Sample #1. Sizes of particles are reduced in the SEM by the loss of water and volatiles in the vacuum. 39

3.8 Normalised kernel functions (dashes), simulated ambient DMPS-APS size distributions (dotted), and distributions of d_{ve} (solids) on Sample #2 for stages 8 to 5. The distributions were fitted with lognormal functions of parameters given in Table 3.3. 40

3.9 SEM image of a particle with a large halo (the dark circular area). The liquid component adsorbed on the particle reacted with the aluminium substrate before it was lost either during storage or in the SEM vacuum. The averaged surface diameter of the halo is 5.7 μm and the agglomerated particle is about 1.7 μm. 43

3.10 Ratios of geometric mean diameters of the kernel functions (d_ρ) and equivalent volume distributions (d_{ve}) in Table 3.3. The lines are the best fits to the plots and exclude the out-layers labelled X. 44

4.1 (a) SEM image with a large field of view to show how aggregates had deposited on the filters without overlapping, $d_e = 350$ nm. (b) A single soot aggregate, $d_e = 350$ nm, imaged with a resolution of 17.1 $pixels/2a_p$. Inserts are binary images of the aggregate at 17.1 and 3.4 $pixels/2a_p$ (125 kX and 25 kX, respectively). The arrows point to narrow features which are not resolved at 25 kX. 53

4.2 (a) Soot aggregates of $d_e = 200$ nm and (b) $d_e = 275$ nm. 53

4.3 Primary particle size distribution of soot aggregates, with mean radius $a_p = 25.5 \pm 3.5$ nm and standard deviation of $\sigma_g = 1.27 \pm 0.09$. 54

4.4 Parameters measured from 2D projected surfaces of aggregates. The aggregate is a computer simulated cluster-cluster aggregate of $D_f = 1.79$ (from *Oh and Sorensen*, 1997, their Figure 4). The fractal dimension measured with the box counting method varied between $D_f = 1.75$ to 1.81 depending on the orientation of the aggregate. 56

4.5 Influence of image resolution on projected surface area A_a and fractal dimension D_f on 3 soot aggregates. Aggregates were centred in images while resolutions were varied from 4 to about 50 $pixels/2a_p$ (corresponding to 25 kX to 350 kX). Aggregate #1 is shown in Figure 4.2(b). 57

4.6 (a) $D_{f,2}$ as a function of image resolution on 205 aggregates analysed with the box counting method. Included in the plot is the best fit (line) observed from aggregate #2 by varying the resolution. (b) The limitation in resolution is due to restricted field of view because of aggregate length L. Aggregates with higher L are imaged at courser resolutions. 58

4.7 Number of primary particles in an aggregate as a function of radius of gyration. The plot of ln N versus ln R_g/a_p yielded a fractal dimension $D_f = 1.83 \pm 0.05$, $k_g = 2.77 \pm 0.31$, and $R^2 = 0.90$. N was calculated from equation 4.1 with area prefactor $k_a = 1.16$ and structural coefficient $\alpha = 1.10$. 61

4.8 Distributions of N on aggregate ensembles of electric mobility diameter $d_e = 200$, 275, 350 and 450 nm in (a) to (d), respectively. The first peaks to the left of each spectrum represent singly charged aggregates and an increase in charge is indicated by the subsequent peaks. Solid lines are the lognormal bimodal fits to the distributions. 63

4.9 Ratio $\beta = d_{mob}/2R_g$ as a function of the Knudsen number $Kn = 2\lambda/d_{mob}$ (see text). For $a_p = 25.5$ nm, $\beta = 1.29$ and $Kn = 2.6$, (solid square). As the number of particles in aggregates N increase, β will follow the slope and decrease to 0.81, the mean of the scatter. 64

4.10 Relationship of d_{mob} and number of primary particles per aggregate N. The solid circles represent singly charged and open circles represent doubly charge aggregates. 65

4.11 The overlapping of primary particles in 2D projected surfaces. 66

5.1 Geographic location of the study area. 77

5.2 PM2.5 source apportionment (left) and visibility apportionment averaged over four monitoring sites during modelled haze episodes in the CTBH I study, from *Wicking-Baird et al.* (1997). 78

5.3 Schematic representation of a diurnal development of the continental boundary layer under anticyclonic conditions (adapted from *Garratt*, 1992; *Oke*, 1993). 80

5.4 Flight paths, haze meter stations and major industry locations. Flights 9, 13, 14 and 16 were conducted on August 6 (1020 − 1200 UTC), 15 (1230 − 1500 UTC), 22 (0700 − 0920 UTC) and 23 (0630 − 0840 UTC), respectively. A detailed map of the haze meter sites is given in Figure 5.5. 81

5.5 Haze meter sites used to identify ground locations of flight paths. These locations are schools in Cape Town that were involved in collecting solar intensity measurements with haze meters, for details see *Piketh et al.* (2004). Site locations of two major industries A - an oil refinery and B - a glass manufacturing industry. 82

5.6 Segments of flight tracks where vertical profiles were performed on Flight 10, August 7 Profile A from 0651 − 0702 UTC; Flight 4, August 2, Profile B from 0923 − 0935, Profile C from 1002 − 1007 UTC; Flight 13, August 15 Profile D from 1257 − 1305, Profile E from 1403 − 1418 UCT, Profiles F and G from 1421 − 1433 UTC. 84

5.7 Schematic view of the collection of aerosol particles on an ABS filter. 85

5.8 Locations where ABS aerosol samples were collected for microscopy analysis on Flights 9, 13, 14 and 16 - August 6, 15, 22 and 23, respectively. 87

5.9 Averaged particle number-size distributions of each flight as measured by the optical particle counters. Distributions showed a discontinuity between d_p of $3-4$ μm. Flights 4 and 5 (in black and red) are profound cases highlighted, with a discrepancy of a factor of up to 14 (dN_{PCASP}/dN_{FSSP}). 89

5.10 Relative humidity RH (%, black), rainfall (x 20 mm, blue), temperature (°C, red), and barometric pressure (hPa, magenta) at Goodwood meteorology station (18.56°E, 33.90°S). All parameters were measured 10 m above ground, from 30 July to 26 August 2003. The rainfall column plot is exaggerated 20 times to fit the scale. Boxes on the time scale indicate days when ABS samples used in the case studies were collected. The gap on August 4 to 5 was due to instruments malfunction. 91

5.11 (a) 5-day back trajectories initiated on Flights 9, 13, 14 and 16 (August 6, 15, 22 and 23). Solid marks on the trajectory tracks indicate 6-hour time intervals. (b) Trajectory vertical histories of pressure. 93

5.12 (a) Large and compact soot aggregate collected with the ABS sampler. (b) A chained soot particle with agglomerated spheroids. This particle was collected on a gold-coated filter with a ground sampler and the morphology is similar to those soot aggregates collected with the ABS. 95

5.13 Distributions of equivalent surface diameter d_a for soot aggregates and all particles on samples collected on Flight 9 (a) Sample #1 and (b) Sample #4. Soot aggregates contribute to the largest surface diameters. 97

5.14 (a) Mineral dust particles with complex composition, mainly Na, Si, Ca, Fe, Zn, and Mn with traces of S, Mg and Al (see text for description of labels X and Y). (b) Mineral dust particle made of agglomerated spheroids and composed of Na, Si, S, Fe and Zn and minor components of Al, Mg, K, Ca and Mn. (c) Silica (quartz) particles. (d) An iron silicate particle. EDX spectra of (a) to (c) are shown in Figure 5.15. 98

5.15 EDX spectra of mineral dust particles shown in Figure 5.14, respectively. Shaded plot in (d) shows the substrate spectrum with C and O, on an area void of particles. Energy values labelled refer to K(α) levels unless indicated. 99

5.16 SEM images of sulphate particles collected on Flight 14. Particles have satellite droplet rings typical of dehydrated sulphuric acid, encircling core particles, in the box (b). Arrows point to distortions in the image due to sample charging effects. 100

5.17 (a) An euhedral sea-salt particle (b) an aged sea-salt particle (see text). 101

5.18 Typical SEM images of (a) tar spheroid of 0.68 μm in diameter and (b) large spherical fly ash particle with a diameter of 1.59 μm. 102

5.19 Relative contributions of seven particle groups identified in the SEM analyses of 12 samples collected on Flights 9, 13, 15 and 16 (August 6, 15, 22 and 23). 105

5.20 (a) Relationship between circularity Cr and (a) equivalent diameter of projected surface and (b) aspect ratio, AR. 109

5.21 Distribution of (a) aspect ratio AR and (b) circularity $Cr = 4\pi Area/(Perimeter)^2$ for Samples #1 and #4. The frequencies were normalised with the maximum frequency of each distribution. 110

5.22 Vertical profiles of θ, N, and V_{tot} on a looping descent from Camps Bay - False Bay - Belhar on Flight 10, August 7 from 0651 to 0702 UTC - Profile A. The labels on the right side represent stratifications defined based on thermal stability, where ML = mixing layer, SBL = stable boundary layer, RL = residual layer and FT = free troposphere. 112

5.23 Vertical profiles of θ, N, and V_{tot} on Flight 4, August 2; An ascent followed by descending spirals as indicated by the arrows from 0923 to 0935 UTC, Profile B (solid circles) around Wallacedene: and Profile C from 1002 to 1007 UTC (open circles) at Fishoek. The labels on the right side represent stratifications defined based on thermal stability, where ML = mixing layer, SBL = stable boundary layer and RL = residual layer. 113

5.24 Vertical distributions of θ, N and V_{tot} on a looping descent from Wynberg-False Bay-Belhar, Flight 13, August 15, Profile D from 1257 to 1305 UTC. The labels on the right side represent stratifications defined based on thermal stability, where CBL = convective boundary layer, EZ = entrainment zone and FT = free troposphere. 114

5.25 Vertical distributions of θ, N and V_{tot} on Profile E made in pristine conditions around the Cape Point on Flight 13, August 15 from 1402 to 1420 UTC. The labels on the right side represent stratifications defined based on thermal stability, where SL = surface layer, CBL = convective boundary layer, EZ = entrainment zone and FT = free troposphere. 115

5.26 Vertical profiles of θ, N, V_{tot} on Flight 13, August 15, Profile F from 1421 to 1426 UTC (solid circles); and Profile G from 1426 to 1433 UTC (open circles). Both profiles were conducted downwind of Cape Town. The labels on the right side represent stratifications defined based on thermal stability, where SL = surface layer, CBL = convective boundary layer, EZ = entrainment zone and FT = free troposphere. 116

5.27 Particle number-size and volume distributions averaged along thermal stratifications identified in Profiles A to G. Lognormal fits to volume distribution and error bars are shown on some profiles. The rest are excluded for clarity. The stratifications were defined based on thermal stability, where SL = surface layer, CBL = convective boundary layer, RL = residual layer, EZ = entrainment zone and FT = free troposphere. 120

5.28 Size distributions of maximum N measured in the time intervals corresponding to the 12 ABS samples analysed with SEM. Optical properties are determined from these distributions in Section 5.6.3. Highlighted size distributions with prominent coarse modes are fitted with multimodal fits in Figure 5.29. 121

5.29 Multimodal fits to three volume distributions highlighted in Figure 5.28 to show effects of size truncations by the PCASP in the presence of a coarse mode. These effects are discussed in Section 5.6.5. 121

5.30 (a) Surface number density n_{SEM} of particles from SEM analyses of ABS samples collected on Flights 9, 13, 14 and 16. (b) N_{SEM} and mean number concentrations measured by the PCASP, N_{PCASP}, and normalised to concentrations of Sample #3. Correlation coefficient $R^2 = 0.82$. Error bars are the standard deviations of N_{PCASP}. (c) Relationship between absolute N_{PCASP} and N_{SEM}. The equivalent number concentrations from the SEM N_{SEM} are systematically underestimated by a factor of 4.3 ± 0.3. 124

5.31 Normalised size distributions of particles on Sample #1 and Sample #4, $dN_{PCASP}/dlog\,d_p$ measured by the PCASP and $dN_{SEM}/dlog\,d_a$ from SEM analysis. 125

5.32 PCASP responses to PSL spheres and aerosol particles of different refractive indices at a wavelength of 0.635 μm. The functions are integrated over scattering angles of $35^0 - 120^0$ to correspond to theoretical response functions of the PCASP. 128

5.33 Diameter ratios $d_{aerosol}/d_{PSL}$ as a function of d_{PSL} for particles with response functions in Figure 5.32. For $d_{aerosol}/d_{PSL} > 1$, the PCASP overestimates particle sizes and for $d_{aerosol}/d_{PSL} < 1$, particle sizes are underestimated. 129

1 Vertical profiles of relative humidity on August 6, 15, 22 , and 23 (for Flights 9, 13, 14 and 16, respectively) at Cape Town International Airport weather station as provided by the South African Weather Services. Flights 9 and 13 were conducted within 2 hours after these soundings, and Flights 14 and 16 were made 3 to 4 hours prior to the soundings. . 177

2 Vertical distributions of particle concentrations N and θ. In the mornings, before 0900 UTC (solid circles), high number concentrations are confined to a more stable layer below 400 m asl. As day time progresses, particle concentrations are mixed by turbulence in the growing convective boundary layer to about 1200 m asl (open circles). 179

3 Vertical distributions of particle concentrations N and θ. In the mornings, before 0900 UTC (solid circles), high number concentrations are confined to a more stable layer below 400 m asl. As day time progresses, particle concentrations are mixed by turbulence in the growing convective boundary layer to about 1200 m asl (open circles). 180

List of Tables

2.1 Specifications of the Atomic Force Microscope, CP-Research Model. 18

2.2 Specifications of the Leo 1530 Scanning Electron Microscope. 21

3.1 Calibration parameters of the MOUDI impactor. 27

3.2 Ratio of surface diameters to heights, d_a/h_a and aspect ratio AR of projected surfaces. 35

3.3 Geometric mean diameters derived from fitting lognormal functions to size distributions in Figures 3.6 and 3.8 where, d_{ve} = equivalent volume diameter projected in AFM images, d_a = averaged surface diameter, d_ρ = Stokes diameter at particle density of ρ_p = 1.15, 1.4 or 1.5 g/cm^3 and $R^2 > 78\%$. 41

4.1 Equivalent mobility diameters of multiply charged particles, number of primary particles per aggregate N retrieved from Figure 4.8, and dynamic shape factors χ_D (see equation 4.8). 62

5.1 A summarised inventory of major primary source strengths of particulates and trace gas emissions in Cape Town from *Wicking-Baird et al.* (1997). 78

5.2 Flight summary of selected flights. 83

5.3 Flight numbers, dates, times (UTC), ABS samples analysed with the SEM and locations where samples were collected (see Figures 5.5 and 5.8 for ground locations). 86

5.4 Channel parameters of the PCASP before and after midpoint corrections by calibrating with PSL spheres of refractive index $m = 1.585 - 0.0i$. 88

5.5 Parameters of multimodal lognormal fits to averaged size distributions plotted in Figure 5.27, d_{gi} and σ_{gi} are the geometric mean diameter and deviation of modes i = 1 to 4. The stratifications were defined based on thermal stability, where SL = surface layer, SBL = stable boundary layer, CBL = convective boundary layer, RL = residual layer, EZ = entrainment zone and FT = free troposphere. 122

5.6 Refractive indices and densities of particle groups identified in SEM analysis. . . . 126

5.7 Optical properties of particles determined from maximum number concentrations measured by the PCASP, refractive indices determined from SEM analyses and $\lambda = 550$ nm. Sample #10 (in italics) was collected inside an industrial plume. . . . 132

5.8 Optical properties of particles determined from mean and minimum number concentrations measured by the PCASP, refractive indices determined from SEM analyses and $\lambda = 550$ nm. Sample #10 (in italics) was collected inside an industrial plume. 133

5.9 Averaged clear sky net radiative forcings at the top of the atmosphere (TOA) estimated from the radiative transfer model for different aerosol mixtures. 138

1 Coordinates of Cape Town brown haze measurement stations 178

2 Coefficients of 8-order polynomial functions fitted to the response functions of the PCASP at refractive index of PSL spheres $m = 1.585 - 0.0i$ and ambient particles with $m = n_j - k_j$ for particle groups $j = 1$ to 7 identified in the SEM analyses. . . 181

LIST OF ABBREVIATIONS

ABL	Atmospheric Boundary Layer
ABS	Air Borne Streaker sampler
AFM	Atomic Force Microscope
APS	Aerodynamic Particle Sizer
asl	above sea level
BL	Boundary Layer
CBD	Central Business District
CBL	Convective Boundary Layer
CCN	Cloud Condensation Nuclei
CMB	Chemical Mass Balance receptor model
CNC	Condensation Nuclei Counter
CTBH (I, II)	Cape Town Brown Haze (Study I, II)
DLCC	Diffusion Limited Cluster-Cluster aggregation
DLPA	Diffusion Limited Particle-Cluster Aggregation
DMA	Differential Mobility Analyser
DMPS	Differential Mobility Particle Sizer
ECWMF	European Centre for Medium-Range Weather Forecasts
EDX	Energy Dispersive X-ray
EFEU	Impact of Vegetation Fires on Composition and Circulation of the Atmosphere. The abbreviation is in German and stands for 'Einfluss von Vegetationsfeuern auf die Zusammensetzung und Zirkulation der Atmosphre'.
EPA	Environmental Protection Agency
EUSTACH	European Studies on Trace Gases and Atmospheric Chemistry
FSSP	Forward Scattering Spectrometer Probe
IPCC	Intergovernmental Panel on Climate Change
LBA	Large-Scale Biosphere-Atmosphere Experiment in Amazonia
MPI	Max Planck Institute (for Chemistry, Mainz)
MPG	Max-Planck-Gesellschaft
MOUDI	Micro-Orifice Uniform Deposition Impactor
NBL	Nocturnal Boundary Layer
OPC(s)	Optical Particle Counter(s)
PCASP	Passive Cavity Aerosol Spectrometer Probe
PIXE	Proton Induced X-ray Emission
PM	Particulate Matter

PMS	Particle Measuring Systems
PSL	Polystyrene Latex (spherical particles)
RL	Residual Layer
SAFARI	Southern African Regional Science Initiative
SBL	Surface Boundary Layer
SEM	Scanning Electron Microscope
SMOCC	Smoke Aerosols, Clouds, Rainfall and Climate
TBL	Top of the Boundary Layer
TEI	Thermo Environmental Instruments
TEM	Transmission Electron Microscope
TOA	Top of the Atmosphere
TSP	Total Suspended Particulate
UN	United Nations
UTC	Universal Time, Coordinated
VOC(s)	Volatile Organic Compound(s)

NOMENCLATURE

α	Projected area exponent (Chapter 3)
α	Ångstrom exponent (Chapter 4)
β	Ratio of mobility diameter to twice the radius of gyration
$\overline{\beta}$	Spectrally weighted upscatter function
Γ	Dry adiabatic lapse rate
λ	Mean free path of gas molecules
λ_{550}	Wavelength of incident light at 550 nm
θ	Potential temperature
ρ_p	Density of particle
$\sigma_{ag,ap}$	Light absorption by gas, particles
$\sigma_{eg,ep}$	Light extinction by gas, particles
σ_{ext}	Light extinction by both particles and gases $= \sigma_{ep} + \sigma_{eg}$
$\sigma_{sg,sp}$	Light scattering by gas, particles
σ_g	Geometric standard deviation of a distribution
μ	Air viscosity
χ	Dynamic shape factor
ω_0	Single scattering albedo
τ	Aerosol optical depth
A_a	Projected surface area of a particles in the SEM image
a_p	Radius of primary particle of soot aggregates
A_p	Projected surface area of primary particle
AR	Aspect Ratio, ratio of major axis L to perpendicular minor axis W of the best fit ellipsoidal envelope to particle projection
A_s	Fractional cloud amount
C_{ov}	Sintering of primary particles in 3D
$C_{ov,proj}$	Overlap parameter of primary particles in SEM images
C_{dx}	Cunningham slip correction factor of particle with respective diameter d_x
D	Fractional daylength
d_{50}	Nominal particle diameter at 50 % collection efficiency of single impactor stage
d_a	Equivalent circular surface diameter of the projected surface area of particle A_a in the SEM image
d_e	Mean electrical mobility diameter of a particle exiting the DMA

D_f	3D fractal dimension
$D_{f,2}$	2D fractal dimension from projected surfaces in SEM images
d_{mob}	Mechanical mobility diameter
d_{ve}	Spherical volume equivalent diameter of an irregular particle
$E_n(d_p)$	Collection efficiency function of a single plate of an impactor at a particle diameter d_p
F_D	Drag force on a particle
F_{DM}	Drag force on an irregular particle
F_0	Solar constant
$f(RH, xx\%)$	Hygroscopic growth factor at relative humidity of xx%
g_0	Asymmetry parameter
k_a	Projected area prefactor of an aggregate
k_g	Gyration prefactor of an aggregate
Kn	Knudsen number
$k_n(d_p)$	Kernel functions of an impactor stage n at particle diameter d_p
L	Projected maximum length of an aggregate in SEM image
L_v	Visibility range
N	Number of primary particles per soot aggregate (in Chapter 3)
N	Particle number concentrations, cm^{-3} (elsewhere)
n_{SEM}	Surface density of particles on SEM images, $\mu\mathrm{m}^{-2}$ cm^{-3}
N_{SEM}	Equivalent number concentrations of particles from surface density in SEM images, cm^{-3}
N_{PCASP}	Total number concentration measured by the PCASP in the range of $0.09 < d_p < 3\,\mu$m, cm^{-3}
R_g	Radius of gyration of soot aggregates
RH	Relative humidity
R_s	Surface reflectance
s	Steepness factor on an individual impactor stage n
s_A	Specific surface area of aggregates
S_A	Exposed surface area of aggregates
T_a	Atmospheric transmission
V	Velocity of a particle in motion
V_t	Total volume sampled per ABS deposition spot, cm^3
V_{tot}	Total volume of particles, $\mu\mathrm{m}^3$ cm^{-3}
W	Width of an aggregate orthogonal to L

Chapter 1

Introduction

1.1 Overview of atmospheric aerosol particles

Aerosol particles are an important constituent of the atmospheric system. Particles may be created as primary aerosol particles - those that are released directly into the atmosphere as particulate matter or as secondary aerosols - those formed during gas-to-particle conversion of gaseous precursors emitted into the atmosphere. Particles are emitted from both natural and anthropogenic activities. Sources vary from widespread surface sources like deserts and arid surfaces (mineral soil dust), oceans (sea-salt), biosphere (pollen, bacteria, plant debris) and biomass and fuel burning (organic and graphitic carbon, fly ash). Industries and diffuse sources like traffic emit mainly carbonaceous aerosols and secondary gaseous precursors, while intense point sources, e.g., volcanic eruptions, inject large volumes of particles and traces gases into the atmosphere. Extraterrestrial sources are usually negligible. The major gaseous precursors are sulphur dioxide (SO_2), ammonia (NH_3), oxides of nitrogen (NO_x), dimethyl sulphide (DMS) and volatile organic compounds (VOCs). Estimates for global source strengths of particles and their precursors can be found elsewhere (*IPCC*, 2001).

Distributions of aerosol particles over the globe are highly variable and heterogeneous both in time and space because of the multiple sources and short lifetimes of particles, unlike for example long-lived greenhouse gases (*IPCC*, 2001). Generally, highest concentrations of particles are observed close to their sources, but meteorological influences of winds, advection, turbulences and convective processes transport and disperse aerosol particles and their precursors within the troposphere (*Baumbach*, 1996).

Particles contribute to several processes in the atmosphere on local, regional and global scales. On local and regional scales, particles can have adverse health effects on humans, or by impairing visibility. Exposure to fine particulate matter (particles smaller than 100 nm in diameter) from combustion processes is now regarded as the major atmospheric environmental threat to human health, particularly in major cities (*Lippmann et al.*, 2003; *World Bank Report*, 1998). Such exposure increases the occurrences of respiratory diseases

such as pneumonia, influenza and more (*Nemmar et al.*, 2003). Aerosol particles scatter and absorb solar radiation, thereby degrading visibility, phenomena familiar in mega cities worldwide and in the tropics during biomass burning seasons. On a global scale, aerosol particles perturb the radiation budget and contribute to cloud formation and precipitation processes. Particles can take part in heterogeneous chemical processes in mechanisms where they may be transformed, or change the oxidation state of the atmosphere (*Andreae and Crutzen*, 1997). For example interactions of SO_2, nitrogen pentoxide (N_2O_5), ozone (O_3), organic compounds or hydroxyl radial (OH) with mineral dust have been postulated to affect sulphate production, transfer nitrates to remote areas or reduce tropospheric O_3 in high dust loadings (*Dentener et al.*, 1996). Particles can be activated to form cloud condensation nuclei (CCN), depending on the chemical composition (i.e., amount of soluble material), size of particles and ambient super saturation (*Seinfeld and Pandis*, 1998).

Aerosol particles have direct and indirect radiative forcings on the Earth's radiation balance (*Charlson et al.*, 1992). A radiative forcing is defined as a perturbation of the radiation budget at the tropopause after adjustment of stratospheric temperature, but with temperature and humidity profiles of the troposphere (and surface) kept constant (*IPCC*, 2001). Direct effects relate to extinction of incoming solar and outgoing infra-red radiation by particles under clear skies. For example, anthropogenic sulphate particles are effective at light scattering and are now known to contribute to a cooling radiative forcing over the globe (*Adams et al.*, 2001; *Boucher et al.*, 1998). In semi-direct aerosol effects, absorbing aerosols in and around a cloud may increase temperature and reduce humidity profiles, leading to a decrease in low-cloud cover and cloud formation (*Ackerman et al.*, 2000; *Johnson et al.*, 2004).

Indirectly, aerosol particles perturb the radiation budget through interaction of clouds with radiation. In the presence of super saturation of water vapour, particles can be activated to grow as CCN and form cloud droplets. High particle concentrations increase the number of cloud droplets that may be formed, but reduce the mean sizes of cloud droplets below the threshold of 14 μm needed to initiate efficient precipitation of clouds (*Seinfeld and Pandis*, 1998). It has been shown that anthropogenic aerosol particles produce brighter clouds by this effect, coupled with suppressed precipitation (*Andreae and Crutzen*, 1997; *Charlson et al.*, 1992; *Hobbs and Radke*, 1969; *Rosenfeld*, 2000). These impacts might be enhanced by feedback mechanisms, e.g., suppression of wet removal of aerosol particles would increase the lifetime of particles, further enhancing both their direct and indirect effects (*Ramanathan et al.*, 2001a). These are termed aerosol indirect effects of second kind.

Aerosol particles exist as either externally mixed particles - when discrete particles are made of homogeneous chemical compositions, or as internally mixed particles - when chemical compositions of particle are heterogeneously mixed. The degree of mixing usually increases with ageing of particles when: gaseous species or small particles condense on particles surfaces; particles are processed in cloud droplets that will later evaporate; and particles are photochemically processed during their transportation. Such observations have been made in biomass burning emissions (*Li et al.*, 2003b; *Reid et al.*, 1998) and urban emissions in remote locations (*Ebert et al.*, 2004).

Atmospheric lifetimes of aerosol particles vary from a few minutes to weeks (*Wayne*, 1991). Particles are removed by either dry or wet deposition. In wet deposition, particles are deposited in precipitation (rain, ice or snow). Smaller particles are scavenged through Brownian motion, collision and inertial impaction onto liquid (or ice) droplets in cloud processes, or during fallout, at which stage droplets have large surface areas (*Jennings*, 1998).

Dry deposition involves those processes where aerosol particles are transported to surfaces without precipitation, e.g., by Brownian diffusion, interception or inertial forces. Large particles (> 1 μm) sediment by gravitational forces, and generally close to their sources. However large scale transport mechanisms can carry coarse mode particles over long distances, e.g., Saharan dust particles are observed in Puerto Rico (*E.A Reid et al.*, 2003a), over Israel (*Falkovich et al.*, 2004) and North America (*Dentener et al.*, 1996). Haze layers of biomass burning aerosols originating from Africa and South America where observed over the equatorial and tropical South Atlantic Ocean (*Andreae et al.*, 1994).

A brief overview on size, dynamic and optical properties of particles will be given in this introduction, and detailed reviews are made in the chapters 3, 4 and 5.

1.2 Particle sizes and size distributions

Particle sizes have to be known as precisely as possible in order to estimate and predict radiative forcings of particles and also their effects on human health (*IPCC*, 2001; *Nemmar et al.*, 2003). Sizes, morphology and shapes of aerosol particles vary depending on formation mechanisms, composition and age of particles (Figure 1.1).

Atmospheric aerosol particles exist in four modes, with particle diameters extending over five orders of magnitude from $d_p = 0.001$ to 100 μm. The modes are denoted

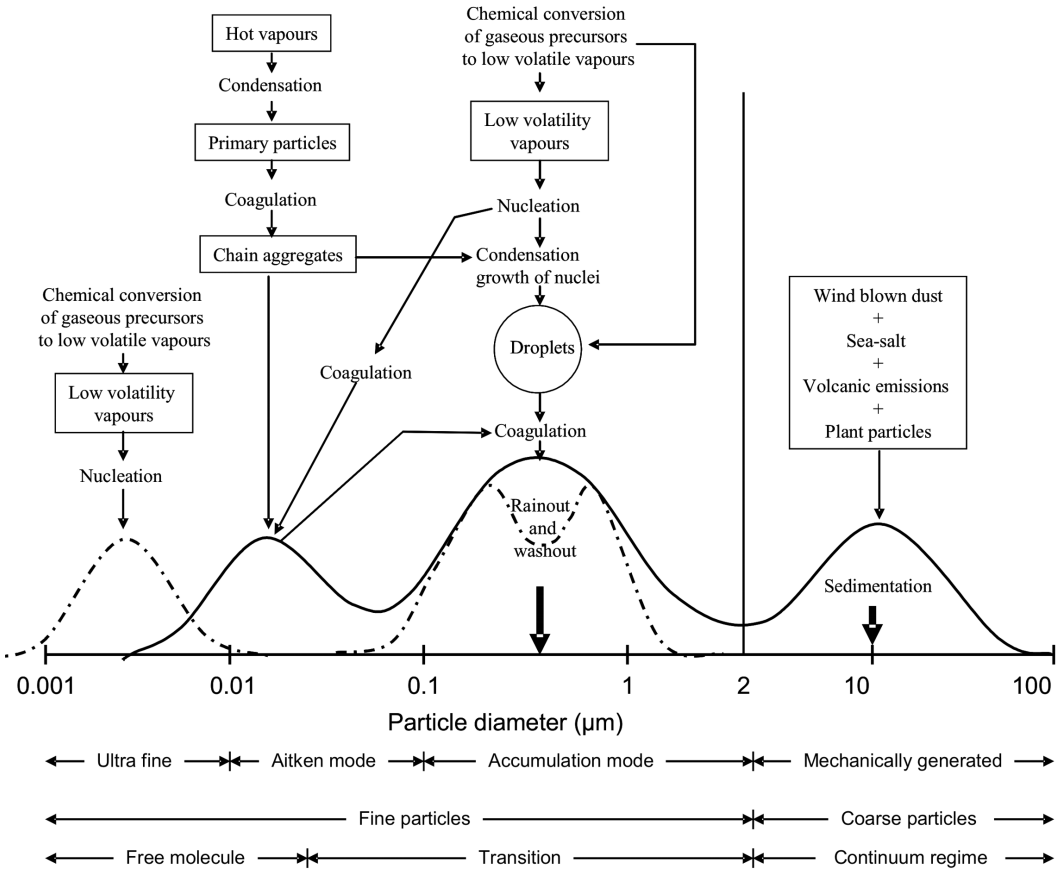


Figure 1.1: Schematic of sources, formation mechanisms, size ranges and sinks of atmospheric aerosol particles. The dashed line in the accumulation mode shows two peaks sometimes observed (adapted from *Finlayson-Pitts and Pitts*, 2000).

as: the ultra fine mode with particles in the diameter range $0.001 \leq d_p \leq 0.1$ μm; Aitken mode, $0.01 \leq d_p \leq 0.1$ μm; accumulation mode, $0.1 \leq d_p \leq 2$ μm; and coarse mode, $d_p > 2$ μm. Lifetimes and removal mechanisms of particles are influenced by particle sizes. The nucleation mode originates mainly from gas-particle conversion of reactive species (*Kulmala et al.*, 2004). The accumulation mode consists mainly of coagulated particles from the Aitken mode and combustion generated particles. Coarse mode particles are generated mostly from mechanical abrasion, biosphere and sea-salt particles. Removal mechanisms are least efficient in the accumulation mode, hence this mode has a longer lifetime compared to the nucleation and coarse modes. The accumulation mode accounts for most of the tropospheric aerosol mass and surface area. Particles in the accumulation mode are also most efficient in scattering and absorbing light (*Seinfeld and Pandis*, 1998).

Particle sizes are defined based on properties by which they are measured, as indicated in Figure 1.2 (*Baron and Willeke*, 2001b). Sizing instruments define an equivalent diameter of a sphere that would have the same response as the irregular particles being

measured, e.g., optical particle counters measure the scattering intensity of particles and derive equivalent spherical sizes through the Mie scattering theory. The frequently used parameter is the aerodynamic equivalent particle size d_p, which is the diameter of a sphere with unit density (1.0 gcm^{-3}) and the same gravitational settling velocity as the particle being measured. While aerosol sizes extend over five orders of magnitude, generally sizing instruments based on a specific physical principle can be designed to measure accurately only one to three orders of magnitude in size. Technically, microscopy techniques have the capacity to span nearly the entire aerosol size range from 0.03 nm to 100 μm.

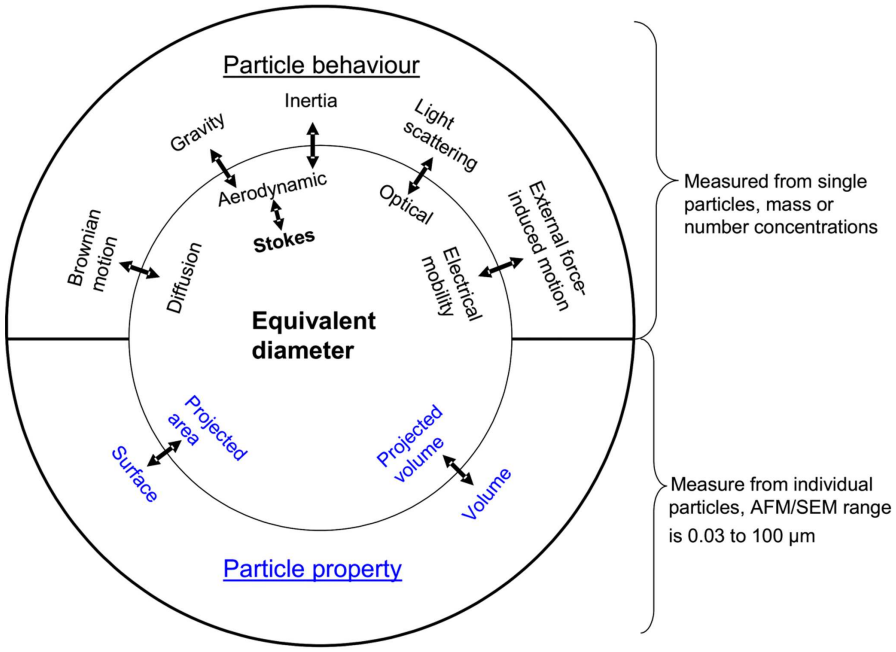


Figure 1.2: Sizes of atmospheric particles as defined from properties utilised in aerosol sizing instruments (adapted from *Baron and Willeke*, 2001b, pp 50).

When among other parameters of the carrying medium, shapes and density of sampled particles are known, sizes distributions derived from different techniques can be computed as a function of any equivalent diameter. Uncertainties in size distributions and limitations of sampling techniques (e.g., detection limits and knowledge of particle shapes) make modelling of aerosol size distributions difficult. Some of these uncertainties and inconsistencies between different sizing techniques are investigated in Chapter 2.

1.3 Particle morphology and motion

Most sizing techniques (impactor, Aerodynamic Particle Sizer - APS, Differential Mobility Analyser - DMA, Differential Mobility Particle Sizer - DMPS) define particle sizes corre-

sponding to particle motion. Aerodynamic sizing methods segregate particles based on their mass-to-drag characteristics, while DMPS and DMA define particle size from electrical mobility in an external electric field. Particle density and morphology have important effects on these size measurements.

A particle in motion with negligible inertial force compared to the viscous force will experience a resistance force F_D due to the particle form and frictional force of the surrounding gas given by Stokes law

$$F_D = 3\pi\eta V d_p \tag{1.1}$$

where V is the velocity of particle relative to gas, η is the gas viscosity, d_p is the diameter of particle, assumed to be spherical.

The motion of the gas molecules at the particle surface is not zero and therefore a Cunningham slip correction factor C_{dp} is applied to Stokes law to account for the reduced drag on particle motion. For solid particles at ambient conditions, the slip factor is given by

$$C_{dp} = 1 + Kn[1.142 + 0.558exp(-0.999/Kn)] \tag{1.2}$$

where Kn is the Knudsen number of a particle given by $Kn = 2\lambda/d_p$ and λ is the mean free path of the carrying medium.

While most of the sizing instruments assume aerosol particles to be spherical, this approximation only holds for cloud droplets, cloud processed particles, and most secondary derived aerosols. Mineral dust particles are irregular, and other particles have complex shapes, e.g., agglomerates (soot aggregates[1]), amorphous (biological particles), elongated fibres (asbestos) or cubic structures (sea salt). For non-spherical particles, a further correction to Stokes equation is defined by the dynamic shape factor χ where the drag force on the irregular particle $F_{DM} = \chi F_D$. The shape factor depends on the flow regime due to the differences in the effect of the non-sphericity on the drag (*DeCarlo et al.*, 2004). The drag force on any particle with equivalent volume diameter d_{ve}, dynamic shape factor χ and Cunningham slip factor C_{dve} is

$$F_{DM} = 3\pi\eta V\chi d_{ve}/C_{dve} \tag{1.3}$$

(*Baron and Willeke*, 2001c; *Hinds*, 1999).

[1]The term 'soot particles' will be used in this study to denote aggregated graphitic carbon formed from all combustions processes. For clarity and consistency the terms 'elemental carbon', EC, and 'black carbon', BC, will be avoided. Measurements of black carbon or elemental carbon are based on optical and thermochemical techniques, respectively, and microscopy measurements define soot aggregates based on particle morphology.

Values of χ have been derived for mineral dust particles (*J.S Reid et al.*, 2003b) and aggregated particles (*Nyeki and Colbeck*, 1994; *Schmidt-Ott*, 1988). For several particle morphologies *DeCarlo et al.* (2004) have given a summary on how these morphologies relate to particle density (density including particle voids), material density (without voids), and shape factors. However, applying shape factors to a heterogeneous aerosol is complicated by varying composition, particle shape and dynamic behaviour of particles.

1.4 Optical properties of aerosol particles

When solar radiation enters the atmosphere, part of the radiation is scattered and absorbed by particles and gases. Particles scatter and absorb radiation in amount and angular distribution depending on shape, size, chemical composition of particles, and their mixing states. Absorbing particles convert illuminating radiation to thermal energy on reradiation. The solar spectral range of importance in describing the interaction of particles with radiation is between wavelengths (λ) of 300 to 800 nm. Below 300 nm, incoming radiation is attenuated by atmospheric O_3 and above 800 nm radiation is absorbed by O_2, O_3, H_2O, and CO_2 (*Seinfeld and Pandis*, 1998).

Elastic scattering is considered in atmospheric aerosols. Particles much smaller than the wavelength of light, $d_p < 0.1\,\mu$m scatter light isotropically, with irradiance proportional to λ^{-4}. This is termed the Rayleigh scattering regime. Particles in the accumulation mode have sizes comparable to wavelengths of visible light, and scatter light more efficiently in the forward direction. This is termed the Mie scattering regime. Scattering by coarse particles, $d_p > 2.5$ μm, can be treated in terms of basic geometrical optics.

Effects of the interactions of particles and gases with light are apparent as visibility reduction in air-polluted areas. Such visibility reduction can be determined from optical properties of aerosol particles. For an aerosol ensemble, the fraction of light removed per unit thickness of an aerosol by scattering and absorption is expressed from the Beer-Lambert law of extinction. The extinction coefficient σ_{ext} is given by

$$\sigma_{ext} = \sigma_{sp} + \sigma_{ap} + \sigma_{sg} + \sigma_{ag} \tag{1.4}$$

where σ_{sp} and σ_{ap} are the scattering and absorption coefficients by particles, respectively and extinction coefficient σ_{ep} the sum of σ_{sp} and σ_{ap}. σ_{sg} and σ_{ag} are the scattering and absorption coefficients of the gas phase, respectively. σ_{sp} and σ_{ap} are functions of particle number concentration, size distribution, wavelength of light and aerosol refractive index

(chemical composition and mixing state). In polluted areas σ_{ext} is dominated by attenuation due to aerosol particles (*Dzubay et al.*, 1982). These coefficients can be measured directly or computed from the Mie theory for an ensemble of particles with known sizes and chemical composition (*Bohren and Huffman*, 1983).

The ratio of scattering coefficient to extinction coefficient defines the single scattering albedo $\omega_0 = \sigma_{sp}/\sigma_{ep}$, an optical parameter which gives information on the radiative forcing of an aerosol. Particles with $\omega_0 = 1$, e.g., sulphates, scatter all incident light and some of it back into space. This reduces the amount of light reaching the earth surface, producing a cooling effect (negative radiative forcing). In global climate modelling, annual mean forcing by sulphates is between -0.26 to -0.80 Wm^{-2} (*Haywood and Boucher*, 2000). For absorbing particles like soot aggregates and mineral dust, ω_0 is less than unity and particles contribute to a positive radiative forcing (warming). The magnitude of the forcing depends on ageing and mixing state of absorbing particles with non-absorbing components (*Jacobson*, 2001). For externally mixed soot, the global annual mean forcing is $+0.16$ Wm^{-2} and assuming an internal mixture of soot/sulphates increases the forcing to $+0.42$ Wm^{-2} (*Haywood and Boucher*, 2000).

1.5 Single particle analysis

Scientific understanding of aerosol properties, their direct and indirect effects of the first kind is regarded as very low (*IPCC*, 2001). These understandings are related to factors needed to estimate radiative effects of particles. Factors pertain to several uncertainties due to limitations of sampling and measurement devices, difficulties in modelling aerosols (source strengths, spatial and temporal variability) and understanding microphysical and optical properties of aerosol particles. Uncertainties in deriving radiative impacts of particles arise from understanding chemical composition and mixing states of particles in order to derive complex refractive index of an aerosol, $m = n - ik$. For particle microphysical properties, radiative forcings are sensitive to particle size distributions. As has been discussed in Section 1.2, particle size distributions are measured using a variety of aerodynamic, geometric, optical and dynamic methods. These methods can produce dissimilar size distributions, which when input into radiative models, will result in disparate radiative effects (*J.S Reid et al.*, 2003b).

Physical properties (number concentrations, size, surface area, mass, morphology, shape, mixing states) and chemical properties are fundamental parameters of aerosol par-

ticles, but usually not directly measured or readily available. These parameters can be obtained at single particle level by analyses of *individual* particles. A statistical distribution of parameters of interest is generated from measurements of individual particles to define attributes of an aerosol ensemble, as opposed to *bulk* analyses. Such parameters are required as inputs into numerical models, particularly small scale numerical models.

1.5.1 Aim and objectives of study

The aim of this study is to use high resolution microscopy techniques to characterise atmospheric aerosol particles by using refined analytical and interpretative techniques to derive fundamental physical and chemical properties of the particles. Microscopy techniques are compared and complemented with conventional techniques to characterise particle sizes, shapes, chemical compositions and mixing states. This rather broad aim is concentered on two main objectives:

1. To compare particle size distributions as measured by microscopy techniques and conventional sizing instruments (cascade impactor and optical particle counter). The focus in this objective is to understand the extent to which particle sizes are characterised by different instruments, consistency between sizing techniques and uncertainties in defining particle sizes, when shapes and density of sampled particles are known.

2. To complement microscopy and conventional techniques and determine morphological, chemical and optical properties of two aerosol types by:

   (i) characterising soot particles produced in wood combustion using a verified microscopy procedure by *Brasil et al.* (1999) in order to
   - give a quantitative description of particle morphology (geometry, fractal dimension, specific surface area)
   - determine dynamic properties of soot particles.

   (ii) using microscopy techniques to investigate urban aerosols in a specific case study, namely the Cape Town brown haze and
   - provide chemical composition, elemental composition, mixing states and size distributions of particles
   - use the information to apportion contributions of different aerosol particle sources

– study the spatial distribution of particles

– determine refractive indices of aerosols

– quantify optical properties and radiative effects of particles.

1.5.2 Research rationale

Microscopy techniques have become effective and powerful tools in atmospheric research, particularly the use of electron beam microscopes, the Scanning/Transmission Electron Microscope, S/TEM (*Chen et al.*, 1998; *Ebert et al.*, 2002b; *Fletcher et al.*, 2001; *Hasegawa and Ohta*, 2002; *Kojima et al.*, 2004; *Li et al.*, 2003a,b; *McInnes et al.*, 1994; *Okada and Hitzenberger*, 2001; *Pósfai et al.*, 2003) and (*E.A Reid et al.*, 2003a). The Atomic Force Microscope, AFM has been used to a less extend (*Friedbacher et al.*, 1995; *Köllensperger et al.*, 1999; *Pósfai et al.*, 1998). The techniques are versatile and can be applied to study a range of aerosol properties including: ageing processes, heterogeneous interactions, mixing states and water-uptake of particles to mention just a few examples.

Size, morphologies, chemical compositions, relative abundances and ageing processes of particles produced in biomass burning in southern African were studied with SEM and TEM (*Li et al.*, 2003b; *Pósfai et al.*, 2003). Chloride depletion and sulphur enrichment of individual sea-salt particles was investigated with the TEM on marine air masses (*McInnes et al.*, 1994). Particles were observed to contain a large fraction of non seas-salt sulphate mass, indicating heterogeneous reactions of sea-salt with sulphur compounds in the atmosphere, particularly for samples that had been in contact with polluted continental air masses (*Pósfai et al.*, 1995). Mixing states and hygroscopic properties of particles were studied by observing changes in particle morphologies before and after extracting water from individual particles (*Hasegawa and Ohta*, 2002; *Okada and Hitzenberger*, 2001).

Microscopy methods have also allowed complex morphologies of aggregated soot particles to be described by relating 2-dimensional microscope imagery to actual 3-dimensional structures through computer modelling (*Baron et al.*, 2001; *Brasil et al.*, 1999; *Cai et al.*, 1993; *Köylü et al.*, 1995b; *Neimark et al.*, 1996; *Park et al.*, 2004; *Rogak et al.*, 1993; *Samson et al.*, 1987; *Wentzel et al.*, 2003). Most of these cited experiments have considered particles generated in combustion of petrol, diesel, butane, and other petroleum fuels; or metallic aggregates of silver (Ag), titanium oxide (TiO_2), iron(III) oxide (Fe_2O_3). There is limited information on particles produced from biomass combustion, particles relevant to assess atmospheric impacts of large scale biomass burning processes (*Andreae and Merlet*, 2001).

An approach to study aggregated particles outlined by *Brasil et al.* (1999) will be applied in Chapter 4 to characterise soot particles produced from combustion of wood.

Single particle analysis can also be applied to classify particles abundance, chemical composition and mixing states. The information can be used to derive complex refractive indices of aerosols, and to date this approach has been applied for the first time and only by *Ebert et al.* (2002a, 2004). Using a similar approach in Chapter 5, refractive indices determined from single particle analyses are complemented with conventional techniques of measuring number-size distributions in order quantify optical properties and radiative forcings of particles in an urban environment.

There are several advantages in using single particle analysis compared to ensemble techniques. Firstly, as indicated by examples given, microscopy technique is versatile. The technique can be used to study a range of particle properties since 'important information on particles resides in the morphology and chemical composition of the individual particles' (*Fletcher et al.*, 2001). Secondly, particle sizes are defined from 'direct' techniques of measuring particle geometry (as opposed to conventional sizing techniques where sizes are defined from particle behaviour). Lastly, most analytical techniques require long sampling times to collect adequate sample amount for quantitative analyses, e.g., frequently used ion chromatography technique on impactor and gravimetry samples (*Solomon et al.*, 2001). Single particle analysis is better suited for measurements were high spatial and temporal resolutions are required, e.g., in analysing airborne samples since small sample mass and short sampling times are preferred (Chapter 5).

However, there are some limitations and analytical uncertainties which have to be considered in the analyses of collected and stored samples, both in bulk and single particle analysis techniques. Particles might be altered during or after deposition, changing morphology, chemical composition or both. Samples might be degraded during sampling, e.g., losses of nitrates during sampling by impactors (*Zhang and McMurry*, 1992) or through the interaction of deposited particles with substrates. Losses of H_2SO_4 have been observed on beryllium substrates (*Huang and Turpin*, 1996). Volatile compounds in particles are lost in the high vacuum of electron microscopes, or during interaction of the electron beam with the sample, thereby limiting analytical observations. Particle parameters are derived from digital images, and data quality depends on image resolution, contrast depth in image and operator's visual interpretation and experience. Lastly, single particle analyses is a comprehensive and labour intensive technique, which requires the presence of the operator during microscopy measurements or rigorous verification of results from automated microscope platforms. Hence the number of particles that can be investigated is inferior compared to

other conventional techniques.

1.5.3 Research design

Aerosol types chosen in this study were collected with different sampling techniques and in three atmospheric environments, namely the Amazonia ecosystems, controlled combustion experiments and Cape Town urban area. These samples were collected in experimental campaigns conducted in the Biogeochemistry Department of the Max Planck Institute for Chemistry and the Climatology Research Group of the University of Witwatersrand. Detailed rationale for using microscopy techniques to investigate these aerosol particles are given in the respective Chapters 3 to 5. Because this Ph.D was conducted in the Biogeochemistry Department and the Climatology Research Group, investigations were also appropriated in-line with the research objectives of these institutes. The broader rationale of conducting experiments and at each of the three sites chosen will be given here briefly.

For objective 1 (Chapter 3), impactor samples collected from ground sampling sites in rural areas of the Amazonia ecosystems were investigated. The samples were collected during the Large-Scale Biosphere-Atmosphere Experiment part of the European Studies on Trace Gases and Atmospheric Chemistry (LBA-EUSTACH) and during the Smoke Aerosols, Clouds, Rainfall and Climate (SMOCC) campaigns. These campaigns were aimed at understanding the atmospheric processes in the Amazonian ecosystems, the linkages between trace gas exchanges, aerosols and clouds formation mechanisms (*Andreae et al.*, 2002, 2004; *Artaxo et al.*, 2002; *Zhou et al.*, 2002). Sampling techniques, trajectory analyses chemical properties of these Amazonia aerosols are given elsewhere (*Guyon*, 2002; *Guyon et al.*, 2003; *Rissler et al.*, 2004, 2005). The hygroscopic properties, chemical compositions and particles densities of these Amazonia aerosol particles have been investigated by several researchers (*Guyon et al.*, 2003; *Rissler et al.*, 2004; *Zhou et al.*, 2002). The aim of this study was not to further describe Amazonia ecosystem aerosols, but to use microscopy techniques on these well characterised aerosols to compare the physical definition of particle 'size' as given by several sizing instruments. As discussed in Section 1.2, the definition of size depends on the measurement technique, particle morphology and chemical composition. Because sizing measurements define some equivalent 'spherical particle size', knowledge of the hygroscopic properties and particle density allows these equivalent sizes to be related to physical dimensions which can be retrieved from microscopy techniques.

For objective 2(i) (Chapter 4), soot particles investigated were generated in a laboratory combustion facility of Max Planck Institute for Chemistry, Mainz, as part of the

'Impact of Vegetation Fires on Composition and Circulation of the Atmosphere' (EFEU) project (*Wurzler et al.*, 2001). This combustion facility is described in details elsewhere (*Lobert et al.*, 1991; *Schmid et al.*, 2004). The aim of EFEU project was to characterise biomass burning emissions of various typical biomass fuels ranging from central Europe to tropical fuel types. Aerosol parameters (aerosol optical parameters, number-size distributions, morphology, hygroscopic growth factors and trace gases abundances) were measured in controlled laboratory combustions. These parameters are required as inputs to large scales numerical models to address questions on contributions of biomass burning emissions to aerosol budgets in the atmosphere; extent to which these emissions affect the radiation budget of the atmosphere; emissions influence on cloud processes and; the influence of emissions on the energy budgets of the atmosphere and small scale atmospheric circulation. Emissions from biomass burnings are a significant source of atmospheric trace gases and aerosol particles (*Crutzen and Andreae*, 1990). These emissions can be transported by convection from the local scale to mesoscale and even global scale where they influence the physical, chemical and optical properties of the atmosphere and the formation and microphysical processes in clouds (*Andreae and Merlet*, 2001; *Andreae et al.*, 2004). To enhance current knowledge on these emissions, controlled burning experiments may provide physical and chemical properties of pyrogenic particulate matter by simulating forest or savanna fires (*Lobert et al.*, 1991; *Yokelson et al.*, 1996).

For objective 2(ii) (Chapter 5), aerosols samples were collected on board an aircraft as part of an airborne experiment, Cape Town Brown Haze II (CTBH II) to investigate the atmosphere over Cape Town during intense haze periods in July to August 2003 (*Piketh et al.*, 2004). CTBH II was a follow-up project to CTBH I (*Wicking-Baird et al.*, 1997). It had been observed in CTBH I that emissions from fossil fuel and biomass burning processes were the major contributors to the haze formation. CTBH II was therefore designed to further enhance the understanding of the brown haze with particular emphasis on the chemical apportionment of particulate matter, aerosol particles spatial, number and size distributions, and to characterise elemental carbon using microscopy analyses.

1.6 Outline of thesis

The outline of the thesis is as follows:

Chapter 2. Instrumentation - AFM and SEM

Brief descriptions of the Atomic Force Microscope (AFM) and Scanning Electron Microscope

(SEM) are given. Although the same microscope were employed, parts of the methodologies will also be described in Chapters 3 to 5. This is because information that was extracted to describe particles and the imaging and analytical techniques used were different for each of Chapters 3, 4 and 5. The methodologies are separated in order to maintain coherence in individual chapters.

Chapter 3. Comparative measurements of particle size distributions derived from an aerosol impactor, AFM, and SEM

Aerosol particles collected in the Amazonian ecosystems during dry and wet seasons are studied for particle sizes distributions (*Gwaze et al.*, submitted, a). Sizes defined from aerodynamic and electrostatic sizing techniques are compared to direct physical sizes of particles defined in microscopy analyses. Consistency and uncertainties in sizing parameterisations between microscopy and conventional techniques are discussed.

Chapter 4. Morphological characterisation of soot aggregates from the combustion of wood

Freshly formed soot particles generated from a controlled laboratory combustion are investigated for fractal and dynamic properties (*Gwaze et al.*, 2005). Fractal properties are related to parameters derived from projected surfaces in the SEM images (projected surface area, length, width, and 2D fractal dimension). Influences of resolution in SEM images on these parameters are investigated. Fractal dimension, dynamic shape factors, and specific surface area (surface area to mass ratio) of soot particles are quantified from image analyses.

Chapter 5. Physical, chemical, and optical properties of aerosol particles collected over Cape Town during winter brown haze episodes

This chapter presents airborne measurements of aerosol particles conducted in Cape Town, South Africa during winter of 2003 (*Gwaze et al.*, submitted, b). Measurement techniques and sampling procedures are described. Single particle analysis is applied to time and spatially resolved filter samples collected during four selected flights to determine chemical composition, relative abundance, and mixing states of particle species. Refractive indices of aerosols are determined from chemical compositions of particles identified in SEM analyses. Using these refractive indices and simultaneous in-situ measurements of number-size distributions, optical properties of particles (scattering and absorption coefficients, single scattering albedo, asymmetry parameter, Ångstrom exponent) and direct radiative forcings are quantified from Mie scattering computations.

Chapter 6. Summary, overall conclusions and outlook

Major contributions of this work and future outlooks are summarised in this chapter.

Appendix

A. A list of peer reviewed publications and conference proceedings from parts of this thesis and other research activities undertaken during the study are given.

B. This section of the appendix lists some of the analytical expressions used in this thesis. The expressions were adapted from *Baron and Willeke* (2001a); *Hinds* (1999); *Seinfeld and Pandis* (1998).

C. Other figures and tables relevant to discussions in Chapter 5 are given in this section of the appendix.

Chapter 2

Microscopy Instrumentation - AFM and SEM

Two high resolution microscopes were used to investigate atmospheric particles, an Atomic Force Microscope (AFM) and a Scanning Electron Microscope (SEM). Aerosol particles were collected with different sampling techniques and in various atmospheric environments, namely: (i) impactor samples collected from ground sampling sites in rural Amazonia ecosystems; (ii) filter samples of soot particles produced in controlled laboratory experiments; and (iii) Air Borne Streaker (ABS) samples collected on board an aircraft over Cape Town urban area. Various sampling techniques that were used will be discussed in respective chapters dealing with each of the case studies.

Aerosol samples from the Amazonia were collected on conductive aluminium substrates. For laboratory combustion experiments, substrates (Nuclepore polycarbonate with pore size of 0.2 μm) were coated before sampling with a thin layer of gold (less than 10 nm in thickness) in order to enhance contrast in SEM images and to minimise electrostatic charging of particles. In the Cape Town brown haze study, particles were collected on uncoated Nuclepore straight-through filters with pore sizes of 0.3 μm. The filters were not coated to enhance electrical conductivity (as is common with non-conductive substrates) because coating would interfere with elemental analytical measurements.

Filter samples were cut and glued to magnetic/conductive metal disks for mounting in AFM/SEM. Precautions were taken to avoid contaminating samples by using sterilised instrumentation for cutting and handling samples. Samples were stored in protective casings before and after microscopy analyses.

Brief descriptions of the AFM and SEM will be given in the following sections.

2.1 Atomic Force Microscope

The Atomic Force Microscope used in this study is the CP-Research Model (Digital Instruments CP-II Scanning Probe Microscope, SPM, Veeco Instruments[1]). AFM specifications are given in Table 2.1. Generalised schematics of an AFM are shown in Figure 2.1. To study a sample surface, an AFM probe tip raster-scans the sample with a sharp tip attached to the free end of a cantilever. Inter-atomic van de Waals forces (attractive or repulsive forces) between the tip and sample surface cause the cantilever to bend or deflect. The deflection is measured by a laser beam detector system (in this instrument, a position sensitive photodetector, PSPD) and converted to a map of the specimen topography. SEM image of an AFM tip is shown in Figure 2.2. Further details on the AFM can be found elsewhere (*Binnig et al.*, 1986; *Goldstein et al.*, 1992; *Reimer*, 1998).

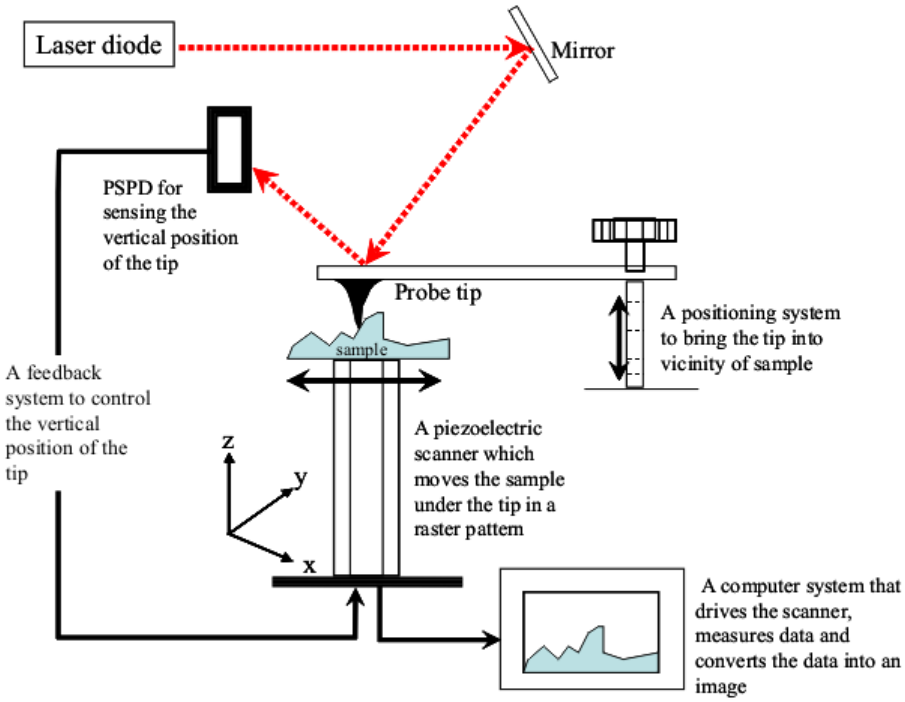


Figure 2.1: Schematics of the Atomic Force Microscope.

In principle, the AFM allows direct physical measurement of a particle's size and shape by measuring its surface in 3D (2π). Possibilities of measuring atomic forces allow the AFM to achieve atomic resolutions on samples at atmospheric pressure (*Binnig et al.*, 1986; *Friedbacher et al.*, 1995). Samples can be investigated under ambient conditions with minimal degradation of sample. Description of particle sizes are independent of some of the confounding physical properties that complicate size measurements by indirect aerodynamic

[1] http://www.veeco.com/

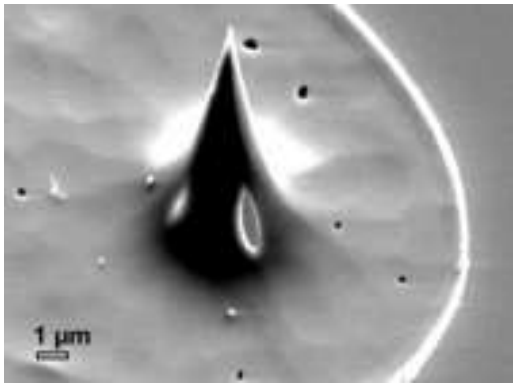


Figure 2.2: SEM image of an AFM probe tip. The tip is attached to a free end of a cantilever *(imaged by J. Huth, MPI, Mainz.)*

Table 2.1: Specifications of the Atomic Force Microscope, CP-Research Model.

Working environment	Ambient temperature and pressure
Working area	Up to 100 μm x 100 μm
Resolution per image	64 to 1024 pixels per profile
Lower limit resolution	0.03 nm
Sample height	Max 3 μm
Oblique view	No
Image information	3D (2π)
Chemical composition	Indirectly from phase information

or optical techniques, e.g., shape factors, particle density or refractive index. The main drawbacks of AFM pertain to the failure in recovering any re-entrant volume of a particle (*Roe et al.*, 2004), and effects of the finite dimensions of the tip which 'convolves' with the sample surface (*Dongmo et al.*, 1996; *Villarrubia*, 1997). Tip convolution will be discussed in detail in Section 3.3.2.

High resolution microscopes are sensitive to ambient noises. This AFM is enclosed in a transparent casing to minimise draughts, and the casing is positioned on a hydraulic table to reduce mechanical vibrations of the building. A metal case covering the sample and probe was used in instances when higher sensitivity was required, to further reduce draughts. Measurements were conducted under ambient conditions, with no control of temperature and humidity.

The AFM was operated in both 'repulsive forces' contact mode and 'attractive forces' non-contact modes (*Binnig et al.*, 1986). Lateral (xy) dimensions of the AFM were calibrated and checked regularly using standard calibration grids of lateral length between

0.9 and 15 μm, and standard grids with heights (z) of 19 ± 1, 104 ± 1.5 and 540 ± 2 nm. To investigate effects of tip geometry, certified polystyrene latex spheres (PSL) of 0.126 ± 0.001 μm (Duke Scientific Corp. USA) and 0.356 ± 0.007 μm (Polyscience, Inc., USA) were analysed (Section 3.3.2). Figure 2.3 shows an AFM image of PSL particles of diameter of 0.356 μm. Only isolated particles which had not been deformed by neighbouring spheres were analysed.

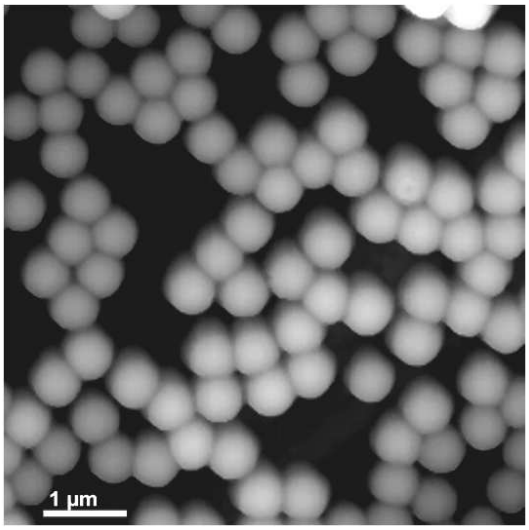


Figure 2.3: 5 μm x 5 μm AFM image of polystyrene latex spheres of diameter 0.356 ± 0.007 μm. The image has a colour depth of 743 nm (0 black and 743 white).

2.2 Scanning Electron Microscope

The Scanning Electron Microscope (Leo 1530 SEM, E. M. Ltd., Cambridge, England, now Nano Technology Systems, Zeiss[2]) used in this study is shown in Figure 2.4 (located in the Particle Chemistry Department, MPI, Mainz). To investigate a sample, a beam of electrons raster-scans the sample surface. Changes in direction (backscattering) or energy (secondary electron excitation, X-ray generation) of the electron beam upon interaction with the sample surface is detected to create an image. Specifications of the SEM are given in Table 2.2.

The microscope is also equipped with a Si(Li) X-ray detector (Oxford Instruments, Link Pentafet detector). The X-rays detection area is 10 mm^2 with a detection accuracy of 10%, resolution of 138 eV at 5.9 keV, and elemental concentration nominal detection limit of 1% by weight (nominal figures). Theories, principles, and techniques of the SEM, particularly on the interaction of the electron beam with the specimen to generate images

[2]http://www.smt.zeiss.com/

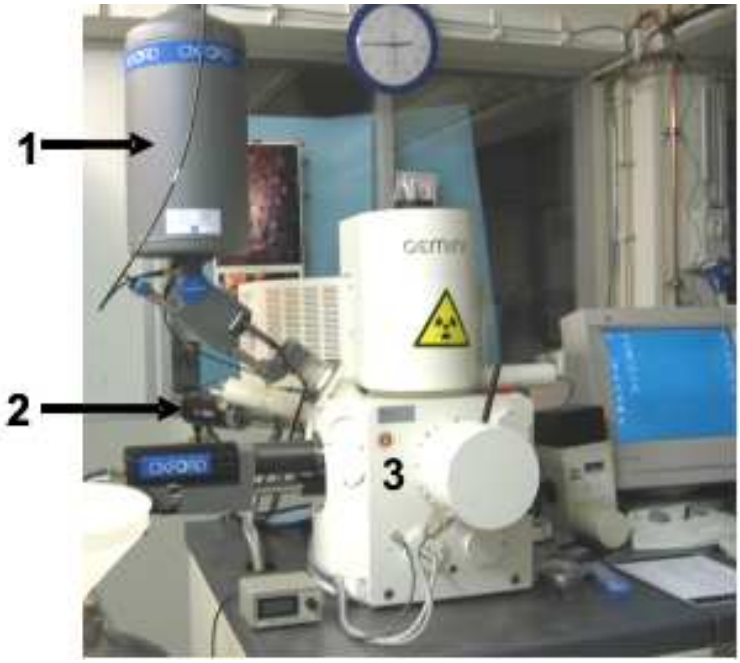


Figure 2.4: Scanning Electron Microscope, Leo 1530 SEM used in this study. Highlighted features are (1) Energy dispersive X-ray (EDX) detector (2) Backscatter electron detector (BSED) and (3) high vacuum sample chamber.

or X-rays can be found elsewhere (*Goldstein et al.*, 1992; *Reimer*, 1998).

The Leo 1530 SEM is a high resolution field emission microscope, capable of investigating particles as small as 3 nm in size. The field emission electron source has advantages of providing a bright electron beam with minimum thermal and current drifts, hence higher resolutions in images can be achieved compared to other electron sources. The SEM provides 2-dimensional (2D) information of particle surface (surface diameter and equivalent diameter of projected surface), complementary elemental composition, and a detailed optical imagery with a large field of view. However, samples are susceptible to mass loss of adsorbed water or volatiles due to the necessity of operating in vacuum and possible damage to particles by the electron beam heating or electrostatic disruption. There is lack of 3D information, and this might introduce bias on sizing measurements of particles that could orient on during deposition on filter, e.g., fibres, aggregates and flat dust particles. Although it is possible to tilt the sample support and measure particle sizes in several electron beam projections, which can then be computed to particle volumes, the procedure is rather laborious, and was not applied in this study.

Images were acquired by selectively combining output of the backscattered electron detector (BSED) with an in-lens annular secondary electron detector (SED) using low acceleration voltages between 1.5 to 2.0 kV. These voltages allowed detection of particles

Table 2.2: Specifications of the Leo 1530 Scanning Electron Microscope.

Resolution	3 nm at 1 kV, 1 nm at 20 kV
Magnification	20X to 900 000X
Accelerating Voltage	200 V to 30 kV
Probe Current	4 pA to 10 nA
Electron Gun	Thermal field emission type
Specimen Stage	x=75 mm, y=75 mm, z=25 mm (all motorized)
Detectors	In-Lens annular Secondary Electron Detector (SED), Backscattered Electron Detector (BSED) and Electron Backscatter Diffraction (EBSD), Energy Dispersion X-ray (EDX)
EDX	Working distance 8.5 mm
Image Processing	Pixel averaging, Frame integration, Continuous averaging
Image Resolution	512 x 384 to 3072 x 2304 pixels
Image information	2D
Working environment	10^{-5} to 10^{-4} Pa

with a low energy, narrow beam, and minimum degradation of samples. The output image used was 1024 x 768 pixels, with 256 grey levels. Although it is possible to achieve higher image resolutions of up to 2304 x 3074 pixels, such resolutions are limited by the hardware capacity and costs of processing images.

Analytical elemental measurements were performed by evaluating X-rays emitted during electron bombardment on individual particles to determine elements with atomic numbers higher than 5 using Energy Dispersive X-ray (EDX) microanalysis. Corrections of matrix effects, electron scatter and internal particle inhomogeneities need to be considered for quantitative chemical analyses. The interaction volume of the sample with the energy beam is a function of the atomic number of the sample and the electron beam energy (*Goldstein et al.*, 1992). For accelerating voltages of 15 and 20 kV used here, the interaction volume could be of the order of a few micrometers for low atomic-number-samples, thus negatively biasing bulk analyses of Aitken and accumulation mode size particles. The EDX analyses were therefore mainly useful for deriving elemental composition of coarse mode and mineral dust aerosol particles.

Calibration of the SEM was verified by measuring standard grids of alternating SiO_2/Si surfaces with lateral (xy) dimensions between of 0.9 and 15 μm, and PSL spheres of diameters 0.126 ± 0.001 μm and 0.600 ± 0.005 μm (Duke Scientific Corp. USA) and 0.356 ± 0.007 μm (Polyscience, Inc., USA). Figure 2.5 shows an SEM image of PSL spheres of $d_p = 0.600$ μm. Deviations between measured sizes of both the standard grids and

PSL spheres and nominal specifications were below 5%. The X-ray detector was calibrated regularly with a Cu standard sample using the 8.04 keV Kα and 0.93 keV Lα energy levels (J. Huth, *pers. comm.*).

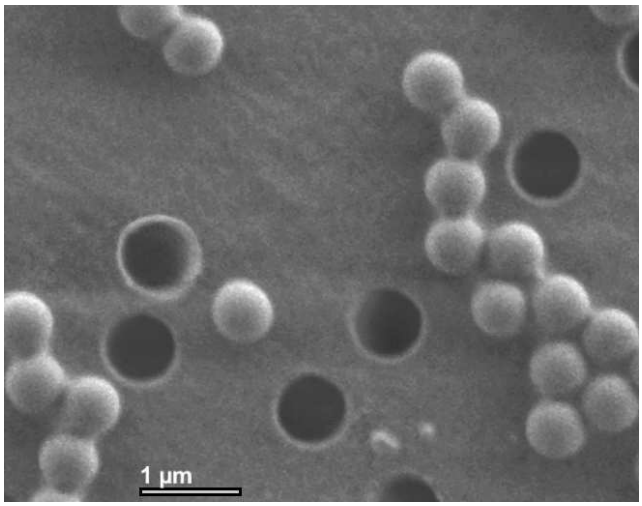


Figure 2.5: 6.22 μm x 5.61 μm SEM image of polystyrene latex spheres of diameter 0.600 ± 0.005 μm. Only isolated particles which had not been deformed by neighbouring spheres were analysed.

Chapter 3

Comparison of Particle Sizes Determined with Impactor, DMPS-APS, AFM and SEM

Contents of this chapter were submitted to Atmospheric Research journal with Harold J. Annegarn, Joachim Huth and Günter Helas as co-authors.

Abstract

Individual particles deposited on four stages of the MOUDI^{TM} (Micro-Orifice Uniform Deposition Impactor) were studied for particle volume, projected surface diameter, and morphology with an Atomic Force Microscope (AFM) and a Scanning Electron Microscope (SEM). Particles were collected in the Amazonia ecosystems during wet and dry seasons, with aerodynamic diameters in the range from 0.1 to 2.5 μm. Samples collected in the wet season were dominated by biological particles, while those from the dry season showed particles with morphologies typical of biomass burning influenced aerosol. Microscopy sizes distributions were verified against distributions derived from response functions of individual MOUDI stages as specified by *Winklmayr et al.* (1990) and for known particle densities. Derived particle volumes were systematically lower than expected from impactor, by factors of up to 3.6. Such differences have been attributed to loss of mass, presumably water adsorbed on particles. However, these losses are high and cannot be accounted for by known humidity growth factors, suggesting losses of other adsorbed volatile compounds as well, particularly on particles collected in the wet season. Findings suggest that, there are inherent problems in defining particle sizes with different sizing techniques, despite accounting for humidity growth and particle density. There are mass losses on individual particles, as opposed to particle losses to walls during sampling, losses which can bias mass measurements of collected particles.

3.1 Introduction

Size of aerosol particle is a fundamental parameter essential in understanding contributions of particles to the radiation budget (*IPCC*, 2001) and effects of particles on human health and air quality (*Nemmar et al.*, 2003). Sizes are defined corresponding to specific physical properties measured with sizing devices, and usually on irregular particles. Direct physical particle sizes can be measured with the Atomic Force Microscope (AFM) and for less volatile aerosols with the electron beam microscope techniques (Scanning and Transmission Electron Microscope - S/TEM).

Some of the earliest studies with the AFM were made by *Friedbacher et al.* (1995). They measured size distributions of particles collected with a 11-stage impactor, and derived size distributions of aerosols with equivalent surface diameters between 0.015 and 3.0 μm comparable to expected impactor performance. Volatile losses and hygroscopic growth of ammonium sulphate particles were studied by measuring particles sizes with the AFM before and after shortly exposing particle to TEM vacuum, while the AFM was kept at ambient conditions (*Pósfai et al.*, 1998; *Simonics and Pósfai*, 2004). *Köllensperger et al.* (1999) observed changes in morphology and surface properties of aggregated soot-like test aerosols by exposing particles to different humidity states in the AFM.

Ideally, sizes derived from different techniques are consistent and similar, when among other parameters of carrying medium, shapes and density of sampled particles are known. It has been shown recently that large dissimilarities can occur when size distributions of mineral dust particles are compared over several sizing techniques, particularly between optical particle and aerodynamic sizing methods (*J.S Reid et al.*, 2003b). Uncertainties can be translated into significant bias when different size distributions are implemented into models to predict radiative forcings of aerosols.

The purpose of this study is to investigate and compare particle size distributions as characterised by microscopy single particle analyses and other conventional instruments - a cascade impactor, an aerodynamic particle sizer and an electrostatic classifier. Physical sizes of particles on four stages of a cascade impactor are measured with the AFM and SEM and verified against size distributions derived from known response functions of impactor stages as specified by *Winklmayr et al.* (1990). The analyses will focus on stages 5 to 8, stages which capture particles with aerodynamic diameters of $0.1 < d_p < 2.5$ μm, as large particles on stages 1 to 4 are beyond the limiting range of height = 3 μm for the AFM employed. The sub-micrometer range studied here is significant since it accounts for

most of the aerosol number, surface area and mass, and particles are known to scatter and absorb light most efficiently in general (*Seinfeld and Pandis*, 1998) and particularly in the Amazonian ecosystems, where samples analysed here have been collected (*Guyon et al.*, 2003).

3.2 Particle sizing techniques

A brief overview on sizing principles of the cascade impactor, electrostatic classifier and aerodynamic particles sizer used in this study will be given first.

3.2.1 Aerodynamic and electrical mobility sizing

Size distributions of particles collected with cascade impactors are well characterised in literature (*Dong et al.*, 2004; *Dzubay and Hasan*, 1990; *Marple et al.*, 1991, 2001; *Winklmayr et al.*, 1990). In cascade impactors, aerosol particles are passed through a number of stages and selectively removed from the gas flow in discrete size ranges by turning the gas flow and capturing particles with sufficient inertia to escape the flow. The size distribution of particles on stages is derived from knowing the response functions of impactor stages, upper and lower size limits of the instrument (*Marple et al.*, 1991). Characteristic of individual stages of the MOUDI (Micro-Orifice Uniform Deposition Impactor) used in this study have been described by *Marple et al.* (1991).

The collection efficiency function $E_n(d_p)$ of a single plate of the impactor at aerodynamic particle diameter of d_p is given by

$$E_n(d_p) = \left[1 + \left(\frac{d_{50}}{d_p}\right)^{2s}\right]^{-1} \tag{3.1}$$

where d_{50} is the nominal particle diameter at 50% collection efficiency, s is the steepness factor on an individual stage n, the number of stage 1 to 10 where stage 1 collects the largest particles. Figure 3.1 shows collection efficiencies of the MOUDI from equation 3.1 as functions of aerodynamic particle diameter.

Calibration parameters of individual stages of a MOUDI are listed in Table 3.1. Steepness factors and cut-off diameters were calculated from the cut-points from *Marple et al.* (1991) for stages 1 to 5, and are based on nozzle pressure drops defined by the manufacturer for stages 6 to 10 (*Roberts et al.*, 2002). The probability of capturing a

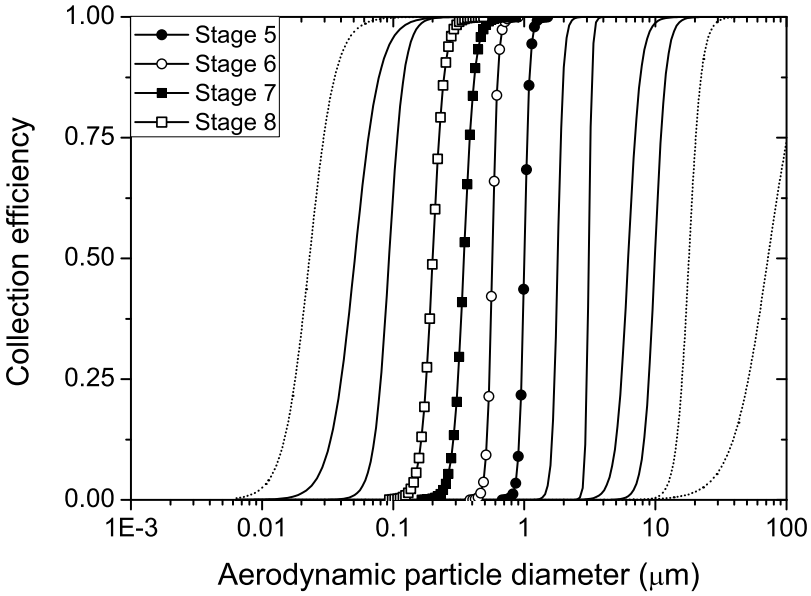


Figure 3.1: Collection efficiency curves of individual impactor stages of a MOUDI. The dotted lines are artificial stages included in the inversion algorithm to recover observed mass distribution (*Roberts et al.*, 2002).

particle with aerodynamic diameter d_p on stage n is given by the stage-specific response function, the kernel function $k_n(d_p)$ (*Winklmayr et al.*, 1990). The function represents the fractional deposition of particles on each impactor stage as a function of particle diameter. For stage n, $k_n(d_p)$ is given by

$$k_n d_p = E_n d_p \tag{3.2}$$

$$k_i(d_p) = E_i(d_p)\ [(1 - E_{i+1}(d_p)) \times (1 - E_{i+2}(d_p)) \ldots (1 - E_n(d_p))] \tag{3.3}$$

where $i = n-1, n-2, n-3, \ldots 1$.

Recovery of aerosol size distributions from cascade impactors has been explored using algorithms that assume no functional form, non-linear smoothed Twomey algorithm (*Dong et al.*, 2004; *Winklmayr et al.*, 1990) or an algorithm which assumes a multimodal log-normal distribution function (*Dzubay and Hasan*, 1990). These algorithms have been used successfully in recovering aerosol mass distribution models to fit experimental observations.

A Differential Mobility Particle Sizer (DMPS) segregates particle sizes on the principle of electrostatic classification, as is detailed elsewhere (*Flagan*, 2001; *Knutson and Whitby*, 1975). Number-size distributions exiting the mobility sizers are narrow, with uncertainties depending on the performance of the mobility sizer, but are within experimental error margins of less than 10% for the setup used in this study (*Birmili et al.*, 1999).

The Aerodynamic Particle Sizer (APS) is a single particle counter measuring the

Table 3.1: Calibration parameters of the MOUDI impactor.

Stage No	**Nominal** d_{50} (μm)	**Calibrated** d_{50} (μm)	**Steepness factor** s
-1^a	-	*72*	*1.6*
0^a	*18*	*18*	*4.6*
1	10	9.9	5.2
2	5.6	6.2	4.6
3	3.2	3.1	17.3
4	1.8	1.8	10
5	1.0	1.0	10.9
6	0.56	0.57	10.4
7	0.32	0.346	5.3
8	0.18	0.20	4.9
9	0.10	0.093	3.8
10	0.056	0.051	2.3
11^a	*0.023*	*0.023*	*2.2*

a - artificial stages included in the inversion routine

number-size distribution of aerosol particles in a jet. Particle size measurement is based upon a particle's transit time between two laser beams that are perpendicular to an accelerating airflow. Smaller particles will follow the jet velocity closely, while larger particles will lag behind because of the higher mass-to-drag ratios. Signal processors measure each particle's transit time between the two pulses of scattered light that are generated as particle intercept two laser beams. The APS measurement technique is fully detailed elsewhere (*Baltensperger et al.*, 2001; *Wilson and Liu*, 1980).

Main concerns with sizing particles with impactors are due to particle losses and effects of particle shapes on the drag coefficient. Interstage losses of small particles ($d_p < 0.1\,\mu$m) due to Brownian motion are between 5-10% (*Marple et al.*, 1991) and might significantly affect sizing measurements if not accounted for in quantitative analysis (*Dong et al.*, 2004). For non-spherical particles, a dynamic shape factor χ has to be applied to the drag and settling velocity to account for particle's shape on its motion (*Hinds*, 1999). Though values of χ can be found in literature for particle species like mineral dust particles, applying shape factors to a heterogeneous aerosol is complicated by the varying composition, particle shapes and dynamic behaviour. For example, on fractal soot particles χ is a function of particle mass and morphology (*Baron et al.*, 2001; *Gwaze et al.*, 2005). Shape of particles affects how particles will align in the streamline, e.g., fibres and chained particles have been observed to align perpendicular to the settling velocity in centrifuges and parallel in electric mobility classifiers (*Wen and Kasper*, 1984).

3.2.2 Microscopy sizing

Several equivalent sizes can be determined from projections of particles in microscope images (*Hinds*, 1999). This study will focus on the volume equivalent diameter of 3 dimensional (3D) volume projected in the AFM image - d_{ve}, and averaged surface diameter (average between the longest axis of particles silhouette and its orthogonal axis). Distributions of d_{ve} can be directly compared to mass of particles on impactor stages when the density of particles is known. The main drawbacks in AFM analysis pertain to the failure in recovering the actual volume of an amorphous particle, the re-entrant volume of a particle (*Roe et al.*, 2004), and effects of probe 'convolution' with sample as will be discussed later. Additionally, size parameters are derived from analysing a small number of particles with comparatively inferior counting statistics to numbers deposited on substrates and numbers probed by other techniques. While automated SEM procedures allow several thousands of particles to be analysed (*Laskin and Cowin*, 2001; *Reid et al.*, 2003a), the AFM used in this study requires a constant presence of the operator, and fewer particles can be investigated. However, particles are studied at ambient conditions in the AFM with minimum damage to obtain 3D information. AFM derived descriptions of particle sizes are independent of some of physical properties that complicate size measurements, e.g., shape factors, particle density or refractive index.

The SEM provides 2D information of particle surface (surface diameter and equivalent diameter of projected surface), complementary elemental composition, and a detailed optical imagery with a large field of view. However, the technique suffers from mass loss in vacuum, from adsorbed water and volatiles on particles, and possible damage of particles by the electron beam. There is lack of 3D information, and this might introduces bias on particles that orient on filter, e.g., fibres and flat dust particles (*E.A Reid et al.*, 2003a). Though it is possible to tilt the sample support and measure particle size in several electron beam projections, which can then be computed to particle volume, the procedure is rather laborious, therefore hardly applied. Other common errors inherent to single particle analyses include personal bias, when the operator might overlook some particles and consider interesting and more familiar features.

3.3 Experimental techniques

3.3.1 Aerosol sampling

Two aerosol samples were collected in Brazil onto aluminium substrates using a MOUDI (Model 110, MSP Cooperation, Minneapolis, USA). The first sample was collected in Rondônia, during the LBA-EUSTACH (Large-Scale Biosphere-Atmosphere Experiment part of the European Studies on Trace Gases and Atmospheric Chemistry) campaign from 8 to 11 May 1999 at Jaru Biological Reserve (10° 04' 55"S, 61° 55' 48"W, 110 m above sea level). Relative humidity (RH) during sampling was between 80% and 100%. This sample will be called hereafter Sample #1. Details on experimental set-up are described elsewhere (*Guyon et al.*, 2003). The second sample was collected at a representative pasture site, Fazenda Nossa Senhora Aparecida on 15 September 2002 (7:40 to 17:45 local time, 10° 45' 44"S, 62° 21' 2" W, 315 m above sea level), during SMOCC campaign, Smoke Aerosols, Clouds, Rainfall and Climate (*Artaxo et al.*, 2002; *Rissler et al.*, 2005). Averaged RH was 65% during sampling. This sample will be labelled Sample #2 hereafter.

For mass distribution measurements, aluminium substrates were conditioned and weighted in a temperature and relative humidity controlled environment prior to sampling (RH of 50% and temperature of 20°C for 24 hours). The particulate mass collected on each stage was weighed with a Mettler microbalance with sensitivity of 1 μg, and an accuracy of ± 3 μg for aluminium substrates (*Guyon*, 2002). Samples were stored in Petri dishes at -18°C to minimise further reactions before microscope analysis. For magnetic/conductive mounting in the AFM/SEM, aluminium substrates were cut and glued with double sided carbon tape onto steel discs.

During the field sampling of Sample #2, two additional direct reading aerosol samplers were deployed, a DMPS (Differential Mobility Particle Sizer) and an APS (Aerodynamic Particle Sizer). The DMPS measured dry aerosol number-size distribution with diameters of 0.003 to 0.850 μm, while the APS measured dry diameters from 1 to 4 μm. Details on experimental set-up are given elsewhere (*Rissler et al.*, 2005). Size distributions were scanned at synchronised 10 minute intervals in both instruments and combined to represent a size range of 0.003 to 4 μm. The scans were averaged over the time the MOUDI was operational during the collection of Sample #2. This averaged distribution is hereafter called DMPS-APS dry distribution. Unfortunately, there were no DMPS-APS measurements during collection of Sample #1.

The EUSTACH and SMOCC campaigns were aimed at understanding atmospheric processes in the Amazonian ecosystems, linkages between trace gas exchanges, aerosols and clouds formation mechanisms. Wet seasons represent clear atmospheric conditions with average particle concentration of 450 cm^{-3} and typical of a background aerosol (*Zhou et al.*, 2002). In particular Sample #1 was considered 'clean' from trajectory analyses by *Guyon* (2002). Dry seasons are influenced by intense biomass burning with high particle concentrations exceeding 40 000 cm^{-3} (*Artaxo et al.*, 2002).

3.3.2 Microscopy analysis and imaging processing

The MOUDI samples were analysed in ambient conditions with the AFM (CP-R Scanning Probe Microscope from Digital Instruments). Relative humidity, RH, during AFM analysis was not measured or controlled, but assumed to be ambient RH of about 50%. Commercially available gold coated conical tips of boron doped silicon with a half angle of 12° (nominal) were used in both contact and non-contact modes of operation. Imaging force between AFM tip and samples was kept between 1 and 5 nN, with scanning rates between 0.01 and 2 Hz. These rates were chosen to avoid the tip damaging or dragging particles during scanning. Scan sizes were varied between 2 and 10 μm with 256, 512 or 1024 pixels per length. These microscope settings were applied to all samples analysed. Several locations on the deposition spots of each stage were imaged. The tip was moved to areas where particle density was low and individual isolated particles could be identified. A reasonably large area was scanned first, with a scan size depending on size of particles expected. Where particles were identified, higher resolution images were obtained by reducing both scan size and scanning speed. Several spots were imaged on each stage to compensate for deposition inhomogeneity. Lateral (xy) and height (z) dimensions of the AFM were calibrated and checked regularly using standard calibration grids of lateral length of 9.9 μm and grid of heights of 19 ± 1, 104 ± 1.5 and 540 ± 2 nm.

The Scanning Probe Image Processor, SPIP[1], Version 3.0.1.1 by Image Metrology was used offline to process images and measure particle dimensions. Image analyses were performed manually to reduce errors due to overlapping particles and contrast artefacts. A first-order levelling function was always applied to images to compensate for sample tilt relative to the tip plane. Some AFM images were filtered to remove high frequency noise. Diameters and heights of at least 100 particles from each stage were measured. Projected surface diameters of particles silhouette, d_a were calculated as the arithmetic average of

[1] http://www.imagemet.com/

the longest axis, the Feret diameter with no preferential orientation (*Hinds*, 1999) and its orthogonal axis passing through the centre of the 2D projected surface area of the particle. The aspect ratio AR was defined as the ratio of the longest to its orthogonal axis. Average heights in AFM images were taken from the same axes profiles as the vertical distance between the base and top of the particle, h_a. An equivalent volume diameter (d_{ve}) of a spherical particle was then calculated from the volume of the semi-ellipsoidal projection in the AFM images (with height h_a, longest axis and its orthogonal axis as dimensions of the semi-ellipsoid). The d_{ve} distributions were normalised to the maximum frequency on each stage, fitted with lognormal functions and compared to expected kernel functions.

The lognormal distribution is the assumed function for aerosol particle sizes since relevant physical parameters (mass, diffusion coefficient) that govern aerosol formation and growth (nucleation, condensation, and coagulation) are smooth and monotonic functions of size (*Twomey*, 1975). Size distributions were fitted with normalised lognormal functions given by

$$\frac{dN}{d\,log\;d_p} = \frac{1}{\sqrt{2\pi}\;\sigma_g}\;exp\left[-\frac{(log\;d_p - log\;d_g)^2}{2(log\;\sigma_g)^2}\right] \tag{3.4}$$

where d_p is the particle diameter, d_g and σ_g are the geometric mean diameter and geometric standard deviation, respectively.

After AFM analyses, impactor samples were investigated with a high resolution SEM (Leo 1530 SEM, E. M. Ltd., Cambridge, England, now Nano Technology Systems, Zeiss). Images were acquired with sample currents of between 5 to 10 picoampere (10^{-12}A) with magnifications of between 30 000 and 80 000 - equivalent to 12.40 to 4.65 nm per pixel, respectively. Sample vacuum was between 10^{-5} and 10^{-4} Pa and RH of less than 10%. Images were 1024 x 768 pixels with 256 grey levels. Some particles had halos around them which had presumably been formed by spreading of a liquid component adsorbed on particles. Such halo silhouettes were excluded in measurements.

The output from scanning probe microscopes is a convolution of the probe (shape and size of AFM tip or SEM beam) with the sample surface (*Dongmo et al.*, 1996; *Todd and Eppell*, 2001; *Villarrubia*, 1997; *Williams et al.*, 1996). This means that the probe adds to the projected length of the particle, an artefact that is a function of the sharpness of the probe and edge of sample. This effect has to be removed in quantitative analyses. Probe convolution may be substantial, particularly when the particle size is comparable to the probe diameter. Probe convolution was investigated by measuring particles of known diameters in the same range of aerosol particles. Spherical polystyrene latex (PSL) particles of diameters d_p of 0.126 ± 0.001 μm and 0.600 ± 0.005 μm (Duke Scientific Corp. USA)

and 0.356 ± 0.007 μm (Polyscience, Inc, USA) were analysed with the AFM and the SEM. PSL particles were deposited on straight through pore membrane filters, and diameters and heights of 40 particles of each size were measured. AFM and SEM images of PSL spheres with $d_p = 0.356$ μm and 0.600 μm are shown in Figures 2.3 and 2.5, respectively.

Tip effects were characterised with a routine in SPIP program, similar to other reported tip algorithms (*Villarrubia*, 1997; *Williams et al.*, 1996). First a blind reconstruction of tip geometry was performed on the AFM images to characterise the geometry of a tip that is most likely to have scanned the sample surface. The reconstructed tip was then used to erode images to obtain an upper bound surface of the actual sample surface. PSL heights from the AFM and projected surface diameters from the SEM matched expected ranges with narrow normal distributions of standard deviation between 0.008 and 0.015 μm. The probe effects in the SEM measurements were insignificant because the width of the electron beam (less than 5 nm) is diminutive compared to sizes of PSL particles, and this was expected. In the AFM measurements, tip effects were observed to be substantial on all particle sizes measured, and this effects requires further investigations. The tip geometry was assumed not to have changed during scanning, and such errors cannot be quantified from this algorithm.

Since particles were collected on aluminium substrates, analyses using an AFM can be complicated due to roughness of aluminium (*Friedbacher et al.*, 1995). Three spots on the substrate, void of particles, were analysed for surface roughness on stage 8 of Sample #1 (3.553 μm x 3.553 μm and 2.75 μm x 2.75 μm) and on stage 7, Sample #1 (2.14 μm x 2.14 μm). Average root mean square roughness was found to be 12 nm, which is about 10% of the smallest surface diameter of particles that was measured. Therefore roughness of aluminium was concluded to be within experimental error margin. Additionally, it is impossible to avoid dragging particles on the substrate during scanning, especially those particles that deposit on top of other particles. Such particles are not as stable under the tip as those that are directly deposited on the substrate. Images that showed evidence of such events were excluded from analyses.

3.4 Data Analysis

3.4.1 Particle morphology

A variety of particle morphologies were observed in the AFM and the SEM images. On Sample #1, there was a high loading of biological particles on stages 5 (nominal d_{50} = 1.0 μm) and stage 6 (nominal d_{50} = 0.56 μm), e.g., brochosomes shown in Figure 3.2 (name suggested by *Tulloch and Shapiro*, 1954). Brochosomes are hollow particles whose surface diameters varied from 0.1 to 0.6 μm. There was also a high concentration of fibrous particles on these stages. If these fibrous particles were not hygroscopic and had maintained their morphology during sampling, they were likely aligned perpendicular to the settling velocity. It is possible that they would bias surface diameter distributions determined in microscopy analysis.

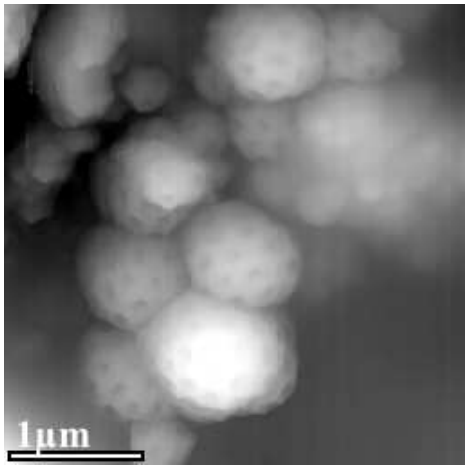


Figure 3.2: AFM topographic image of brochosomes collected on stage 6, Sample #1. The image size is 3 μm x 3 μm with a colour depth scale of 873 nm (0 black and 873 nm white). The image shows distinct surface structure of particles with surface diameters of 0.3 μm to 1 μm.

Figure 3.3 shows surface and topographic AFM images of aerosol particles from stage 6. Apart from sizes, this was the general morphology of most particles observed with the AFM on stages 7 (nominal d_{50} = 0.32 μm) and stage 8 (nominal d_{50} = 0.18 μm). In the SEM vacuum, particles on stages 7 and 8 were highly volatile on both samples, and no observations could be made.

Morphologies of particles on Sample #2 were different from Sample #1. On Sample #2, stages 5 and 6, SEM images showed particles with haloes of volatilised liquids. Haloes are formed from residues of what were probably inorganic salts and polar compounds dissolved in original aqueous component of particles. Central particles within haloes were

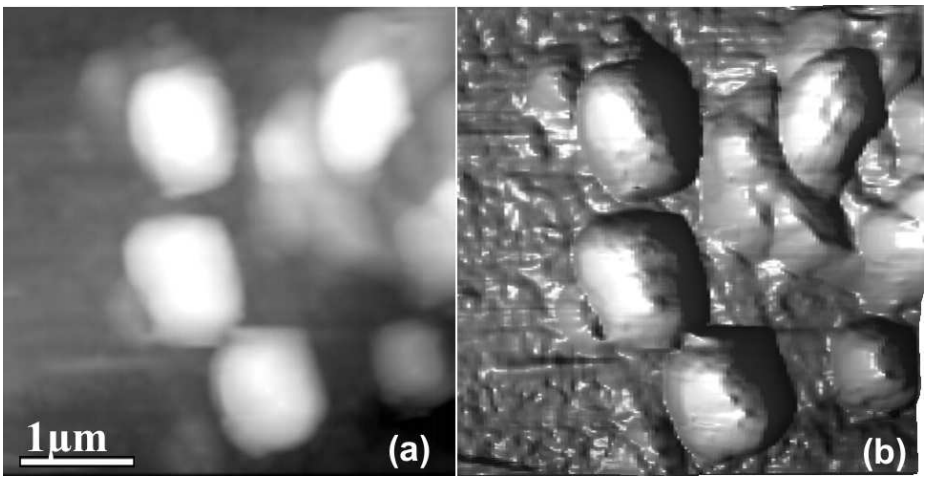


Figure 3.3: AFM topographic image of aerosol particles on collected on stage 6, Sample #1. The image size is 3.89 μm x 3.89 μm. (a) 2D image of particle silhouettes with a colour depth scale of 280 nm (0 black and 280 nm white). (b) 3D image with a shaded relief of surface topography, analogous to shining light onto a 3D surface.

internal mixtures consisting of soot inclusions, volatile euhedral crystalline particles (volatile under SEM electron beam) and large stable spheroids of diameters up to 1 μm. Analytical measurements were not made in this study. However, similar particle morphologies have been observed from single particle analysis of biomass burning influenced aerosol (*Li et al.*, 2003b; *Pósfai et al.*, 2003). With EDS (Energy Dispersive X-ray Spectrometry) the large spheres and the volatile crystalline particles were identified to be tar balls and potassium salts, respectively (KCl for young smoke and K_2SO_4, KNO_3 in ageing smoke).

Although no size measurements were obtained on stage 4, some particles were analysed with the AFM. Figure 3.4 shows a single particle from Sample #1 with distinct surface structure. There was a high concentration of fibrous particles on stage 4, most likely biological in origin, with similar morphologies to particles observed on stages 5 and 6.

In both samples, particles were deposited along the longest axis, and therefore averaged surface diameters d_a were always larger than heights h_a by factors of up to 25. Ratios d_a/h_a are listed in Table 3.2. The ratios decreased with increasing particle diameters, averaging 6.9 on stage 8 to 3.4 on stage 5 for Sample #1. Sample #2 showed a similar trend with larger ratios decreasing from 12.8 to 4.6. Similar differences in d_a and h_a have been observed elsewhere (*Friedbacher et al.*, 1995). As these authors also pointed out, tip dilation alone cannot account for these high ratios. Jet velocities higher than 100 ms^{-1} and moderate pressure drops are encountered in the lower stages of a MOUDI. Differences between heights and diameters might be as a result of high jet velocities experienced upon impaction, velocities which can cause particles to deform as they are pressed and spread to

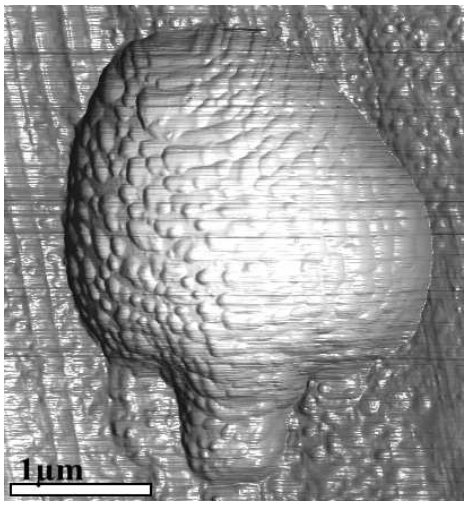


Figure 3.4: 3D image of a single particle observed on stage 4, Sample #1 with $d_a = 3$ μm. The image size is about 4 μm x 4 μm with a colour depth scale of 350 nm (0 black and 350 nm white).

the substrate surface upon, particularly for hydrated particles.

Table 3.2: Ratio of surface diameters to heights, d_a/h_a and aspect ratio AR of projected surfaces.

	d_a/h_a		AR	
Stage No	**Sample #1**	**Sample #2**	**Sample #1**	**Sample #2**
8, AFM	6.9 ± 7.1	12.8 ± 4.6	1.31 ± 0.35	1.23 ± 0.20
7, AFM	4.3 ± 1.9	11.0 ± 5.6	1.21 ± 0.15	1.20 ± 0.19
6, AFM	3.1 ± 1.6	7.7 ± 3.5	1.25 ± 0.74	1.32 ± 0.47
6, SEM	-	-	1.21 ± 0.90	-
5, AFM	3.4 ± 2.1	4.6 ± 2.2	1.51 ± 0.87	1.18 ± 0.18
5, SEM	-	-	1.33 ± 0.65	-

Mean aspect ratios AR are also listed in Table 3.2. Most of the small particle silhouettes were nearly round, while the amount of fibrous particles increasing towards large particle stages on Sample #1, as is indicated by the AR which increases from 1.33 on stage 8 to 1.51 on stage 5.

3.4.2 Particle size distributions

Mass distributions of particles collected with the MOUDI, $dM_{inv}/dlog\, d_p$, were recovered from observed mass distribution $dM_{obs}/dlog\, d_p$ using a Twomey smooth non-linear iterative algorithm (*Kandlikar and Ramachandran*, 1999; *Winklmayr et al.*, 1990). This algorithm calculates collection efficiencies and kernel functions of impactor stages with parameters in

Table 3.1. Additional 'artificial' stages characteristics of real stages are introduced into the routine, before the inlet stage and after the last stage 10, as shown in Figure 3.1. Loadings on stages 1 and 10 were not measured but estimated from a linear extrapolation of $dM_{obs}/dlog\ d_p$. Artificial stages and estimated loadings impose constraints in the inversion in order to recover a reasonable assumed distribution of observed mass distribution (*Winklmayr et al.*, 1990). Number-size distributions of particles $dN/dlog\ d_p$ were then determined from the recovered mass distribution $dM_{inv}/dlog\ d_p$ by assuming spherical particles with known densities. For Sample #1 a particle density $\rho_p = 1.5$ gcm^{-3} was taken as the average of $1.47 < \rho_p < 1.53$ gcm^{-3}, a density range determined from the same samples by *Guyon* (2002). On Sample #2, particle density was defined as the best correlation between simultaneous mass measurements with a TEOM (Tapered-Element Oscillating Microbalance) (*Baltensperger et al.*, 2001) and the DMPS-APS particle mass distribution. Particle densities were $\rho_p = 1.4$ and 1.15 gcm^{-3} for dry and ambient particles, respectively.

To combine the DMPS and APS size distributions, aerodynamic diameters d_p measured by the APS were converted to electrical mobility diameters d_e of dry particles with a density of $\rho_p = 1.4$ gcm^{-3} as

$$d_p = \sqrt{\frac{C_{dp}}{C_{de}}} \cdot \sqrt{\rho_p} . d_e \tag{3.5}$$

where C_{dp} and C_{de} are the Cunningham slip factors of the respective diameters. To recover the ambient aerosol distribution, dry DMPS-APS distribution was simulated with computed growth factors at $RH = 65\%$, the average RH over sampling times. Humidity growth factors had been measured with a Hygroscopic Tandem Differential Mobility Analyzer (H-TDMA) at dry particle diameters of 20, 35, 50, 75, 110, 165, 265 and 440 nm and $RH = 90\%$ with a procedure described elsewhere (*Rissler et al.*, 2005; *Zhou et al.*, 2002). For particles larger than 0.44 μm, growth factors were extrapolated from in-situ measurements, and chemical composition of particles (soluble component) was assumed to be the same as for particles smaller than 0.44 μm. Growth factors were found to be 1.03 to 1.06 for dry particle diameter of 0.1 to 3.0 μm, respectively.

The ambient DMPS-APS size distribution was then computed from growth factors and combined dry distribution for particle diameter of $d_{1.15}$ - representing ambient particles with $\rho_p = 1.15$ gcm^{-3}. The normalised number-size distribution is shown in Figure 3.5. The grey area denotes the deviations of the scans from the arithmetic mean and the solid line is the bimodal fit to the mean distribution. The DMPS-APS distribution can be described by a bimodal lognormal function of geometric mean diameters 0.17 ± 0.03 μm, $\sigma_g = 1.77 \pm 0.15$ and 0.26 ± 0.003 μm with $\sigma_g = 1.46 \pm 0.14$. Size distributions of particles deposited on stages

5 to 8 were then computed from the ambient DMPS-APS distributions through equations 3.1 to 3.3. The dotted line in the plot is the fraction of the distribution collected by the MOUDI on stages 5 to 8.

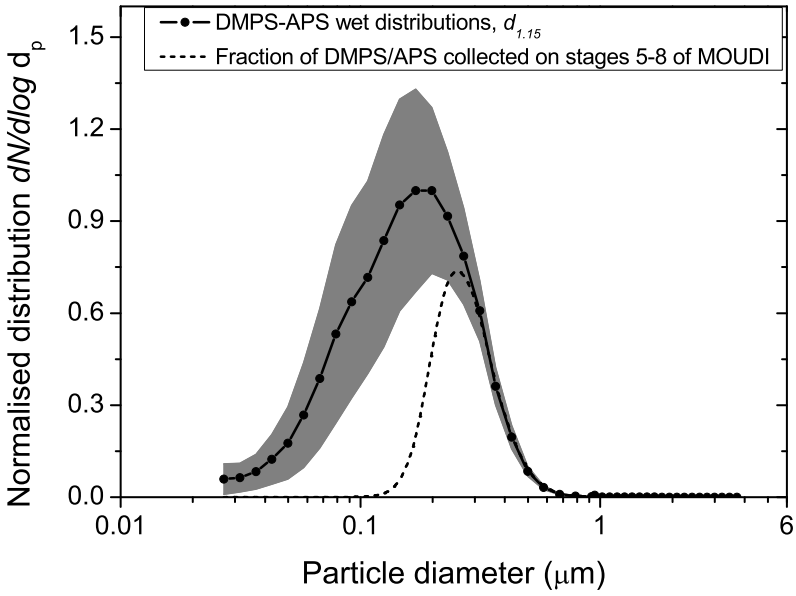


Figure 3.5: Normalised size distribution of particles as a function of Stokes diameter $d_{1.15}$ simulated from combined distributions measured by the DMPS and APS at relative humidity = 65%. The grey area is the standard deviation from the mean, the solid line is the bimodal fit to the mean distribution, and the dotted line is the simulated fraction of the distribution collected by the MOUDI on stages 5 to 8.

3.4.2.1 Sample #1

The kernel functions and measured AFM volume distributions on Sample #1 are plotted in Figure 3.6(a-d). The plots were fitted with lognormal functions of parameters in Table 3.3.

Distributions of equivalent volume diameter, d_{ve}, span an order of magnitude on each stage, unlike the narrow kernel functions. Volumes of particles measured by the AFM are all lower than Stokes diameters of particles with density of 1.5 gcm^{-3} expected on individual MOUDI stages. These observations indicate a loss of particle mass, presumably water. On stage 5 and 6, about 50% of collected particles were brochosomes. Pore spaces of these particles were calculated to be between 30 to 40% of the total particle volume, and increasing with particle sizes. These brochosomes might absorb water into the pores spaces without changing the volume of particles until the pores are filled. This might explain the narrow shift between the expected and measured volumes on stage 6 and on the first peak close to $d_{ve} = 1.0$ μm on stage 5. The second peak of $d_{ve} = 0.35$ μm is likely to be the contribution of a more soluble particle specie.

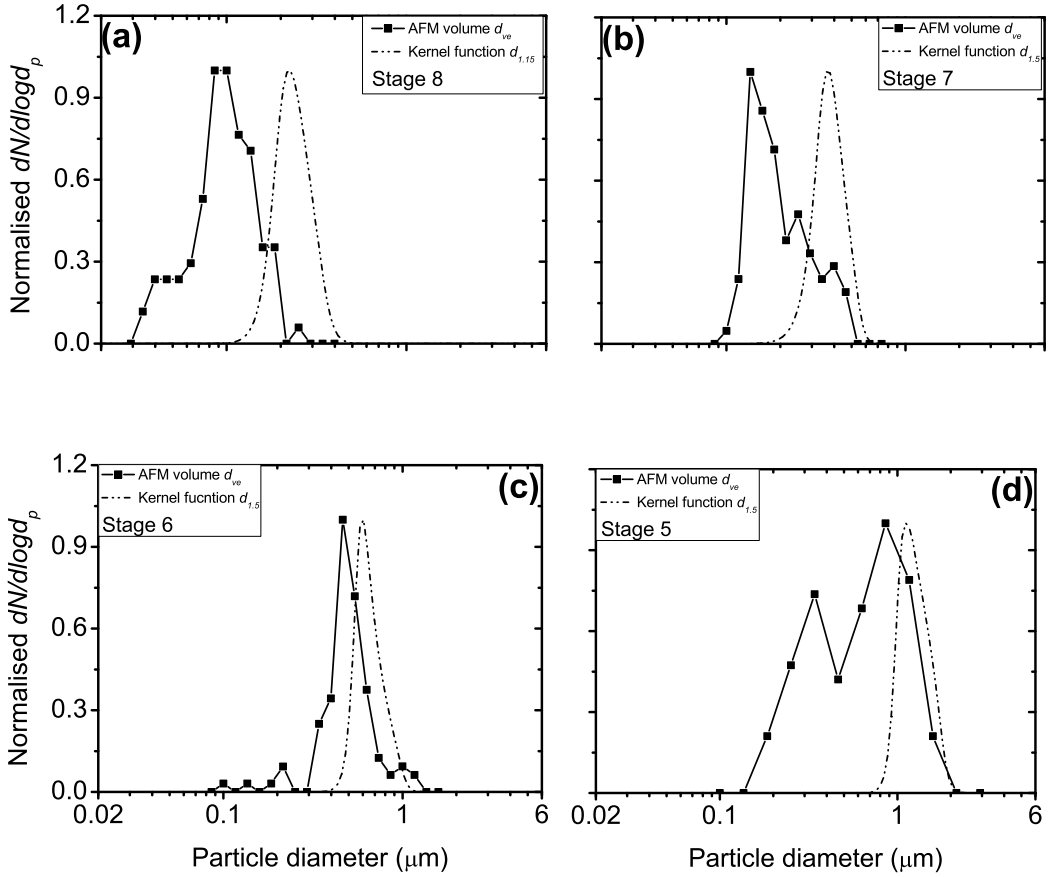


Figure 3.6: Normalised kernel functions (dashed lines) and distributions of d_{ve} (solids) on Sample #1 for stages 8 to 5. The distributions were fitted with lognormal functions of parameters given in Table 3.3.

To compare surface diameters measured between the AFM and SEM, average surface diameters of particles on stages 5 and 6 were plotted in Figure 3.7. Note that here straightforward averaged projected diameter d_a is used, which is directly available from both analyses. On stage 6, AFM particle diameters showed a narrower distribution with a peak at $d_a = 0.63$ μm, while SEM diameters peak are around $d_a = 0.25$ and 0.54 μm. On stage 5, both microscopes show bimodal distributions with smaller SEM diameters. SEM diameters are smaller because the method suffers from mass losses of adsorbed water and volatile compounds on particles in the high vacuum and possibly due to thermal degradation of particles by the electron beam.

Assuming a uniform loss of mass around particles on stage 6, the change between the AFM and SEM is equivalent to a reduction of 54% in volume on particles. Similar observations have been made elsewhere (*Pósfai et al.*, 1998). By measuring the AFM volume of ammonium sulphate particles before and after subjecting them to TEM vacuum for 5 minutes (with the electron beam switched off) *Pósfai et al.* (1998) observed volume decreases of between 30 and 75% on particles with aerodynamic diameters of 0.2 to 0.7 μm (their tip effects were within 5% of measured surface diameters). Their particles were

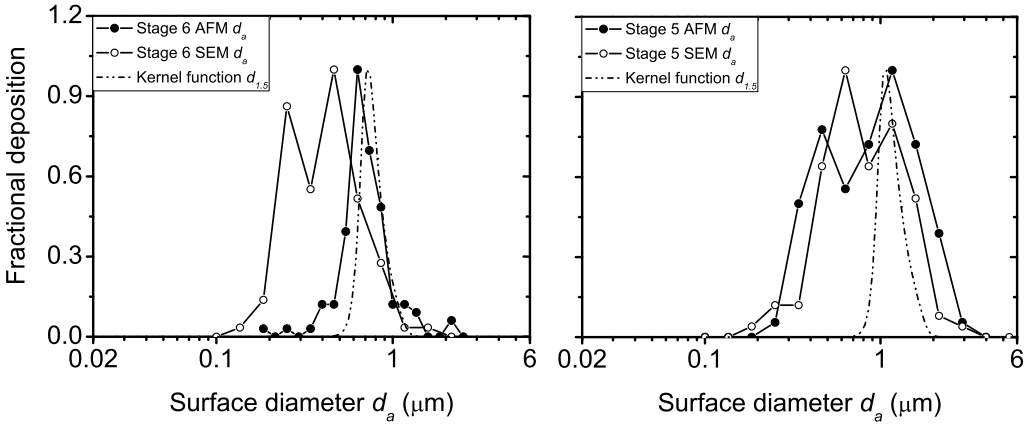


Figure 3.7: Distributions of surface diameters measured with AFM (solid dots) and SEM (open dots) on stages 5 and 6 of Sample #1. Sizes of particles are reduced in the SEM by the loss of water and volatiles in the vacuum.

sampled at $RH = 83\%$, and at these high humidity, sulphates were likely deliquesced, and were sampled as solution droplets (*Tang*, 1996). In this study, Sample #1 was collected in the wet season, when the Amazonia aerosol mass is dominated by up to 40% soluble organic material and 15% inorganic salts (*Roberts et al.*, 2002). It will be shown that these particles likely contained significant amount of water during sampling.

3.4.2.2 Sample #2

Size distributions measured on Sample #2 are shown in Figure 3.8(a-d), and parameters of the lognormal fits are listed in Table 3.3. Distributions of d_{ve} on stages 7 and 8 compare well with the expected kernel functions, with broader distributions of d_{ve}, likely due to tip convolution. Projected surfaces of particles on stage 8 were corrected for tip dilation with the algorithm described in section 3.2. After tip correction heights of particles remained the same (mode of 0.074 ± 0.006 μm before and after tip correction, and not altered as expected) while the geometric mean d_{ve} was reduced by 11% from 0.31 μm to 0.28 μm (and for d_a from 0.67 μm to 0.60 μm). The confidence in the convolved output, measured as the probability of a surface being probed by just the tip apex, was low on the projected edges of particles unless one opted for an unrealistically sharp tip. Since these are critical areas of interest in the measurements, tip deconvolution was not applied to the rest of the samples. It should be noted therefore that particle volumes calculated represents modestly more than the possible upper surface of the particle geometry, notably on small particles while on larger particles, this effect should be of less importance.

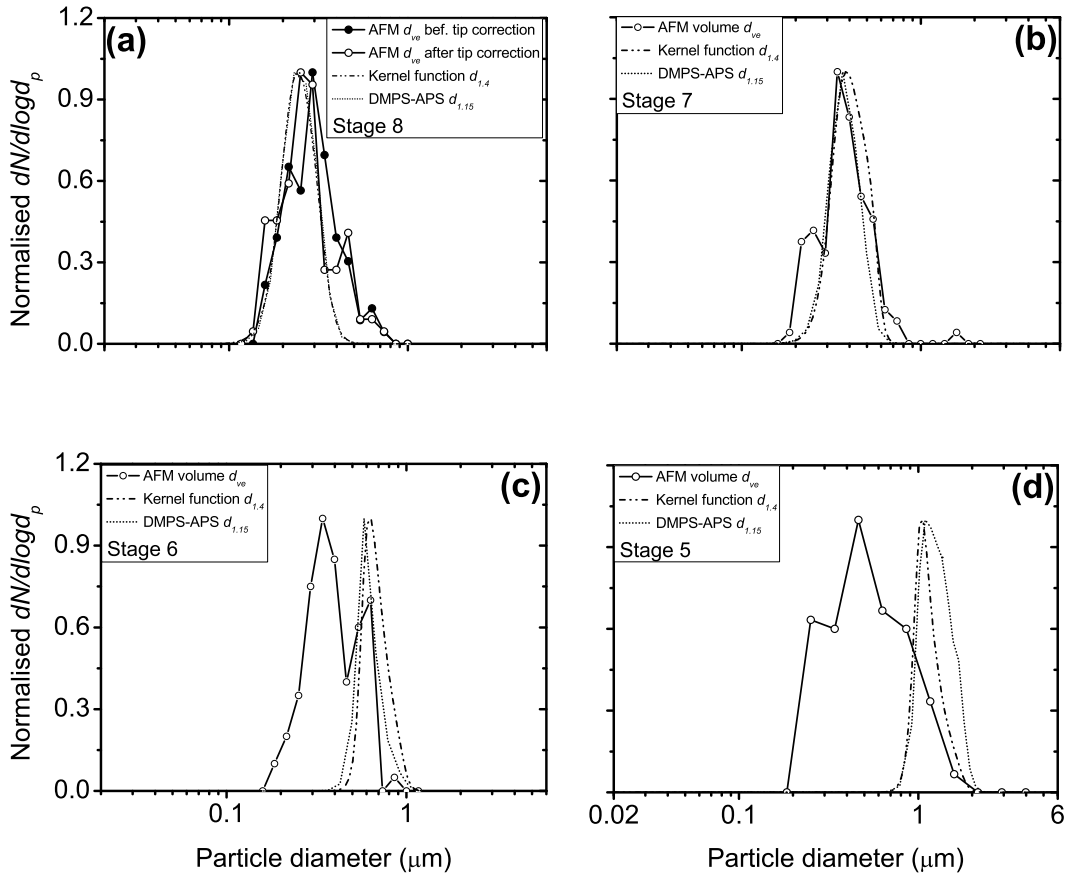


Figure 3.8: Normalised kernel functions (dashes), simulated ambient DMPS-APS size distributions (dotted), and distributions of d_{ve} (solids) on Sample #2 for stages 8 to 5. The distributions were fitted with lognormal functions of parameters given in Table 3.3.

Distributions of d_{ve} on stages 6 show two peaks, one of particles within the expected size range where $d_{ve} = 0.60$ μm and much smaller particles with $d_{ve} = 0.36$ μm. If size discrepancies between the kernel function and d_{ve} distributions are due to water losses, these peaks correspond to two particle species with different hygroscopic properties. Like Sample #1, particles on stage 5 were also smaller than expected.

Table 3.3: Geometric mean diameters derived from fitting lognormal functions to size distributions in Figures 3.6 and 3.8 where, d_{ve} = equivalent volume diameter projected in AFM images, d_a = averaged surface diameter, d_ρ = Stokes diameter at particle density of ρ_p = 1.15, 1.4 or 1.5 g/cm^3 and $R^2 > 78\%$.

Sample #1

Stage No.	**MOUDI**		**AFM volume**		**Averaged surface diameters**	
	$d_{1.5}$	$\sigma_{1.5}$	d_{ve}	σ_{ve}	AFM d_a	SEM d_a
5	1.25 ± 0.01	1.61 ± 0.03	1.00 ± 0.02	1.39 ± 0.10	1.41 ± 0.03	1.35 ± 0.03
5*	1.25 ± 0.01	1.61 ± 0.03	0.35 ± 0.02	1.36 ± 0.14	0.46 ± 0.02	0.65 ± 0.03
6	0.636 ± 0.002	1.22 ± 0.03	0.50 ± 0.01	1.66 ± 0.02	0.70 ± 0.01	0.54 ± 0.12
7	0.38 ± 0.01	1.15 ± 0.02	0.16 ± 0.01	1.23 ± 0.10	0.27 ± 0.01	-
8	0.240 ± 0.001	1.11 ± 0.02	0.12 ± 0.01	1.44 ± 0.12	0.18 ± 0.01	-

Sample #2

Stage No.	**MOUDI**		**DMPS-APS**		**AFM volume**		**AFM surface**
	$d_{1.4}$	$\sigma_{1.4}$	$d_{1.15}$	$\sigma_{1.15}$	d_{ve}	σ_{ve}	d_a
5	1.10 ± 0.01	1.36 ± 0.03	1.28 ± 0.01	1.73 ± 0.08	0.67 ± 0.06	1.96 ± 0.06	0.93 ± 0.03
6	0.664 ± 0.002	1.21 ± 0.03	0.602 ± 0.002	1.13 ± 0.04	0.60 ± 0.01	1.10 ± 0.01	0.79 ± 0.03
6*	0.664 ± 0.002	1.21 ± 0.03	0.602 ± 0.002	1.13 ± 0.04	0.36 ± 0.01	1.24 ± 0.08	-
7	0.417 ± 0.001	1.20 ± 0.02	0.382 ± 0.002	1.15 ± 0.02	0.40 ± 0.02	1.28 ± 0.12	0.81 ± 0.01
8	0.254 ± 0.001	1.11 ± 0.01	0.256 ± 0.001	1.11 ± 0.02	0.31 ± 0.01	1.33 ± 0.03	0.67 ± 0.02
				after tip deconvolution	0.28 ± 0.01	1.37 ± 0.17	0.60 ± 0.02

* additional peaks

3.5 Discussion

Except on Sample #2 stages 7 and 8, the AFM volume distributions did not adequately reproduce the expected distributions recovered from measured mass distributions. Equivalent volume diameters were smaller than Stokes diameters by factors up to 3.6. These observations indicate significant loss of particle mass, presumably water. During the wet season, relative humidity was greater than 64% for 95% of the time (in the range of $98 - 100\%$ for 50% of the time), while in the dry season, relative humidity was greater than 48% for 95% of the time, and $98 - 100\%$ for 31% of the time (*Guyon et al.*, 2003). In these high humidity conditions, hygroscopic particles absorb water, with uptake of water depending on the amount of soluble fraction and sizes of solid particles. Amazonia fine mode aerosols are primarily composed of highly soluble sulphates and organics, with up to 25% of the fine fraction originating from soluble biogenic emissions of reduced compounds in the wet season (*Guyon et al.*, 2003). A soluble fraction of $5 - 10\%$ sulphate was observed to be sufficient in explaining growth of activated CCN (Cloud Condensation Nuclei) in size range of dry diameter of $0.05 < d_p < 0.5$ μm (*Rissler et al.*, 2004; *Roberts et al.*, 2002). Particles investigated here were therefore likely sampled with high water content and therefore likely spherical in shape. This implies that effects of particle shape on the drag coefficient and particle bounce between stages are negligible.

Particles could have changed their morphology during or after deposition on aluminium substrates, as indicated by high d_a/h_a ratios in Table 3.2. The liquid component of particle might have evaporated after deposition and what we are now measuring is a dehydrated component of aerosol particles, at less than 10% relative humidity in the SEM and ambient laboratory relative humidity in the AFM (assumed to be about 50%, though not measured). However, it is not possible to confirm whether particles had recrystallised, or still contained some adsorbed water in equilibrium with ambient air during AFM analyses.

SEM images showed large haloes around most of particles suggesting the presence of a liquid on particles, which might have reacted with the aluminium substrate. Figure 3.9 shows such a typical particle from stage 6, Sample #2. In this image, there are smaller particles in the halo. The smaller particles had either recrystallised and separated from the main particle during evaporation of water or disintegrated on impaction. The averaged surface diameter of the halo is $d_a = 5.70$ μm, for the large particle (treated as an agglomerate) $d_a = 1.70$ μm, and for the smaller particles d_a is about 0.37 μm. The SEM provides a large field of view and contrasting colour depths depending on the topography and also chemical composition, and therefore haloes can be identified. However, in AFM topography

mode used in this study, haloes do not provide enough height contrast. It is possible that smaller particles in the haloes were treated as distinct individual particles, further biasing distributions to smaller sizes. Losses of presumably water are high as indicated by the large halo in SEM image.

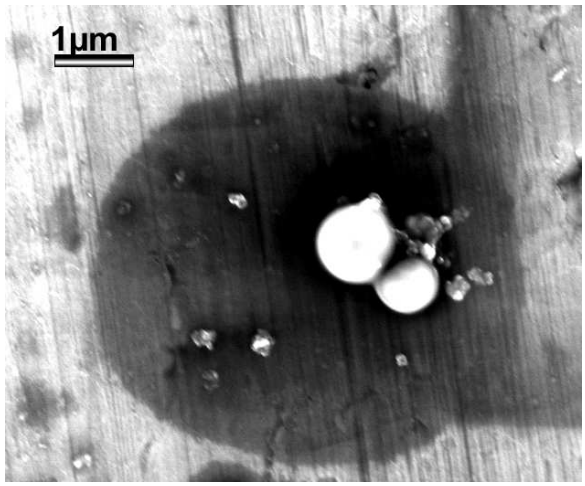


Figure 3.9: SEM image of a particle with a large halo (the dark circular area). The liquid component adsorbed on the particle reacted with the aluminium substrate before it was lost either during storage or in the SEM vacuum. The averaged surface diameter of the halo is 5.7 μm and the agglomerated particle is about 1.7 μm.

Deviations between DMPS-APS size distributions and MOUDI kernel functions are small, as was expected because of the low growth factors of 1.02 and 1.06 for dry diameters of 0.020 μm and 3.0 μm, respectively and at $RH = 65\%$ (1.07 to 1.25 at $RH = 90\%$). However, deviations between the kernel functions and equivalent volume diameter d_{ve} on Sample #2 do not reflect that. There were no hygroscopic growth measurements during the collection of Sample #1, but representative measurements of wet season aerosols from March to April 1998 at Balbina, Manaus (1° 56'S, 59° 25'W) showed averaged growth factors for dry diameters of 0.035 to 0.265 μm to be 1.16 to 1.32 at $RH = 90\%$ (*Zhou et al.*, 2002). Humidity growth factors were measured in increasing RH, whereas microscopy sizes were measured in sinking RH. Hysteresis effects, particularly on mixed particles might have influenced the sizes of the particles in the AFM. However, with just the hysteresis effects, AFM particles sizes should have been slightly larger since particles retain more water in sinking RH than in rising RH (*Seinfeld and Pandis*, 1998; *Winkler*, 1988). Furthermore, at ambient relative humidities (assumed in AFM), differences in particle sizes due to hysteresis effects might be in the range of experimental error. All this implies that hysteresis effects cannot account for the observed difference between microscopy and expected particle sizes.

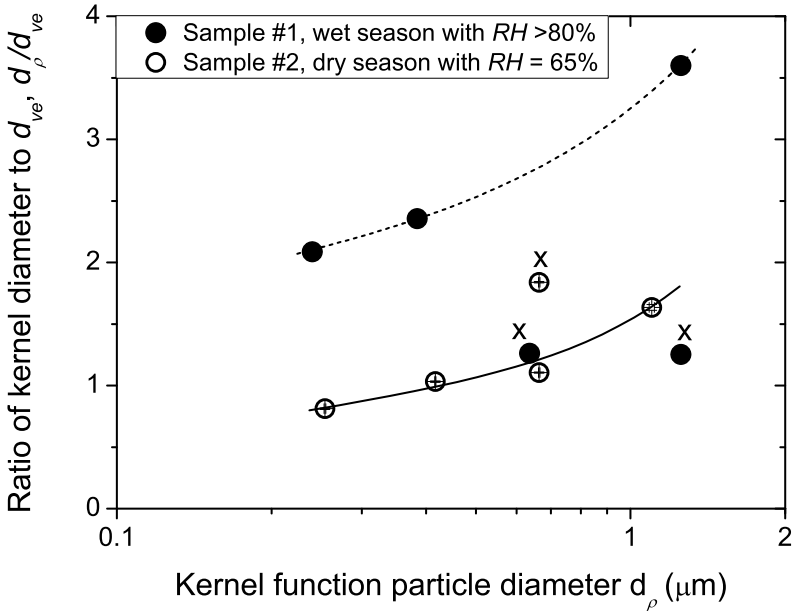


Figure 3.10: Ratios of geometric mean diameters of the kernel functions (d_ρ) and equivalent volume distributions (d_{ve}) in Table 3.3. The lines are the best fits to the plots and exclude the out-layers labelled X.

Figure 3.10 shows ratios of d_ρ/d_{ve}, where d_ρ and d_{ve} are the geometric mean diameter of the kernel functions and AFM volume distributions, respectively. The lines are the best fits to the plots and do not include points with x labels. Although the ratios are not a direct measure of particle growth with humidity, changes in particle volumes reflect higher water content. Three features can be identified in this plot. Sample #1 was collected during higher humidity conditions and shows ratios of d_ρ/d_{ve} up to 3.6 on stage 5, with all ratios higher than on Sample #2 collected at dairy mean $RH = 65\%$. Large particles lost more volume of mass per dry particle, consistent with dependence of humidity growth on size of dry particles. On Sample #1, ratios of d_ρ/d_{ve} on stages 5 and 6 do not show the same response as other stages. As discussed before brochosomes (which constitute more than 50% of the number concentrations on these stages) will take up water by capillary condensation in the pore spaces without the particles necessarily growing. It is worth noting also that other particles were internally mixed, consisting of soluble salts, organics and insoluble material (*Guyon et al.*, 2003). Particles on stage 6 (Sample #2) with $d_\rho/d_{ve} = 1.84$ might correspond to particle specie with larger components of soluble material. Additionally, losses of water higher than expected can be attributed to increased hygroscopicity by organic coatings on particles, particularly on sulphate particles (*Buseck and Pósfai*, 1999).

There are limitations to consider in deriving d_{ve} from projected images. Equivalent

volume diameters were calculated by assuming ellipsoidal hemispheres as projected volumes in AFM images. This assumption is valid on particles with smooth and rounded surfaces on both projected surface silhouette and height profile. The equivalent volume for non-spherical particle like cylindrical (e.g., fibres) and prism (minerals and salts) are underestimated when calculated from ellipsoidal volumes with the same dimensions. Such effects on amorphous particles are not easily obvious. The second assumption made was that particles were compact, and they had deposited firmly on the aluminium without voids. Volumes of particles were therefore overestimated if there were gaps between particles and substrate. In addition, samples #1 and #2 were collected for 70 and 10 hours, respectively. Over such long time intervals variations in the aerosol composition, e.g., due to changes in meteorological conditions are likely to occur. Water-soluble inorganic aerosol species were observed to exhibit a strong diurnal variations due to changes in micro meteorological conditions (*Trebs et al.*, 2004) and also to a less extent the elemental composition of the fine mode aerosol (*Guyon et al.*, 2003). Measurements in this study might be generalising particles with different origins and chemical compositions.

However, despite these possible uncertainties, our observations show systematic shortcomings inherent to size and possible mass measurements on collected particles. Although mixing state of particles and chemical compositions can be obtained from SEM analyses (*Ebert et al.*, 2002a; *Hasegawa and Ohta*, 2002; *Pósfai et al.*, 2003), this study shows there is clear misrepresentation of particle sizes when there are mass losses, even in AFM ambient state. It is not possible in this study to determine how much the observed mass distributions of the MOUDI were underestimated by these losses. However, if they were, there is need to conduct number-mass closure studies to validate and quantify uncertainties on impactor mass distributions when particles are collected in varying humidity conditions. Closure experiments produce an over determined set of observations such that the measured value of an aerosol system property can be compared to a value calculated with an appropriate model based on independent measurements (*Quinn et al.*, 1996). As seen here, reconciling mass losses with humidity growth factors might not be enough to account for water losses. This reconciliation is made complex by the multimodal size distributions seen on some individual stages.

One such a closure experiment could be the use of a number-size concentration counter (e.g., optical particle counter or DMPS-APS) to test for consistency of impactor mass measurements. Mass distributions can be measured at several conditioned RH while the DMPS-APS measure number size distributions of particles at fixed dry conditions of $RH = 10\%$. Growth factors of particles can be measured with the H-TDMA at these con-

ditioned RH. Knowing growth factors and density of dry particles, dry particle diameters can be converted to conditioned (wet) aerodynamic diameters measured by the impactor. The DMPS-APS number-size distributions can be further converted to mass distributions and compared directly to the observed mass distributions measured by the impactor.

3.6 Conclusion

Geometric size distributions of particles deposited on four stages of a MOUDI impactor were measured with the AFM and SEM and compared to the expected distributions defined from the kernel functions of impactor stages. Physical sizes were systematically smaller than expected on each individual stage. Shifts were attributed to losses of mass between sampling and microscope analyses times, particularly losses of water adsorbed on particles. This is supported by large haloes of liquid on particles observed in SEM images. The study shows that large uncertainties in size distributions can occur when analyses are applied to particles collected in high humidity states. There are mass losses on individual particles, as opposed to particle losses to walls during sampling. Losses cannot be accounted for by humidity growth factors, indicating appreciable losses of both water and other volatile compounds. Such losses might bias observed mass distribution and hence number-size distributions of collected particles. As this effect could not be generalised in this study, it would be worthwhile in future to conduct closure experiments to validate and quantify such effects over a range of ambient conditions. One such a procedure could be the measurement of aerosol properties with particle number counters in parallel an impactor at varying humidity. Plausible uncertainties need to be addressed as measurements from collected and stored particles are widely used in the aerosol community.

Chapter 4

Characterisation of Soot Aggregates from Combustion of Wood

Contents of this chapter have been published in Journal of Aerosol Science, with Otmar Schmid, Harold J. Annegarn, Meinrat O. Andreae, Joachim Huth and Günter Helas as co-authors.

Abstract

Morphological and dynamic properties of fractal-like particles produced from combustion of wood are studied in this work. Particles with electrical mobility diameters of 200, 275, 350 and 450 nm were deposited on filters and imaged using a high resolution Scanning Electron Microscope (SEM). Soot particles consisted of aggregated primary spheres with geometric mean radius $a_p = 25.5 \pm 3.5$ nm and geometric standard deviation $\sigma_g = 1.27 \pm 0.09$. The fractal dimension of aggregates D_f was derived from three techniques: (i) $D_f = 1.84 \pm 0.05$ from projected surfaces in SEM images; (ii) $D_f = 1.83 \pm 0.05$ from the relationship between number of primary particle per aggregate N and radius of gyration R_g; (iii) $D_f = 1.80 \pm 0.13$ from the relationship of mobility and N. Thus, there is agreement between the three techniques with an average D_f of 1.83. Dynamic shape factors of soot particles were 1.7 to 2.5 and increasing with N. In the regime $0.2 < Kn < 0.7$ (Knudsen number, $Kn = 2\lambda/d_{mob}$) the mobility diameter d_{mob} was observed to be proportional to the radius of gyration with a ratio $d_{mob}/2R_g = 0.81 \pm 0.07$. The specific surface area of aggregates was determined to be 70 ± 10 m^2/g based on SEM image analysis.

4.1 Introduction

Emissions from combustion of biomass and fossil fuels represent significant sources of anthropogenic aerosols in the atmosphere. Particles are formed mainly from condensation of pyrolysis products, atmospheric oxidation of emitted volatile organic gases, and from complex growth processes that form chained soot particles (a variety of black carbon) (*Cachier*, 1998). Particulate emissions consist of ash, char, resuspended dust, soot particles, condensed high molecular hydrocarbons, and unburnt fuel matrix. Apportionment of these emissions depend on several fire characteristics (*Lobert and Warnatz*, 1993). This study will concentrate on soot particles which are formed from complex polymerisation of reactive gaseous precursors through nucleation, surface growth and coalescence to form small nearly spherical individual primary particles. Primary particles are made of concentric wavy graphitic layers, sometimes with intrusions of crystalline material, e.g., potassium salts or silica in biomass burning soot particles (*Li et al.*, 2003b; *Pósfai et al.*, 2003; *Wentzel et al.*, 2003). Although organics are the largest single fraction of carbonaceous aerosols (estimated source strength of 55 to 110 Tg/yr), black carbon component (12 to 17 Tg/yr) has a strong influence on the radiation budget of the earth because of its high absorption efficiency and its influence on cloud micro-physical processes (*Andreae and Merlet*, 2001; *IPCC*, 2001).

Primary particles cluster and form chained and branched aggregates that have a fractal-like morphology (*Meakin*, 1983). The aggregation process can be represented in computer simulated models by clusters following trajectories of random walks (Brownian motion of fractal dimension = 2), and colliding to generate tenuous particles - diffusion limited cluster aggregation, DLCA (*Meakin et al.*, 1989). The term cluster denotes an agglomerate of at least two primary particles. The fractal dimension D_f, the Hausdorff dimension for self-similar aggregates produced by DLCA in aerosols is around 1.78 (*Julien and Botet*, 1987). For 3D aggregates, the fractal dimension can vary from 1 to 3. For spherical particles in which density of matter is isotropic $D_f = 3$, irregular particles with isotropic density $D_f \approx 3$, and in the limit of long straight chains $D_f \to 1$.

Köylü et al. (1995a) investigated soot aggregation from four fuel types (acetylene, propylene, ethylene and propane). They concluded that although primary particle and aggregate parameters depend to some degree on fuel type and flaming conditions $D_f = 1.82 \pm 0.08$ was the best estimate for soot aggregates independent of fuel types and burning conditions. However, the size of primary particles depends on fuel type. Diesel combustion generates spheres between 10-30 nm in diameter, while larger primary particles are observed in biomass burning soot (*Cachier*, 1998).

Transmission Electron Microscopy (TEM) has become a common technique in investigating structural and geometric properties of soot aggregates (*Brasil et al.*, 1999; *Cai et al.*, 1993; *Köylü et al.*, 1995b; *Neimark et al.*, 1996; *Park et al.*, 2004; *Rogak et al.*, 1993; *Samson et al.*, 1987; *Wentzel et al.*, 2003). Use of the Scanning Electron Microscope (SEM) has been significantly limited due to lower resolution in some SEM models compared to TEMs. In several of these studies, DLCA and diffusion limited particle-cluster (DLPC) numerical simulations were related and compared to 2D projected surfaces from microscopy imagery to determine real 3D properties of aggregates. Using these comparisons and experimental methods *Wentzel et al.* (2003) derived a fractal dimension of 1.70 ± 0.13 from diesel soot aggregates; *Köylü et al.* (1995a) found $D_f = 1.82 \pm 0.08$ from four fuel types; D_f was 1.74 ± 0.04 for soot from premixed methane/oxygen flame (*Cai et al.*, 1995); D_f was $1.5 - 1.6$ on soot aggregates formed in the combustion of acetylene (*Samson et al.*, 1987).

There are limitations inherent to relating 2D projection to real 3D structural properties. Apparent overlap of primary particles in 2D projection increases D_f and the gyration prefactor derived from 2D images (*Oh and Sorensen*, 1997). The number of primary particles and lengths of aggregates are influenced by resting position of the aggregate on the substrate (*Brasil et al.*, 1999). Asymmetry properties depend on the aggregate projection (*Meakin*, 1989). Additionally, deriving fractal dimension of 3D particles from 2D images is limited by the inability to distinguish 3D aggregates with $2 < D_f < 3$, as any $D_f < 2$ results in a projection with $D_f = 2$ (*Katrinak et al.*, 1993; *Tence et al.*, 1989).

Dynamic behaviour of aggregates differ from that of ideal spherical aerosol particles of the same mass, which complicates application of standard devices such as Differential Mobility Analysers (DMAs) to fractal particles. Besides accounting for dynamic properties of particles in an electric field, multiple charging needs to be considered. Schmidt-Ott derived fractal properties and dynamic shape factors of Ag aggregates in-situ by measuring electrical mobility of aggregates before and after heating-induced collapsing of the aggregates (*Schmidt-Ott*, 1988). Kasper and colleagues have published extensive work on aerodynamic, drag and geometric characterisation of linear chains with regards to size distribution determined by a DMA and centrifuge (*Kasper*, 1982; *Wen and Kasper*, 1984). They assigned electric charge in chains by calculating shape factors on the mean chain lengths from the number of primary particle density peaks. *Rogak et al.* (1993) assigned multiple charging in aggregates classified with a DMA by relating the equivalent diameter of projected area d_a with the mobility diameter d_{mob}, and found that for aggregates with $d_{mob} > 1000$ nm, $d_a \approx d_{mob}$.

Most experimental studies on fractal aggregation have considered particles gener-

ated in combustion of petrol, diesel, butane, and other petroleum fuels; or metallic aggregates of Ag, TiO_2, Fe_2O_3 and others. Information on the relationship between structural and dynamic properties of soot aggregates from biomass combustion is therefore still scarce. Morphologies of biomass soot are relevant to assess their atmospheric impacts. Laboratory experiments under controlled combustion conditions may provide physical and chemical properties of pyrogenic particulate matter by simulating forest or savanna fires (*Lobert et al.*, 1991; *Yokelson et al.*, 1996). Challenges are to configure experiments to be representative of forest fires where combustion processes depend on fuel structures, moisture content and prevailing meteorological conditions.

The objectives of this study are to present an experimental description of both morphological and dynamic properties of fractal-like soot aggregates from biomass combustion. Soot particles are produced in a controlled combustion experiment of beech wood and selected for monodisperse equivalent mobility diameters. SEM images of collected soot particles are computer processed to determine their 2D geometry. After conversion to 3D, based on a procedure validated on simulated aggregates by *Brasil et al.* (1999), fractal dimension, dynamic properties (e.g., ratio of mobility to gyroscopic diameter) and specific surface area of particles are derived. Influence of image resolution on 2D parameters derived from SEM images is also investigated.

4.2 Experimental methods

4.2.1 Generation of soot particles and sampling procedure

Soot particles were generated in a laboratory combustion facility at the Max Planck Institute for Chemistry, Mainz, a facility described in details elsewhere (*Lobert et al.*, 1991; *Schmid et al.*, 2004). Dry beech wood (European beech, *Fagus sylvatica*) was cut into $100-150$ mm long and 5 mm thick sticks which were combusted under highly flaming conditions (with combustion efficiency $\Delta CO/\Delta CO_2 < 2\%$) from an open furnace located in a container. Smoke from the combustion was channelled into a metal reservoir container (32 m^3), from where the sample was drawn, while gradual dilution by mixing with unfiltered ambient air was allowed. Dilution of the reservoir container was about 10 m^3 per 30 minutes. Hence after 3 hours the sample was diluted by a factor of about 6.5, which is uncritical considering the high initial aerosol concentrations. Relative humidity and temperature in the reservoir container were $50 \pm 15\%$ and 300 ± 7 K, respectively. Although aerosol dynamical processes like coagulation (in particle concentrations of up to about 10^7 cm^{-3}), condensation of volatile

material, diffusion, and sedimentation occurred, photochemical aging was avoided due to the absence of light in the container. Filter extraction was conducted between 1 and 3 hours after filling the reservoir container. Despite condensation and coagulation-induced increase in mass of single particles with residence time, morphological parameters investigated here (fractal dimension and primary particle size) are expected to be independent of residence time as was confirmed from our analysis.

Aerosol particles were size-classified with a Differential Mobility Analyser (DMA, Model 3071 TSI Inc. Minnesota) at electrical mobility equivalent diameter d_e = 200, 275, 350 and 450 nm. Narrow size distributions exiting the DMA have geometric standard deviations of $\sigma_g = 1.1-1.2$ for d_e of 200 and 275 nm and $\sigma_g = 1.3-1.4$ for d_e of 350 and 450 nm. The sizing accuracy of the DMA was assured by calibration with spherical polystyrene latex (PSL) particles of known sizes. Downstream of the DMA, particles were deposited onto straight-through pore membrane filters by impaction (Nuclepore polycarbonate with pore size of 0.2 μm). Filter extraction times between 7 to 10 minutes provided adequate aerosol loading for SEM analysis. The sampling time was calculated from a rough estimate of the optimum area density on the deposition surface area of the filter for an aerosol flow rate of 1 litre/min and particle concentrations of about 10 000 cm^{-3} (after further dilution of samples flow before size classification).

Filters were coated before sampling with a thin layer of gold ($<$ 10 nm), using a Balzer Sputter Coater (Type 01 120B) in order to enhance contrast in SEM images and minimise electrostatic charging of particles. Our experiences with uncoated filters had shown that particles may 'jump off' the filter surface or restructure due to charging, particularly at high magnifications of better than 5 nm per pixel. High magnifications were essential because primary particles could be as small as 20 nm in diameter, and also because 2D parameters derived from images were observed to significantly depend on the resolution in the images, an effect that will be discussed later.

Solid wood fuel consists of combustible (volatile hydrocarbons and non volatile carbonaceous material), non-combustible (moisture and inorganic ash-forming mineral substances), and other organic chemical constituents depending on the type of wood. Compact particles are generated during smouldering combustion mainly from condensation of both incompletely-combusted volatiles and high molecular hydrocarbons (*Cachier*, 1998). In this study, the combustion process was designed to be highly flaming in order to generate predominantly soot aggregates (see *Edwards*, 1974; *Lobert and Warnatz*, 1993; *Slowik et al.*, 2004, for fire dynamics and soot formation process).

4.2.2 Electron microscopy imaging

A high resolution field emission Scanning Electron Microscope SEM (Leo 1530 SEM, E. M. Ltd., Cambridge, England, now Nano Technology Systems, Zeiss) was used to image collected particles. Calibration of the SEM had been verified by measuring PSL particles with known sizes of diameters 0.126 ± 0.001 μm and 0.600 ± 0.005 μm (Duke Scientific Corp. USA) and 0.356 ± 0.007 μm (Polyscience, Inc, USA).

Filters were analysed immediately after sampling, and on subsequent days. Over the course of these days, there was no change observed in the morphology of particles. Aggregates were selected by changing the field of view and following random trajectories on the filter, and all particles in the field of view were pictured to minimise operator bias. Different areas on the filters were imaged to compensate for deposition inhomogeneity. Magnification was chosen to allocate an individual particle to the whole scan area. Magnifications of between 22 000 to 802 000 (22 kX to 802 kX equivalent to 16.9 and about 0.5 nm per pixel length, respectively) were used depending on the sizes of particles. Output images were acquired with 1024 x 768 pixels and 256 grey levels.

ImageJ[1] software package, which is freely available, was used for image processing and analysing. Images were binarised by selecting brightness thresholds to ascertain entire particles. Since automatic thresholding tended to give hollow primary particles due to its high sensitivity to particle boundaries, thresholding was manually selected for each aggregate. Errors in projected area and fractal dimension due to errors in defining aggregate boundaries were estimated to be less than 5%.

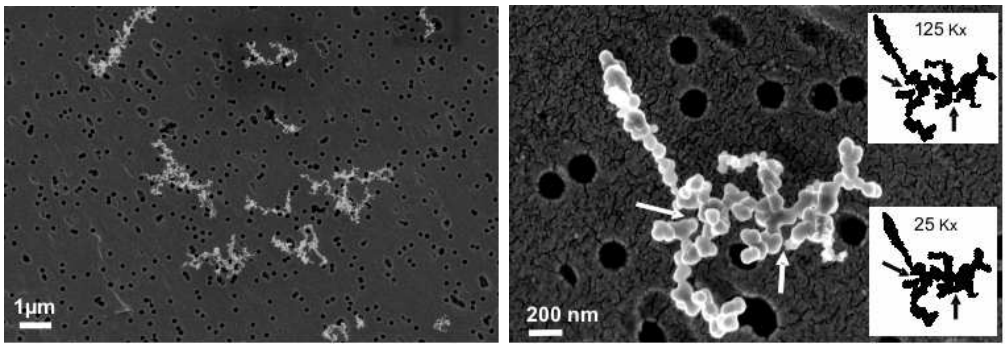
From the binary images the following 2D parameters of aggregates were retrieved: fractal dimension of projected surface area $D_{f,2}$, projected surface area A_a, projected maximum length L and perpendicular width W of the aggregate, aspect ratio of aggregate $AR = L/W$, radius of primary particles a_p and projected surface area of primary particle A_p. These parameters were used to derive 3D properties of aggregates, number of primary particles per aggregate N, radius of gyration R_g, fractal dimension D_f, and gyration prefactor k_g. Conversion of projected surface properties of aggregates into 3D properties is now a widely used technique (*Forrest and Witten*, 1979; *Julien and Botet*, 1987; *Köylü et al.*, 1995b; *Rogak et al.*, 1993; *Samson et al.*, 1987; *Wentzel et al.*, 2003).

[1] http://rsb.info.nih.gov/ij/

4.3 Data analysis

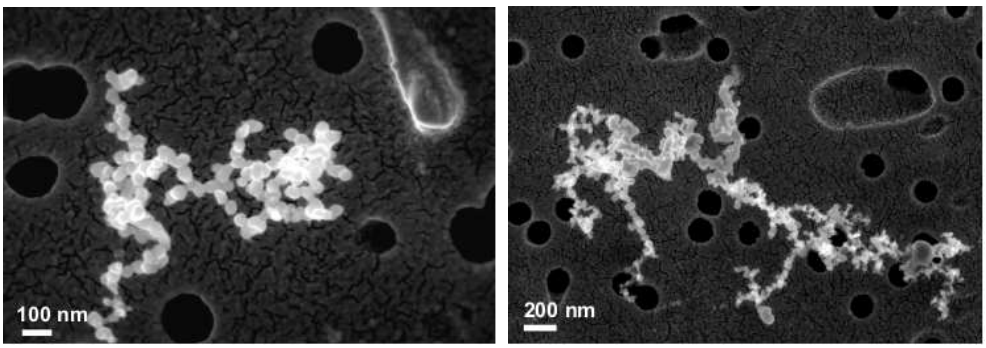
4.3.1 Structure of soot aggregates

Soot particles produced from biomass combustion were aggregated in structure, consisting of small individual spheres of nearly the same sizes. Figure 4.1(a) is a large field view to show how individual aggregates had deposited sparsely on the filter without overlap. Figures 4.1(b), 4.2(a) and (b) show individual aggregates with d_e = 350, 200 and 275 nm, respectively. Although different in sizes, their morphological structures are obviously alike. Some aggregates (not shown here) contained 1 to 3 large spherical particles of diameter above 100 nm ($\cong$ 5% of 760 aggregates imaged). These large spheres are probably tar balls that had been embedded in soot particles during coagulation process in the cooling smoke.



(a) (b)

Figure 4.1: (a) SEM image with a large field of view to show how aggregates had deposited on the filters without overlapping, d_e = 350 nm. (b) A single soot aggregate, d_e = 350 nm, imaged with a resolution of 17.1 $pixels/2a_p$. Inserts are binary images of the aggregate at 17.1 and 3.4 $pixels/2a_p$ (125 kX and 25 kX, respectively). The arrows point to narrow features which are not resolved at 25 kX.



(a) (b)

Figure 4.2: (a) Soot aggregates of d_e = 200 nm and (b) d_e = 275 nm.

Other researchers have observed that particles from wood combustion (Douglas

Fir), though made of small primary particles, were not fractal but compact in shape (*Colbeck et al.*, 1997). Similar compact particle morphologies have also been observed with the SEM (unpublished observations). In general, particulate emissions from wood combustion consist of soot, condensed hydrocarbons, ash and unburnt fuel matrix in varying proportions because morphologies depend on the combustion stage and rate, fuel composition and several other factors (*Edwards*, 1974). Morphologies of soot particles are highly dependant on flame temperature and fuel equivalence ratio (a stoichiometric ratio required for complete combustion of fuel to H_2O and CO_2). By varying this ratio, two types of soot particles were observed from propane flames - one type made of highly irregular fractal-like aggregates composed mainly of black carbon with $D_f \approx 1.7$ and a type of soot with compact particles, increasing mass of organic carbon and $D_f = 2.95$ (*Slowik et al.*, 2004). In this study, particles observed on all filters were exclusively loose soot aggregates, presumably because of the flaming character of the combustion in our experiment.

Diameters of 240 primary soot particles were measured at the edges of several aggregates. The roundness of primary particles vary depending on their position on the aggregate, and how many contact points they had with neighbouring particles. Primary particles at the edges were least distorted by contact with others, by overlapping in the 2D projection, and by the possible distortion of the aggregate on deposition. The size distribution of primary particles is shown in Figure 4.3.

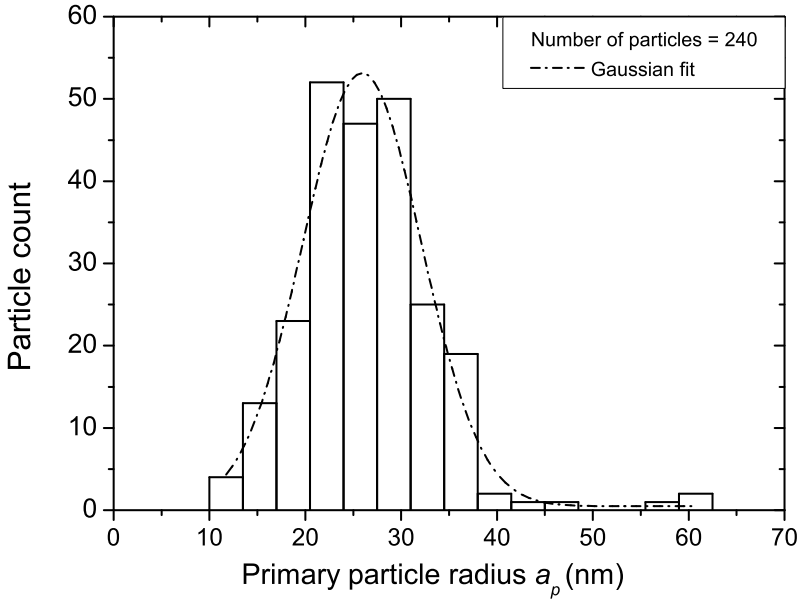


Figure 4.3: Primary particle size distribution of soot aggregates, with mean radius $a_p = 25.5 \pm 3.5$ nm and standard deviation of $\sigma_g = 1.27 \pm 0.09$.

The distribution can be described by a Gaussian function with mean radius

$a_p = 25.5 \pm 3.5$ nm and standard deviation $\sigma = 1.27 \pm 0.09$. The size distributions were independent of the DMA-selected d_e. If only aggregates of a given d_e were selected, the mean a_p ranged from 24 to 29 nm. The width of the distribution is consistent with numerically modelled size distribution function of primary particles formed by hydrocarbon pyrolysis where $\sigma = 1.22$ to 1.65 (*Krestinin*, 2000). Mean sizes of primary particles depend on the combusted fuel. For instance, a_p values of $10 - 15$ nm, $10 - 25$ nm and $25 - 38$ nm were observed for fossil fuel soot (*Cachier*, 1998), biomass burning smoke (*Pósfai et al.*, 2003) and carbonaceous soot particles in the lower stratosphere (*Strawa et al.*, 1999), respectively. High resolution TEM imaging of soot particles from propane-air flame indicate that soot aggregates are made of three distinct classes of particle types - primary spheroids of diameter in the range of $20 - 50$ nm which are themselves made of sub-primary particles between $6 - 9$ nm and elementary particles of less than 5 nm (*di Stasio*, 2001).

Aggregates were asymmetric and elongated with a projected maximum length L of $0.13 < L < 2.29$ μm, and aspect ratios varied between 1.04 and 7.23. The aggregates are therefore self-affine rather than self-similar and more than one exponent is needed to fully describe mass variation with distance (*Neimark et al.*, 1996). The fractal dimension to be derived here from projection therefore characterises the asymptotic behaviour of total mass (*Forrest and Witten*, 1979). Degree of asymmetry is also partially influenced by the projection (*Meakin*, 1989). Additionally, since aggregates are no longer suspended but resting on the substrate with several contact points, the projected aggregate length might be larger than that of the suspended particle (*Brasil et al.*, 1999). Hence the AR defined is the upper limit.

4.3.2 Deriving D_f from projected surfaces

Since parameters used to describe morphological and dynamic properties of aggregates are being derived from SEM images, consistency of the processing software is of critical importance. Therefore, effects of resolution on projected surface area, fractal dimension and other shape parameters derived from 2D images were investigated. Magnification and resolution of the images are important factors because narrow morphological features of aggregates could yield a biased result when they are not adequately resolved (*Bérubé and Jébrak*, 1999). Resolution in the SEM images will be expressed as the number of pixel lengths per primary particle of radius $a_p = 25.5$ nm. For magnifications of 22 kX to 802 kX used in this work, this corresponds to 3 to 110 pixels per primary particle diameter (hereafter $pixels/2a_p$, equivalent to resolutions of 16.9 to about 0.5 nm per pixel length).

The fractal dimension can be determined from digitised 2D projected images (consisting of 1's and 0's) using several techniques. This study will use two approaches namely, box counting and particles counting methods. These techniques are described later. Other techniques include the nested squares/circles method, where $D_{f,2}$ is determined from the length of successive series of squares/circles filling the projection and the number of occupied points (1's) in the squares/circles (*Forrest and Witten*, 1979). In the pair correlation method, $D_{f,2}$ is derived from a function of average density of occupied points in a digital image at distances from each occupied point (*Samson et al.*, 1987). There is also the dilation method, where fractal dimension is determined from surface area of an aggregate and number of dilations in aggregate edges (*Rogak et al.*, 1993).

In the box counting method, the 2D fractal dimension $D_{f,2}$ was derived as the slope on a least square linear fit of a plot of log n vs. log (box size), where n is the number of non-overlapping equal boxes that would fill the projected surface area of an aggregate, as sketched in Figure 4.4 (aggregate from *Oh and Sorensen*, 1997, their Figure 4). The algorithm was validated with this published simulated aggregate (with $D_f = 1.79$) and also ellipsoids and rectangles of different dimensions and aspect ratios.

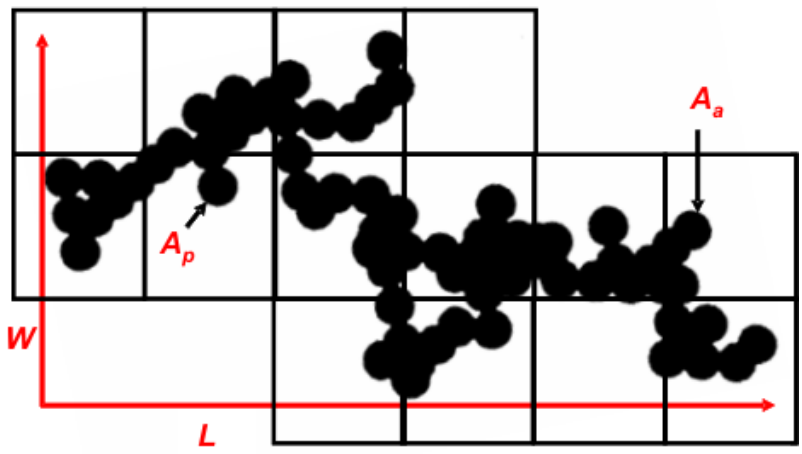


Figure 4.4: Parameters measured from 2D projected surfaces of aggregates. The aggregate is a computer simulated cluster-cluster aggregate of $D_f = 1.79$ (from *Oh and Sorensen*, 1997, their Figure 4). The fractal dimension measured with the box counting method varied between $D_f = 1.75$ to 1.81 depending on the orientation of the aggregate.

To investigate effects of resolution, 2D parameters of three aggregates were measured as image resolution were varied from 4 to 50 $pixels/2a_p$. Figure 4.5 shows the influence of resolution on A_a and $D_{f,2}$ on these aggregates. Aggregate length, L, (not shown in the graph) and projected surface area, A_a, varied from the highest resolution that could be achieved for each aggregate by less than 5%, except on aggregate #1 where the variation

was up to 20%. This aggregate is shown in Figure 4.1(b) and the inserts show the binary images of the same aggregate at 3.4 and 17.1 $pixels/2a_p$ (magnifications of 25 kX and 125 kX, respectively). Two intricate features, indicated by the arrows, are poorly resolved at 25 kX resulting in an overestimated projected surface area. The fractal dimensions of aggregates #1 and #2 increased with resolution from 1.59 to 1.74 and 1.55 to 1.84, respectively. A best fit for aggregate #2 is plotted in the dotted line.

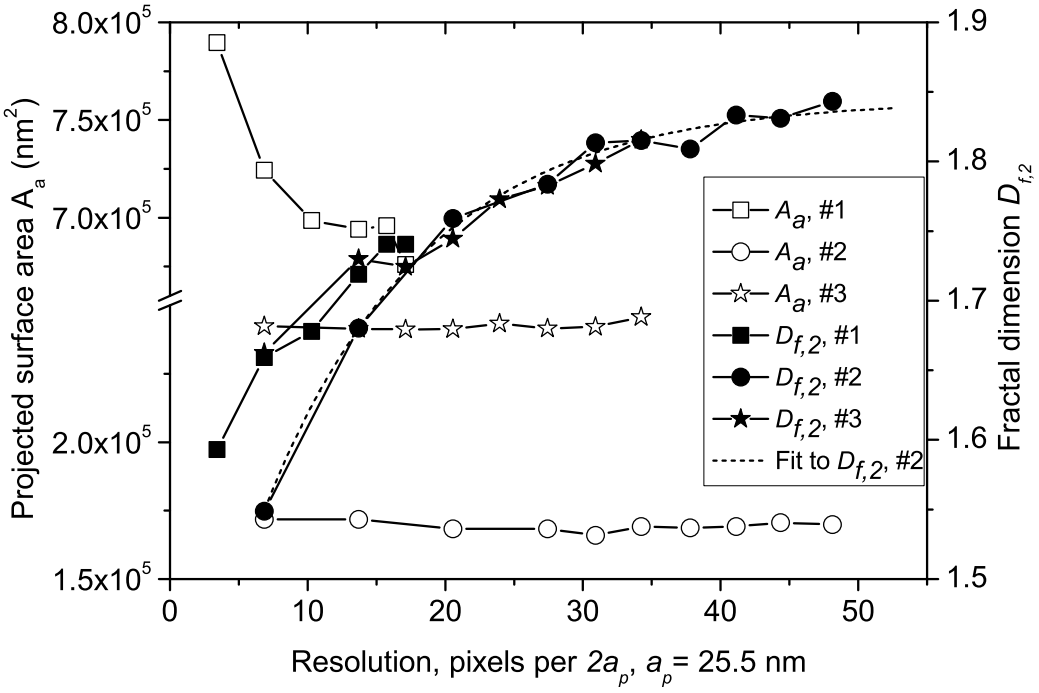


Figure 4.5: Influence of image resolution on projected surface area A_a and fractal dimension D_f on 3 soot aggregates. Aggregates were centred in images while resolutions were varied from 4 to about 50 $pixels/2a_p$ (corresponding to 25 kX to 350 kX). Aggregate #1 is shown in Figure 4.2(b).

The increase of $D_{f,2}$ with magnification can be described by a fit $y = a - bc^r$ where asymptotic value a is $D_{f,2} = 1.82 \pm 0.07$, 1.84 ± 0.01, and 1.97 ± 0.16 for aggregates #1 to #3, respectively; b and c are constants depending on each aggregate fit, and r is the resolution defined by $pixels/2a_p$. Considering these three aggregates, the best 'asymptotic' constants b and c were found to be 0.30 and 0.94, respectively.

The $D_{f,2}$ of 205 aggregates of all electrical mobility diameters were between 1.56 and 1.87, at equivalent resolutions ranging from 3 to 110 $pixels/2a_p$ as shown in Figure 4.6. The mean fractal dimension $D_{f,2}$ was 1.72 ± 0.06. The solid line represents the best fit to the change of $D_{f,2}$ with resolution on aggregate #2 discussed above. The fractal dimensions of all aggregates show a similar systematic trend. Using the best fit, respective asymptotic $D_{f,2}$ were determined for each aggregate. The mean of all asymptotic values was found to

be $D_{f,2} = 1.84 \pm 0.05$.

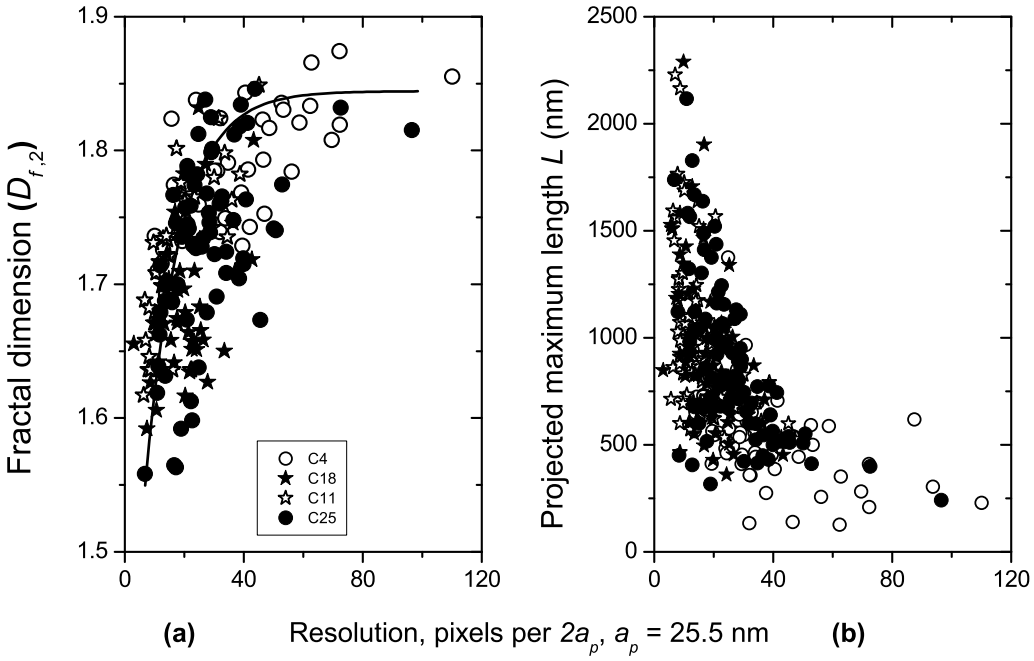


Figure 4.6: (a) $D_{f,2}$ as a function of image resolution on 205 aggregates analysed with the box counting method. Included in the plot is the best fit (line) observed from aggregate #2 by varying the resolution. (b) The limitation in resolution is due to restricted field of view because of aggregate length L. Aggregates with higher L are imaged at courser resolutions.

The scatter in Figure 4.6(a) is due to both influence of resolution and real structural variations of aggregates. To arrive at asymptotic values, obviously resolutions larger than 60 $pixels/2a_p$ are required. Although highest resolution possible was used for each aggregate, the resolution is limited by the output file pixel density and the maximum projected length of aggregates L as shown in Figure 4.6(b). Higher image pixel densities are possible, but pixel density was set to 1024 x 768 pixels due to hardware capacity. The aggregates are not self-similar, an attempt to increase resolution by considering only parts of the aggregates would give a biased $D_{f,2}$.

Changes in $D_{f,2}$ with magnification are due to two effects (i) failure to detect intricate features on aggregates, and (ii) underestimation of primary particle circumference at coarse resolution. When the algorithm was tested on binary full circles of 6 to 2000 $pixels/2a_p$, the fractal dimensions increased from 1.55 to an expected asymptotic value of 2, in a Euclidean plane. For a circle with $2a_p = 60$ pixels, $D_{f,2}$ was 1.89. At coarse resolutions sizes of primary particles are compromised and only features of the entire aggregates are of importance.

If projection of the aggregate does not fill the 2D plane ($D_f < 2$) and there is no overlap between primary particles in the SEM projection, the entire structure of the aggregate is transparent in the projected image and $D_{f,2} = D_f$, fractal dimension in 3D (*Meakin et al.*, 1989). For D_f close to 2, a small correction factor of 1.10 to 1.15 has been previously applied to convert $D_{f,2}$ into D_f due to screening of a small fraction of primary particles (*Baron et al.*, 2001, and references herein). Fractal dimensions from projected surfaces of aggregates were $10-15\%$ lower than 3D aggregates (*Rogak et al.*, 1993; *Samson et al.*, 1987).

However, from Figure 4.6(a) it is realised that this correction is minor compared to the dependence of $D_{f,2}$ on resolution. While this study does not claim that the asymptotic value of $D_{f,2} = D_f$, it is important to realise that depending on image resolution, applying the correction factor alone might not be adequate. The algorithm was also tested on a published aggregate which was simulated with $D_f = 1.79$ and no overlap, Figure 4.4. The fractal dimension of this aggregate varied between $D_{f,2} = 1.75 - 1.81$ depending on its orientation in the image, at equivalent resolution of 61.7 $pixels/2a_p$. Though this aggregate does have apparent overlap due to projection, the recovered averaged fractal dimension at this resolution is within the range of the expected value without the correction of $D_{f,2}$ to D_f. The largest uncertainty is apparently due to aggregate orientation.

Effects of resolution on $D_{f,2}$ derived from projected surfaces have also been investigated by *Samson et al.* (1987). They observed that at resolutions equivalent to 1 to 2.5 $pixels/2a_p$ of $a_p = 15$ nm, the density correlation function $c(r)$ of soot aggregates obeyed a power law with the same D_f (where $c(r) \sim r^{D_f - d}$ and d is the Euclidean dimension). Their soot aggregates were re-evaluated with the box counting method by *Rogak et al.* (1993). They obtained $D_{f,2}$ between 1.53 and 1.73 from digitised images compared to 1.77 to 1.92 expected from computer simulations. From Figure 4.6(a) it is observed that at these resolutions the fractal dimension is also biased by image resolution.

4.3.3 Deriving D_f from primary particle counts

For comparison, D_f was also determined from projected images using the ensemble method (*Baron et al.*, 2001). Number of primary particles of an aggregate is related to projected area of aggregate, A_a and primary particle A_p, if no significant masking of primary particles takes place. In this case

$$N = k_a \left[\frac{A_a}{A_p}\right]^{\alpha} \tag{4.1}$$

where k_a and α are the projected area prefactor and exponent, respectively (*Brasil et al.*, 1999; *Köylü et al.*, 1995b; *Oh and Sorensen*, 1997; *Samson et al.*, 1987). Here prefactor values of $k_a = 1.16$ and $\alpha = 1.10$ were used, and represents DLCA aggregates with $D_f = 1.80$ as given by *Baron et al.* (2001).

Aggregate mass and radius of gyration, R_g are described by the fractal morphology as

$$N = k_g \left[\frac{R_g}{a_p}\right]^{D_f} \tag{4.2}$$

where k_g is a structural coefficient, the fractal gyration prefactor based on R_g. D_f is the 3D fractal dimension. Determination of both D_f and k_g is essential to fully describe fractal properties of aggregates.

For N $>$ 30, the radius of gyration can be calculated from projected maximum length of aggregates in SEM images where L,

$$R_g = L/3 \tag{4.3}$$

(*Brasil et al.*, 1999; *Köylü et al.*, 1995a).

Plotting ln N versus ln R_g/a_p as shown in Figure 4.7 it was found that $D_f = 1.83\pm$ 0.05 and $k_g = 2.77 \pm 0.31$ from a least-square fit (with confidence level of 95%, $R^2 = 0.90$). Figure 4.7 demonstrates the power-law dependence of equation 4.2, and slope defines the fractal dimension from an ensemble of 314 aggregates (77, 70, 84 and 84 aggregates at $d_e = 200$, 275, 350 and 450 nm, respectively). As expected, fractal properties of aggregates do not depend on size selection of the DMA. If only aggregates of a given d_e are selected D_f and k_g varied within experimental uncertainties from 1.82 to 1.85 and from 2.50 to 2.87, respectively. However, since overlap in projection was not considered, number of primary particles determined from equation 4.1 might be underestimated (*Oh and Sorensen*, 1997), while R_g is overestimated through L in the projection due to the deposition position (*Brasil et al.*, 1999). Consequently, the value of D_f might be underestimated.

The gyration prefactor k_g determined is in general agreement with values obtained by Köylü from both simulated aggregation and TEM analysis of soot aggregates with $D_f = 1.7\pm$ 0.15 using a similar approach (*Köylü et al.*, 1995b). However, other studies reported values of k_g between 1.05 and 1.59 for D_f of 1.74 to 1.91 (*Wu and Friedlander*, 1993) and $k_g = 1.19$ to 8.5 for $D_f = 1.82 \pm 0.04$ (*Köylü et al.*, 1995a; *Sorensen and Roberts*, 1997). The prefactor depends on the coagulation mechanism, increasing with packing of primary particles in cluster aggregation and being constant for aggregates in the free molecule regime (*Wu and Friedlander*, 1993). The variation could be a result of varying overlap of primary

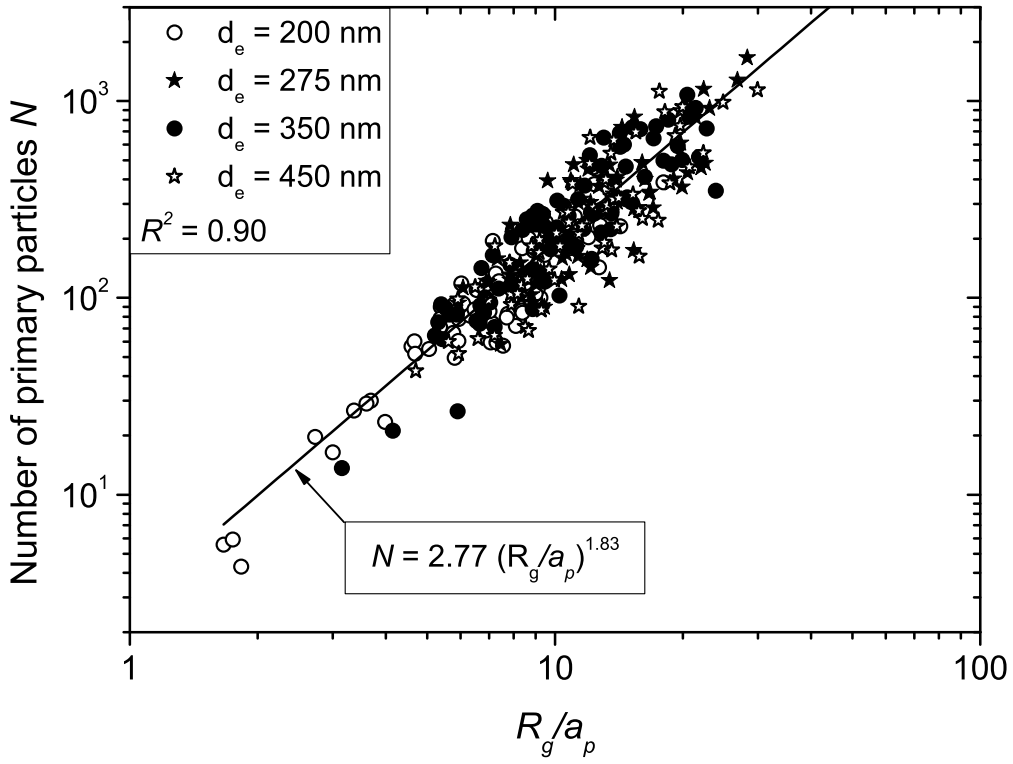


Figure 4.7: Number of primary particles in an aggregate as a function of radius of gyration. The plot of ln N versus ln R_g/a_p yielded a fractal dimension $D_f = 1.83 \pm 0.05$, $k_g = 2.77 \pm 0.31$, and $R^2 = 0.90$. N was calculated from equation 4.1 with area prefactor $k_a = 1.16$ and structural coefficient $\alpha = 1.10$.

particles since computer simulations of DLCA performed by Oh and Sorensen showed that the prefactor gyration could increase with increasing overlap of primary particles (*Oh and Sorensen*, 1997) yet without changing D_f (*Brasil et al.*, 1999). Although this prefactor is an important parameter in understanding the structure of aggregates, this work will be focused on fractal dimension and mobility of aggregates since we do not have an independent approach to determine k_g in equation 4.2.

4.3.4 Mobility of aggregates

The mobility of aggregates in an electric field and how it is related to the radius of gyration determined from the SEM images using equation 4.3 will now be considered. Although preferential orientation of irregularly shaped particles in an electric field is possible, it will be assumed that orientation of soot aggregates in the DMA was random, because aligning forces are too weak to significantly alter translational motion (*Schmidt-Ott*, 1988). Electrical mobility of any particle depends mainly on its size, morphology and charging state. Since for a given equivalent electrical mobility size, aggregates with multiple charges have

larger projected area than singly charged particles and therefore more primary particles, a frequency plot of N, number of primary particles per aggregate for a given mobility, provides information on the charge states of aggregates.

Distributions of N for different DMA classes (d_e = 200, 275, 350 and 450 nm), as seen in Figure 4.8, have peaks corresponding to charge states, where the first peak represents singly charged aggregates (*Wiedensohler*, 1988). While peaks for singly and doubly charged particles are readily identified, higher charge states are obscured by the limited counting statistics. Values of N for each peak were retrieved from fitting a bimodal lognormal functions to number distributions in Figure 4.8, see Table 4.1. The geometric standard deviations of the fits were set to the theoretical predicted width of size distributions exiting the DMA. The radius of gyration values for each d_e were determined from fitting lognormal functions to fractional distributions of R_g and identifying charge states $n = 1$ and 2, as has been done in retrieving N from plots in Figure 4.8

Once the charge state is identified, the mechanical mobility diameter d_{mob}, which characterises the Stokes drag of a particle (*Hinds*, 1999), can be calculated by dividing the electrical mobility by the charge on the particle q ($q = ne$ with $e = 1.6 \times 10^{-19} C$ and $n = 1$ or 2, depending on the charge state). For the four DMA size classes selected here, d_e = 200, 275, 350 and 450 nm, singly charged particles have equivalent mechanical mobility diameters d_{mob} = 200 , 275, 350 and 450 nm, while doubly charged particles have d_{mob} = 324, 461, 601, and 792 nm, respectively. The mechanical mobility diameter of aggregates d_{mob} has now been defined from charge states and will from hereon be referred to as d_{mob} = 200 to 792 nm.

Table 4.1: Equivalent mobility diameters of multiply charged particles, number of primary particles per aggregate N retrieved from Figure 4.8, and dynamic shape factors χ_D (see equation 4.8).

Single charge			**Double charge**		
d_{mob} (nm)	Number of primary particles N	Dynamic shape factor χ	d_{mob} (nm)	Number of primary particles N	Dynamic shape factor χ
200	23 ± 14	1.66	324	113 ± 8	1.47
275	64 ± 3	1.55	461	184 ± 7	1.85
350	94 ± 1	1.77	601	272 ± 10	2.14
450	152 ± 18	1.96	792	421 ± 10	2.45

Mobility diameter d_{mob} is directly proportional to radius of gyration, such that

$$\beta = d_{mob}/2R_g \tag{4.4}$$

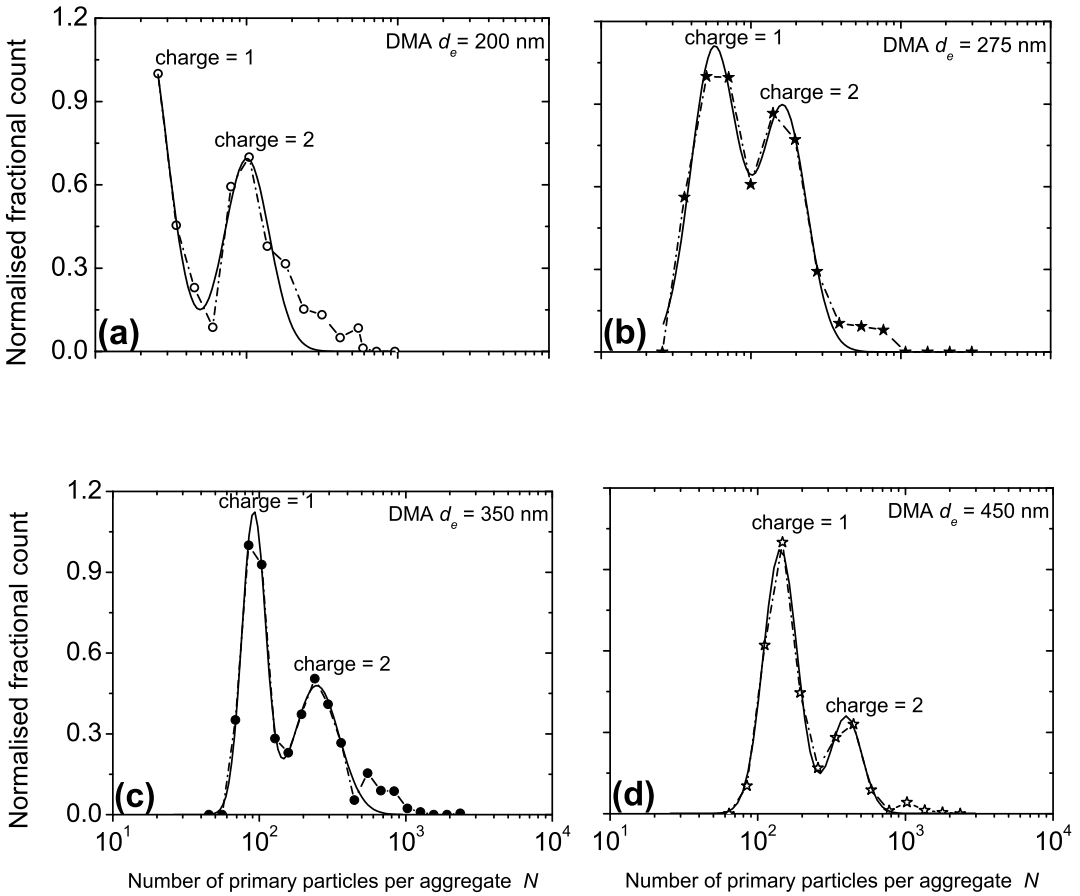


Figure 4.8: Distributions of N on aggregate ensembles of electric mobility diameter d_e = 200, 275, 350 and 450 nm in (a) to (d), respectively. The first peaks to the left of each spectrum represent singly charged aggregates and an increase in charge is indicated by the subsequent peaks. Solid lines are the lognormal bimodal fits to the distributions.

where β varies depending on N, D_f and a_p between about 0.6 and 1.29 for aggregates with $D_f > 1.3$ (*Schmidt-Ott*, 1988; *Wang and Sorensen*, 1999; *Wiltzius*, 1987). In the limit of $N = 1$, $\beta = 1.29$. For large aggregates in the continuum regime where the Knudsen number $Kn \ll 1$, β is a constant depending on D_f (*Wang and Sorensen*, 2001). The Knudsen number is here defined for the motion of aggregates with respect to their mobility, where $Kn = 2\lambda/d_{mob}$ and $\lambda = 66.5$ nm is the mean free path in air.

The Knudsen numbers were $0.2 < Kn < 0.7$, and for $N = 1$, $Kn = 2.6$. Figure 4.9 shows β as a function of Kn for $Kn < 3$. Although Kn is not entirely in the continuum regime, β is found to be 0.81 ± 0.07 and nearly constant with respect to the Knudsen numbers. Note that 'error margins' shown in the plot are due to the distribution in the number of primary particles per aggregate at a given charge as shown in Figure 4.8. Also included in the graph is the interpolated plot to show how β might evolve from 1.29 to 0.81.

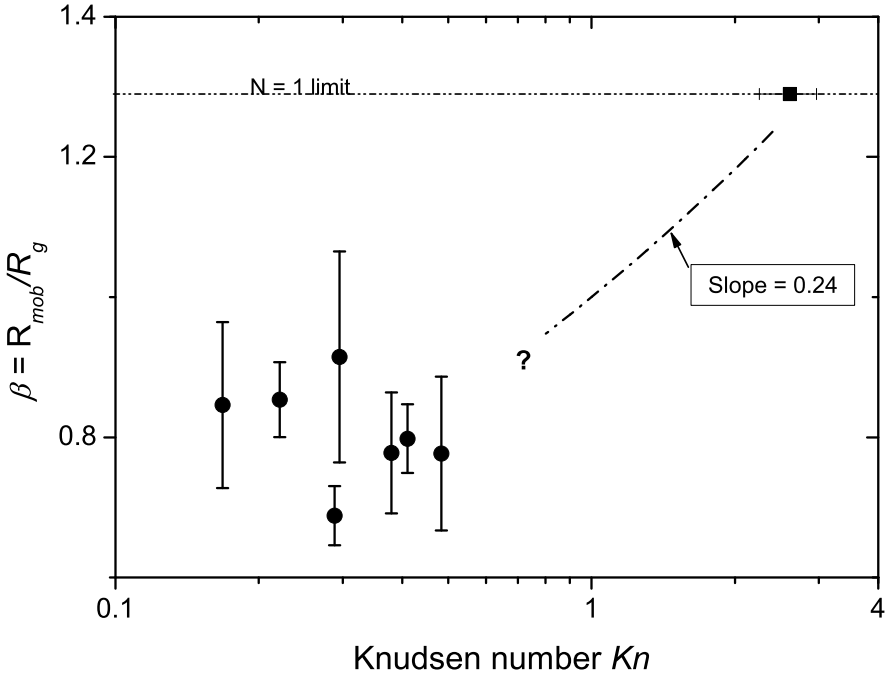


Figure 4.9: Ratio $\beta = d_{mob}/2R_g$ as a function of the Knudsen number $Kn = 2\lambda/d_{mob}$ (see text). For a_p = 25.5 nm, $\beta = 1.29$ and $Kn = 2.6$, (solid square). As the number of particles in aggregates N increase, β will follow the slope and decrease to 0.81, the mean of the scatter.

Thus, as discussed by *Wang and Sorensen* (2001), Kn is always less than a limiting value of about 7 for these aggregates, and therefore aggregates will evolve into the continuum regime as N increases without entering a 'complex' region when $\beta < 0.81$ in the free molecular regime. The limit of Kn is defined as $Kn > (1.29/0.81)^{1/0.24}$ where 0.24 is the slope of the function β as N increases from 1 with $\beta = 1.29$ to large N and $\beta = 0.81$ (for $D_f = 1.83$ derived from aggregates in the previous section). Compared to previous studies, for DLCC aggregates with $D_f = 1.78$, β was found to be 0.97, independent of cluster size (*Chen et al.*, 1987).

Therefore equations 2 and 4 can be combined to relate N to d_{mob} as

$$N = k_g \left[\frac{d_{mob}}{2\beta a_p}\right]^{D_f} \tag{4.5}$$

which implies for β = constant

$$d_{mob} \propto N^{\,1/D_f} = N^{\,x} \tag{4.6}$$

Figure 4.10 shows a plot of d_{mob} vs. N and a best fit to the data, with $x = 0.56 \pm 0.04$ and therefore $D_f = 1.80 \pm 0.13$. There is good agreement between these three approaches used to determine the fractal dimension of the aggregates.

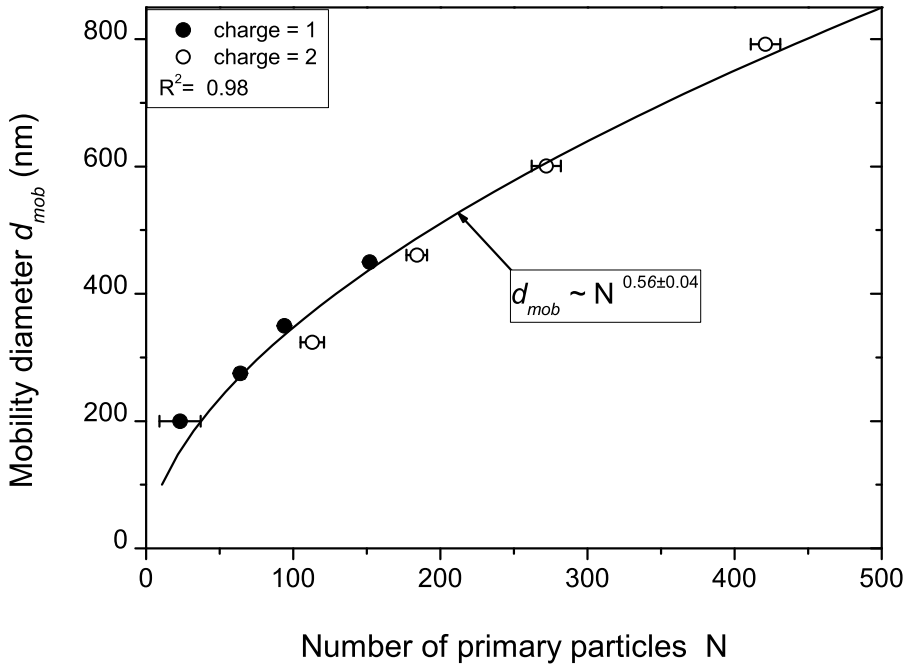


Figure 4.10: Relationship of d_{mob} and number of primary particles per aggregate N. The solid circles represent singly charged and open circles represent doubly charge aggregates.

4.3.5 Dynamic shape factors

Dynamic shape factor χ relates the drag on an irregular particle, F_D, to the drag on a sphere of equivalent mass, F_{DM}, and is applied to Stokes law to account for the effect of shape on the motion of a particle (*Hinds*, 1999). The larger the dynamic shape factor, the greater the drag, the slower the settling velocity and hence the longer the atmospheric lifetime of such a particle. If we consider an equivalent spherical volume of aggregates containing no voids, for an aggregate with dynamic shape factor χ and volume equivalent diameter d_{ve}, Stokes drag force F_{DM} is given by

$$F_{DM} = \frac{3\pi\mu V\chi d_{ve}}{C_{ve}} \tag{4.7}$$

where V is the velocity of particle, μ is the air viscosity and C_{ve} is the Cunningham slip correction of a particle with diameter d_{ve}. The volume equivalent diameter of aggregates d_{ve} was calculated as the solid sphere that has the same volume as the aggregate, $d_{ve} = 2a_pN^{1/3}$, where a_p is the radius of primary particle and N is the number of primary particles per aggregate (and $0.15 < d_{ve} < 0.38$ μm). The equivalent volume diameter d_{ve}, d_{mob} and χ are related by

$$\chi = \frac{C_{ve}d_{mob}}{C_{mob}d_{ve}} \tag{4.8}$$

where $C_{ve,mob}$ is the Cunningham slip correction of a particle with diameter $d_{ve,mob}$. Slip factors were calculated as $C = 1+Kn[\alpha+\beta_c exp(-\gamma/Kn)]$, where $\alpha = 1.207$, $\beta_c = 0.558$ and

$\gamma = 0.999$ for solid particles at STP, and Kn is the Knudsen number (*Baron and Willeke*, 2001c). The slip factors were $1.41 < C_{ve} < 2.22$ and $1.19 < C_{mob} < 1.84$. Shape factors were found between 1.66 and 2.45 and increasing with N, see Table 4.1. As mentioned, orientation of particles was assumed to be random. However, aggregates were not isometric, but elongated. If they would orient in the electric field (depending on the location of charge on the particle surface and strength of the electric field) dynamic shape factors derived here represents orientation-averaged properties. The values are consistent with previous studies. Dynamic shape factors of soot particles generated from butane combustion were between 2.6 and 5.3 for d_{ve} of 1.03 to 2.29 μm with $a_p = 25$ nm and D_f between 1.87 and 2.14 (*Nyeki and Colbeck*, 1994).

4.3.6 Specific surface area

Surface area is an important parameter governing particle gas-phase interaction; in particular it determines adsorption kinetics and particle growth by condensation (*Baron and Willeke*, 2001c). The exposed surface area of an aggregate can be defined as the area which is not involved in aggregation of primary particles and can therefore take part in heterogeneous chemistry in the atmosphere. When neglecting contact points between primary particles, the total surface of an aggregate is the sum of all primary particle surfaces. To evaluate the exposed area in this study, the surface area of primary particles was assumed to be smooth and spherical.

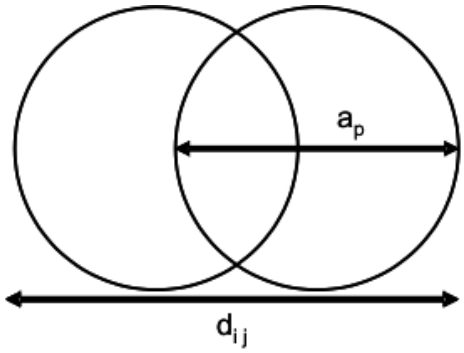


Figure 4.11: The overlapping of primary particles in 2D projected surfaces.

In SEM images, projected surface depends on overlapping and number of contacts per primary particle, as sketched in Figure 4.11. Overlap parameter of primary particles, $C_{ov,proj}$ was measured as

$$C_{ov,proj} = \frac{4a_p - d_{ij}}{2a_p} \tag{4.9}$$

where $C_{ov,proj} = 1$ for total overlap, $C_{ov} = 0$ for touching primary particles and d_{ij} is the projected length of the overlapping primary particles that passes through their centres. The overlap parameter was measured on 82 pairs of all mobility diameters and found to be $C_{ov,proj} = 0.26 \pm 0.01$ with a standard deviation $\sigma = 0.10 \pm 0.02$.

The exposed surface area of aggregated particles with $D_f = 1.78$ has been modelled by *Brasil et al.* (1999). They investigated the relationship between overlapping of primary particles in 2D by comparing overlap measured on projected images of aggregates at known sintering in simulated aggregates. They observed a linear relationship of the form $C_{ov} = \zeta_1 C_{ov,proj} + \zeta_2$, where C_{ov} is sintering in 3D, $\zeta_1 = 1.1 \pm 0.1$, $\zeta_2 = 0.2 \pm 0.02$, and derived a relationship between N, C_{ov} and exposed surface area of aggregates S_A

$$S_A = S_{A_{C_{ov=0}}}[1 - \phi C_{ov}(1 - 1/N)] \tag{4.10}$$

where $\phi = 1.3$ and $S_{A_{Cov=0}} = N4\pi a_p^2$ is the total surface of primary particles without overlap.

Using $C_{ov,proj}$ and N measured in our SEM images, equation 4.10, mass of aggregate is given by $M = N\rho_p \frac{4}{3}\pi a_p^3$ and assuming a density of $\rho_p = 1500$ kgm^{-3} for soot (*Horvath*, 1993), specific surface area s_a was found to be 70 ± 10 m^{2}g^{-1}. The specific surface area for aggregates with no overlap was 78 ± 13 m^{2}g^{-1} and for compact spherical particles of the same mass and volume $s_a = 10$ to 30 m^{2}g^{-1}. The exposed surface area is a function of primary particle diameter, fractal dimension and surface properties. For comparison, the specific surface area of hexane soot was found to be $89 - 91$ m^{2}g^{-1}, when reactivity of soot particles ($a_p = 20 - 35$ nm, D_f around 1.8) was investigated for uptake of O_3, NO_2, SO_2 and N_2O_4 (*Smith et al.*, 1989). Clearly the specific surface area derived from projected surface area would be lower than that derived from reactivity of soot with gases, due to the assumption that primary surface area is smooth.

4.4 Discussion

The fractal dimension of aggregates have been derived from three techniques: $D_{f,2} = 1.84 \pm 0.05$ from the asymptotic $D_{f,2}$ corrected for resolution in projected surfaces of 205 aggregates, $D_f = 1.83 \pm 0.05$ from mass and radius of gyration relationship and $D_f = 1.80 \pm 0.13$ from mobility and mass relationship in the DMA. There is agreement between the three approaches despite different plausible uncertainties inherent with each approach. Uncertainties in obtaining aggregate parameters from projected images due image

resolution have been highlighted. In previous reports, it has been shown that in determining the fractal dimension from projected surfaces through N and radius of gyration, N and k_g might be overestimated by $10 - 15\%$ depending on the resting position of aggregates (*Brasil et al.*, 1999). However, N is also reduced by overlapping of primary particles in the projection. In this study, these uncertainties have not been accounted for in deriving $D_{f,2}$ from the projections. Its unclear how such effects will contribute to overall uncertainty in N, or if they would cancel.

Soot particles are potentially covered by a coating of volatile components, e.g., volatile organic compounds and water from the combustion processes. These volatiles might be lost in the vacuum of the SEM leading to more loosely packed aggregates and a slightly lower fractal dimension from SEM images compared to that measured from the DMA. Such effects have been observed by *Burtscher et al.* (1995) who found that the fractal dimension of young soot particles in diesel combustion decreased from 3 to 2.2 due to changes in morphology after removing volatiles with a thermodenuder. The change of D_f in our measurements due to such effects are expected to be less prominent, and might be in the margin of experimental uncertainty, due to reduced amount of volatiles expected from our flaming burning conditions (*Lobert et al.*, 1991).

When considering uncertainties in the mass-mobility relationship, the charge probability distribution on aggregates might be distorted by the large surface area of aggregates. The charge probability approximation used in this study is representative of spherical particles (*Wiedensohler*, 1988). Size distributions exiting the DMA are broadened when particles are not spherical and for multiply charged particles, the fractal dimension derived from the mobility size distributions might therefore be underestimated (*Wentzel et al.*, 2003). Uncertainties in mobility diameters depend on the performance of the DMA but are within experimental error margins of less than 5% (see *Kinney et al.*, 1991).

The specific surface area determined is an important parameter in understanding the interaction and ageing of soot particles. Aggregated particles provide a large specific surface area, and can participate in heterogeneous chemical reactions with atmospheric gaseous species. This in turn might change both the morphology and chemical composition of the particles with ageing (*Cachier*, 1998). For example, sulphur dioxide might oxidise and condense on soot surface creating a mixed soot/sulphate aerosol particle (*Buseck and Pósfai*, 1999). Soot/sulphate mixtures are indications of aged biomass burning plumes in southern Africa (*Li et al.*, 2003b; *Pósfai et al.*, 2003). Interactions between NO_2 and soot have been postulated to account for high HNO_2 concentrations in urban atmospheres polluted with high combustion emissions (*Ammann et al.*, 1998). Modelling results show

that discrepancies in photochemical models and atmospheric observations on the uptake on soot particles might be reduced, if fractal morphology is taken into account, particularly in the boundary layer of urban areas where high loadings of soot particles can be found (*Bekki et al.*, 2000; *Strawa et al.*, 1999).

4.5 Conclusion

The primary objective of this study was to describe morphological and dynamic properties of fractal-like soot aggregates produced from wood combustion. For aggregates with mechanical mobility diameters between 200 and about 800 nm, a procedure suggested and validated on simulated aggregates by *Brasil et al.* (1999) to obtain 3D morphology from 2D parameters utilising SEM images has been applied. Particles were observed to be aggregated, with fractal-like morphology that is consistent with kinetic growth of diffusion-limited cluster aggregation. The primary particle radius a_p was 25.5 ± 3.5 nm. The fractal dimension of aggregates was derived from three techniques: $D_f = 1.84 \pm 0.05$ from the asymptotic fractal dimension corrected for resolution in projected surfaces, $D_f = 1.83 \pm 0.05$ from mass and radius of gyration relationship, and $D_f = 1.80 \pm 0.13$ from the relationship between mobility and mass in the DMA. The fractal dimension determined from the three approaches is in agreement and the average D_f of 1.82 is consistent with aggregate formation by diffusion limited cluster aggregation (DLCA). This value is regarded as the lower limit when taking into account limitations discussed in the techniques applied.

The box counting method was observed to underestimate the fractal dimension of aggregates in this study and in other reports cited. The underestimation is compounded when microscopy images are acquired at coarse resolutions. This was described by imaging soot particles over a range of resolutions. A critical resolution of around 60 $pixels/2a_p$ was observed. Although resolution was maximised by allocating a single particle to a microscope image, resolutions rarely exceeded 50 $pixels/2a_p$. The projected surface area A_a, projected maximum length L and perpendicular width W of aggregate were nearly insensitive to resolution (for the given values).

For $200 < d_{mob} < 800$ nm, the ratio of mobility diameter to twice the radius of gyration was nearly constant with $d_{mob}/2R_g = 0.81 \pm 0.07$. The relationship of mobility to mass of aggregates $d_{mob} \propto N^x$ and $x = 0.56 \pm 0.04$, which is consistent for $x = 1/D_f$ and $D_f = 1.83$, as is expected for the continuum regime. Hence the measurements show that $x = 1/D_f$ hold into the transition regime to a least $Kn = 0.7$. However, it is acknowledged

that aggregates are in the slip regime, when the transition from free molecular to continuum is not fully established. The shape factors were found between 1.66 and 2.45 and increased with N. The specific surface area of soot particles was 70 ± 10 m^2g^{-1}, and this has to be considered a lower limit, since a smooth primary particle surface was assumed. Physical and dynamic properties derived here relate to freshly generated wood soot particles.

Chapter 5

Physical, Chemical and Optical Properties of Aerosol Particles Collected over Cape Town During Winter Haze Episodes

Contents of this chapter were submitted to the South African Journal of Science with Günter Helas, Harold J. Annegarn, Joachim Huth and Stuart J. Piketh as co-authors.

Abstract

Airborne measurements were conducted in the winter months of July to August 2003 over the metropolitan area of Cape Town to characterise physical, chemical and optical properties of aerosol particles during intense brown haze episodes. Collected particles were investigated on temporal and spatially resolved filters using a high resolution Scanning Electron Microscope (SEM). Based on morphology and elemental composition, particles were categorised into seven particle groups of: aggregated soot particles, mineral dust, sulphates (SO_4^{2-}), sea-salt, tar balls/fly ash, rod-shaped particles associated with soot agglomerates and those that could not be attributed to any of these groups were labelled as 'others'. Particles were externally mixed. They exhibited strong spatial and temporal variability in chemical compositions. Refractive indices of aerosols were derived from chemical apportionment in SEM analyses and combined with in-situ measurements of number-size distributions to determine optical properties of dry particles in the size range of $0.09 < d_p < 3.45$ μm. To provide an overview of optical properties, optical parameters were computed from point measurements of maximum, mean and minimum number concentrations probed during the collection of each sample, with the maximum number concentrations as possible pollution episodes encountered. Based on maximum number concentrations, mean light extinction and absorption coefficients were $\sigma_{ep} = 194 \pm 195$ Mm^{-1} and $\sigma_{ap} = 41 \pm 25$ Mm^{-1}, respectively at $\lambda = 550$ nm (and from mean number counts $\sigma_{ep} = 29 \pm 21$ Mm^{-1} and $\sigma_{ap} = 8 \pm 9$ Mm^{-1}). Single scattering albedo, ω_0, varied from 0.61 to 0.94 with a mean value of 0.72 ± 0.08. Asymmetry

parameter, g_0, was found to vary over a narrow range with mean of 0.59 ± 0.06. Visibility range, L_v, was $5-125$ km. The haze could be attributed to extinction of light by the fine aerosol mode composed mainly of anthropogenic particles. The single scattering albedo is much lower than generally reported in literature, and this was attributed to high concentrations of highly absorbing anthropogenic soot, where fractional number concentrations of up to 46% were observed in the SEM analyses. High extinction coefficients and low single scattering albedo computed here demonstrate quantitatively the contributions of particulate matter to visibility reduction and the observed brown haze phenomenon in Cape Town.

5.1 Introduction

5.1.1 Cape Town brown haze

Cape Town, several other city centres and industrial sites in South Africa, such as South Durban, Johannesburg and the Vaal Triangle have been identified as environmental 'hot spots' due to persistent high levels of mainly anthropogenic emissions from transport, industry and domestic activities (*Zunckel et al.*, 2006)[1]. Cape Town is a major city situated on the south-western tip of South Africa, with a population of just over 3 million residents (*Statistics South Statistics South Africa*, 2001). During winter season (May to August) and under stable meteorological conditions, the city suffers from poor visibility episodes associated with accumulation of anthropogenic, natural aerosol particles and trace gas emissions in the boundary layer as a brown haze. The term 'brown haze' has been adopted for the brown colour of the haze during the more severe haze episodes, whose colour is attributed to high concentrations of highly absorbing soot particles (as opposed to photochemically produced 'white haze' composed of highly scattering sulphate and nitrate particles). Impacts of anthropogenic emissions over metropolitan cities have been known in Europe since 61 A.D (*Baumbach*, 1996) and still pose environmental challenges world wide (*Bergin et al.*, 2001; *Carrico et al.*, 2003; *Dzubay et al.*, 1982; *Mallet et al.*, 2003; *Senaratne and Shooter*, 2004; *World Bank Report*, 1998). Haze defines an aerosol consisting of water droplets, pollutants and dust particles of diameter $d_p < 1$ μm that impedes vision (*Seinfeld and Pandis*, 1998). Typically hazes consist of anthropogenic sulphates (SO_4^{2-}), nitrates (NO_3^-), organics, soot, industrial dust, fly ash particles and natural aerosols like mineral dust and sea-salt. Urban aerosol particles are formed mainly from anthropogenic emissions from combustion of fossil fuels in traffic, industrial and domestic processes. Particles typically consist of three size modes. The coarse mode range consists of mineral dust, fly ash and sea-salt particles. The nucleation and accumulation modes contain most of combustion components both as primary particles and particles derived from gas-particle conversion of reactive gases from combustion processes (*Baumbach*, 1996; *Seinfeld and Pandis*, 1998).

Exposure to fine particulate matter from combustion processes is now regarded as the main environmental threat to human health in major cities causing, e.g., respiratory diseases, pneumonia cases, influenza and more (*Nel*, 2005; *World Bank Report*, 1998). Long term exposure to fine particulate matter from combustion processes increases risks of lung cancer and cardiopulmonary mortality (*Nemmar et al.*, 2003; *Pope et al.*, 2002). Fine particulate matter in the nano scale range can be inhaled deep into the pulmonary system

[1] http://www.environment.gov.za//Documents/Documents/2006Jan6/AQ_info_review_final_report.pdf

where it may pass from lungs into the blood stream, vital organs or into the brain via sensory nerve endings (*Lippmann et al.*, 2003). Examples to prove the link between air pollution episodes and mortality rate include reports on fog that affected people along the Meuse Valley, Belgium in December 1930 (*Nemery et al.*, 2001) and the Lethal London fog of 1952 as reported by *Wilkins* (1954) and reassessed by *Bell and Davis* (2001). Though it is apparent that effects of air pollution mainly from anthropogenic emissions extend beyond obvious visibility problems, the focus of this study will not relate to health issues.

Research studies on Cape Town brown haze have been carried out before to understand aerosol chemical composition and contributions of both particulate matter and trace gases to visibility degradation (*Pineda and de Villiers*, 1995; *Walton*, 2005; *Wicking-Baird et al.*, 1997, and several citations herein). Winter haze episodes were also identified from SO_2 and NO_x measurements in $1985-86$ from a study by *Jury et al.* (1990). As part of an ongoing air quality monitoring network, the City of Cape Town also measures atmospheric concentrations of PM2.5, PM10, H_2S, CO, CO_2, NO_x, SO_2 and VOCs at 13 strategic locations around the metropole area. Long term annual trends from these monitoring sites (1990 to 2002) show that while averaged concentrations of NO_2 and SO_2 have been steadily decreasing, particulate levels in the Central Business District, CBD, and Khayelitsha have increased *(City of Cape Town State of Environment Report Year 5,* 2002)[2]. High concentrations of aerosol particles can have considerable effects not only at the local scale (e.g., on health and visibility reduction) but if transported into the upper troposphere, particles can perturb cloud properties and possibly change the regional climate.

An intensive experiment to study air pollution in Cape Town was conducted between 1992 and 1996 - the Cape Town Brown Haze I, CTBH I study (*Wicking-Baird et al.*, 1997). The aims of CTBH I were to determine contributions of major sources to haze and to understand mechanisms of haze formation with emphasis on visibility effects. Research recommendations were made from limitations identified in CTBH I to further understand the brown haze such as: (i) chemical apportionment of particulate matter was based on bulk analyses of ground samples collected at selected sites over relatively long sampling periods of 24 hours. Such sampling intervals did not allow for investigations of aerosol temporal dynamics; (ii) elemental carbon was shown to be the most significant component of the haze, and needed to be further characterised; (iii) microscopy analysis was recognised to be essential in identifying aerosol sources directly; (iv) there was need to further understand aerosol spatial distributions within the brown haze.

As a follow-up to CTBH I, an airborne experiment Cape Town Brown Haze II

[2]http://www.capetown.gov.za/airqual/

(CTBH II) was initiated to investigate the atmosphere over Cape Town during intense haze periods in July and August 2003 (*Piketh et al.*, 2004). The overall objectives of CTBH II were to: (i) characterise microphysical, chemical and optical properties, spatial distribution and contributions of particles to haze (this study); (ii) describe the distribution and contributions of trace gas emissions to haze formation (see *Walton*, 2005); (iii) identify the importance of VOCs contribution to local the atmospheric chemistry (see *Chiloane*, 2005); (iv) understand possible health effects associated with haze.

5.1.2 Objectives of this study

As part of CTBH II, the aims of this study are twofold. The first part of the research is to use microscopy single particle analyses and in-situ measurements to characterise physical (morphology, shape, size, mixing states) and chemical properties (chemical composition) of aerosol particles in the Cape Town brown haze. The objectives are to:

- provide chemical composition, elemental composition, mixing states and size distributions of particles
- use the information to apportion contributions of different aerosol particle sources
- study the spatial distribution of particles
- determine refractive indices of aerosols and
- quantify optical properties and radiative effects of particles.

The second part of this research is to investigate the extent to which particle size distributions and number concentrations are characterised by an optical particle counter (OPC) and single particle analyses techniques. Similar to Chapter 2, consistence in aerosol parameterisations by both microscopy techniques and the OPC are investigated. Finally, a theoretical approach for correcting particle size distributions measured by the OPC is applied to study effects of different refractive indices on particle size distributions.

5.1.3 Research rationale and design

Microscopy single particle analyses have been successfully applied to classify particle abundance, chemical composition, and mixing states, particularly the use of electron beam microscopes, the Scanning/Transmission Electron Microscope, S/TEM (*Chen et al.*, 1998; *Ebert*

et al., 2002b; *Fletcher et al.*, 2001; *Hasegawa and Ohta*, 2002; *Kojima et al.*, 2004; *Li et al.*, 2003a,b; *McInnes et al.*, 1994; *Okada and Hitzenberger*, 2001; *Pósfai et al.*, 2003; *Reid et al.*, 2003a). The information can be used to derive aerosol complex refractive index, $m = n - ik$. To date this approach has been applied for the first time and only by *Ebert et al.* (2002a, 2004). The refractive index determines the phase velocity change of the light wave by a particle through n and attenuation k (*Bohren and Huffman*, 1983). Both parameters are functions of wavelength of light (*d'Almeida et al.*, 1991).

Averaged complex refractive index derived from single particle analyses in previous studies were found to be in good agreement with conventional photometer measurements of dried filter samples (*Bundke et al.*, 2002; *Ebert et al.*, 2002a). Using a similar approach in this study, refractive indices, one of the least well-characterised properties of aerosols, are determined from single particle analyses of particles collected in highly resolved spatial and temporal aircraft measurements. Microscopy results are complemented with conventional techniques of measuring number-size distributions to quantify optical properties and radiative forcings of particles in an urban environment.

This chapter is structured as follows: In Section 5.2, experimental designs, aircraft flight patterns, particle sampling and in-situ aerosol measurements are described. Morphologies of aerosol particles collected on spatial and temporal resolved aircraft samples are investigated with SEM microscopy techniques to determine chemical compositions, abundances and distribution of particles in Section 5.3. In Section 5.4, size distributions, number concentrations and spatial distributions of particles from in-situ Passive Cavity Aerosol Spectrometer Probe (PCASP-100X) measurements are described. Simultaneous measurements of aerosol number concentrations and size distributions are compared between microscopy techniques and the PCASP measurements in Section 5.5. Chemical compositions and particle abundances determined from SEM analysis are used to derive refractive indices of aerosol particles in Section 5.6.1. Effects of aerosol refractive indices on size distributions derived from the PCASP are investigated for different aerosol species identified in microscopy analysis in Section 5.6.2. In Section 5.6.3 to 5.6.4, refractive indices determined from SEM single particle analyses are combined with in-situ PCASP number-size distributions to quantify light scattering and absorption coefficients, single scattering albedo, asymmetry parameter, Ångstrom exponent and radiative forcings of particles. Sensitivity studies are performed on the quantified optical parameters. A summary of major findings and conclusions are given in Section 5.7. Limitations in aerosol parameterisation, uncertainties and recommendations are discussed.

5.1.4 Literature review: Previous research on Cape Town brown haze

Figure 5.1 shows the location of the study area[3]. The brown haze in Cape Town is most located over the flat plain lying to the east of Cape Town and north of the False Bay, an area known as the Cape Flats. Land use in the area comprises extensive formal and informal residential areas, manufacturing industries, an international airport and major roads. Depending on the strength and direction of winds, the haze may drift southwards over False Bay or eastwards, where it is obstructed by the range of mountains. The brown haze is therefore an urban rather than a regional phenomenon.



Figure 5.1: Geographic location of the study area.

To provide background knowledge on the Cape Town brown haze, a summary of experiments reported in CTBH I by *Wicking-Baird et al.* (1997) is given in this section. In CTBH I, emissions of PM2.5 (particles with diameter less than 2.5 μm) and PM10 (particle diameters are between 2.5 μm and 10 μm), NO_x, SO_2 and VOCs were investigated over the Cape Town metropolitan area to compile an emission inventory. Table 5.1 shows a summarised inventory of major primary source emissions.

[3]image adapted from Microsoft MapPoint http://encarta.msn.com/

Table 5.1: A summarised inventory of major primary source strengths of particulates and trace gas emissions in Cape Town from *Wicking-Baird et al.* (1997).

	Emission Rates (tons/year)				
Primary source type	PM10	PM2.5	SO_2	NO_x	VOCs
Residential (all fuels)	1 927	1 340	530	649	2 451
Petrol and diesel vehicles	2 489	2 245	430	18 629	34 156
Paved and unpaved roads, brakes and tyre wear	3 606	352	-	-	-
Aviation	46	576	470	33	30
Ship and ship bunker oil	119	107	1 214	1 321	140
Industry and Commerce 2 622	1 556	25 846	7 055	1 752	
Others (tyre burning, wildfires etc)	798	493	282	122	6 372

Figure 5.2 shows PM2.5 source and visibility apportionments that were averaged over haze episodes identified on four monitoring sites. PM2.5 particulate levels over Cape Town were found to be comparable to those measured in heavily polluted cities (*World Bank Report*, 1998). Loadings of particulate matter were confined to discrete peaks lasting between 3 to 5 days. Nearly all contributions were from anthropogenic sources through transport, industrial and domestic emissions.

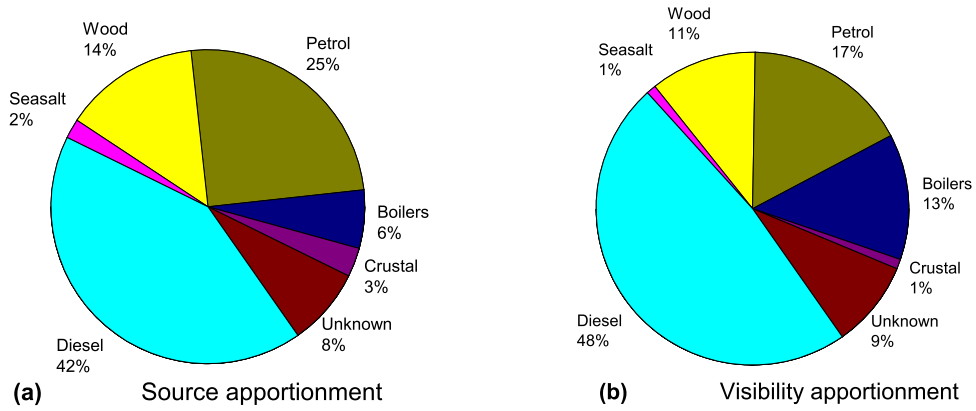


Figure 5.2: PM2.5 source apportionment (left) and visibility apportionment averaged over four monitoring sites during modelled haze episodes in the CTBH I study, from *Wicking-Baird et al.* (1997).

Although CTBH I focused on local emission sources, distant sources have to be taken into account as well. Relevant aerosol sources besides metropolitan ones include biomass burning from savanna wildfires, industrial and mining processes, domestic fossil fuels combustions, and aeolian dust from dry arid surfaces. Large-scale transport within the troposphere is efficient over southern Africa in the dry season - from August to October. Stable and persistent layers at 700 and 500 hPa (*Garstang et al.*, 1996; *Tyson and D'Abreton*,

1998) and at 300 hPa (*Freiman et al.*, 2002) control lateral transportation of aerosols and trace gases, and prohibit vertical mixing. Anticyclonic circulations (and recirculations) prevail over the subcontinent and allow trace gases and aerosols to be transported within these layers over thousands of kilometres. Over coastal areas like Cape Town, a lower stable layer at 850 hPa also persists, and is disrupted and mixed with upper level layers almost weekly (*Freiman et al.*, 2002). A study to apportion sources of inorganic components of aerosol particles at a remote site north-north-west of Cape Town, at Brand se Baai (18°E, 30°45′S, 50 m above sea level, asl) confirmed these circulations of aerosol (*Piketh et al.*, 1999). In another study, increased aerosol optical depths were associated with biomass burning aerosols (2 to 3 days old) reaching Sutherland, a remote site NE of Cape Town, 20°48′E, 32°22′S (*Formenti et al.*, 2002b)

5.2 Experiment and methodology

5.2.1 Boundary layer structure

Using detailed observations, statistical and numerical model simulations, the atmospheric conditions conducive to brown haze formation over Cape Town are described elsewhere (*Jury et al.*, 1990). Development of the brown haze is linked to the structure and dynamics of the lower troposphere, the atmospheric boundary layer (ABL) below 2 km. To understand the experimental design (flight times and patterns), describe aerosol number concentrations and other properties, a brief description of an idealised diurnal development of the ABL will be given.

Figure 5.3 shows an idealised diurnal development of a continental boundary layer under anticyclonic conditions (*Garratt*, 1992; *Oke*, 1993). After sunset, the surface is cooled by the escape of thermal infra-red radiation. This leads to the development of a stable (nocturnal) boundary layer (SBL) with positive gradient of potential temperature θ. The height of the SBL is increased by weak mechanical wind shear and turbulence. Emissions from the previous daytime that have been mixed in the convective boundary layer (CBL) during the daytime are preserved in the residual layer (RL) sandwiched between the SBL and an inversion at the top of the boundary layer. The boundary layer is capped from the free troposphere by an inversion at heights of $1 - 2$ km.

After sunrise (which is about 0600 UTC[4] in Cape Town for July and August)

[4]UTC, Universal Time Coordinated is local time zone minus two hours for Cape Town.

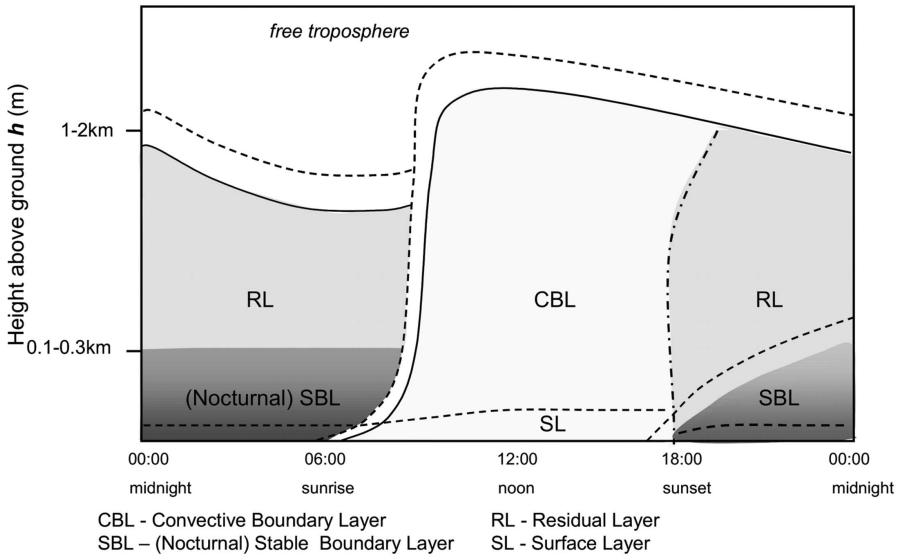


Figure 5.3: Schematic representation of a diurnal development of the continental boundary layer under anticyclonic conditions (adapted from *Garratt*, 1992; *Oke*, 1993).

the surface is heated by insolation, giving rise to turbulent mixing by thermally induced and mechanical turbulences, dissolving the SBL, a layer which comprised remnants of the preceding night. The potential temperature increases and a new mixing layer, the CBL develops from the SBL. The height of the CBL is increased by convection and entrainment of air from the free troposphere. The height depends on the partitioning of the absorbed radiation between sensible heat, latent heat of evaporation of water and entrainment of aloft air (*Stull*, 1999). The transition from the CBL to the surface is defined by a thin unstable surface layer (SL), usually tens of meters in thickness.

With this diurnal development of the atmospheric boundary layer in mind, flights were conducted at different times of the day in order to contrast measurements of particle properties in the mornings and afternoons on haze and no-haze days. Morning flights were conducted to sample relatively fresh haze still concentrated close to the ground. Afternoon flights were conducted to sample the mature haze which had become mixed within the convective boundary layer, and possibly transported laterally.

5.2.2 Flight patterns

Airborne sampling of aerosol particles and online measurements of trace gases were performed over the Cape metropole area with the South African Weather Service Aerocommander 690A ZS-JRB aircraft. This is a twin-prop-engine aircraft with an operational ceiling of 4 km and speed of 200 ms^{-1}. Seventeen flights, confined to altitudes below 2000

m, were conducted between July 29 and August 26 with a total flying time of about 24 hours. Figure 5.4 shows tracks of four flights selected as case studies in this work, flights on which aerosol samples were collected for microscopy analysis, Flights 9, 13, 14 and 16 - August 6, 15, 22 and 23, respectively. Flight details are given in Table 5.2, together with flights selected as case studies to describe vertical distributions of particles. Other flights were excluded from microscopy analyses because of low aerosol particle loadings and restricted Scanning Electron Microscope (SEM) image quality due to sample charging.

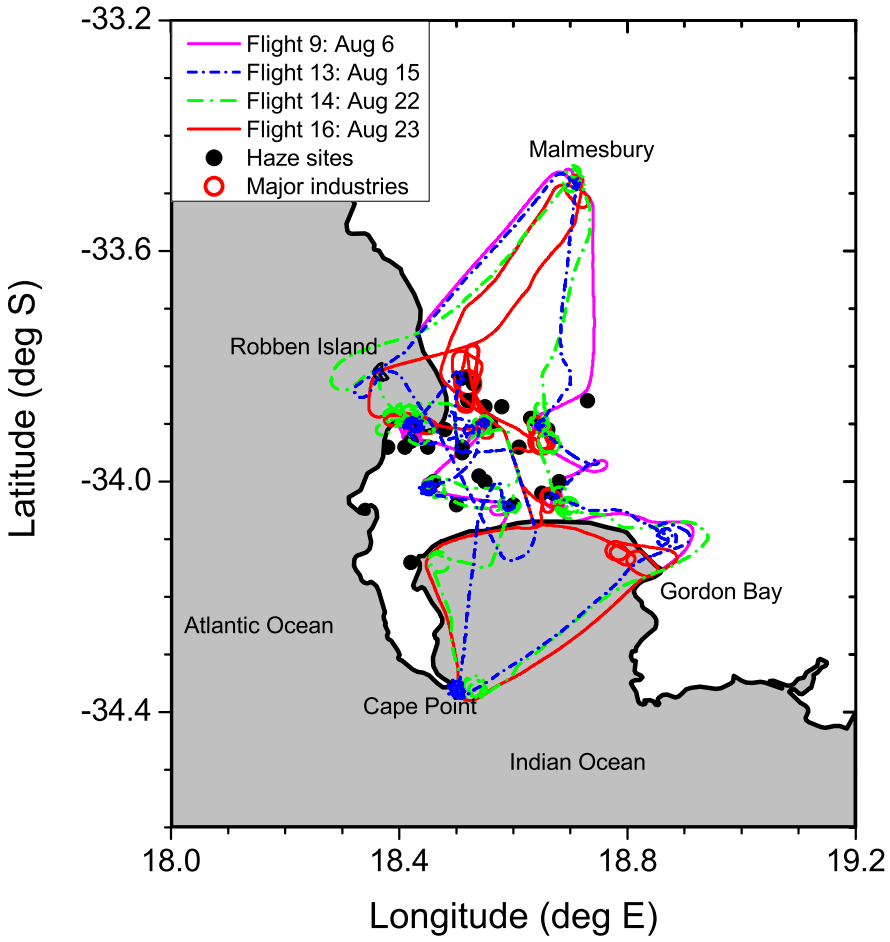


Figure 5.4: Flight paths, haze meter stations and major industry locations. Flights 9, 13, 14 and 16 were conducted on August 6 (1020 – 1200 UTC), 15 (1230 – 1500 UTC), 22 (0700 – 0920 UTC) and 23 (0630 – 0840 UTC), respectively. A detailed map of the haze meter sites is given in Figure 5.5.

The research crew was based at Malmesbury (18°43′E, 33°29′S, 101 m above sea level) about 60 km north of Cape Town. All flights originated at Malmesbury and went over Robben Island, Cape Point, Gordons Bay and terminated at Malmesbury. To avoid the Cape Town International airport approach zone that runs nearly NNW-SSE of the study area, short legged turns were made to the east and west of the approach zone, with loops between the Cape Point and Gordon Bay. This was the general flight pattern, though details

of each flight differed depending on daily planning, focus and meteorological conditions.

On board the aircraft were instruments for measuring aerosol particles, cloud micro-physical parameters and trace gases. Aerosol instruments consisted of two Optical Particle Counters (OPCs), a Passive Cavity Aerosol Spectrometer Probe (PCASP Model 100) and a Forward Scattering Spectrometer Probe (FSSP Model 100) both by Particle Measuring Systems (PMS). Filter samples of aerosol particles were collected using an Air Borne Streaker (ABS) sampler. Trace gases sampled were CO, CO_2, H_2S, O_3, NO, NO_2, SO_2 (all analysers used are from Thermo Environmental Instruments Inc., TEI). There were problems with CO and CO_2 instruments (R. Burger *pers. comm.*) and further corrections needed are beyond the scope of this study. VOCs were analysed from collected samples in canisters soon after each flight with gas chromatography - flame ionisation detection technique, GC-FID (*Chiloane*, 2005).

Besides the global positioning system used in the aircraft, several locations were also identified to coordinate flight paths. These locations are shown in Figure 5.5, and the coordinates are listed in Appendix C Table 1. The locations will be referred to extensively to identify locations where ABS samples were collected and to describe the distribution of aerosol particles in the haze.

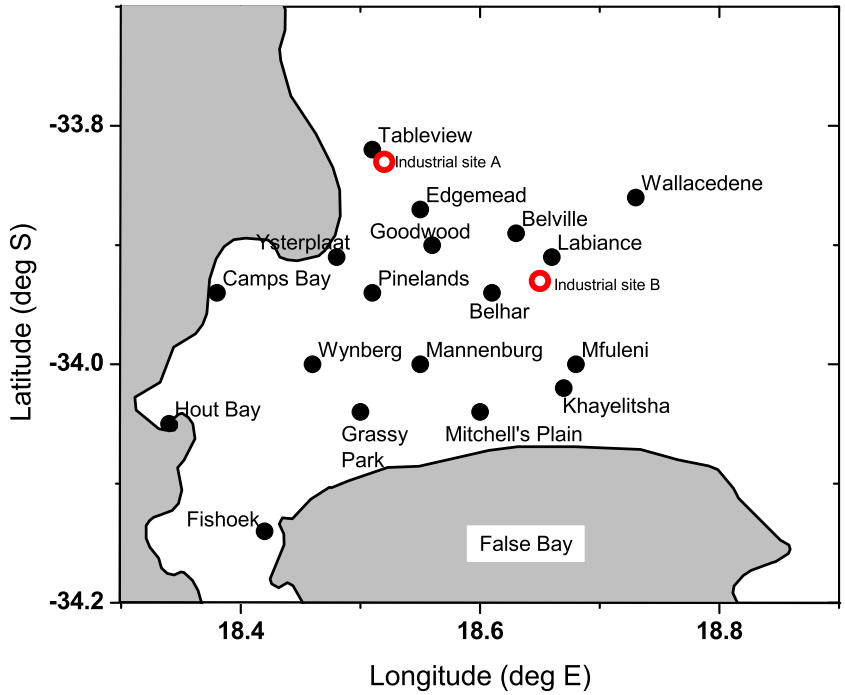


Figure 5.5: Haze meter sites used to identify ground locations of flight paths. These locations are schools in Cape Town that were involved in collecting solar intensity measurements with haze meters, for details see *Piketh et al.* (2004). Site locations of two major industries A - an oil refinery and B - a glass manufacturing industry.

Table 5.2: Flight summary of selected flights.

Day dd-mm	**Flight No.**	**Times UTC**	**Meteorological conditions**	**Aerosol type**	**ABS samples and comments**
02-08	4	0915 – 1030	E winds, low level inflow, $\Gamma = -9.7$ K km^{-1}	predominantly marine	No ABS sampling, morning flight
06-08	9	1020 – 1200	NW winds, fast descending air masses, $\Gamma = -8$ K km^{-1}	marine origin with continental influence	Samples #1 to #4, afternoon flight
07-08	10	0640 – 0750	Unsettled conditions. The air masses had circulated over the Northern, Eastern and Western Cape Provinces	both marine and continental origins	No ABS sampling, morning flight
15-08	13	1230 – 1500	NW winds. Some low level inflow for 5 days on or close to the sea surface, $\Gamma = -6.2$ K km^{-1}	predominantly marine	Samples #5 and #6, afternoon flight
22-08	14	0700 – 0920	NE winds that originated at high altitudes over the Atlantic Ocean and travelled into the interior of South Africa to the western area of North West Province before descending to Cape Town. Elevated surface inversion layer extending to 1006 hPa ($\approx$ 170 m), $\Gamma = -8.2$ K km^{-1}	marine origin with continental influence	Samples #7 to #9, morning flight
23-08	16	0630 – 0840	North winds that originated at high altitudes over the Atlantic Ocean and travelled into the interior of South Africa to the western area of North West Province and the north of Northern Cape Province before descending to Cape Town. Low level flow over continent for a day before being sampled.	marine with continental influence	Samples #11 and #12, morning flight

ABS = Air Borne Streaker, Γ = dry adiabatic lapse rate, UTC=Local time zone-2 hours.

Short interval ascents and descents were performed on flights to describe vertical distributions of particles. Vertical profiles on three flights were selected as case studies to demonstrate typical vertical distributions in the boundary layer at several locations. The flight tracks of selected segments are shown in Figure 5.6. These profiles have been labelled Profile A to G.

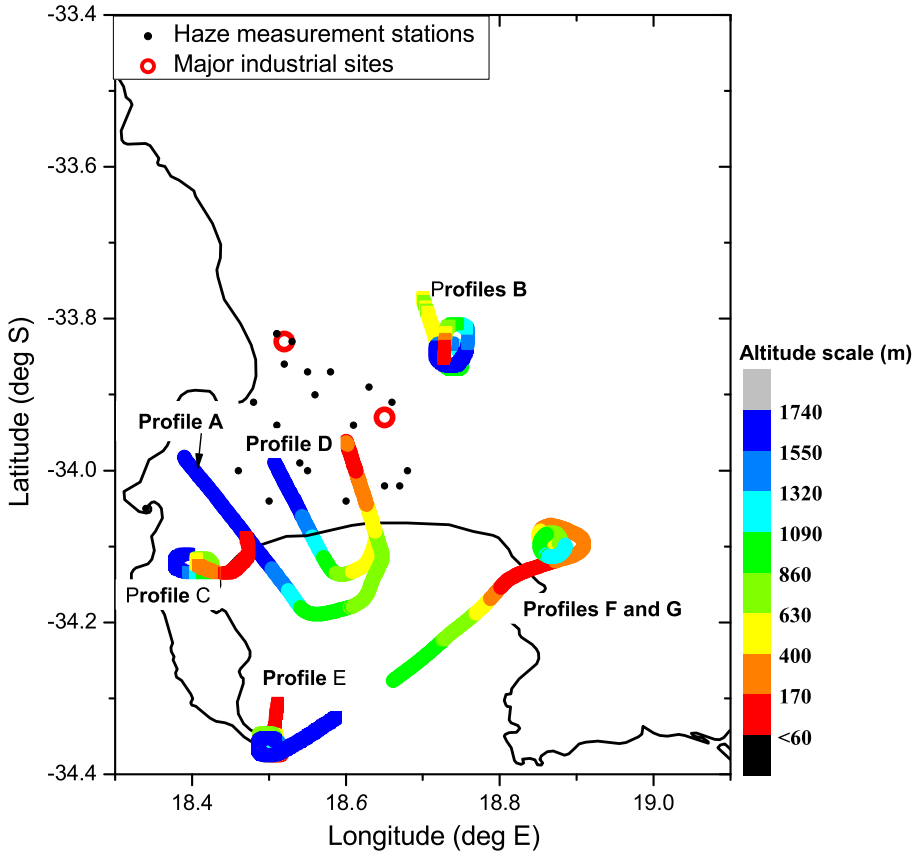


Figure 5.6: Segments of flight tracks where vertical profiles were performed on Flight 10, August 7 Profile A from 0651 – 0702 UTC; Flight 4, August 2, Profile B from 0923 – 0935, Profile C from 1002 – 1007 UTC; Flight 13, August 15 Profile D from 1257 – 1305, Profile E from 1403 – 1418 UCT, Profiles F and G from 1421 – 1433 UTC.

5.2.3 Measurement techniques

5.2.3.1 ABS aerosol sampler

The ABS sampler is an aerosol particle sampling device designed at the Max Planck Institute for Chemistry, Mainz, Germany and based on the PIXE[5] International (Proton Induced X-ray Emission) circular streaker sampler (*Annegarn et al.*, 1996). Aerosol particles are

[5]http://www.pixeintl.com/Streaker.asp

collected on temporal and spatially resolved filter samples during airborne measurements. A full description of the ABS design and specifications is given by *Annegarn et al.* (1996) and therefore the description here will be brief.

The ABS sample inlet was positioned on the right wing of the plane. Aerosol particles are collected isokinetically with a 10 μm cut-off diameter onto a filter (Nuclepore straight-through filters, pore size 0.3 μm). The filter is fixed on a frame that is rotated by a stepping motor at steps of 22.5° per position, hence 15 deposition samples on the filter are collected without overlapping on a complete frame, with a reference point as the zero position as sketched in Figure 5.7. Particles are deposited on a surface area of about 1 cm^2 on each position.

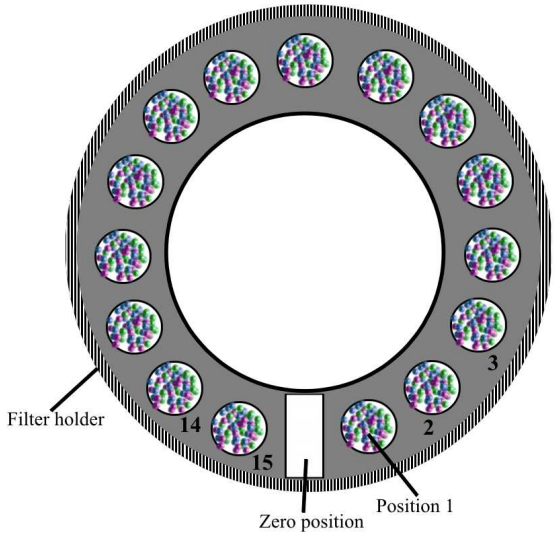


Figure 5.7: Schematic view of the collection of aerosol particles on an ABS filter.

Stepping time intervals of the streaker were controlled either manually or in an automated mode using a microprocessor to sample between 45 to 50 litres on each deposition spot with a flow rate of 4.5 ± 0.5 l/min. A computer interface with the ABS generated a data file with pump and environmental parameters (temperature, pressure, volume, flow rate) every 10 seconds. Collection times on each deposition sample were manually correlated to flight paths to locate areas over which samples had been collected, because the ABS was not connected to aircraft data acquisition systems. Times on the aircraft system and ABS were checked regularly and synchronised to within certainty of ±30 seconds.

Thirteen ABS samples were investigated with the Scanning Electron Microscope (SEM). The ABS sampled flight segments are described in Table 5.3 and shown in Figure 5.8 (for coordinates of haze meter stations see Figure 5.5 and Appendix C Table 1). Note that Sample #5 coincided with Profile D, and this sample was collected at the lowest altitude levels possible over the Cape Town International Airport runway. Other flights

were excluded because of restricted SEM image quality due to sample charging or due to low aerosol particle loadings. Due to low aerosol loadings, no ABS samples from clean background locations could be characterised for comparison with polluted locations. All samples chosen were collected during intense haze days.

Each sample was collected over an average time of 10 minutes, at an average ground speed of 80 ms^{-1}, giving track coverage of about 50 km. It is not possible, therefore to resolve variations of particle morphologies with altitude due to short time scales of ascents or descents, which were less than 10 minutes. ABS sampling was confined within the boundary layer within 50 to 700 m asl except for Sample #5. Therefore samples were collected in the residual or newly forming mixing layer on morning Flights 14 and 16, and in the convective boundary layer, for afternoon Flights 9 and 13. No attempt will be made to resolve chemical compositions of particles based on the structure and dynamics within the boundary layer, because flight altitudes were never confined to individual boundary layer stratifications described in Section 5.2.1. In subsequent sections, particle origins, morphologies and abundance will be discussed as representative of aerosols in the entire boundary layer.

Table 5.3: Flight numbers, dates, times (UTC), ABS samples analysed with the SEM and locations where samples were collected (see Figures 5.5 and 5.8 for ground locations).

Flight No & time	**ABS sample ID**	**Alt. ± std (m)**	**Ground locations**
Flight 9 August 6 1020 – 1200	Sample #1	355 ± 155	Central Business District (CBD) to Pinelands
	Sample #2	280 ± 109	Goodwood, Pinelands to Wynberg
	Sample #3	130 ± 12	Wynberg, Grassy Park, Mitchell's Plain
	Sample #4	269 ± 126	Khayelitsha, Mfuleni, Belville
Flight 13 August 15 1230 – 1500	Sample #5	1068 ± 641	around Ysterplaat, to Mitchell's Plain and the Cape Town International Airport runway
	Sample #6	227 ± 209	Goodwood to Wynberg
Flight 14 August 22 0700 – 0920	Sample #7	143 ± 49	Goodwood, Mannenburg, Wynberg
	Sample #8	111 ± 67	Mitchell's Plain over sea to Fishoek
	Sample #9	190 ± 18	several turns over Khayelitsha
	Sample #10	261 ± 44	several turns around industrial site B, Labiance and Belville
Flight 16 August 23 0630 – 0840	Sample #11	166 ± 45	Malmesbury to Robben Island
	Sample #12	136 ± 13	Ysterplaat and Central Business District (CBD)

std=standard deviation around the mean altitude

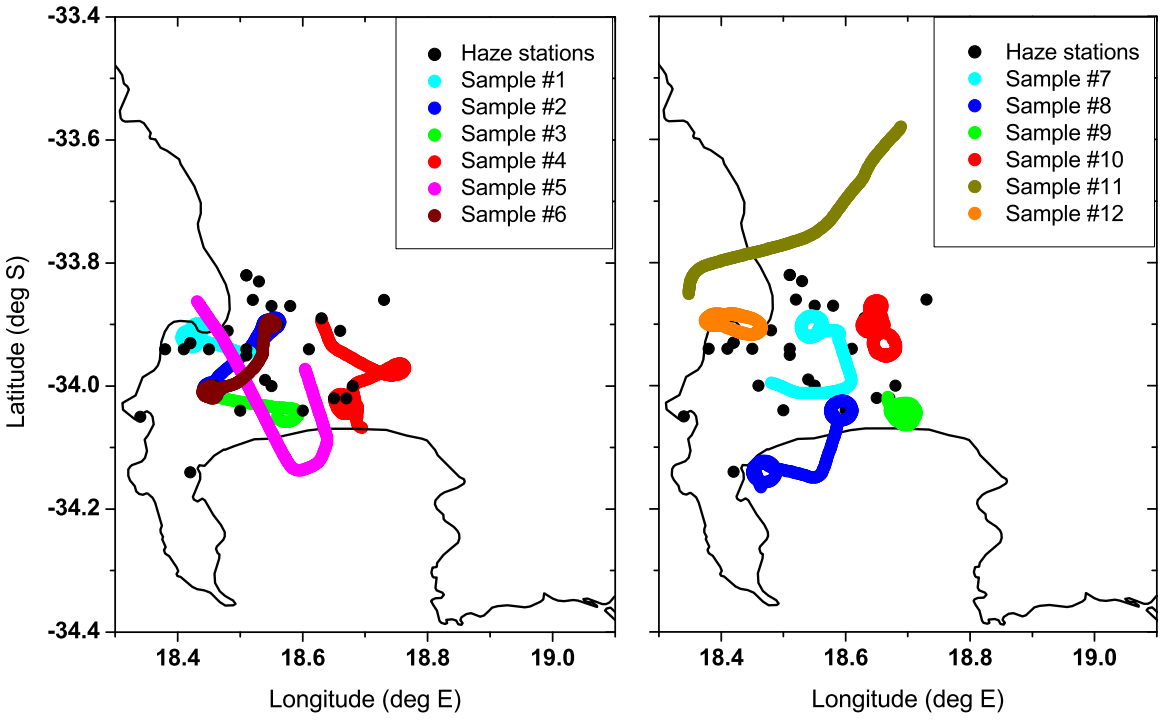


Figure 5.8: Locations where ABS aerosol samples were collected for microscopy analysis on Flights 9, 13, 14 and 16 - August 6, 15, 22 and 23, respectively.

5.2.3.2 Optical particle counters

The Passive Cavity Aerosol Spectrometer Probe (PCASP-100X, PMS Inc., Boulder, Colorado) was used to measure size distributions of dry aerosol particles with optical diameters of 0.1 to 3.5 μm in 15 size channels. The sample inlet was positioned on the left wing of the aircraft. Inlet heating systems were switched on to prevent icing. The PCASP is an optical particle counter that measures sizes of single aerosol particles from their scattering intensity. An air stream is passed through an aerodynamic focusing inlet. Particles intercept a HeNe laser beam (with wavelength = 635 nm) and scatter light in all directions. Light scattered at angles between $35° - 120°$ is captured by the parabolic mirrors, directed onto the 45° mirror, reflected onto an aspheric collector and then focused into the scattering photodetector module. Particle sizes are determined from the intensity of scattered light through Mie scattering theory.

The PCASP was pre-campaign calibrated in June 2003 by Particle Metrics Inc. (PM Inc., Boulder, CO) using spherical polystyrene latex (PSL) particles of diameters 0.123,

0.176, 0.198, 0.22, 0.269, 0.3, 0.491, 0.705, 1.04 and 1.992 μm. Table 5.4 lists the nominal and calibrated midpoints. From the calibration fit, sizes of particles with $d_p = 0.10$ μm were overestimated by 11% to 0.11 μm, while the effect systematically changed with particle size to an underestimation of 14% for $d_p = 3.15$ μm to 2.75 μm. This correction considers particles to be spherical, and the PCASP response is slightly sensitive to shapes of particles being measured (*Liu et al.*, 1992). These authors found the lower size limit on PSL spheres to be 0.125 μm $\pm$ 5% instead of the nominal size of 0.100 μm. Shifts in size channels measured in our PCASP are significantly larger over the entire range as shown in Table 5.4.

Table 5.4: Channel parameters of the PCASP before and after midpoint corrections by calibrating with PSL spheres of refractive index $m = 1.585 - 0.0i$.

PCASP channel number	**Calibrated midpoint** d_{PMS} **(μm)**	**Nominal midpoint** d_{PSL} **(μm)**	$\frac{(d_{PSL}-d_{PMS})}{d_{PSL}}\%$
1	0.11	0.10	-10.57
2	0.13	0.12	-9.42
3	0.155	0.14	-8.19
4	0.185	0.17	-6.94
5	0.225	0.21	-5.53
6	0.275	0.26	-4.07
7	0.35	0.34	-2.28
8	0.45	0.45	-0.38
9	0.60	0.61	1.84
10	0.80	0.83	4.11
11	1.05	1.12	6.30
12	1.35	1.46	8.36
13	1.75	1.93	10.54
14	2.25	2.54	12.69
15	2.75	3.15	14.43

Total particle counts measured with the PCASP were corrected for dead-time using activity signal of the instrument. The activity signal is the 1 kHz oscillator that is gated while the probe is processing particle data and cannot measure any incoming particle. Total counts with activity signals greater than 50% were excluded (as recommended by S. Matthews, PM Inc., *pers. comm.*). This is to reduce coincidence errors and to ensure that the probe electronics have time to return to the passive state.

There are several potential sources of errors in the PCASP sizing of particles. Firstly, losses of small particles due to detection sensitivity and losses of larger particles in the instrument inlet walls are inevitable, but cannot be quantified in this study. Secondly,

the PCASP defines particle sizes based on PSL spheres with complex refractive index of $m = 1.585 - 0.0i$. Corrections have to be made for particle sizes with different refractive indices. This effect will be discussed in Section 5.6.1. Lastly, since the heating systems were switched on, the PCASP measured dry diameters of aerosol particles. In high relative humidity (RH) conditions where some particles might contain water, particles might be partially evaporated, e.g., due to short residence times inside the heating column. Therefore measurements might be biased, particularly for hygroscopic particles of diameters above 1 μm (*Garrette et al.*, 2002). Effects of RH will be addressed in Section 5.6.3. Additionally, due to effects of pitch angle of aircraft which can disrupt isokinetic sampling of the PCASP inlet, particle number distributions are slightly underestimated during ascents than descents (*Haywood et al.*, 2003a).

Number-size distributions of particles in the range between 2 and 47 μm in diameter were measured with the Forward Scattering Spectrometer Probe (FSSP Model 100, PMS Inc., Boulder, Colorado). Light intensity scattered by a particle at angles between $4° - 12°$ in the forward direction is measured and related to particle size using the Mie scattering theory. Sizes are determined assuming that light has been scattered by a spherical liquid droplet of refractive index $m = 1.33 - 0i$ and therefore need to be corrected for particles with different refractive indices and non-spherical shapes. Number concentrations were corrected for dead time activity losses using the output of the instrument.

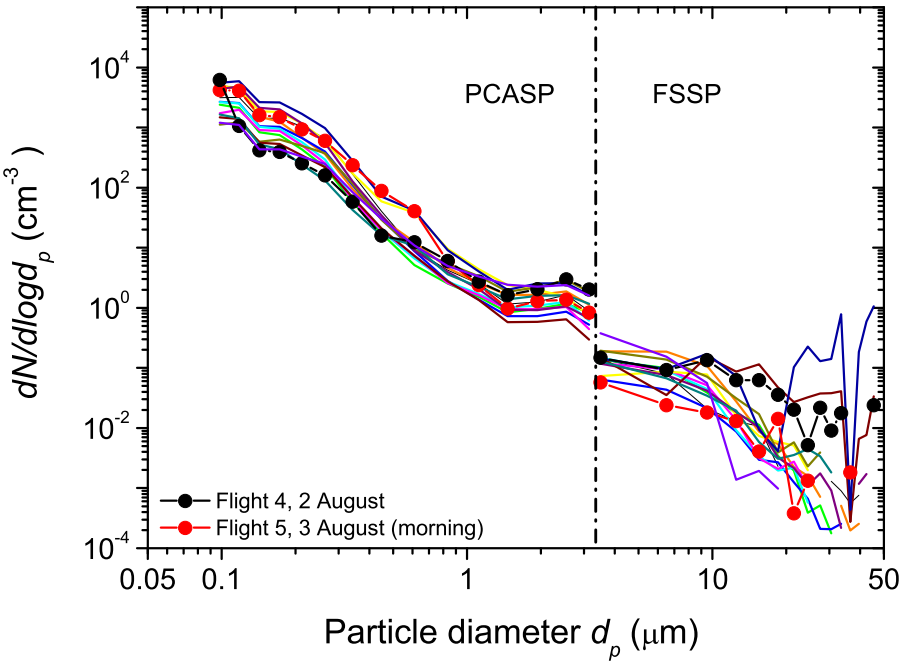


Figure 5.9: Averaged particle number-size distributions of each flight as measured by the optical particle counters. Distributions showed a discontinuity between d_p of $3 - 4$ μm. Flights 4 and 5 (in black and red) are profound cases highlighted, with a discrepancy of a factor of up to 14 (dN_{PCASP}/dN_{FSSP}).

To check for consistency between the PCASP and FSSP, averaged number distributions were computed over entire flights and plotted in Figure 5.9: N_{PCASP} for the PCASP and N_{FSSP} for the FSSP. A significant discontinuity in number concentrations measured by the two OPCs exists between particle diameters d_p of 3 μm to 4 μm. The FSSP number concentrations are between 2 to 14 factors lower than the PCASP on all flights. Although these size distributions cannot be directly compared, because instruments are assuming different refractive indices and water content of particles, such factors are not enough to account for the discrepancy. The supermicron FSSP size distribution are sensitive to particle sphericity and higher discrepancies of 2 orders of magnitude have been observed on these OPCs in the regional biomass-influenced haze of southern Africa (*Haywood et al.*, 2003b). This sensitivity might be pronounced in an urban environment like Cape Town where high concentrations of aggregated soot particles are expected. Additionally, both OPCs might not be reliable at measuring low particle concentrations (see Section 5.4.2). Because of uncertainties in the FSSP size distributions, only the PCASP aerosol measurements will be considered hereon.

5.2.4 Meteorology conditions during campaign period

Airborne measurements were focused on capturing periods with the most intense brown haze episodes. From CTBH I study, these episodes were observed during winter season between the months of March to August. In general, brown haze episodes are associated with low winds, clear sky conditions and elevated inversions. These meteorological conditions are typical of high pressure systems (anticyclonic conditions) usually centred in the south, south-east or to the east of the subcontinent, with peak surface pressures greater than 1020 hPa.

In this study, a meteorological station was set up in Goodwood (18.56°E, 33.90°S and 40 m asl). Continuous measurements of wind parameters, solar radiation, ambient temperature, relative humidity (at 5, 8 and 10 m above ground) and barometric pressure were recorded every 15 minutes (except for the gap on August 4 and part of August 5 due to instrument malfunction). Figure 5.10 shows a time series of temperature (°C), relative humidity (%) and barometric pressure (hPa) from July 30 to 26 August 2003 at 10 m above ground. Temperatures generally increased from about 5° at sunrise to around 20° at midday. Radiative heating of surface after sunrise gives rise to turbulent vertical mixing, and is the main mechanism for transporting emissions released in the boundary layer.

Daily relative humidity soundings available from a meteorological station at Cape

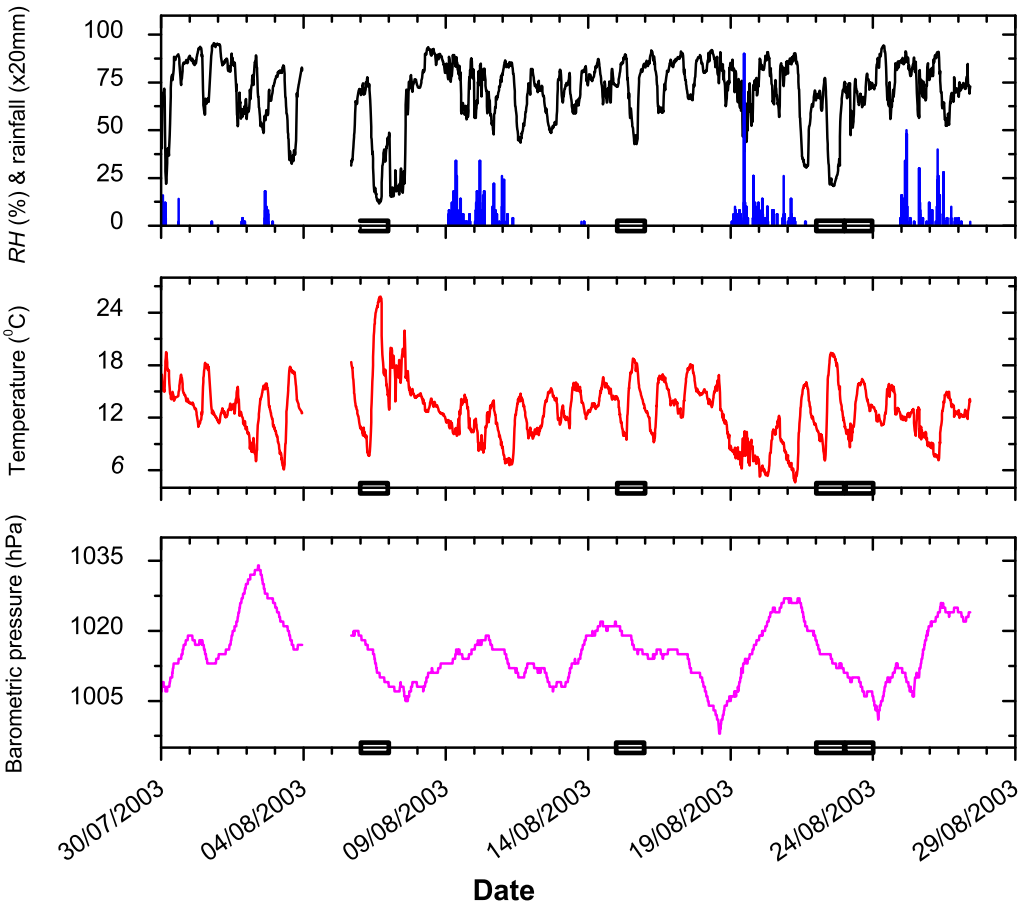


Figure 5.10: Relative humidity *RH* (%, black), rainfall (x 20 mm, blue), temperature (°C, red), and barometric pressure (hPa, magenta) at Goodwood meteorology station (18.56°E, 33.90°S). All parameters were measured 10 m above ground, from 30 July to 26 August 2003. The rainfall column plot is exaggerated 20 times to fit the scale. Boxes on the time scale indicate days when ABS samples used in the case studies were collected. The gap on August 4 to 5 was due to instruments malfunction.

Town International Airport (18°36′E 33°59′S, 42 m asl) were taken to be representative of the domain, since there were no *RH* measurements during flights. Vertical soundings conducted on August 6, 15, 22, and 23 between 1020 and 1045 UTC are plotted in Appendix C Figure 1 (data provided by South African Weather Service). Appendix C Figure 1 shows relative humidity profiles at Cape Town International Airport weather station, soundings made at least 2 hours prior, or 3 to 4 hours after flights. The *RH* stayed between 50 and 80% most of the time, which is consistent with profiles shown for Cape Town in Appendix C, Figure 1. But above 200 m, the *RH* remained below 37%. Therefore, on August 6, 15 and 23, *RH* was likely less than 40%, consequently PCASP size distributions on Flight 9, 13, and 16 were probably representative of ambient aerosols. On August 22, *RH* soundings showed a decrease in *RH* from 80% at 2316 UTC (August 21) to below 25% at 1044 UTC. Since Flight 14 was conducted between these profiles, it is likely that *RH* was between 25

and 80% during this flight.

Potential temperature θ for dry adiabatic change was computed from static pressure and Poisson's equation as

$$\theta = T \left[\frac{p_0}{p} \right]^{0.286} \tag{5.1}$$

at measured pressure and static temperature p and T respectively, and reference pressure of $p_0 = 1000$ hPa (*Seinfeld and Pandis*, 1998). Aerosol vertical distributions will be discussed based on the boundary layer development and θ determined from equation 5.1. θ is a measure of the static stability of the atmospheric boundary layer (ABL). The ABL is stable, neutral or unstable for negative, neutral or positive gradient of θ, respectively.

5.2.5 Trajectory analysis

Five-day backward trajectories were calculated with program LAGRANTO, LAGRangian ANalysis TOol (*Wernli and Davies*, 1997) using ECWMF[6] data (European Centre for Medium-Range Weather Forecasts). Trajectories were initiated along flight tracks at user-defined pressure levels. Trajectory paths and vertical histories of pressure for four case studies of Flights 9, 13, 14 and 16 (August 6, 15, 22 and 23) are shown in Figure 5.11 and for the rest of the flights short descriptions are given in Table 5.2. The trajectories showed varying histories of sampled air masses from day to day. The meteorology of Cape Town is subject to synoptic mid-latitude frontal systems that cross the area from the west. Most trajectories show descending trends of air masses initiated in the marine troposphere at altitudes below 300 hPa (9 000 m) originating in the Atlantic Ocean, i.e., a few thousand kilometres south, south-west or west of Cape Town. In the southern hemisphere, these are usually pristine areas dominated by sea-salt and natural sulphate aerosols, and with limited influence of anthropogenic emissions (*Myhre et al.*, 2004). Depending on the time trajectories had been travelling over the continent, they were characterised as with/without continental influence, to better understand processes affecting chemical composition of particles.

Backward trajectories compared well with on-line models computed from NOAA HYSPLIT4 transport and dispersion algorithm using FNL Meteorogical data[7].

[6] http://www.ecmwf.int/

[7] http://www.arl.noaa.gov/ready/hysplit4.html

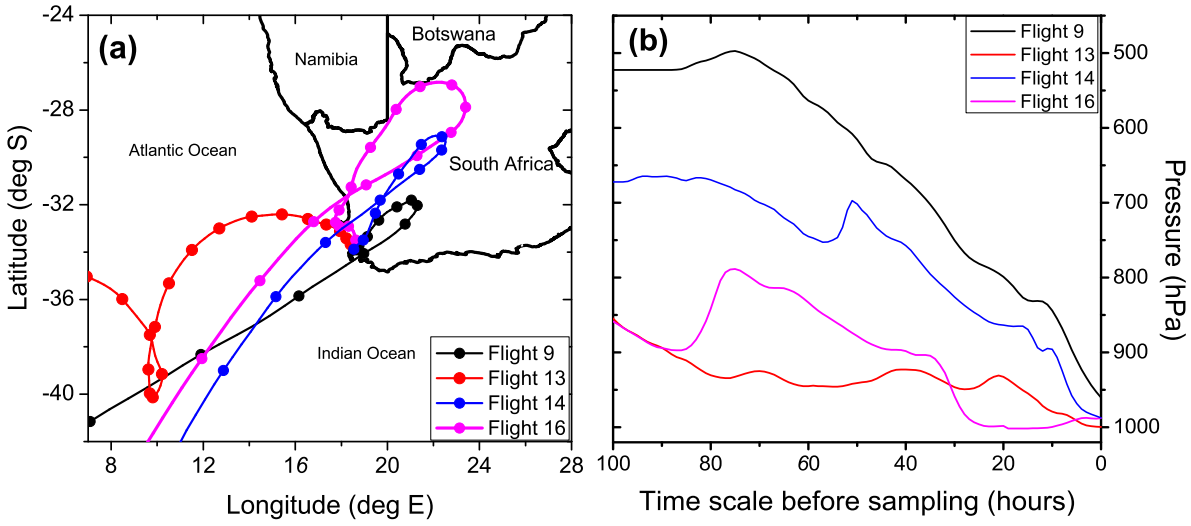


Figure 5.11: (a) 5-day back trajectories initiated on Flights 9, 13, 14 and 16 (August 6, 15, 22 and 23). Solid marks on the trajectory tracks indicate 6-hour time intervals. (b) Trajectory vertical histories of pressure.

5.2.6 Electron microscopy

Aerosol samples collected with the ABS sampler were analysed for morphology, size distributions and elemental composition of individual aerosol particles using a high resolution field emission Scanning Electron Microscope SEM (Leo 1530 SEM, E. M. Ltd., Cambridge, England, now Nano Technology Systems, Zeiss). Individual deposition spots were cut from the filter holder and glued with double sided carbon tape onto aluminium discs for conductive mounting in the SEM. Some samples were visible by naked eye when relatively high concentrations of aerosol particles had been collected. SEM images were taken by selectively combining the output of the backscattered secondary electron detector (BSD) with an in-lens annular secondary electron detector (SED) using acceleration voltages between 1.5 to 2.0 kV.

Analytical measurements were performed by evaluating X-rays emitted during electron bombardment on individual particles to determine elements with atomic numbers higher than 5 using Energy Dispersive X-ray (EDX) microanalysis. The detector was calibrated regularly with a Cu standard using the 8.04 keV Kα and 0.93 keV Lα energy levels (Mr Huth, *pers. comm.*). Although the EDX is able to detect light elements of C, N and O, the spectra were contaminated by background signals of C and O from the filter substrate. EDX analyses therefore provided semi-quantitative information on elemental composition of particles, excluding light elements.

To image particles (or analyse particles with EDX) random trajectories were followed on several positions on each deposition sample to avoid operator bias and deposition inhomogeneity. Particle had deposited sparsely on substrates and errors due to overlapping particles were negligible. Filters were not coated to enhance electrical conductivity (as is common with non-conductive substrates) because coating would interfere with elemental analytical measurements. Electrostatic charging presented difficulties on some samples by making particle identification impossible or particles would reshape due to charge built-up. For these reasons, resolutions of less than 6 nm per pixel length could not be achieved, except on individual particles larger than 0.5 μm.

5.3 SEM single particle analysis

5.3.1 Aerosol composition

Several particle morphological features were identified from SEM images. Based on morphology and elemental composition, particles were categorised into seven particle groups of: aggregated soot particles, mineral dust, sulphates (SO_4^{2-}), sea-salt, tar balls/fly ash, rod-shaped particles (some were associated with soot agglomerates) and those that could not be attributed to any of these groups were labelled as 'others'. Relative abundances of the seven groups were determined from 12 ABS samples, identified as Samples #1 to #12. The samples were collected on Flights 9 (Samples #1 to #4), Flight 13 (Samples #5 and #6), Flight 14 (Samples #7 to #10) and Flight 16 (Samples #11 to #12). Several images from each sample were selected to obtain reasonable statistical counts. All visible particles on selected images were counted, with total number counts of 731, 630, 492, 1410, 271, 297, 589, 388, 671, 954, 114 and 157 particles on Samples #1 to #12, respectively. In total 6704 particles were manually identified and categorised. In subsequent sections, particle origins, morphologies and abundance are discussed in detail.

5.3.1.1 Soot particles

Soot particles are formed from combustion processes of fossil fuels in vehicles, industries, biomass and domestic burning and in Cape Town also from old tyre burning. These processes contribute mostly to the accumulation mode of aerosol particles in the atmosphere. Soot aggregates were identified as agglomerates of small nearly spherical primary carbonaceous particles. Their morphology is fractal-like, formed from primary particles that had clustered

to form chains and branches whose fractal dimensions are between 1.4 and 3 (*Gwaze et al.*, 2005; *Meakin*, 1983). High resolution Transmission Electron Microscope (TEM) imagery show that primary particles are made of concentric wavy graphitic layers, sometimes with intrusions of crystalline material, e.g., potassium salts and or silica in biomass burning soot particles (*Li et al.*, 2003b; *Pósfai et al.*, 2003; *Wentzel et al.*, 2003). Morphological and dynamic properties of soot aggregates are described in more detail in Chapter 4.

Compactness of soot aggregates varied from closely packed particles Figure 5.12(a), to chained and branched aggregates as shown in Figure 5.12(b). Some aggregates were agglomerated with large spherical particles with diameter larger than 100 nm - and these are likely tar balls that were embedded in soot particles during the coagulation process in the cooling smoke.

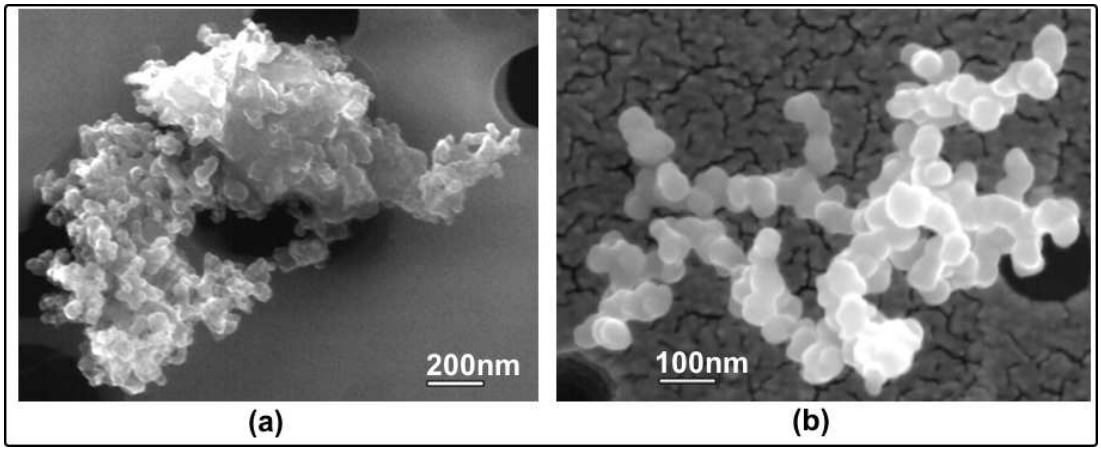


Figure 5.12: (a) Large and compact soot aggregate collected with the ABS sampler. (b) A chained soot particle with agglomerated spheroids. This particle was collected on a gold-coated filter with a ground sampler and the morphology is similar to those soot aggregates collected with the ABS.

Some of the large aggregates with morphology similar to the aggregate shown in Figure 5.12(a) had surface diameters larger than 10 μm. EDX spectra of these particles revealed C and O, with traces of Si, P, and S indicative of carbonaceous particles from vegetation combustion. Although their number density calculated on the samples was low (approx 10^{-4} particles per μm^2, compared to $>10^{-1}$ particles per μm^2 for the rest of the particles), these large soot particles contribute significantly to mass of carbonaceous particulate matter (PM). Similar 'giant' combustion particles were observed in ground samples collected in an urban residential area of Soweto, Johannesburg, South Africa (*Wentzel et al.*, 1999). The particles were attributed to combustion emissions from domestic stoves[8].

[8]The domestic stoves commonly referred to as 'Mbaula', are of a particular type used in Southern African for heating and cooking. Fuel is combusted in a perforated metallic container. Bituminous coal, wood or charcoal are the main fuel types (see, e.g., *Ballard-Tremeer*, 1997)

Soot particles were the most absorbing specie, and in an urban aerosol burden where higher volume fractions of soot are observed, the mixing state will affect optical properties of aerosols. Such effects have been demonstrated with theoretical calculations on plausible soot/sulphate and soot/mineral dust mixtures (*Ackerman and Toon*, 1981). Mixing states of particles were considered for soot/sea-salt, soot/mineral dust or soot/sulphates. Particles observed in this study were externally mixed, suggesting either recent emissions or particles that had not been processed in clouds. This is in agreement with several studies of urban environments where external mixed soot dominated light absorbing component of urban aerosols (*Hasegawa and Ohta*, 2002; *Jacobson*, 2001; *Mallet et al.*, 2004). Soot particles must spend considerable time from the emission source to interact in the atmosphere, for example to create soot/sulphates mixtures on aged biomass burning emissions (*Li et al.*, 2003b; *Pósfai et al.*, 2003). Evolution of mixing state of particles with soot approaches those of internally mixed states within five days (*Jacobson*, 2001), and with an increase in particle size from externally mixed soot particles (*Hasegawa and Ohta*, 2002).

Soot particles were the most prevalent type in the boundary layer, with percentage fractional number concentrations of up to 46% observed on Sample #11 collected on August 23. Due to the large surface area of aggregates (see Section 4.3.6), such high concentrations of soot particles are likely to enhance heterogeneous reactions in the polluted atmosphere of Cape Town, e.g., production of nitrous acid (*Ammann et al.*, 1998). However, these fractional concentrations might also be slightly overestimated because soot particles are stable both under the electron beam and in the SEM vacuum unlike secondary derived aerosols, which might have sublimated and were not counted.

Fractional number concentrations of soot particles were highest on days with the lowest relative humidity, particularly on August 23, when contributions were between 41% and 46%. In comparison with other studies, mass contribution of elemental carbon at a site representative of central Europe was $10\% - 31\%$ in the size range of d_p of $0.05 - 1.20$ μm (*Neusüß et al.*, 2002). Higher apportionments have been reported at an urban site in Japan where soot particles of diameter range of 0.08 to 1.60 μm were present in $42\% - 49\%$ of the fractional number concentrations (*Hasegawa and Ohta*, 2002), and urban polluted air masses at a rural site in Germany were characterized by up to 80% soot in the diameter range of 0.1 to 0.2 μm (*Ebert et al.*, 2004).

Equivalent diameters of projected surface areas, d_a, were measured on particles on Samples #1 and #4. Distributions of d_a were separated into those of soot aggregates and all particles as shown in Figure 5.13. The two soot size distributions are similar, with sizes between 0.1 and 2 μm and lognormal fits of geometric mean diameter $d_a = 0.59 \pm 0.02$

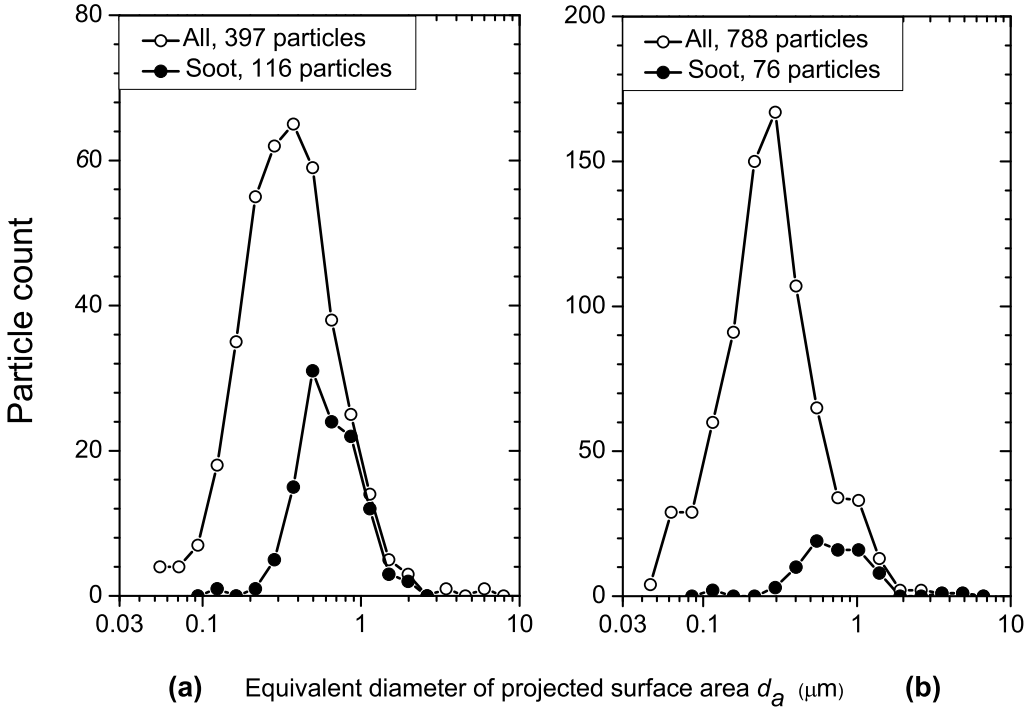


Figure 5.13: Distributions of equivalent surface diameter d_a for soot aggregates and all particles on samples collected on Flight 9 (a) Sample #1 and (b) Sample #4. Soot aggregates contribute to the largest surface diameters.

μm with $\sigma_g = 1.45 \pm 0.11$ on Sample #1 and $d_a = 0.66 \pm 0.05$ μm with $\sigma_g = 1.50 \pm 0.25$ on Sample #4. When compared with size distributions of the rest of particles, soot aggregates contribute to large sizes, particularly on Sample #1. However, it should be noted that the deposition position of soot aggregates exposes a large surface area for imaging. As observed in Chapter 4, the surface diameter might be larger than the actual volumetric diameter by more than a factor of 2, because the third dimension (which is unknown) might just be the depth of the diameter of primary spheres ($20 - 70$ nm) that have aggregated.

5.3.1.2 Mineral dust

Mineral dust particles are emitted into the atmosphere from industrial processes, as aeolian particles from exposed soil surfaces or vehicle entrainment from unpaved roads. Particles were identified both from their morphology and elemental compositions from EDX micro-analysis. The particles were abundant in the coarse mode. Figure 5.14 shows some typical dust particles. Morphologies of dust particles varied from crystalline (labelled X in Figure 5.14(a)), agglomerates made of spheroids with diameters between 20 nm and 1 μm (labelled Y in Figure 5.14(b)) to crystalline shaped particles with sharp edges Figure 5.14(c, d). EDX

spectra of these particles are shown in Figure 5.15.

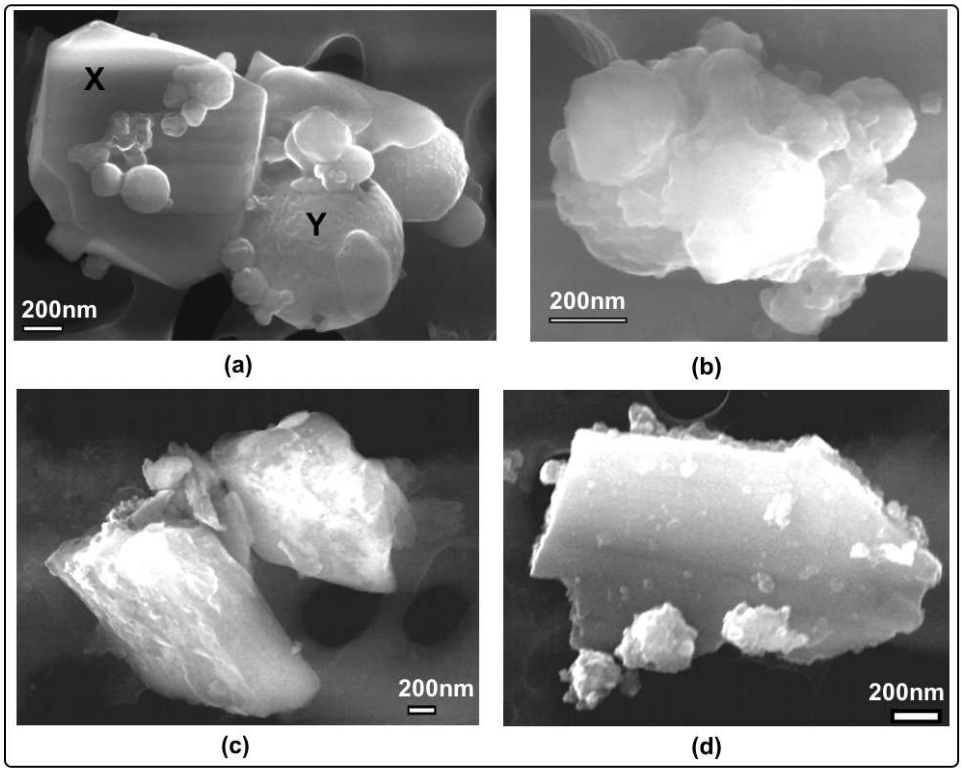


Figure 5.14: (a) Mineral dust particles with complex composition, mainly Na, Si, Ca, Fe, Zn, and Mn with traces of S, Mg and Al (see text for description of labels X and Y). (b) Mineral dust particle made of agglomerated spheroids and composed of Na, Si, S, Fe and Zn and minor components of Al, Mg, K, Ca and Mn. (c) Silica (quartz) particles. (d) An iron silicate particle. EDX spectra of (a) to (c) are shown in Figure 5.15.

EDX spectra collected on several particles from all samples show that particles consist mainly of Na, Mg, Al, Si, K, Ca, Ti, Fe and Zn. About 10% of 97 particles observed on Sample #1 were silicon oxide particles. Majority of particles were aluminosilicates sometimes with calcium carbonate, and iron oxides mixed with silicates of several oxides/hydroxides from Na to Zn on the periodic table.

The maximum fractional number concentration of dust particles on all samples was less than 2%. Such low concentrations are to be expected in Cape Town during the winter season, which is also the wet season, since source strengths of particles from exposed land surfaces are reduced. Mineral dust particles also showed varying amounts of sulphur, which might have been adsorbed from gas phase onto particle surfaces. Sulphur was identified on most particles except on silica particles and this is consistent with laboratory observations (*Usher et al.*, 2003). Soil dust particles can provide alkaline surfaces for heterogeneous conversion of gaseous SO_2 and also NO_x to sulphates and nitrates (*An-*

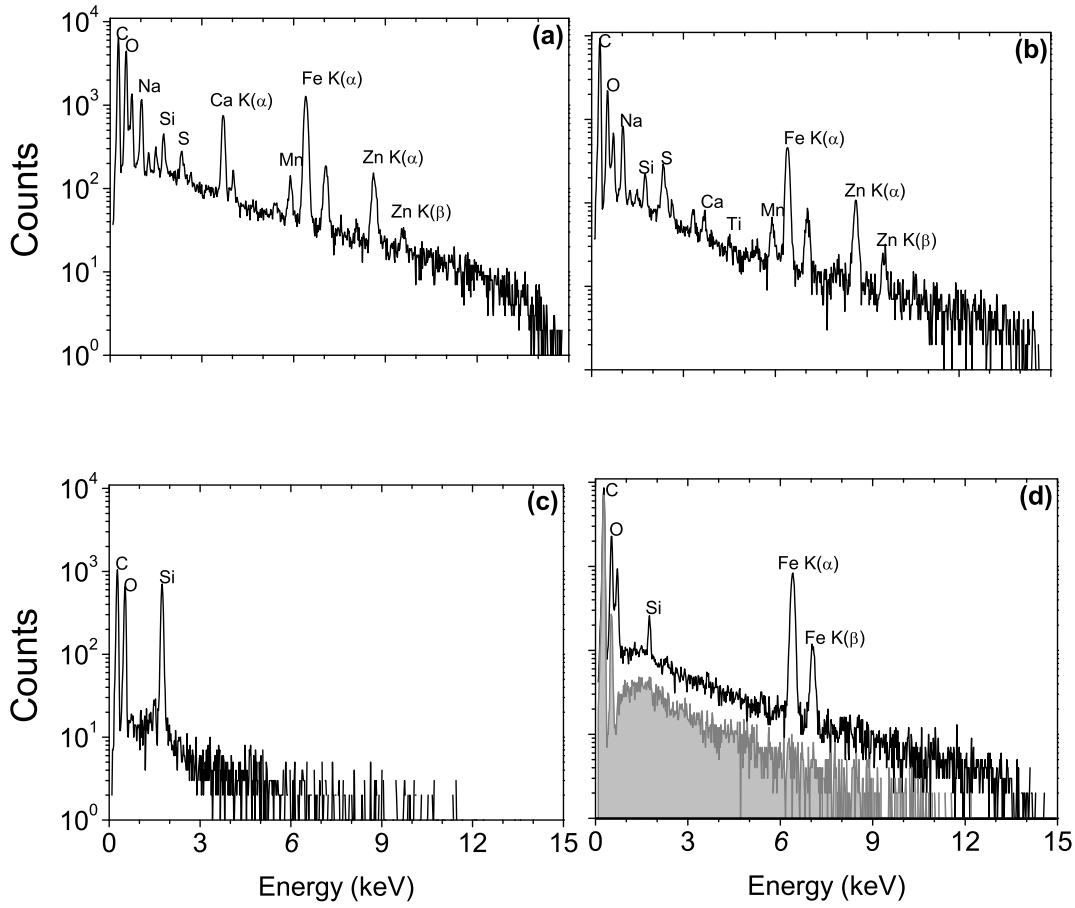


Figure 5.15: EDX spectra of mineral dust particles shown in Figure 5.14, respectively. Shaded plot in (d) shows the substrate spectrum with C and O, on an area void of particles. Energy values labelled refer to K(α) levels unless indicated.

dreae and Crutzen, 1997). Mineral dust particles could contribute to a sink for SO_2 in Cape Town area, however the impact might be trivial due the low loading of dust particles. Average elemental concentrations of mineral dust over Cape Town as measured with the PIXE analysis (Proton Induced X-ray Emission) during the winter of 1992 indicated that dust aerosol particulate matter was contributing to less than 5% of total mass collected on filters samples (*Pineda and de Villiers*, 1995). Considering mineral dust particles were in the coarse mode, the present study therefore indicates higher fractional mass of mineral dust content than has previously been reported.

5.3.1.3 Sulphates

Sulphate particles are formed in the atmosphere from oxidation and condensation of SO_2 (*Seinfeld and Pandis*, 1998; *Sievering et al.*, 1994). Aqueous H_2SO_4 formed is neutralised

to $(NH_4)_2SO_4$ or intermediate products depending on the amount of ammonia present. Sulphate particles were identified by the presence of a deposition 'ring' of small nearly spherical 'satellite' droplets around central core particles, Figure 5.16. White arrows in Figure 5.16(a) show the distortion of the SEM image due to sample charging, one of the limitations of using non-conductive substrates.

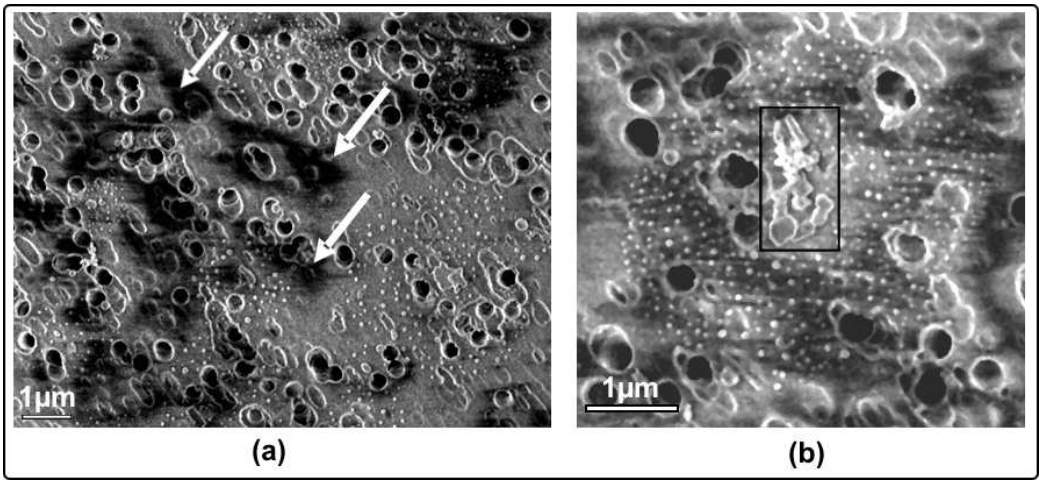


Figure 5.16: SEM images of sulphate particles collected on Flight 14. Particles have satellite droplet rings typical of dehydrated sulphuric acid, encircling core particles, in the box (b). Arrows point to distortions in the image due to sample charging effects.

Sulphate particles were most abundant on Flight 14, August 22, with fractional number concentrations of 77% and 82% on Samples #8 and #10, respectively. Surface diameters of 'satellite' ring particles were between 60 and 200 nm (measured on 550 particles). The rings were spread over a couple of μm^2 and this area probably depended on the size and dilution of the deposited particles. Satellite particles were sensitive to the electron beam and sublimated entirely, more rapidly than the core particles. Morphology of the central cores (enclosed in the insert of Figure 5.16b) varied from spheres clearly larger than the satellite droplets, small clustered particles to single amorphous grains of sizes up to 0.5 μm. Some amorphous grains might not have been entirely dissolved upon deposition or sulphates had condensed on existing particles. Similar morphologies (satellite rings with cores) of sulphates have been observed on SEM and TEM images elsewhere (*Buseck and Pósfai*, 1999; *Ebert et al.*, 2002b; *Hara et al.*, 2003; *Huang and Turpin*, 1996; *Ikegami et al.*, 2004). In these studies, the satellite droplets were identified from electron diffraction patterns as sulphate crystals formed from the dehydration of sulphate droplets.

Inclusion of soot particles within sulphates changes the radiative properties of sulphates depending on whether they are internally or externally mixed. Defining mixing

states of particles from visual inspection is rather uncertain especially when particles are not stable under the electron beam. However, the sulphate rings or cores contained no inclusions of soot aggregates, which might have survived the electron beam during vaporisation. Soot aggregates were always intact, isolated and with morphology typical of freshly emitted soot (see Chapter 4) and different from mixed/aged soot observed by other researchers (*Ebert et al.*, 2002b; *Hara et al.*, 2003; *Li et al.*, 2003b; *Pósfai et al.*, 2003).

5.3.1.4 Sea-salt

Sea-salt particles are formed when trapped air bubbles escape from the sea surface and burst producing sea-salt droplets (*Woolf and Monahan*, 1988). Sea-salt particles in the samples were either euhedral tabular particles or grouped rods. Figure 5.17 shows (a) a fresh euhedral tabular particle and (b) altered and aged sea-salt particles. The particle labelled X has a halo from the dehydration of the deliquescent component of the particle after deposition on the filter. Particles in Figure 5.17(b) were volatile under the SEM beam.

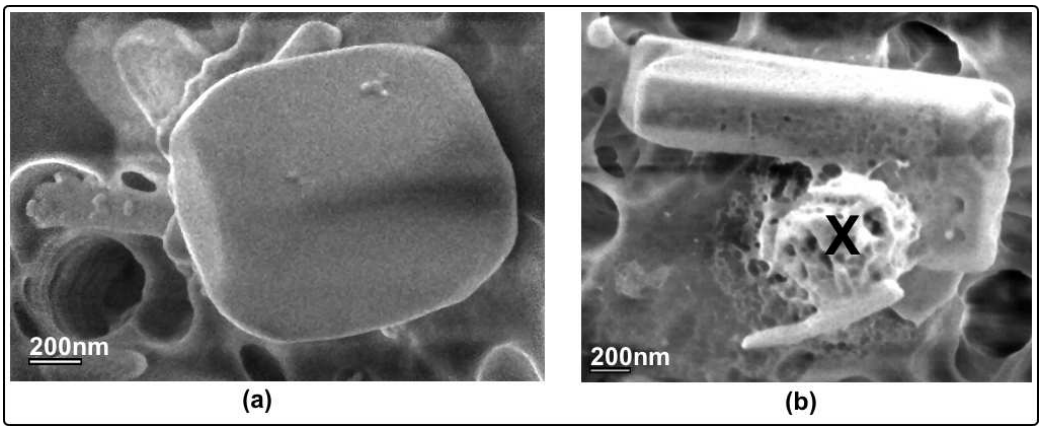


Figure 5.17: (a) An euhedral sea-salt particle (b) an aged sea-salt particle (see text).

EDX analysis of an aged sea-salt particle showed Na, S, Ca and traces of Cl and Si indicating chloride depletion and sulphur enrichment. This is expected from atmospheric reactions of sea-salt with sulphuric acid (*Li et al.*, 2003a; *McInnes et al.*, 1994). Contributions of aged sea-salt particles on all samples was negligible - only two particles were identified from 6704 analysed, while the maximum contribution of both fresh and aged sea-salt particles was 1.4%. This indicates that, under conditions samples were collected, Cape Town was not subjected to aged or fresh marine air masses with high sea-salt particle loadings. Concentrations of freshly formed sea-salt particles are usually higher at coastal areas and decrease to background levels with distance, and with seasonal variations depending

on meteorology, e.g., winds strengths, sea surface temperatures (*Hara et al.*, 2004). Concentrations of sea-salt particles observed here are low, but a conclusive account cannot be given because seasonal dependence is not known. PM2.5 source apportionment of ground samples collected around Cape Town also indicated low concentrations of sea-salt aerosol during the winter season with averaged fractional mass of 2% (*Wicking-Baird et al.*, 1997).

5.3.1.5 Tar balls, fly ash and other combustion generated particles

All individual spherical particles were identified as tar balls and fly ash. SEM images of typical tar balls and fly ash particles are shown in Figure 5.18(a) and (b). The particles have similar morphologies, though tar balls are smaller (within a size range of diameters between 0.02 and 1 μm) while fly ash particles could be up to 2 μm in size. Without chemical information from each individual particle, it is not possible in this study to distinctively identify these particles due to the overlap in size and similarity in morphologies. However, from the few large spheroids that were analysed, EDX spectra showed that tar balls are mainly carbonaceous, while the fly ash contained mainly aluminosilicates, with minor traces of other metallic elements.

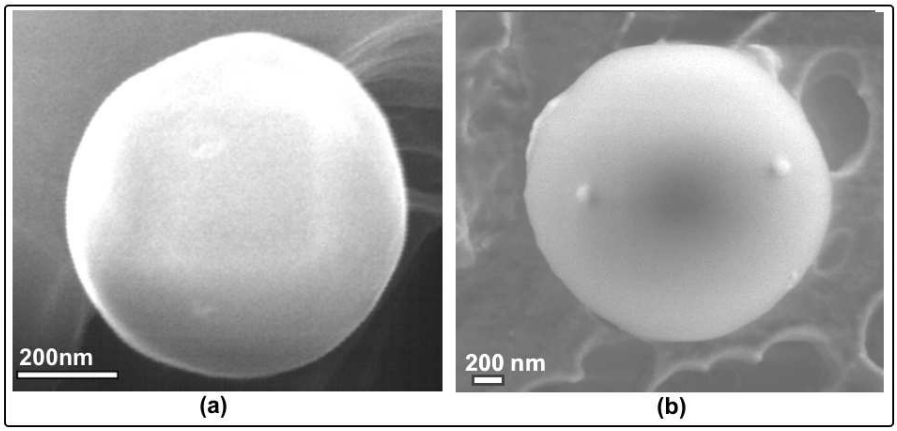


Figure 5.18: Typical SEM images of (a) tar spheroid of 0.68 μm in diameter and (b) large spherical fly ash particle with a diameter of 1.59 μm.

The particles were externally mixed but sometimes smaller spherical particles were attached to the surfaces of larger spheres, Figure 5.18(b). Both particle types were stable under the electron beam, and therefore could be distinguished from, e.g., sulphates. The highest fractional number concentrations were on samples collected on Flight 9, August 6, with combined relative number concentrations of up to 60%. Isolated spheres of diameters

less than 100 nm diameter might also be primary soot particles that have either detached from soot aggregates or never agglomerated. However, from laboratory combustion experiments, the smallest soot aggregates were agglomerated made mostly of pairs or triplets of primary particles (unpublished observations).

Tar balls are spherical carbonaceous particles formed in smouldering fires, and the abundance increases in the atmosphere with the age of smoke plumes (*Pósfai et al.*, 2003). SEM analysis of different biomass fuel samples in laboratory combustions showed that they could be embedded in soot aggregates younger than a couple of hours even in flaming conditions (unpublished observations). A mechanism of tar balls formation has been proposed from the condensation of high-molecular hydrocarbons emitted predominantly in biomass/biofuel combustion processes (*Pósfai et al.*, 2004, and references cited herein). Unlike soot particles that contained wrapped graphitic layers with onion-shell structures, high resolution TEM images show that tar balls have amorphous internal structures (*Li et al.*, 2003b; *Pósfai et al.*, 2003; *Wentzel et al.*, 2003). Fly ash particles are formed by vaporisation and condensation of mineral components in the fuel matrix during combustion, particularly in coal and peat combustion (*Baumbach*, 1996). High resolution TEM imaging shows that fly ash particles are amorphous in structure (*Li et al.*, 2003b). Main sources in Cape Town are coal power plants and industry boilers.

On Sample #1, rod-shaped particles with a 12% relative abundance were identified, but only on this sample. Some of these particles were associated with both compact and branched soot aggregates. Just like soot particles, the rods were stable under the SEM beam. They might be part of an incompletely combusted fuel matrix that have been agglomerated with soot during aggregation process.

5.3.1.6 Other particles

The rest of particles labelled 'others' were difficult to categorise into any of these groups discussed above because of their indistinguishable morphologies. Since Cape Town is dominated by aerosol particles from local anthropogenic sources (*Wicking-Baird et al.*, 1997), 'other' particles are likely to be internally mixed particles, organic carbonaceous aerosol, nitrates - basically photochemically produced secondary aerosols derived from gaseous precursors listed in Table 5.1. Particles might have been subjected to ageing processes. It has been shown that local emissions can accumulate over the area for between 3 - 5 days, because of stable meteorological conditions, before they are removed by wet deposition (*Jury et al.*, 1990). During this time, particles might undergo ageing processes (coagulation, heteroge-

neous reactions, chemical reactions, cloud processes) leading to formation of new particles with morphological properties different from externally mixed particles categorised above and also with different optical properties, particularly when the particles are mixed with soot aggregates (*Jacobson*, 2001). If nitrate particles were present, they might have been lost in the SEM vacuum or by evaporation after deposition on the filters as the equilibrium with ammonia and nitric acid changes in the atmosphere (*Zhang and McMurry*, 1992). Fresh photochemically produced particles are found in the Aitken range unless they have condensed on existing particles (*Väkevä et al.*, 2000). It is therefore possible that secondary generated aerosols (other than sulphates) were not accounted for in the SEM analysis due to volatilisation and/or the coarse resolution of SEM images.

5.3.2 Relative abundance of particles

The study of individual particles with the SEM was aimed at identifying major aerosol species and their sources. Figure 5.19 shows fractional contributions of seven particle groups on Samples #1 to #12. Aerosol samples collected within haze layers on three flights will be discussed in detail.

5.3.2.1 Flight 9, August 6

The flight was conducted from 1020 to 1200 UTC, and to a maximum altitude of 890 hPa (1200 m). The relative abundance of aerosol particles on four samples, Samples #1 to #4, investigated on this flight are shown in Figure 5.19. Combustion generated aerosols dominated particle number concentrations on all samples, with fractional number concentrations of between 65% to 80%. Within combustion products were strong spatial variability of soot particles ($12\% - 37\%$), tar balls/fly ash particles ($21\% - 63\%$) and rod-shaped particles ($0\% - 12\%$). The presence of tar balls is a signature of biomass burning sources, probably associated with domestic wood burning in Cape Town.

Highest fractional concentrations of soot particles were measured on Sample #2 collected over Pinelands, Goodwood and Wynberg areas, while large concentrations of tar balls/fly ash particles were collected over Khayelitsha, Mfuleni and Belville areas on Sample #4. Contributions of soot particles in Samples #1 to #3, which can all be attributed to vehicles emissions from the Central Business District, Goodwood and Pineland areas are more than double the contributions from Khayelitsha (a formal and informal residential

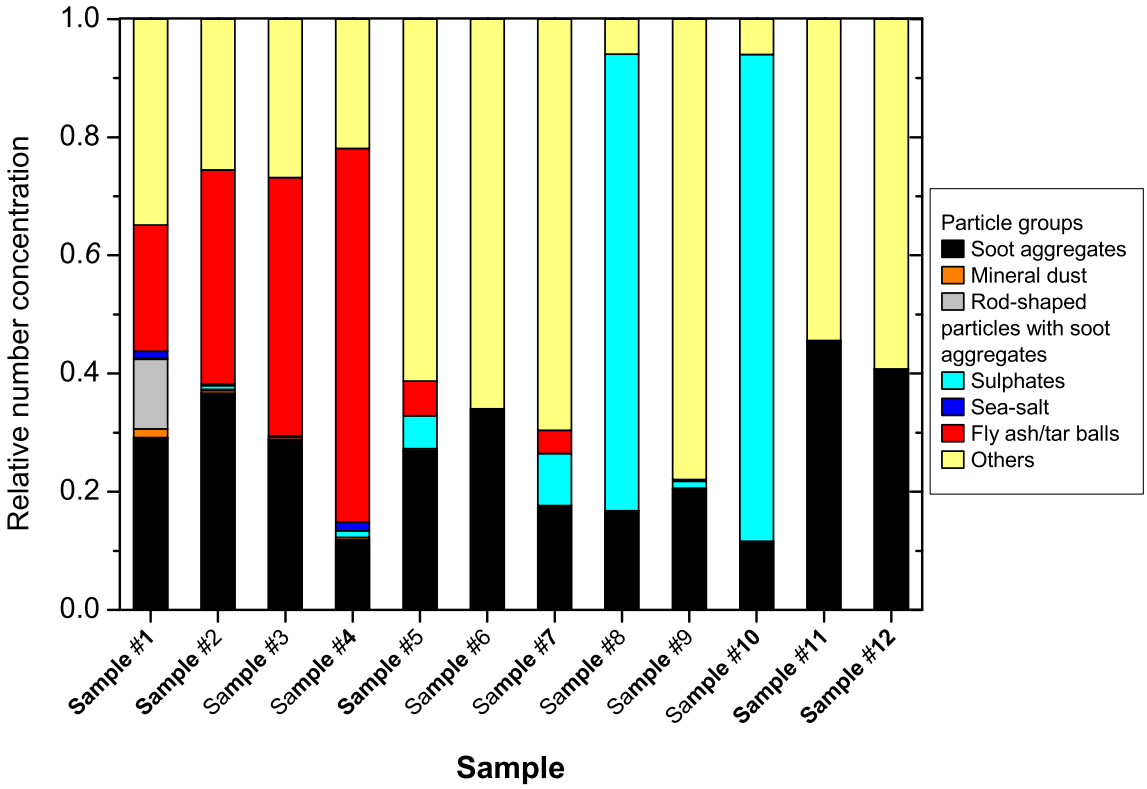


Figure 5.19: Relative contributions of seven particle groups identified in the SEM analyses of 12 samples collected on Flights 9, 13, 15 and 16 (August 6, 15, 22 and 23).

area). Samples #2 and #6 were collected on different days, and contributions of soot are the same over these locations (37% and 34%, respectively).

Backward trajectories computed on this flight indicated fast descending air masses that had originated SW of Cape Town and travelled east of the Western Cape Province before arriving at Cape Town from the NE as loop-back inflows, Figure 5.11. Air masses had been in contact with the continental boundary layer for 48 hours. On this day, aerosol loadings over Cape Town were dominated mainly by combustion generated aerosols from local and possibly near-region sources if air masses had been in contact with a polluted continental boundary layer.

5.3.2.2 Flight 14, August 22

Flight 14 was performed on the morning of August 22 from 0650 to 0920 UTC, to a maximum altitude of 924 hPa (879 m). Samples #7 to #10 were collected on this flight. Particle

species were dominated by externally mixed soot aggregates and sulphates. Sulphate particles were highly variable with fractional concentrations of between 9% and 82%. The averaged fractional contribution of soot particles was 17%, and this was the lowest on the four flights considered here. The maximum fractional concentration of 21% soot particles was collected over Khayelitsha. Highest mixing ratios of trace gases were also observed on the same flight, in particular SO_2 mixing ratios, though variable, were up to 50 ppb, compared to an average of less than 5 ppb observed on all other flights. This excludes isolated measurements made in regions directly over industrial sites A (an oil refinery) and B (a glass manufacturing plant) where mixing ratios of SO_2 could be over 100 ppb depending on altitude.

Backward trajectories of air masses sampled on Flight 14 had originated at high altitudes over the Atlantic Ocean and travelled into the interior of South Africa, crossing North West Cape and Northern Cape Provinces before arriving at Cape Town as loop back inflows, Figure 5.11. The air masses had been in contact with the continental boundary layer for 50 hours before sampling. High sulphate loadings on this flight are likely to be secondary combustion products of anthropogenic SO_2. While natural sulphates might also be present particularly at a coastal location like Cape Town, they contribute to a background fine particulate mode which is outweighed by anthropogenic sulphates (*Norman et al.*, 2004). Sulphates observed on this flight might be due to recirculated pollutants from Cape Town or emissions in the interior of the country where air masses sampled had travelled. The emissions need to spend considerable time in the atmosphere to be photochemically processed to sulphates. Additionally, sulphur dioxide is highly soluble in water and existing hydrated particles might have provided efficient surfaces for converting SO_2 to sulphates (*Seinfeld and Pandis*, 1998).

5.3.2.3 Flight 16, August 23

Flight 16 was conducted on August 23 from 0630 to 0840 UTC, and to a maximum altitude of 927 hPa (820 m). Samples #11 and #12 were investigated. The aerosol was dominated by soot particles with average fractional concentrations of 43%. Some ABS samples also showed sulphate particles. However, these samples were not shown in Figure 5.11 because particles had disintegrated on substrate making counting impossible. The maximum fractional concentration of soot particles of 46% were collected on Sample #12 around the CBD.

Trajectory analyses on Flight 16 showed tracks similar to those on August 22,

Figure 5.11. The air masses had travelled for 80 hours over the continent before sampling. During the entire campaign, only back trajectories on Flight 14 and 16 had crossed furthest into interior of the country before looping back to Cape Town. Differences in aerosol compositions between the two days can be attributed to differences in meteorological conditions, considering fractional concentrations of sulphates have been observed to increase with ambient humidity (*Baumgardner et al.*, 2000). August 23 was characterised by dry conditions in the boundary layer compared to August 22, hence low sulphate concentrations (see relative humidity profiles in Appendix C Figure 1). Soot fractional concentrations doubled between August 22 and 23.

In summary, chemical composition of aerosol particles in the Cape Town brown haze was highly heterogeneous, where:

- soot particles were externally mixed, suggesting either fresh emissions or particles that had not been aged by coagulation, restructuring, gas uptake or chemical reactions.
- variations in soot fractional contributions can be attributed to localised, possibly point sources within the Cape Town area. Locations like the CBD, Goodwood and Pinelands showed the highest soot concentrations mainly from vehicle emissions and Khayelitsha, where soot particles are emitted largely from domestic combustion processes.
- variations in sulphate contributions from day to day were related to ambient relative humidity.
- there were large variations in the apportionment of other particle species from day to day and spatially. These variations indicated that mixing of the boundary layer by horizontal advection was relatively poor. Considering that most sources identified in CTBH I were similar continuous sources with diurnal patterns (e.g., vehicle and domestic emissions), a high resolution dispersion model of particulate matter in Cape Town is needed to explain these variations.

While contributions of the main absorbing component (soot) and its mixing state in the Cape Town haze have been identified in this study, future studies need to address more closely the role of secondary aerosols, particularly organics and nitrates in order to reduce uncertainty in the particle group assigned 'others'. The main source of organics is through atmospheric photooxidation of anthropogenic volatile organic compounds from fossil fuel and biomass burning. The particles exist predominately in the submicrometer range and are therefore more efficient at light extinction. Measurement studies have shown that not only sulphates, but also organics may scatter as much light in polluted environments (*Hegg*

et al., 1997). Other than soot particles (elemental carbon), organics from biomass burning may contribute to light absorption (*Mayol-Bracero et al.*, 2002). Aerosol nitrate was not considered in this study. These particles are highly volatile and had likely evaporated from filters before or during SEM analysis. In regions with elevated emissions of NO_x and possibly NH_3 like Cape Town (*Walton*, 2005; *Wicking-Baird et al.*, 1997), nitrate aerosol might play a major role in the light scattering, e.g., as has been observed in polluted regions of Europe (*ten Brink et al.*, 1996).

5.3.3 Sizes distributions from SEM analyses

Two ABS samples collected on Flight 9 (Samples #1 and #4) were investigated for particle size distributions. ImageJ[9] software package which is freely available was used for image processing and particle analyses. After high frequency filtering was applied to remove random noise and to enhance contrast on particle edges, images were binarised by manually selecting brightness thresholds to ascertain all particles. A diameter d_a was calculated as the equivalent diameter of the projected surface area in the image. The error in estimating d_a from projected surfaces depends on image resolution. Unless particles had intricate details that could be lost at coarse resolution, projected surface area has been found to be within an error margin of 5% (see Chapter 4).

Size distributions were fitted with lognormal functions given by

$$\frac{dN}{d\,log\,d_a} = \frac{N}{\sqrt{2\pi}\,log\,\sigma_g}\,exp\left[-\frac{(log\,d_a - log\,d_g)^2}{2(log\,\sigma_g)^2}\right] \tag{5.2}$$

where $N = N_{SEM}$ for SEM analysis, the total number of particles measured - 397 and 788 on Samples #1 and #4, respectively, d_g is the geometric mean surface diameter and σ_g is the geometric standard deviation calculated as the root of ratios at the 84th and 16th percentile.

Number distributions as functions of d_a are shown in Figure 5.13(a) and (b). The distributions can be described with lognormal functions with geometric mean diameters of 0.34 μm and $\sigma_g = 1.88$ on Sample #1; and 0.29 μm and $\sigma_g = 2.13$ on Sample #4. A small peak around 60 nm on the size distributions of Sample #4 is due to the abundant tar balls/fly ash particles observed on this sample. While, the rest of the samples were not analysed due to charging effects, particle morphologies were similar to these two samples expect when high concentrations of sulphate particles were observed. Still, size distributions might be shifted slightly towards larger sizes, due to low concentrations of tar balls/fly ash

[9]http://rsb.info.nih.gov/ij/

particles on the rest of the samples. There were secondary peaks of particles larger than 2 μm in the surface area and volume distributions (not shown in plots). These large particles contribute to less than 1% of the number concentrations and the peaks were due to mainly mineral dust particles and large soot aggregates. The peaks might have been diminished by eminent losses of larger particles in the sampling inlets and from particle bounce.

5.3.4 Particle morphology

The same Samples #1 and #4 were also investigated for particle morphology by characterising aspect ratio, AR, and circularity, Cr, of particles from projected surfaces. The aspect ratio was defined as the ratio of the major axis to the perpendicular minor axis of the best fit ellipsoidal envelope to the particle projection, a measure of the particle roundness. The AR increases from unity with elongation of a particle projection. Circularity describes how irregular (or complex) a particle is, by relating the projected surface area to the projected perimeter as $Cr = 4\pi * area/(perimeter)^2$. A Cr of unity describes a circle and $Cr \rightarrow 0$ for elongated or amorphous particles, e.g., loose soot or rod-shaped particles.

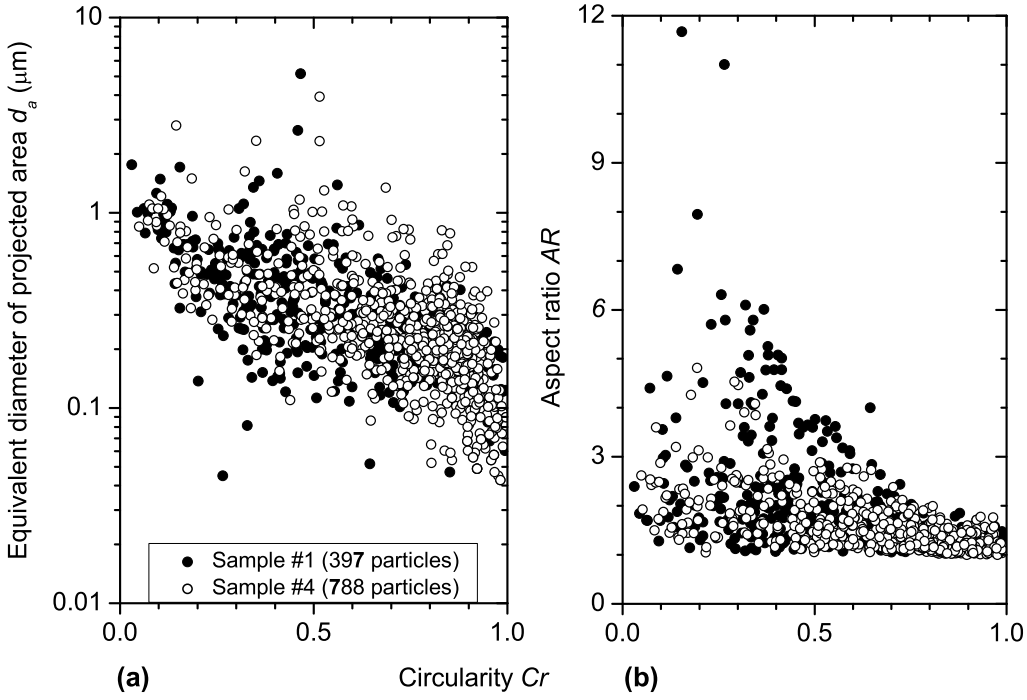


Figure 5.20: (a) Relationship between circularity Cr and (a) equivalent diameter of projected surface and (b) aspect ratio, AR.

Unlike AR, Cr was observed to be dependent on particle sizes d_a as is illustrated in Figure 5.20(a). This means that, complexity of particles increased with increasing projected

surface area of particles. The dependence is to be expected considering soot particles contributed to larger surface projections, as shown in Figure 5.13. Therefore approximating large particles with circular projections increases uncertainties in size distributions derived.

The dependence of AR on Cr are shown in Figure 5.20(b). While high aspect ratios are always associated with low Cr, because the perimeter of particle increases with elongation, low AR might imply either circular ($Cr \approx 1$) or amorphous particles. It is therefore necessary to use both parameters to best describe particle shapes.

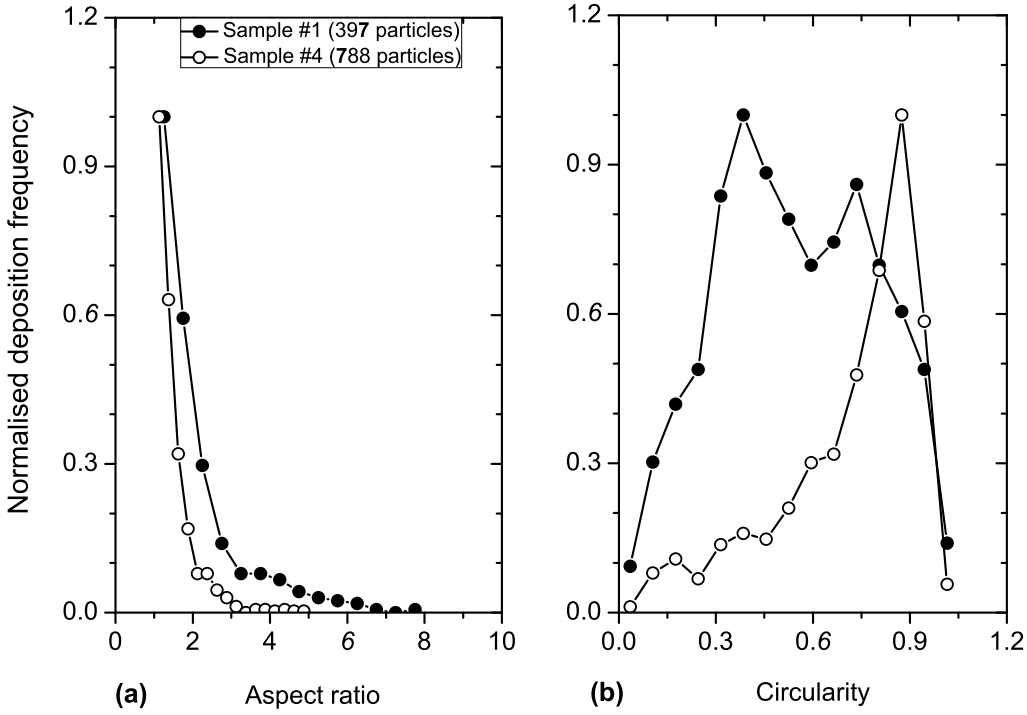


Figure 5.21: Distribution of (a) aspect ratio AR and (b) circularity $Cr = 4\pi Area/(Perimeter)^2$ for Samples #1 and #4. The frequencies were normalised with the maximum frequency of each distribution.

Frequency distributions of AR and Cr were normalised to the highest frequency of each distribution and plotted in Figure 5.21(a) and (b). The AR distributions are similar and most particles have $AR < 3$. The Cr distributions in Figure 5.21(b) shows that most particles on Sample #4 are not complex in shape ($Cr \approx 1$), and they had low AR, hence projected surfaces could be approximated by circular particles. This is expected because of high number concentration of spherical tar balls/fly ash particles on this sample, which have $Cr \approx 1$. The Cr distributions on Sample #1 is bimodal, with peaks at $Cr = 0.39$ due to soot particles and at $Cr \approx 1$ from tar balls/fly ash particles. Although the distributions of size and AR on these two samples are quite similar, the morphologies of the particles they represent are different. It implies therefore that size distributions of these two samples cannot be directly compared to other size distributions where the responses of a sizing

instruments are sensitive to particle shapes.

5.4 Aerosol number concentrations and size distributions - PCASP

5.4.1 Particle spatial distribution

Vertical distributions of particle number concentrations N and potential temperature, θ, on Flights 4 to 16 are plotted in Appendix C Figures 2 and 3. Evolution of the atmospheric boundary layer controlled the stratification of particles and trace gases (SO_2, NO_2, and O_3, although not shown). In the mornings (Flights 10, 14 and 16 conducted between 0500 to 0930 UTC) θ profiles had characteristics features of stable boundary layer, SBL, to altitudes[10] of 400 m. Variable aerosol concentrations of $10 < N < 30\,000$ cm^{-3} were confined to these SBLs. High particle concentrations are likely to be due to primary emissions from local diffuse sources, particularly from vehicles during morning traffic rush hours (*Carrico et al.*, 2003). Fine particles in size range of $30 - 500$ nm are formed during rapid dilution and cooling of vehicle exhaust emissions (*Kittelson et al.*, 2000; *Rogge et al.*, 1993). The particles might also have accumulated in the SBL from overnight and morning emissions in domestic combustion processes. Fine particles dominate number distributions in all profiles. The residual layer, RL, in the mornings (between 400 and 1400 m) was depleted of particles by subsidence of air masses from the free troposphere to concentrations of N less than 100 cm^{-3}. The exceptional case is Flight 10, when concentrations in the RL were $N = 200 \pm 40$ cm^{-3} possibly due to advection or early mixing.

In the late mornings (0930 to 1100 UTC) and afternoons some θ profiles were isothermal. Lapse rates in the convective boundary layer, CBL, were between $3 - 11^\circ$ K km^{-1}, and for some profiles, less than the dry adiabatic lapse rate of $\approx 9.8^\circ$ K km^{-1}. For dry air masses, this would lead to stable stratification with suppressed vertical turbulence (*Oke*, 1993). Particle concentrations varied from $30 < N < 30\,000$ cm^{-3} to maximum altitudes of 1400 m.

Flight tracks of vertical profiles selected to demonstrate typical vertical distributions of particles in the boundary layer are shown in Figure 5.6. Vertical profiles are plotted in Figures 5.22 to 5.26. Particle total volumes, V_{tot} (μm^3 cm^{-3}) were computed from the

[10] Altitude units are all in meters above sea level

PCASP number-size distributions. To identify stratifications in the profiles, layers were defined with preference on stability, i.e., from changes in gradient of θ, then changes in N and finally changes V_{tot}. These stratifications are indicated by horizontal lines in Figures 5.22 to 5.26. These vertical profiles will now be described in detail, and evaluated for variations of particle size distributions with altitude in Section 5.4.2.

5.4.1.1 Profile A, Flight 10, August 7 early morning

A descent from 1730 m was made between 0651 to 0702 UTC, looping from Camps Bay to False Bay and Belhar (sunrise was at 0550 UTC). Profiles of θ, N, and V_{tot} are shown in Figure 5.22. There is a stable new mixing layer, ML, to 400 m, with particle concentrations decreasing steadily from $N > 3000$ cm^{-3}. The stable boundary layer, SBL, between 400 and 860 m is well mixed with a nearly constant $N = 260 \pm 20$ cm^{-3}. While number concentrations decrease by an order of magnitude between the ML and the SBL, the average V_{tot} is around 20 μm^3 cm^{-3} in both layers indicating that N in the ML is dominated by the Aitken mode particles (particles with $d_p < 0.1\mu$m).

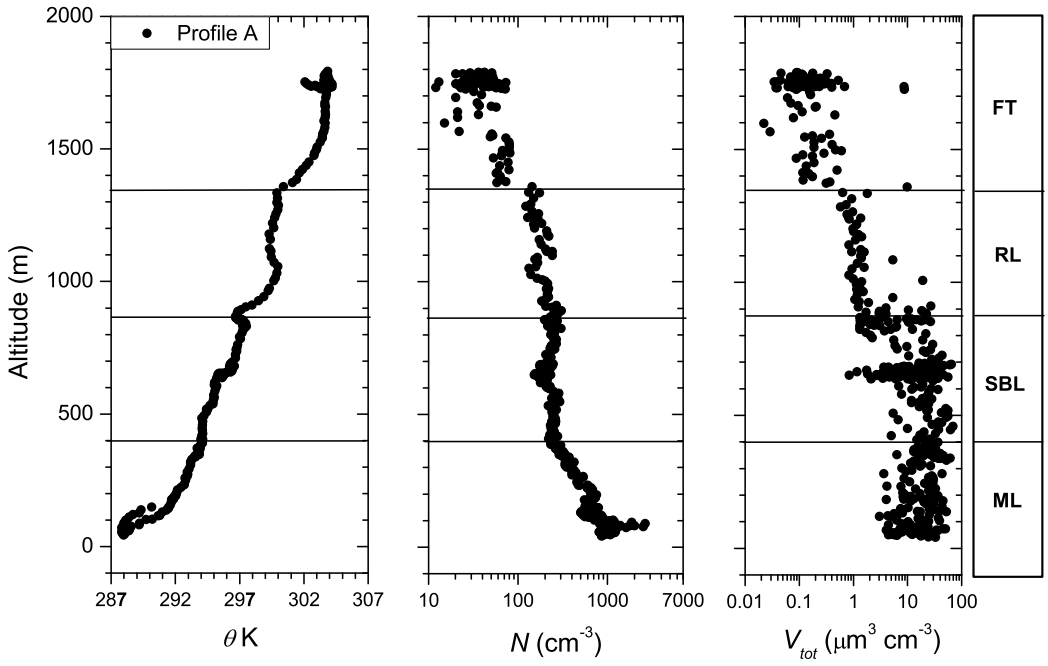


Figure 5.22: Vertical profiles of θ, N, and V_{tot} on a looping descent from Camps Bay - False Bay - Belhar on Flight 10, August 7 from 0651 to 0702 UTC - Profile A. The labels on the right side represent stratifications defined based on thermal stability, where ML = mixing layer, SBL = stable boundary layer, RL = residual layer and FT = free troposphere.

In the residual layer RL between 860 and 1350 m, N decreases slightly to about 200 cm^{-3} while V_{tot} decreases abruptly to around 1 μm^3 cm^{-3}. The RL is separated from the

free troposphere, FT, by an inversion at 1350 m, as supported by further abrupt decreases of N and V_{tot} to low concentrations of less than 80 cm $^{-3}$ and 0.1 μm^3 cm^{-3}, respectively. The FT is depleted of particles, particularly in the coarse mode.

5.4.1.2 Profiles B and C, Flight 4, August 2 late morning

Profile B was made on an ascent followed by descending spirals from 0923 to 0935 UTC around Wallacedene (a formal and informal low income settlement), Figure 5.6. Distributions of θ, N and V_{tot} are shown in Figure 5.23 (solid circles). The ascent (indicated by the upward arrow) probed the SBL with N decreasing from $\approx$ 2000 cm^{-3} at 570 m to N of less than 300 cm^{-3} in the RL. On the spiral descent (indicated by the downward arrow), particle number concentrations increased gradually in the RL to 2000 cm^{-3} at 680 m. Number concentrations continued to increase sharply in the SBL between 680 and 440 m. The ML below 440 m is neutral and well mixed with an average $N = 5240 \pm 230$ cm^{-3}, indicative of a highly polluted layer directly above Wallacedene.

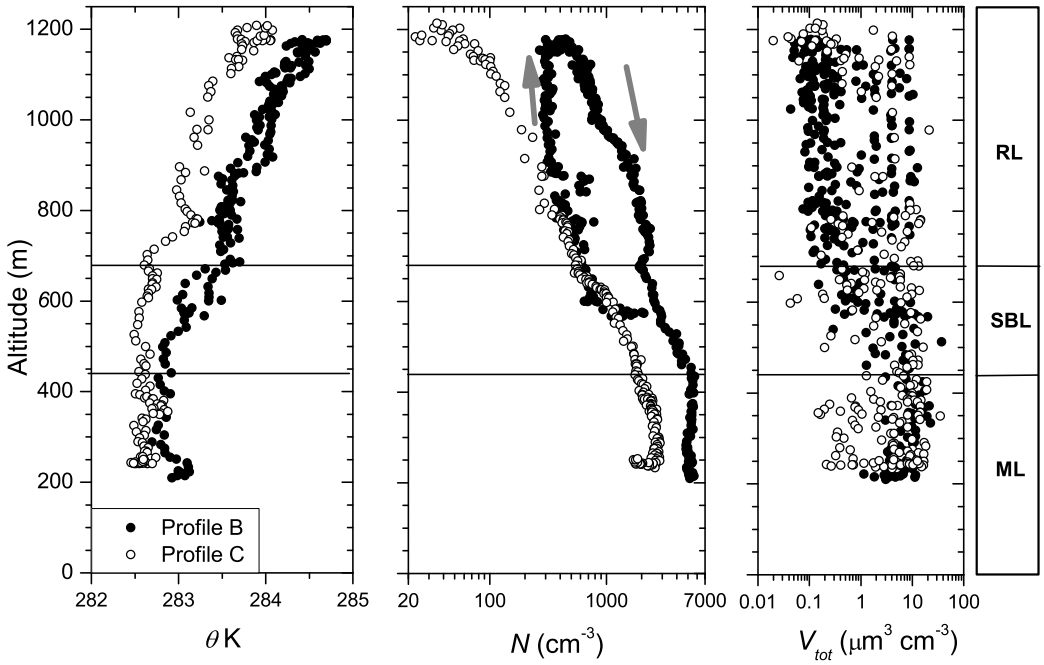


Figure 5.23: Vertical profiles of θ, N, and V_{tot} on Flight 4, August 2; An ascent followed by descending spirals as indicated by the arrows from 0923 to 0935 UTC, Profile B (solid circles) around Wallacedene: and Profile C from 1002 to 1007 UTC (open circles) at Fishoek. The labels on the right side represent stratifications defined based on thermal stability, where ML = mixing layer, SBL = stable boundary layer and RL = residual layer.

Profile C was conducted over Fishoek (a middle-class neighbourhood) between 1002 to 1007 UTC (open circles), Figure 5.6. The profile shows a similar trend to the

descent on Profile B, but with lower number concentrations, particularly in the ML were $N < 3000$ cm^{-3}. While the stratifications are persistent between the locations, aerosol number concentrations are up to an order of magnitude higher on the descent of Profile B at Wallacedene compared to Profile C from Fishoek. This indicates different aerosol emission strengths and possibly different advection between Wallacedene and Fishoek.

5.4.1.3 Profiles D, E, F and G, Flights 13, August 15 afternoon

Flight 13 was conducted at $1230 - 1500$ UTC to an altitude of about 1750 m. The flight was specifically dedicated to describing vertical variability of particles and trace gases at several locations. Four profiles labelled D, E, F and G were selected, Figure 5.6. Profile D was made on a descending loop from Wynberg to False Bay and Belhar ($1257 - 1305$ UTC). Profiles of θ, N and V_{tot} are shown in Figure 5.24.

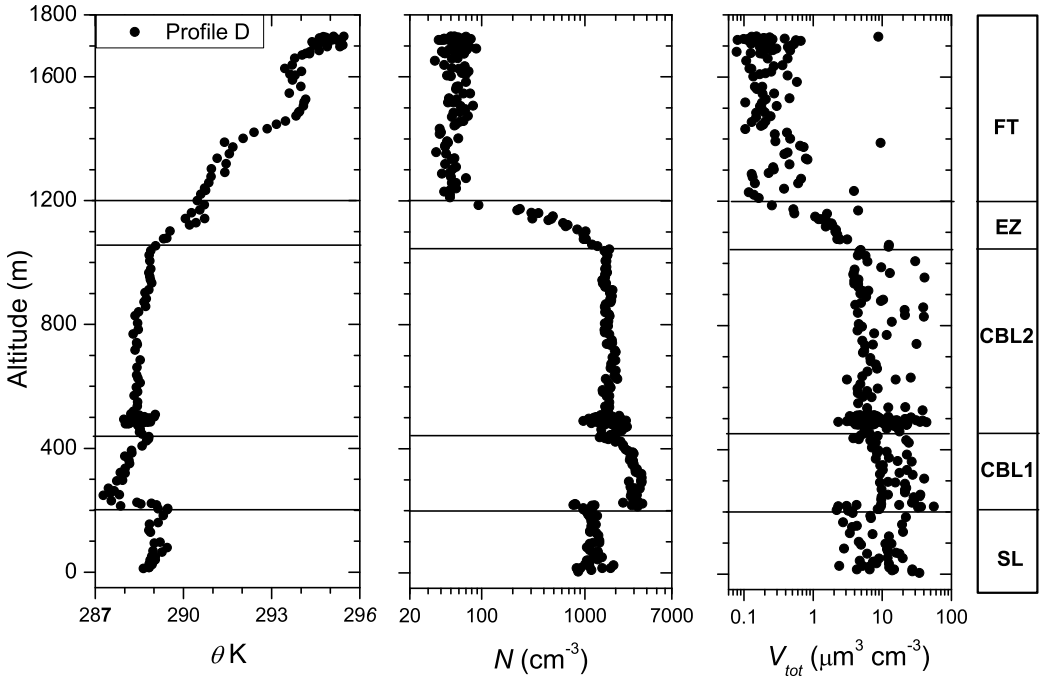


Figure 5.24: Vertical distributions of θ, N and V_{tot} on a looping descent from Wynberg-False Bay-Belhar, Flight 13, August 15, Profile D from 1257 to 1305 UTC. The labels on the right side represent stratifications defined based on thermal stability, where CBL = convective boundary layer, EZ = entrainment zone and FT = free troposphere.

The warmer surface layer (SL to 200 m) is well mixed with low concentrations of $N = 1202 \pm 909$ cm^{-3}. The CBL is statically neutral and well mixed with $N = 2594 \pm 878$ cm^{-3} in the layer CBL1 between 200 to 420 m; and $N = 1700 \pm 249$ cm^{-3} in layer CBL2 between 420 and 1030 m. In the entrainment zone, EZ, N and V_{tot} decrease steadily with

a smooth transition between the CBL and the free troposphere FT above 1200 m. The FT is depleted of particles, with average $N = 58 \pm 11$ cm^{-3} and $V_{tot} = 0.1 - 1$ μm^3 cm^{-3}.

Profile E (a combination of 2 ascents and 2 descents) was made around the Cape Point between 1403 and 1418 UTC. Vertical profiles are plotted in Figure 5.25. There is uniform vertical distribution of particles on these ascents and descents. N increases slightly in the near-surface layer SL to 200 cm^{-3} at 200 m. The CBL between 200 and 725 m is neutral and well mixed with $N = 80 \pm 10$ cm^{-3}. These are very low particles concentrations in the CBL compared on the rest of the vertical profiles investigated. In the entrainment zone ($725 - 1050$ m), there is a thin layer between $820 - 950$ m with N up to 400 cm^{-3}. Particles concentrations decrease in free troposphere FT above 1050 m to $N = 52 \pm 10$ cm^{-3}. V_{tot} vary significantly from 0.1 to 30 μm^3 cm^{-3} along the entire profiles.

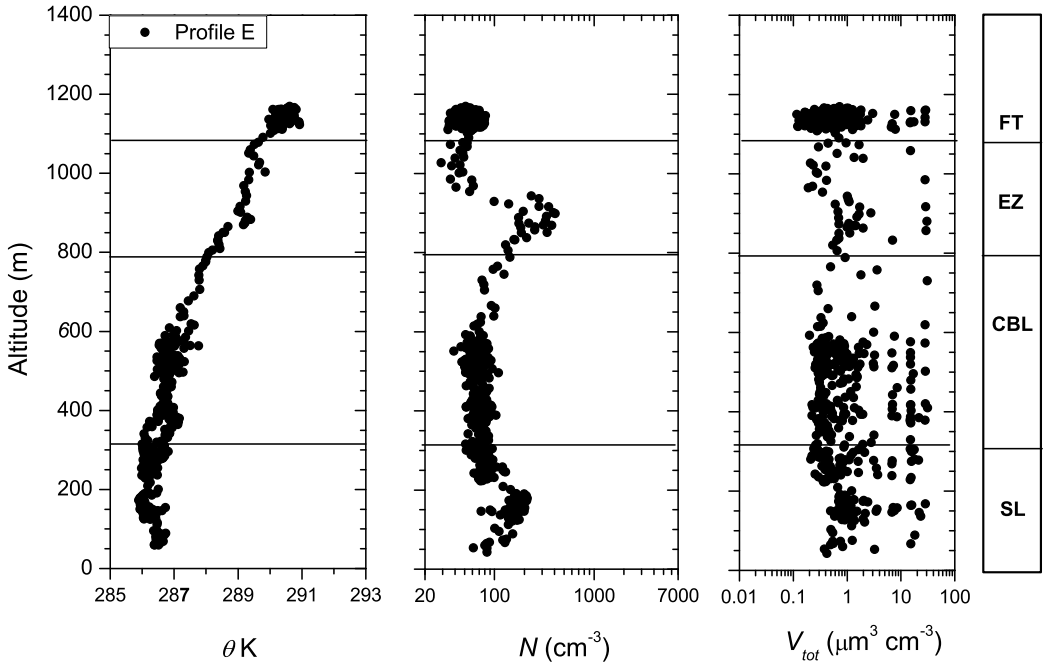


Figure 5.25: Vertical distributions of θ, N and V_{tot} on Profile E made in pristine conditions around the Cape Point on Flight 13, August 15 from 1402 to 1420 UTC. The labels on the right side represent stratifications defined based on thermal stability, where SL = surface layer, CBL = convective boundary layer, EZ = entrainment zone and FT = free troposphere.

Profiles F and G were performed during a descent over sea (F) and a spiral ascent (G) around Gordons Bay area from 1421 to 1433 UTC, Figure 5.26. The profiles are similar except for gradients of N in the surface layers, and a narrow layer between 950 and 1050 m, a persistent layer that has been observed on Profile E. The profiles have stable CBL with particle concentrations higher than at the Cape Point (Profile E) by factors of up to 40. Both profiles show transition to the free troposphere at 1270 m.

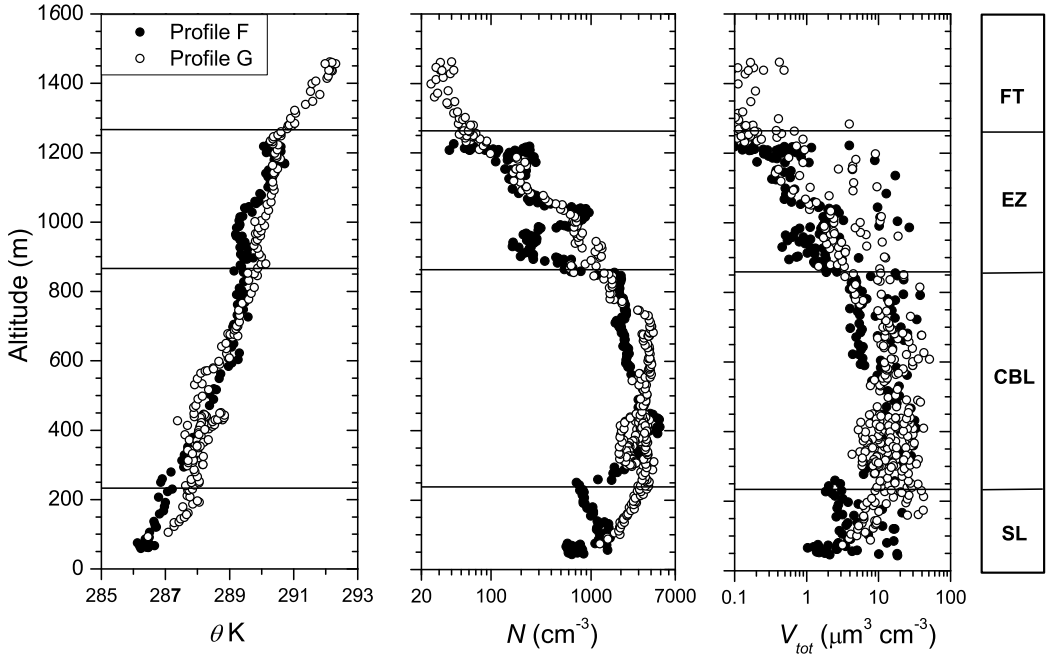


Figure 5.26: Vertical profiles of θ, N, V_{tot} on Flight 13, August 15, Profile F from 1421 to 1426 UTC (solid circles); and Profile G from 1426 to 1433 UTC (open circles). Both profiles were conducted downwind of Cape Town. The labels on the right side represent stratifications defined based on thermal stability, where SL = surface layer, CBL = convective boundary layer, EZ = entrainment zone and FT = free troposphere.

The synoptic chart on August 15 indicate NW winds over Cape Town (*South African Weather Service*, 2003, 1200-1400 UTC). Differences in aerosol concentrations between Profiles E, F and G might be explained by a simplified scenario of lateral transport where Profiles F and G were sampled downwind of the city centre, unlike Profile E where pristine marine air masses were received. Differences in aerosol concentrations between Profiles E, F and G provide an excellent contrast between the pristine background conditions of clean marine air, represented by Profile E over Cape Point, and air contaminated by emissions from the urban conglomeration of Cape Town, represented by Profiles F and G, sampled in the afternoon mature haze downwind of the urban source areas.

In summary, vertical distributions of particles in the haze were characterised by several factors. The vertical distributions of particles in all Profiles A to G could be described from the diurnal development of the boundary layer described in Section 5.2.1. High number concentrations of particles in the boundary layer ($N > 1000$ cm^{-3}) are consistent with polluted urban environments (*Seinfeld and Pandis*, 1998). The decrease of aerosol concentrations with altitude suggest most of particles were emitted locally and at low altitudes, hence long-range transported particles do not contribute to the haze. Aerosol number and volume concentrations, N and V_{tot}, were one to three orders of magnitude higher in the boundary layer than the free troposphere. Extinction of light by particles is proportional

to total volume of particles, and changes in V_{tot} translate directly to visibility changes of the same magnitudes. As indicated by Flight 13 with Profiles E to G, there is strong variability in the aerosol number concentrations between locations indicating variable source strengths and lateral transportation of particles. The persistent inversion at the top of the boundary layer between the morning and afternoons means the boundary layer was continually decoupled from the free troposphere. Particles in the two layers would evolve and age differently.

Vertical distributions of particles on Figures 5.22 to 5.26 were described from thermal stratification of an idealised BL. What were characterised as the RL or CBL showed multiple layering, where aerosols concentrations were controlled by inversions. The boundary layer in Cape Town might be modified by complex structure of orography, urban surface roughness, and the coastal boundary layer (*Oke*, 1993). Knowledge of source locations, small scale surface temperature and wind field among other meteorological parameters are needed to explain finer structures in the boundary layer, and beyond the scope of this study.

5.4.2 Particle size distributions

Particle number-size distributions were integrated along the thermal stratifications resolved in vertical profiles A to G discussed above and plotted in Figure 5.27. [Also included in Figure 5.28 are number-size distributions of maximum N in the intervals corresponding to the 12 ABS samples analysed with the SEM. These distributions are used in Section 5.6.3 to derive optical properties of particles.] Error bars were calculated as standard deviations around the mean and only shown on some distributions. The rest of the deviations were excluded for clarity. Standard deviations corresponded to total uncertainty and were defined as the root mean square of the counting errors. Deviations were functions of number counts per size bin (and independent of PCASP bin sizes) and were within 40% of mean for particle concentrations for $N > 10$ cm^{-3}. These deviations were critical for particle sizes > 1 μm and in the free troposphere where particle concentrations were low.

Size distributions were fitted with lognormal functions of 2 to 4 modes with a form

$$\frac{dN}{d\,log\,d_p} = \sum_{i=1}^{4} \frac{N_i}{\sqrt{2\pi}\,log\,\sigma_{gi}}\,exp\left[-\frac{(log\,d_p - log\,d_{gi})^2}{2(log\,\sigma_{gi})^2}\right] \tag{5.3}$$

where d_p is particle diameter, d_{gi} and σ_{gi} are the geometric diameter and deviation for mode i with number concentrations N_i. Three main modes corresponded to the accumulation ($i = 1$ and 2) and the coarse ($i = 3$) modes. Parameters of lognormal fits are summarised in Table 5.5.

Particle number concentrations in the SL, ML, and CBL were dominated by fine particles (both Aitken and accumulation modes) while the accumulation and coarse modes dominated the volume of aerosols. Size distributions were multimodal consisting of three size modes as follows: $0.07 - 0.09$ μm in the Aitken mode; two peaks in the accumulation mode at $0.14 - 0.22$ μm and $0.5 - 0.90$ μm; and the coarse mode with $d_p > 2$ μm. The accumulation mode showed two peaks typical of urban aerosols (*Seinfeld and Pandis*, 1998).

Unlike on other days, Profiles B and C (Flight 4, August 2) showed complex size distributions with four modes. A prominent Aitken mode dominated the number concentrations throughout this flight. Particle sizes in the Aitken mode decreased slightly with increasing altitude. The mode might be due to subsequent growth of new particles generated in a nucleation event (*Väkevä et al.*, 2000). Under favourable meteorological conditions, nucleation events with high number concentrations of particles in the size range of $3 - 500$ nm were correlated to polluted air masses (*Boy and Kulmala*, 2001). If similar conditions do influence new particle formation in Cape Town, such events could be an important source of new aerosols in the haze, and correlations with trace gas concentrations (particularly NO_x) need to be investigated.

Except for Profile E, free troposphere aerosol distributions are bimodal with the accumulation mode of $0.12 - 0.14$ μm and a coarse mode of particles with $d_p > 2$ μm. The coarse modes are rather poorly determined due to discontinuities in the distributions. This is because of poor statistics of particles larger than about 1 μm, and might have affected the detection of the PCASP at low concentrations. Although the SL and CBL show typical aerosol distributions within the magnitudes observed in urban environments, distributions in the FT are decoupled from the boundary layer because of suppressed vertical mixing by the inversion that is capping the boundary layer.

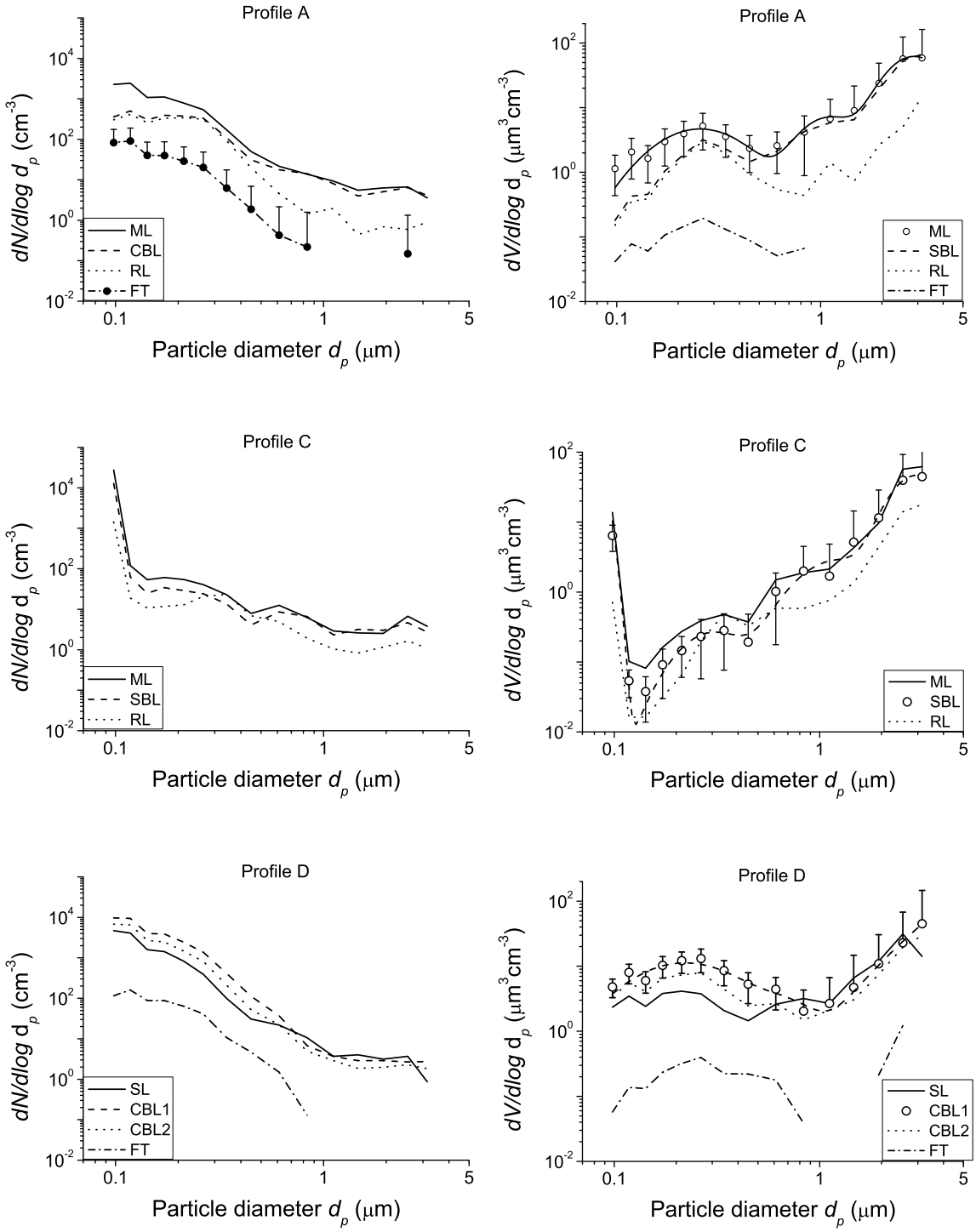


Figure 5.27 *continued next page.*

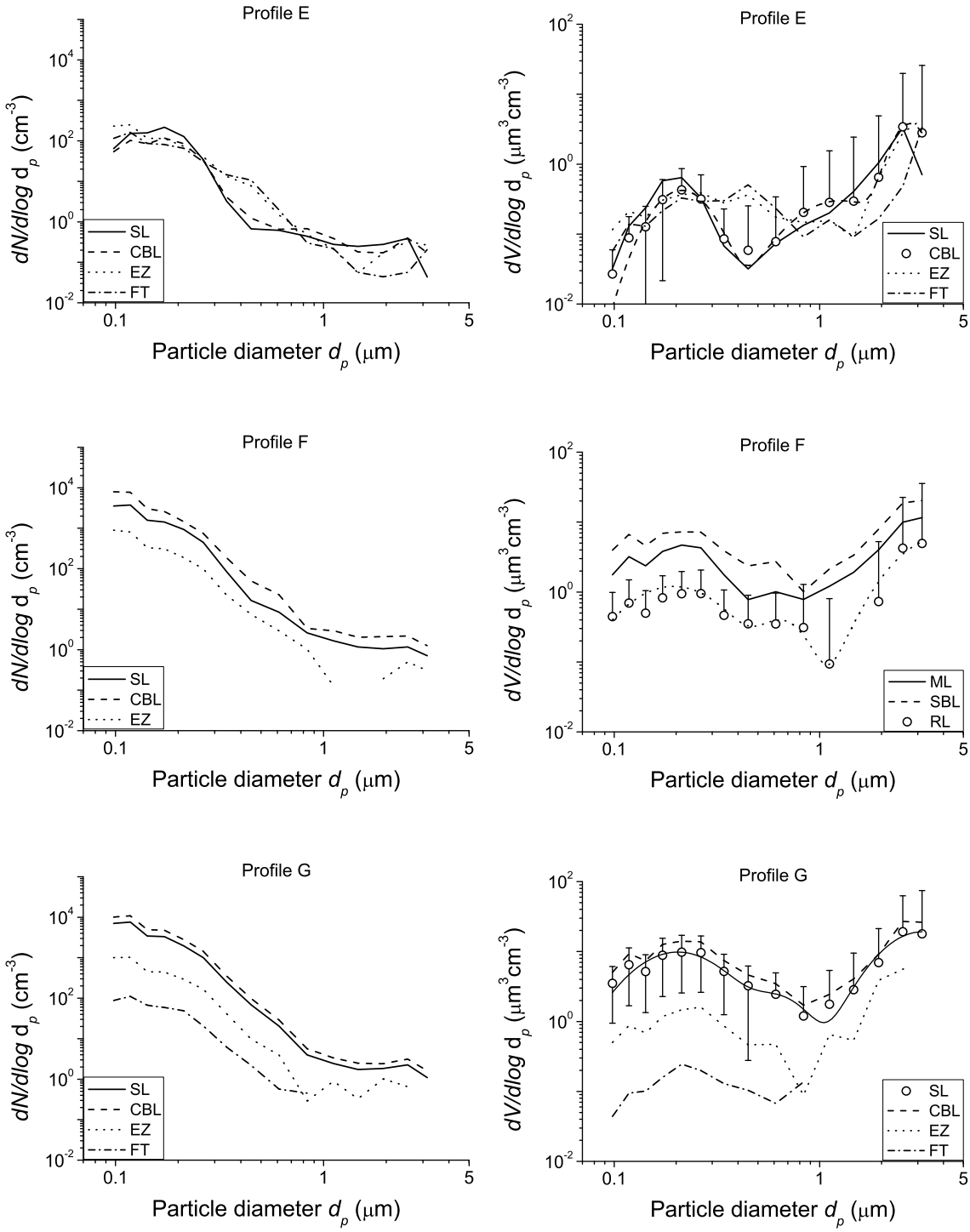


Figure 5.27: Particle number-size and volume distributions averaged along thermal stratifications identified in Profiles A to G. Lognormal fits to volume distribution and error bars are shown on some profiles. The rest are excluded for clarity. The stratifications were defined based on thermal stability, where SL = surface layer, CBL = convective boundary layer, RL = residual layer, EZ = entrainment zone and FT = free troposphere.

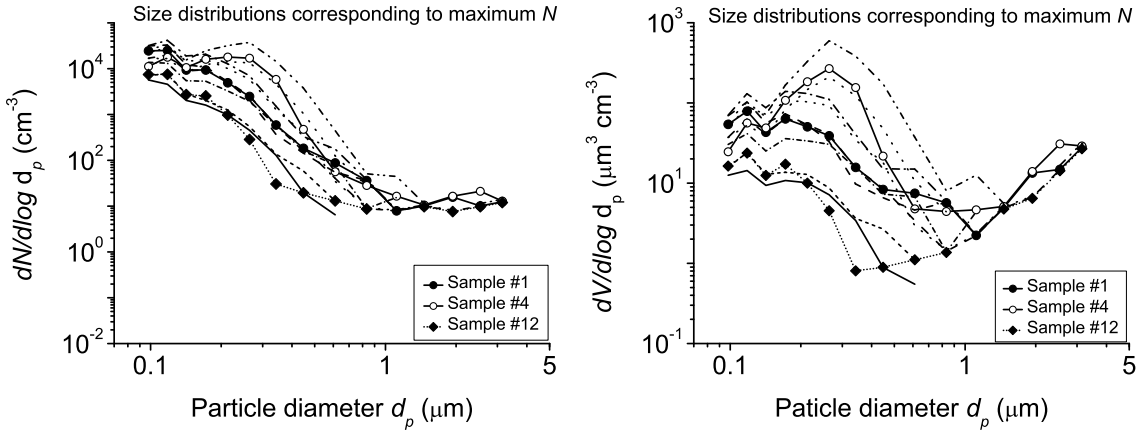


Figure 5.28: Size distributions of maximum N measured in the time intervals corresponding to the 12 ABS samples analysed with SEM. Optical properties are determined from these distributions in Section 5.6.3. Highlighted size distributions with prominent coarse modes are fitted with multimodal fits in Figure 5.29.

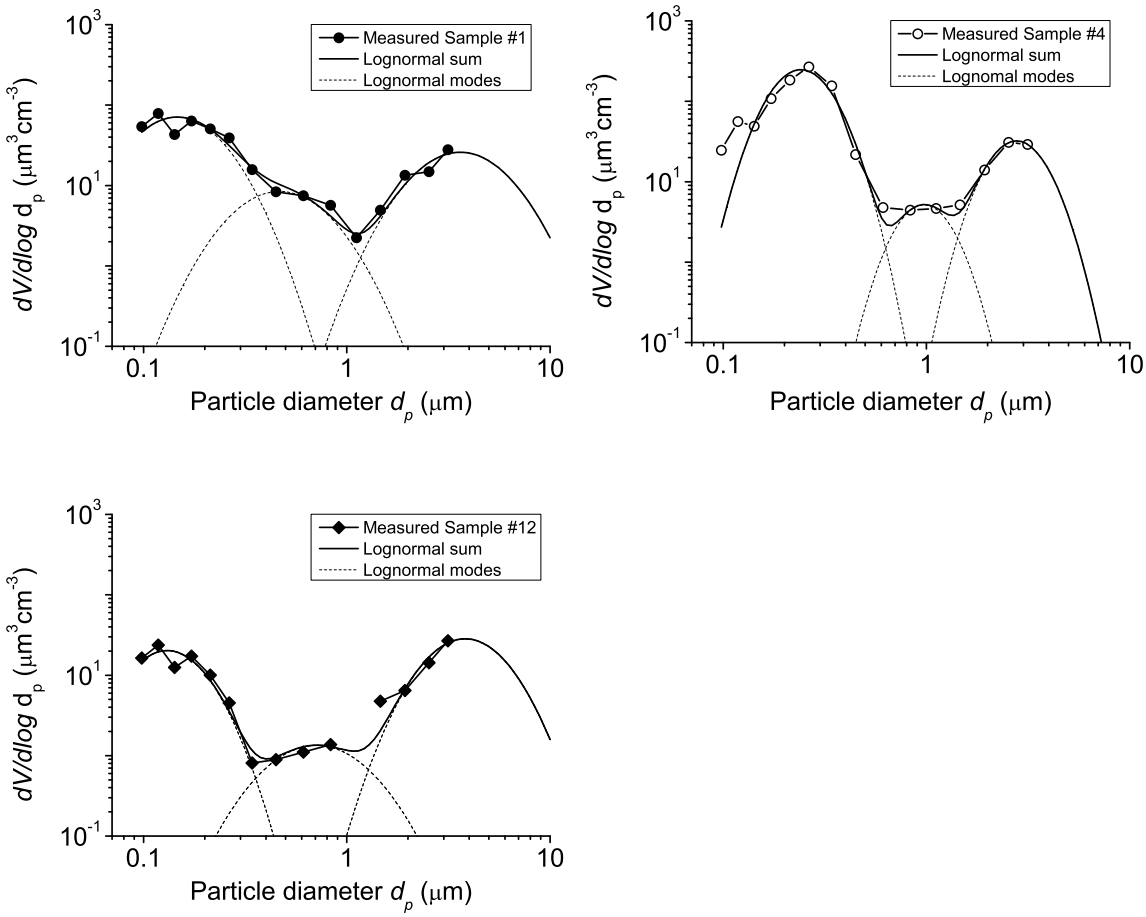


Figure 5.29: Multimodal fits to three volume distributions highlighted in Figure 5.28 to show effects of size truncations by the PCASP in the presence of a coarse mode. These effects are discussed in Section 5.6.5.

Table 5.5: Parameters of multimodal lognormal fits to averaged size distributions plotted in Figure 5.27, d_{gi} and σ_{gi} are the geometric mean diameter and deviation of modes $i = 1$ to 4. The stratifications were defined based on thermal stability, where SL = surface layer, SBL = stable boundary layer, CBL = convective boundary layer, RL = residual layer, EZ = entrainment zone and FT = free troposphere.

Thermal stratifications identified in Figures 5.22 to 5.26

		ML	SBL	RL	FT			SL	CBL	CBL/EZ	FT
Profile A	d_{g1}	0.165	0.198	0.244	0.133	Profile D	d_{g1}	0.136	0.153	0.162	0.140
	σ_{g1}	1.60	1.49	1.35	1.81		σ_{g1}	1.57	1.57	1.46	1.78
	d_{g2}	0.916	0.839	0.846	3.126		d_{g2}	0.610	0.450	0.573	2.657
	σ_{g2}	1.35	1.45	1.90	1.19		σ_{g2}	1.43	1.36	1.25	1.22
	d_{g3}	2.448	2.614	3.774	-		d_{g3}	2.147	5.849	3.838	-
	σ_{g3}	1.33	1.32	1.31	-		σ_{g3}	1.32	2.53	2.40	-
Profile B	d_{g1}	0.084	0.072	0.074	-	Profile E	d_{g1}	0.176	0.182	0.165	0.170
	σ_{g1}	1.16	1.20	1.16	-		σ_{g1}	1.30	1.32	1.67	1.77
	d_{g2}	0.185	0.186	0.214	-		d_{g2}	1.181	0.827	0.936	1.153
	σ_{g2}	1.53	1.49	1.40	-		σ_{g2}	1.98	1.58	1.22	1.22
	d_{g3}	0.506	0.650	0.725	-		d_{g3}	2.297	2.594	2.839	3.565
	σ_{g3}	1.52	1.39	1.30	-		σ_{g3}	1.10	1.19	1.31	1.28
	d_{g4}	2.827	2.357	2.461	-	Profile F	d_{g1}	0.149	0.127	0.127	-
	σ_{g4}	1.52	1.39	1.30	-		σ_{g1}	1.49	1.58	1.58	-
Profile C	d_{g1}	0.087	0.076	0.077	-		d_{g2}	0.697	0.575	0.592	-
	σ_{g1}	1.11	1.14	1.13	-		σ_{g2}	1.54	1.22	1.27	-
	d_{g2}	0.223	0.217	0.252	-		d_{g3}	2.531	2.327	2.771	-
	σ_{g2}	1.49	1.49	1.35	-		σ_{g3}	1.35	1.51	1.51	-
	d_{g3}	0.699	0.908	1.014	-	Profile G	d_{g1}	0.136	0.136	0.136	0.119
	σ_{g3}	1.34	1.34	1.34	-		σ_{g1}	1.57	1.57	1.57	1.82
	d_{g4}	2.610	2.564	2.653	-		d_{g2}	0.534	0.534	0.534	1.298
	σ_{g4}	1.34	1.34	1.34	-		σ_{g2}	1.35	1.35	1.35	1.35
							d_{g3}	2.288	2.341	1.848	-
							σ_{g3}	1.49	1.49	1.35	-

5.5 Comparisons of number concentrations and size distributions - SEM and PCASP

Equivalent number concentrations from SEM analyses were compared with mean in-situ number concentrations measured with the PCASP over the same time intervals, N_{PCASP}. Surface number density of particles deposited on ABS filters n_{SEM} (μm^{-2} cm^{-3}) was calculated from counted particles N_A and total area on SEM images A by assuming a maximum collection efficiency of 100% on the ABS samples and normalised to volume sampled V_t as $n_{SEM} = N_A/(A \times V_t)$. The size range for the PCASP is between 0.1 and 3.5 μm, while particles of sizes up to 10 μm are collected on the ABS samples. However, since particle number concentrations in the coarse mode ($2.5 < d_p < 47$ μm) were several orders of magnitude lower than the PCASP, it is reasonable to compare variations of n_{SEM} and N_{PCASP} within experimental margins of error.

The n_{SEM} for each sample are shown in Figure 5.30(a). In Figure 5.30(b) n_{SEM} and N_{PCASP} were normalised to Sample #3. Relative number concentrations between the ABS and PCASP are well correlated (correlation coefficient $R^2 = 0.82$). Both number concentrations show that highest number concentrations were observed on Samples #1 to #4 (Flight 9, August 6), particularly on Sample #3 collected at the lowest altitudes. High concentrations of particles on Flight 9 might have been enhanced by the accumulation of aerosols with contributions from the previous day. The previous day, August 5, was identified as one of the 'episode' days when health standard levels of particulate matter were exceeded at Khayelitsha, a large, densely populated lower socio-economic and informal settlement suburb[11].

Equivalent SEM number concentrations N_{SEM} were calculated from the surface density n_{SEM}, where $N_{SEM} = \pi r^2 n_{SEM}$ and $r = 4$ mm, the diameter of the ABS deposition spot. N_{SEM} was compared with in-situ number concentrations N_{PCASP} measured by the PCASP over the same time intervals. From a linear regression of these absolute number concentrations plotted in Figure 5.30c, N_{SEM} is underestimated systematically by a factor of 4.3 ± 0.3 compared to N_{PCASP}, despite the good correlation between the relative concentrations in Figure 5.30(b). The underestimation here cannot be explained by inlet losses, vaporisation of volatile particles in the SEM vacuum nor visual under-counting on images. There is no correlation between the underestimation and abundance of individual particle groups. It is possible that these discrepancies might be due to misrepresentation of small particles on the SEM filters (*Ebert et al.*, 2004). From size resolved number distri-

[11] http://www.capetown.gov.za/airqual/

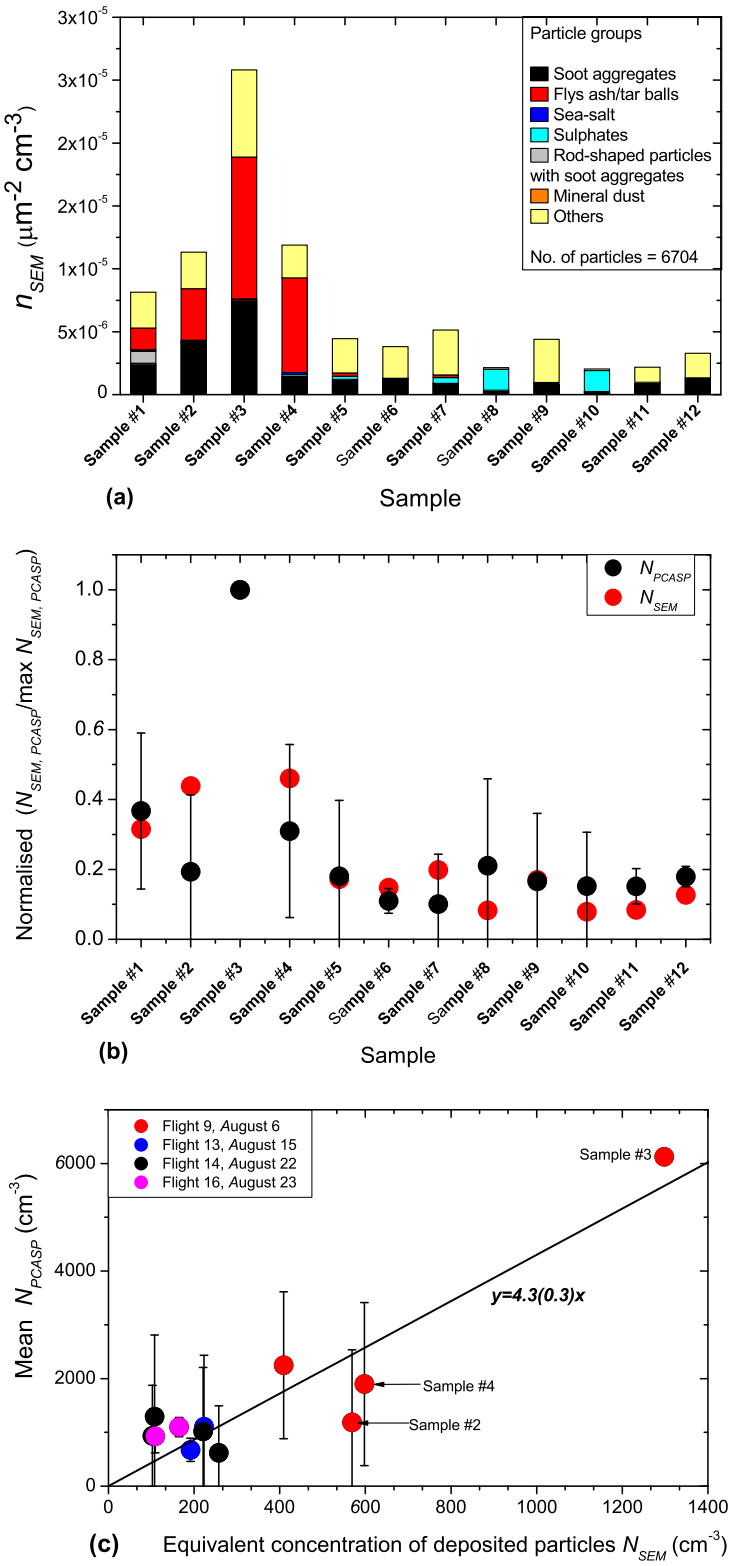


Figure 5.30: (a) Surface number density n_{SEM} of particles from SEM analyses of ABS samples collected on Flights 9, 13, 14 and 16. (b) N_{SEM} and mean number concentrations measured by the PCASP, N_{PCASP}, and normalised to concentrations of Sample #3. Correlation coefficient $R^2 = 0.82$. Error bars are the standard deviations of N_{PCASP}. (c) Relationship between absolute N_{PCASP} and N_{SEM}. The equivalent number concentrations from the SEM N_{SEM} are systematically underestimated by a factor of 4.3 ± 0.3.

butions, these authors found that N_{SEM} was underestimated when compared with in-situ number concentrations measured by a combined DMPS/APS (Differential Mobility Particle Sizer/Aerodynamic Particle Sizer). Depending on particle sizes in the range of particle diameters of 0.1 to 3 μm, N_{SEM} was underestimated by factors of 1.6 to 9.6, respectively. In this study, particles were not size resolved in the SEM analysis, and this underestimation factor of 4.3 is averaged over the entire size range.

A further comparison was made between the SEM and the PCASP size distributions for Samples #1 and #4. As realised above, it is not possible to compare absolute particle concentrations, therefore both distributions were normalised to their maximum $dN/dlog\ d_p$, to compare only shapes of the distributions. The normalised PCASP size distributions $dN_{PCASP}/d\,logd_p$ and distributions of SEM equivalent surface diameters $dN_{SEM}/d\,logd_a$ are shown in Figure 5.31.

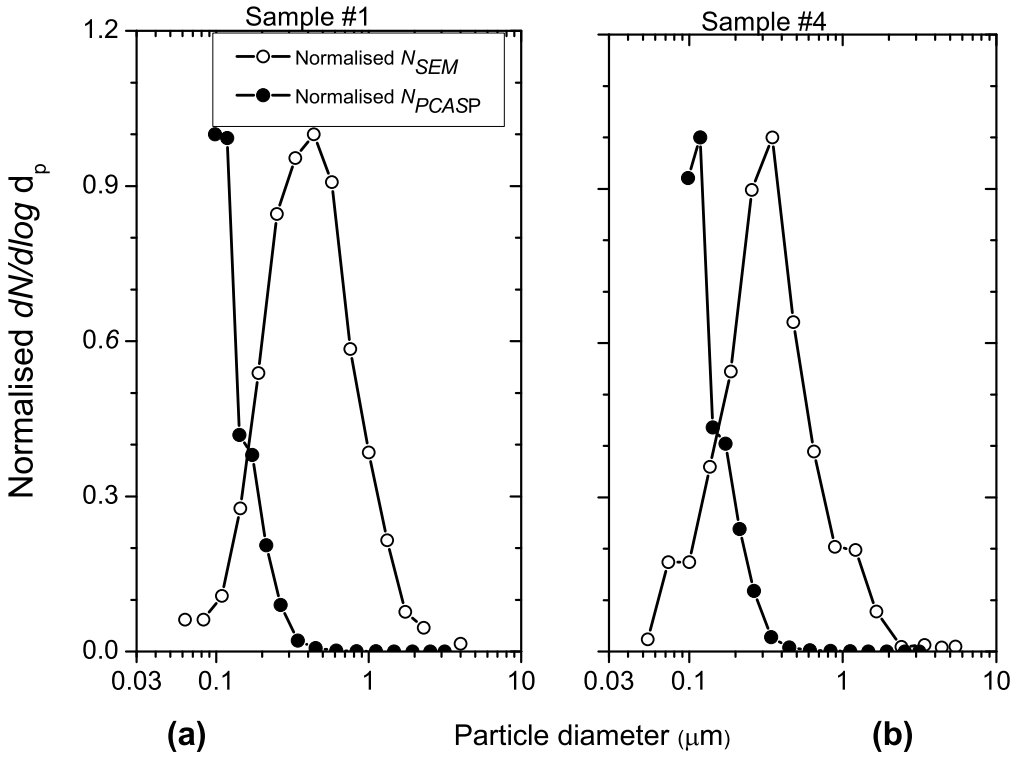


Figure 5.31: Normalised size distributions of particles on Sample #1 and Sample #4, $dN_{PCASP}/dlog\ d_p$ measured by the PCASP and $dN_{SEM}/dlog\ d_a$ from SEM analysis.

There are two main differences in these size distributions. Small particles were clearly under represented in the SEM possibly due to low deposition efficiencies of small particles because of diffusion losses. Small particles might also have been under counted on substrates, because they had slipped through filter holes during sampling, or they were not detected in the SEM images due to limited resolution. Secondly, size distributions from

the SEM are biased toward large diameters because of the resting positions of the particles, which will expose the largest surface area for imaging. Although these distributions are measuring different physical properties of particles, large discrepancies will obviously occur if the distributions are used in the Mie routine to derive aerosol optical properties. Figure 5.31 indicates apparent limitations and inconsistency when comparing microscopy sizes to size distributions derived from conventional sizing techniques.

5.6 Aerosol optical properties - SEM and PCASP

5.6.1 Aerosol refractive index

Aerosol complex refractive indices were defined from the chemical compositions, abundance and mixing states of particle species identified in SEM analyses. Refractive indices were chosen for externally mixed chemical species with refractive indices $m_j = n_j - ik_j$ for groups $j = 1 - 7$ as listed in Table 5.6.

Table 5.6: Refractive indices and densities of particle groups identified in SEM analysis.

Particle group	**Refractive index** $(m_j = n_j - ik_j)$	**Density** gcm^{-3}
Soot aggregates	$1.75 - 0.44i$	1.5
Mineral dust	$1.56 - 0.006i$	2.5
Rod shaped	$1.50 - 0.0i$	1.5
Sulphates	$1.43 - 0.0i$	1.8
Sea-salt	$1.54 - 0.0i$	2.2
Tar balls/fly ash	$1.50 - 0.0i$	1.0/2.0
Others	$1.50 - 0.0i$	1.8

Refractive indices of soot particles given in literature (at a wavelength of 550 nm) vary widely from $m = 1.5 - 0.47i$ (*Horvath*, 1998), $m = 1.75 - 0.44i$ (*d'Almeida et al.*, 1991) to $m = 1.96 - 0.66i$ (*Seinfeld and Pandis*, 1998), because of variable internal molecular structures and substances that might be adsorbed on soot particles, e.g., VOCs and unburnt fuel (*Horvath*, 1993). A wavelength dependent refractive index given by *d'Almeida et al.* (1991) was chosen, because it is representative of anthropogenic soot with a high absorbing component. Sulphate particles were treated as freshly formed H_2SO_4 with a refractive index of $m = 1.43 - 0.0i$, and sea-salt particles were treated as pure sodium chloride with $m = 1.54 - 0.0i$ (*Horvath*, 1998). A refractive index of $m = 1.56 - 0.006i$ was chosen for mineral dust particles. This is representative of crustal material whose composition might

be variable, consisting mainly of oxides and hydroxides of several metals (*Tegen et al.*, 1996). The index is more suitable for these investigations, as evidenced from EDX analyses of individual dust particles. For tar balls/fly ash, rod shaped particle and for the group of particles labelled 'others', a refractive index for a non-absorbing aerosol of $m = 1.5 - 0.0i$ was assigned (*Horvath*, 1998). It was assumed that the only absorbing components were soot particles, and mineral dust particles were weakly absorbing.

Effective refractive indices $m_I = n_I - ik_I$ of Samples #1 to #12 were calculated using the volume averaging mixing rule (*Horvath*, 1998). Particles were externally mixed and therefore number distributions of each particle group $j = 1$ to 7 were weighed against corresponding fractional abundance in Figure 5.30 by assuming size independent fractional compositions with $m_j = n_j - ik_j$ and particle volume V_j. The effective complex refractive indices are given by

$$m = \frac{n_1V_1 + n_2V_2 \ldots n_7V_7}{V_1 + V_2 \ldots V_7} - i\frac{k_1V_1 + k_2V_2 \ldots k_7V_7}{V_1 + V_2 \ldots V_7} \tag{5.4}$$

The effective refractive indices for Samples #1 to #12 are listed in Table 5.7. The real parts n_I varied from 1.47 to 1.61. The complex components k_I varied from 0.05 to 0.20 depending on the fractional percentage of soot particles, with a mean effective refractive index of $m = 1.56 - 0.12i$. While the range of the real component is in agreement with retrievals of n_I in literature, the imaginary component k_I is much larger than observed in urban influenced aerosols (*Mallet et al.*, 2004) or biomass burning aerosols (*Formenti et al.*, 2002a). As seen from the variation of $m_I = n_I - ik_I$ in Table 5.7, a single complex refractive index of $m = 1.50 - 0.1i$ recommended for polluted areas (*Horvath*, 1998) cannot be applied to Cape Town where there are strong spatial and temporal variations in contributions of particle species. Due to varying concentrations of highly absorbing soot particles, deviations in effective refractive indices will result in large uncertainties in calculating optical properties of aerosols in some locations, particularly absorption coefficients and single scattering albedo, parameters which are most sensitive to refractive indices assigned to the aerosol.

5.6.2 Effects of refractive index on particle size

Particle sizes derived from the PCASP assume light is scattered by polystyrene latex (PSL) spheres with a refractive index of $m = 1.585 - 0.0i$, and have to be corrected to represent ambient aerosol particles with different refractive properties. To correct the PCASP size channels for ambient particles with different refractive indices, scattering response functions were determined using a Mie scattering code BH-Mie-Rechner (*Vetter*, 2004) for refractive

index of PSL spheres ($m = 1.585 - 0.0i$) and aerosol refractive indices in Table 5.6. These response functions correspond to the theoretical response of the PCASP over scattering angles of $35° - 120°$, at wavelength $\lambda_{635} = 0.635$ μm, Figure 5.32.

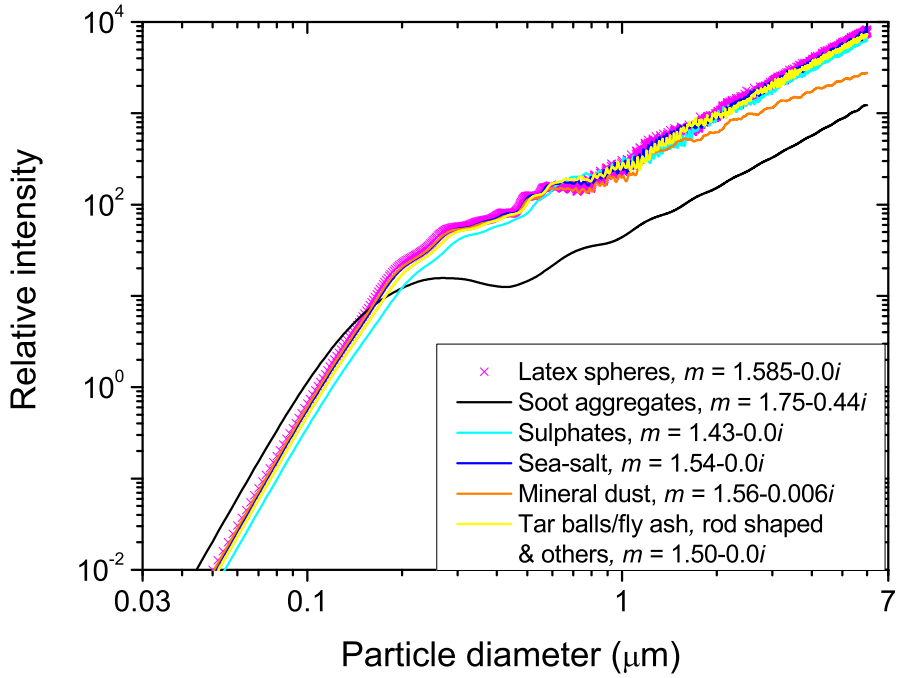


Figure 5.32: PCASP responses to PSL spheres and aerosol particles of different refractive indices at a wavelength of 0.635 μm. The functions are integrated over scattering angles of $35^0 - 120^0$ to correspond to theoretical response functions of the PCASP.

The response functions are multivalued - in certain size ranges the responses do not increase monotonically with size, but rather several values of d_p correspond to a given response amplitude. Functions were fitted with 8^{th} order polynomial functions with coefficients listed in Appendix C Table 2. The polynomials best matched the fluctuating response functions with correlation coefficients R^2 higher than 0.997 over an extrapolated range of $0.04 < d_p < 6$ μm. For a given relative intensity, d_{PSL} (diameter for PSL spheres with $m = 1.585 - 0.0i$) and $d_{aerosol}$ (for $m_j = n_j - ik_j$) were identified from the polynomial fits, and ratios $d_{aerosol}/d_{PSL}$ plotted in Figure 5.33.

For sea-salt particles and those particles assigned a refractive index of $m = 1.5 - 0.0i$, ratios $d_{aerosol}/d_{PSL}$ are within certainty of 10% on the entire PCASP size range. Sizing errors on sulphate and mineral dust particles vary by up to 25% depending on particle size. The PCASP will severely underestimate sizes of absorbing particles with diameter larger than 0.3 μm by factors of up to 3.6, while slightly overestimating sizes of soot particles below 0.3 μm. In all particle groups, maximum under sizing occurs when particle diameters were comparable to the wavelength of light.

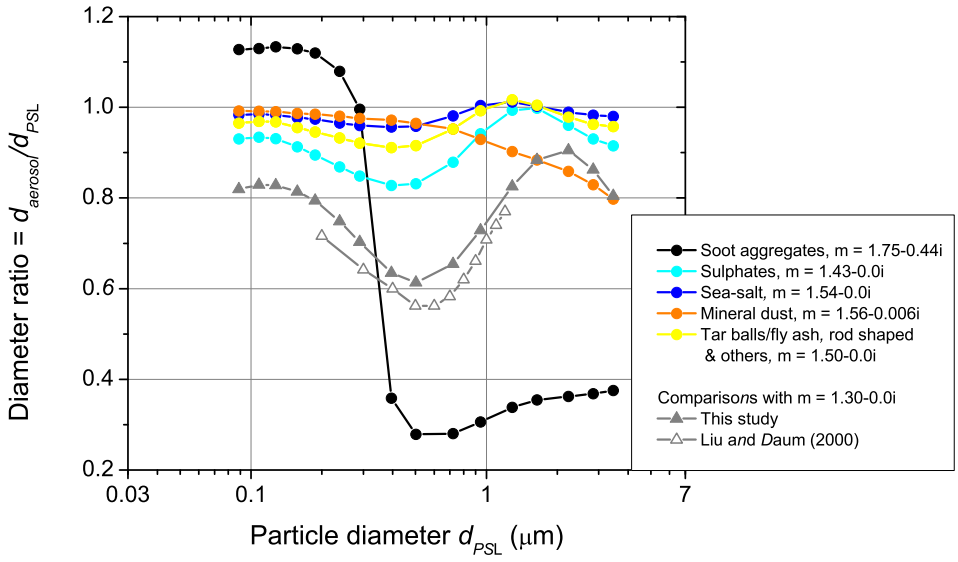


Figure 5.33: Diameter ratios $d_{aerosol}/d_{PSL}$ as a function of d_{PSL} for particles with response functions in Figure 5.32. For $d_{aerosol}/d_{PSL} > 1$, the PCASP overestimates particle sizes and for $d_{aerosol}/d_{PSL} < 1$, particle sizes are underestimated.

When the PCASP size distributions were corrected for refractive index, calculated light scattering coefficients were closer to those measured by the nephelometer (*Liu and Daum*, 2000). In that study, theoretical formulations of the scattering response functions were based on what was termed the summed-field response (SFR) and the summed-amplitude response (SAR) (response functions where the scattering intensities or amplitudes were added, respectively). The SFR was found to model better the PCASP scattering functions. To compare model ratios in this study with those from *Liu and Daum* (2000), ratios $d_{aerosol}/d_{PSL}$ for ambient particles with $m = 1.3 - 0.0i$ were plotted in Figure 5.33, together with *Liu and Daum* (2000) ratios from their SFR formulations. The model ratios in this study are consistent with the authors' results (and comparisons herein) and show a minimum ratio occurring at the same diameter, despite a constant difference of $\cong 0.06$ between the absolute ratios.

Effects of refractive indices on PCASP size distributions therefore need to be applied to size resolved chemical distributions. The only size-resolved information was derived from the SEM analysis of soot aggregates, where surface diameters were between 0.6 and 0.7 μm. This size range is an upper limit because the agglomerate structure of soot aggregates exposes the largest area. There are uncertainties in determining in detail the real 3D particle shapes from 2D projections from the SEM images (see Chapter 4 and *Brasil et al.*, 1999). Due to uncertainties in the 2D SEM diameters and lack of size-resolved chemical information on other particle groups, effects of ambient aerosol refractive indices cannot be corrected for in this study. These effects will be acknowledged as major limitations

in determining size distributions of particles with the PCASP.

5.6.3 Aerosol optical properties

Optical properties of dry particles were determined for segments of flights tracks corresponding to sampling times of ABS deposition spots investigated with the SEM in Section 5.3. The particles were dry because the heating system in the PCASP inlet was switched on. Extinction coefficients σ_{ep} (the sum of scattering σ_{sp} and absorption σ_{ap} coefficients), single scattering albedo (ω_0), asymmetry parameter (g_0), and Ångstrom exponents (α) were calculated with a Mie scattering routine at wavelengths of light $\lambda = 450$, 550 and 700 nm for homogeneous and spherical particle ensembles (*Bohren and Huffman*, 1983; *Wiscombe*, 1980). Number-size distributions were measured with the PCASP in the size range of 0.1 to 3.5 μm and refractive indices were determined from the chemical composition of particles in the SEM analyses, as discussed above.

Particles were assumed to be spherical in the Mie scattering routine. However, its been shown in SEM analyses that aggregated soot particles, euhedral mineral dust and sea-salt particles were nonspherical. Influence of particle shape on light scattering depends on particle size. For particles smaller than the wavelength of light, irregular particles can be approximated by the equivalent volume diameter with marginal error (*Coetti*, 1984; *Gebhart*, 2001). When a particle's physical diameter is larger than the wavelength, scattering is a function of particle cross-sectional area. Since particles were randomly oriented, the scattering can be approximated by a spherical particle with the same refractive index and equivalent cross-section area diameter (*van de Hulst*, 1957). Effects of shape have been quantified for nonspherical particles (*Mishchenko et al.*, 2000) though uncertainties still remain on aggregated particles. Hence these effects will not be considered in optical parameters derived here. Scattering and extinction coefficients (and hence single scattering albedo) are insensitive to particle shapes (*Eck et al.*, 2005; *Pilinis and Li*, 1998), unlike the asymmetry parameter, which describes the size distribution of the measured ensemble.

Optical parameters were computed as

$$\sigma_{ep} = \sum_{j=1}^{7} (\sigma_{sp,j} + \sigma_{ap,j}) \tag{5.5}$$

$$\omega_0 = \frac{\sum (\sigma_{sp,j} + \sigma_{ap,j}) * \omega_j}{\sum (\sigma_{sp,j} + \sigma_{ap,j})} \tag{5.6}$$

$$g_0 = \frac{\sum (\sigma_{sp,j} + \sigma_{ap,j}) * g_j}{\sum (\sigma_{sp,j} + \sigma_{ap,j})} \tag{5.7}$$

where $j = 1$ to 7 are the defined particle groups. Extinction coefficients are additive (*Horvath*, 1998). Composite aerosol single scattering albedo ω_0 and composite aerosol asymmetry parameter g_0 were determined on the basis of weighed contributions of each chemical specie (*Mallet et al.*, 2003). The single scattering albedo is a fundamental optical parameter defining the contribution of absorbing particles to radiative forcing (*Dubovik et al.*, 1998). The asymmetry parameter, g_0, represents an estimate of asymmetry of dispersed radiation. For small particles in the Rayleigh regime $g_0 = 0$ and for forward purely scattering particles $g_0 = 1$. Ångstrom exponents were calculated from scattering coefficients at wavelengths $\lambda_1 - \lambda_2$ of $450 - 550$ and $550 - 700$ nm as

$$\alpha_{\lambda_1 - \lambda_2} \cong -\frac{log(\sigma_{ep,\,\lambda_1}/\sigma_{ep,\,\lambda_2})}{log(\lambda_1/\lambda_2)} \tag{5.8}$$

Ångstrom exponents describe the wavelength dependence of the extinction coefficient and is strongly influenced by particle sizes. For particle sizes larger than 0.2 μm, $\alpha > 2$, and for particles larger than 2 μm, $\alpha \approx 0$ (*Seinfeld and Pandis*, 1998).

There was strong spatial variability of particle number concentrations as shown in Appendix C Figures 2 and 3. Therefore to give an overview of optical properties, parameters were computed from point measurements of maximum, mean, and minimum number concentrations N probed during collection of each ABS sample. The maximum number concentrations were representative of the highest levels observed in the most polluted locations within the boundary layer. Although volume distributions would be more appropriate in defining ranges of optical parameters (because optical properties are sensitive to particle volume rather than number concentrations) there were very low concentrations of particles larger than 1 μm, and volume distribution might have been biased by the low detection of the PCASP at low concentrations. Optical parameters derived for maximum number concentrations are given in Table 5.7 and in Table 5.8 for mean and minimum number concentrations. These optical properties will now be discussed in detail, based on maximum N as possible pollution episodes encountered.

Table 5.7: Optical properties of particles determined from maximum number concentrations measured by the PCASP, refractive indices determined from SEM analyses and $\lambda = 550$ nm. Sample #10 (in italics) was collected inside an industrial plume.

	Effective refractive index		**Maximum number concentrations**							
Sample	$m_I = n_I - ik_I$		σ_{ep}	σ_{ap}	ω_0	g_0	Å	N	$Volume$	Alt. ± std
ID	n_I	k_I	Mm^{-1}	Mm^{-1}			$450-550$	cm^{-3}	$\mu m^3\, cm^{-3}$	m asl
Flight 9										
Sample #1	1.57	0.18	**163.7**	56.6	**0.65**	0.63	0.79	6279	53.3	355 ± 155
Sample #2	1.59	0.16	**119.1**	42.5	**0.64**	0.56	1.14	5273	29.4	280 ± 109
Sample #3	1.57	0.13	**173.4**	57.2	**0.67**	0.52	1.43	8897	32.0	130 ± 12
Sample #4	1.53	0.05	**368.5**	47.1	**0.87**	0.60	1.52	8555	98.6	269 ± 126
Flight 13										
Sample #5	1.56	0.12	**82.6**	22.0	**0.73**	0.59	1.05	3631	16.5	1068 ± 641
Sample #6	1.59	0.15	**18.9**	7.3	**0.61**	0.50	1.31	1278	3.4	227 ± 209
Flight 14										
Sample #7	1.54	0.08	**79.0**	20.8	**0.74**	0.51	1.45	7751	17.0	143 ± 49
Sample #8	1.49	0.07	**265.1**	53.7	**0.80**	0.60	1.49	7702	54.3	111 ± 67
Sample #9	1.55	0.09	**201.0**	51.1	**0.75**	0.54	1.49	11175	36.7	190 ± 18
Sample #10	*1.47*	*0.05*	***755.1***	*103.0*	***0.86***	*0.63*	*1.52*	*16172*	*162.6*	261 ± 44
Flight 16										
Sample #11	1.61	0.20	**41.8**	15.7	**0.62**	0.62	0.72	1774	11.6	166 ± 49
Sample #12	1.61	0.18	**61.6**	17.4	**0.72**	0.71	0.46	1751	34.3	136 ± 13
Arithmetic mean	1.56	0.12	**194.2**	41.2	**0.72**	0.59	1.20	6686	45.8	
Standard deviation	0.04	0.05	**194.6**	25.4	**0.08**	0.06	0.35	4182	42.7	

Table 5.8: Optical properties of particles determined from mean and minimum number concentrations measured by the PCASP, refractive indices determined from SEM analyses and $\lambda = 550$ nm. Sample #10 (in italics) was collected inside an industrial plume.

	Mean number concentrations						**Minimum number concentrations**						
Sample ID	σ_{ep} Mm^{-1}	σ_{ap} Mm^{-1}	ω_0	g_0	N cm^{-3}	$Volume$ $\mu m^3\, cm^{-3}$	σ_{ep} Mm^{-1}	σ_{ap} Mm^{-1}	ω_0	g_0	N cm^{-3}	$Volume$ $\mu m^3\, cm^{-3}$	Alt.±std m asl
Flight 9													
Sample #1	**32.1**	12.7	**0.61**	0.57	1624	8.4	**0.7**	0.5	**0.26**	0.38	88	0.1	355 ± 155
Sample #2	**31.1**	11.5	**0.63**	0.55	1607	7.7	**1.3**	0.7	**0.32**	0.45	150	0.2	280 ± 109
Sample #3	**95.1**	30.3	**0.68**	0.54	4748	20.5	**71.0**	20.3	**0.58**	0.71	2881	15.8	130 ± 12
Sample #4	**27.2**	4.1	**0.85**	0.58	1669	8.0	**3.4**	0.4	**0.55**	0.87	182	1.0	269 ± 126
Flight 13													
Sample #5	**18.8**	4.93	**0.74**	0.61	835	5.5	**0.6**	0.2	**0.56**	0.72	17	0.1	1068 ± 641
Sample #6	**13.8**	4.28	**0.69**	0.61	606	4.5	**4.4**	1.2	**0.64**	0.74	138	0.6	227 ± 209
Flight 14													
Sample #7	**15.1**	3.3	**0.78**	0.58	1022	4.1	**1.8**	0.5	**0.47**	0.72	139	0.4	143 ± 49
Sample #8	**32.0**	6.0	**0.81**	0.63	1198	9.2	**2.5**	0.5	**0.61**	0.79	162	0.5	111 ± 67
Sample #9	**21.0**	4.5	**0.79**	0.60	962	5.9	**0.9**	0.3	**0.41**	0.64	106	0.2	190 ± 18
Sample #10	***17.9***	*2.7*	***0.85***	*0.62*	*951*	*5.9*	***2.7***	*0.3*	***0.71***	*0.90*	*98*	*0.5*	261 ± 44
Flight 16													
Sample #11	**21.8**	7.9	**0.64**	0.64	807	7.0	**1.5**	0.5	**0.64**	0.67	51	0.2	166 ± 49
Sample #12	**27.1**	8.6	**0.68**	0.65	945	9.5	**14.1**	5.2	**0.57**	0.63	686	2.5	136 ± 13
Arithmetic mean	**29.4**	8.4	**0.73**	0.60	1415	8.0	**8.7**	2.6	**0.69**	0.53	392	1.8	
Standard deviation	**20.8**	7.3	**0.08**	0.03	1059	4.1	**7.3**	5.5	**0.14**	0.13	768	4.3	

5.6.3.1 Light scattering and absorption coefficients

From the maximum number concentrations, light extinction coefficients, σ_{ep}, varied from 19 to 755 Mm^{-1}, while absorption coefficients varied from 7 to 103 Mm^{-1} (Mm^{-1} is inverse megameters = $10^{-6}m^{-1}$ and all coefficients were computed at $\lambda = 550$ nm unless stated). The mean extinction coefficient of 194 Mm^{-1} is an order of magnitude larger than Rayleigh extinction by gases, indicating dominance of particles in light extinction (extinction by gases σ_{eg} is approximately 12.4 Mm^{-1} at 400 m asl, $\lambda = 550$ nm, *Seinfeld and Pandis*, 1998). Extinction and absorption coefficients from mean N are $\sigma_{ep} = 29 \pm 21$ Mm^{-1} and $\sigma_{ap} = 8 \pm 7$ Mm^{-1} and 1 to 14 factors less than those derived from maximum N (excluding Sample #10). Extreme values of $\sigma_{ep} = 755$ Mm^{-1} and $\sigma_{ap} = 103$ Mm^{-1} on Sample #10 were observed at low altitudes directly over an industrial site B (glass manufacturing industry) and were likely to be in the plume of stack emissions. Such magnitudes are not representative of the entire brown haze.

In section 5.4.1, it was shown that particle number distributions showed strong spatial variability between different locations. Considering maximum number concentrations in Table 5.7, areas like Khayelitsha (Sample #4, Sample #9) and industrial site B (Sample #10) show highest aerosol volume (hence more light extinction). Despite peaks being in these areas, Table 5.8 shows that it is the Cape Flats, areas west of Khayelitsha that experience the highest averaged extinction coefficients of 95.1 Mm^{-1} (Sample #3), and in general Flight 9, as compared to other flights.

Extinction coefficients in Cape Town are much higher than expected in clean and average background continental conditions where σ_{ep} are 23 Mm^{-1} and 57 Mm^{-1}, respectively (*Seinfeld and Pandis*, 1998). In comparison with other studies in Europe/USA urban sites, the mean magnitude of σ_{ep} observed in Cape Town is more than measured in Atlanta where $\sigma_{sp}(\lambda_{530}) = 121 \pm 48$ Mm^{-1} and $\sigma_{ap} = 16 \pm 12$ Mm^{-1} (*Carrico et al.*, 2003). Scattering coefficients on coastal and surrounding areas influenced by urban-industrial emissions from Marseille were between 35 ± 28 Mm^{-1} to 63 ± 43 Mm^{-1} depending on the type of breeze, and σ_{ep} was overall less than 100 Mm^{-1} (*Mallet et al.*, 2005). Three year mean values of σ_{ep} in several US locations were lower than 164 Mm^{-1} (*Malm et al.*, 1994). However, coefficients in this study are less than those observed in Beijing, China, where mean values were $\sigma_{sp} = 488 \pm 370$ Mm^{-1} and $\sigma_{ap} = 83 \pm 40$ Mm^{-1} (*Bergin et al.*, 2001).

Extinction coefficients were computed for dry particles at relative humidity RH of $30\% - 40\%$ in the PCASP, a range assumed by several researchers when the heating system is on (*Formenti et al.*, 2002a; *Reid et al.*, 1999). In higher ambient humidity, scattering is

enhanced by growth of hygroscopic particles (*Tang*, 1996). Unless coated by hygroscopic material, soot, tar balls/fly ash, mineral dust particles are non-hygroscopic particles and were likely dry at $RH = 35\%$; sea-salt particles were treated as NaCl with deliquescence relative humidity $DRH = 75\%$ and were crystalline in the PCASP (*Seinfeld and Pandis*, 1998). Sulphate particles (treated as H_2SO_4) are highly hygroscopic and do not exhibit a deliquescent behaviour, hence they contained water during size measurements. Changes in scattering properties are defined by the hygroscopic growth factor $f(RH)$, a ratio of scattering coefficient at $RH = 80\%$ to that of a dry particle at $RH = 40\%$ where $f(RH) = \sigma_{ep,\,80\%}/\sigma_{ep,\,40\%}$. Assuming ambient $RH = 60\%$ during the flight (based on changes of RH between morning and afternoon profiles) and treating sulphates as sulphuric acid droplets with humidity growth factor $f(RH, 60\%)$ of 2.35 (*Malm and Day*, 2001), extinction coefficients could be higher by 79 to 94% on Samples #8 and Sample #10, respectively. The changes due to hygroscopic growth are negligible on the rest of the ABS samples, since sulphate aerosol fractional concentrations were very low. Absorption coefficients are unaltered by humidity growth, since soot particles, identified as the significant absorbing component of the aerosols, do not exhibit considerable growth, rather particles initially collapse with humidity increase (*Weingartner et al.*, 1997).

5.6.3.2 Single scattering albedo, asymmetry parameter, Ångstrom exponent

Computed values of ω_0 varied from 0.61 to 0.94, with a mean value of 0.72 ± 0.08. The lowest ω_0 were observed on Flights 9, 13 and 16 (August 6, 15, and 23). Parameters indicate a large absorption component, due to high fractional number concentrations of soot particles, where fractional contributions of soot particles were between 29% to 46% except on Sample #4 (see Figure 5.11). By assuming internally mixed particles with the same volume of absorbing soot, the mean is $\omega_0 = 0.60 \pm 0.10$, and much lower than that of externally mixed aerosols. This is because for internal mixtures all particle volume absorbs radiation rather than a fraction that is composed of soot.

The range of ω_0 is comparable to magnitudes defined from single particle analysis elsewhere. By determining size resolved chemical compositions in SEM analyses, ω_0 of $0.62 - 0.76$ was derived of externally mixed urban aerosols in central Europe (*Ebert et al.*, 2004). However, from direct optical measurements, mean ω_0 values observed from several techniques are much higher than in Cape Town. A mean ω_0 of 0.83 was observed during winter in central Europe for mass concentrations of elemental carbon between $10 - 31\%$ (*Bundke et al.*, 2002; *Neusüß et al.*, 2002). The average single scattering albedo of dry aerosol particles at a rural site influenced by urban emissions in southern Italy was 0.76

(*Horvath*, 1996). During the INDOEX (Indian Ocean Experiment) anthropogenic aerosol attributed to an absorption component with ω_0 between $0.6 - 0.8$ (*de Reus et al.*, 2002). The single scattering albedoes of anthropogenic influenced aerosols in the boundary layer determined during the ACE-2 (North Atlantic Aerosol Characterization Experiment) were > 0.83 (*Russell et al.*, 2002). Generally magnitudes of $\omega_0 > 0.8$ are reported in urban sites in European and US cities (*Carrico et al.*, 2003; *Dubovik et al.*, 2002; *Horvath*, 1993; *Mallet et al.*, 2005) and eastern Asian cities (*Bergin et al.*, 2001; *Eck et al.*, 2005). Magnitudes of ω_0 as low as 0.5 and 0.6 were common during the 1970s and 1980s in Europe and the USA (*Horvath*, 1993).

The asymmetry parameter, g_0, was found to vary over a narrow range of 0.50 to 0.71 with mean of 0.59 ± 0.06. The range of g_0 indicates that particles scatter light in the forward direction. The mean value agrees well with several g_0 measured over urban sites influenced by high anthropogenic aerosols in submicrometer range. *Mallet et al.* (2003) found $g_0 = 0.59 \pm 0.05$ at a peri-urban site of Marseille at $RH < 60\%$. An asymmetry parameter of 0.58 were observed during the TARFOX experiment on the eastern US coastal region (*Hignett et al.*, 1999).

Ångstrom exponents were between 0.42 to 2.11 with mean $\alpha_{(450-550)} = 1.20 \pm 0.43$ and $\alpha_{(550-700)} = 1.26 \pm 0.36$ (hygroscopic growth of particles was not considered). The range of α indicates that extinction of light is dominated by particles within the size range of about 0.3 to 2 μm. The exponents are independent of altitude in the boundary layer indicating lack of significant variability in particle size distributions with altitude, optically significant variability that could be attributed to, e.g., particle growth by coagulation, gas-to-particle conversion or heterogeneous reactions (*Reid et al.*, 1999). Continuous optical measurements of extinction coefficients at a rural site strongly influenced by urban pollution showed that while the Ångstrom exponent ($\alpha \cong 1.18$) was not affected by humidity changes below 50%, α decreased to zero with humidity increase above 50% due to particle growth (*Horvath*, 1996). Therefore, when hygroscopic growth of sulphates is considered, ambient exponents on Flight 14 might be lower than an average of 1.49 computed here.

Visibility range, L_v, was determined from the Koschmieder relationship $L_v = 3.912/\sigma_{ext}$ where $\sigma_{ext} = \sigma_{ep} + \sigma_{eg}$ is light extinction by both particles and gases. The visibility range was 10 to 125 km with a mean of 37 ± 32 km (excluding Sample #10). The visibility range is reduced considerably when hygroscopic growth is considered on Samples #8 and #10 from 14.1 km and 5.1 km to 8.0 km and 2.6 km, respectively.

5.6.4 Radiative forcing of aerosol particles

Clear sky radiative forcing of aerosol particles over Cape Town were investigated for Flights 9 and 14, flights conducted on August 6 and 22 respectively. The forcing is a measure of the climate significance of aerosol particles. Since the forcings are influenced by the refractive index assigned to the aerosols, Flights 9 was chosen as most appropriate because aerosol chemical compositions had been defined with certainty better than 65% (i.e., less than 35% of particles were defined as 'others'). Flight 14 was selected due to the large contribution of sulphates.

The top of the atmosphere (TOA) forcing ΔF due to an absorbing aerosol is given by *Haywood and Shine* (1995) as

$$\Delta F \approx F_0 D T_a (1 - A_s) \omega_0 \overline{\beta} \tau \left[(1 - R_s)^2 - \frac{2R_s}{\overline{\beta}} \left(\frac{1}{\omega_0} - 1 \right) \right] \tag{5.9}$$

where F_0 is the solar constant of 1370 Wm^{-2}, D is the fractional day length, T_a is the atmospheric transmission, A_s is the fractional cloud amount, ω_0 is the single scattering albedo, $\overline{\beta}$ is the spectrally weighted upscatter function, τ is the aerosol optical depth and R_s is the surface reflectance.

Parameters $T_a = 0.76$ and $\overline{\beta} = 0.22$ were taken to be global mean optical properties of dry aerosol at light wavelength of 550 nm (*IPCC*, 2001). Due to the geographical location of Cape Town, surface reflectance was chosen to be $R_s = 0.06$ over sea, and a conservative $R_s = 0.20$ over land (*IPCC*, 2001). Flights were conducted under anticyclonic conditions with nearly cloud-free conditions on both days hence $A_s \approx 0$. Aerosol vertical column of particles was assumed to be well mixed with mean ω_0 of 0.71 for externally mixed and $\omega_0 = 0.54$ for internally mixed aerosols on Flight 9 and on Flight 14 $\omega_0 = 0.76$ for dry and 0.83 for wet aerosol at $RH = 60\%$, as computed from the Mie routine. A scale height of 1.5 km was assigned, and the scale height represents the maximum aerosol-loading height observed in vertical profiles in Section 5.4.1. From the mean extinction coefficients, optical depths τ were 0.31 on Flight 9 and on Flight 14, $\tau = 0.27$ for dry ($\tau = 0.38$ for wet). Sample #10 was excluded for reasons discussed before. The computed radiative forcings are listed in Table 5.9.

Considering the ranges of σ_{ext} and ω_0 on Samples #1 to #12, the range of the radiative forcing is between -12 and $+10$ Wm^{-2} over land and -33 Wm^{-2} to -10 Wm^{-2} over sea. Large ranges in the radiative forcings are a result of the variability in aerosol loading between locations. Influence of surface reflectance R_s is extremely large, changing aerosol effect from a warming over land to a cooling effect over sea on Flight 9, August

Table 5.9: Averaged clear sky net radiative forcings at the top of the atmosphere (TOA) estimated from the radiative transfer model for different aerosol mixtures.

Flight number, date & mixing state	**TOA Aerosol forcing, Wm^{-2}**		
	ω_0	Land surface $R_s = 0.2$	Sea surface $R_s = 0.06$
Flight 9, 6 August (dry, external)	0.71	$+2 \pm 1$	-10 ± 7
Flight 9, 6 August (dry, internal)	0.54	$+3 \pm 1$	-1.4 ± 0.4
Flight 14, 22 August (dry)	0.76	-1.2 ± 0.6	-14 ± 7
Flight 14, 22 August (wet)	0.83	-7 ± 6	-21 ± 17
Range of forcings on Samples #1 to #12 (dry, external)	0.61 to 0.94	-12 to $+10$	-33 to -10

6. The forcing is also sensitive to particle mixing states. Assuming an internal mixture on August 6 with computed $\omega_0 = 0.54$, the forcing has warming effect of $+3$ Wm^{-2} over land and a significantly lower magnitude of cooling over sea.

The magnitude of the warming in Cape Town (i.e, $+10$ Wm^{-2}) is much larger compared to other studies. Radiative forcing at the top of the atmosphere in urban Atlanta was between -30 and -2 Wm^{-2}, with a mean ΔF of -11 Wm^{-2} (*Carrico et al.*, 2003). During the INDOEX experiment both natural and anthropogenic aerosol contributed to an average TOA clear sky forcing of $+7 \pm 1$ Wm^{-2} over land and -10 ± 1 Wm^{-2} over ocean (*Satheesh et al.*, 2002). The TOA direct forcing over land were between -13 to -5 Wm^{-2} during LACE, Lindenberg Aerosol Characterization Experiment (*Wendling et al.*, 2002). Direct TOA forcings over Cape Town are substantially larger in magnitude than global mean radiative forcing attributed to anthropogenic sulphates, where $\Delta F \approx 1-2$ Wm^{-2} (*Charlson et al.*, 1992) and due to anthropogenic greenhouse gases where $\Delta F \approx +2.5$ Wm^{-2} (*IPCC*, 2001). However, in order to understand the contribution of particles to the atmosphere radiation budget, there is need to know the surface forcing of aerosols as well. Its been shown that absorbing aerosols increase surface forcing and decrease the TOA forcing, resulting in an increase in heating of the atmosphere (*Ramanathan et al.*, 2001b). Atmospheric heating by absorbing aerosol was up to $+20$ Wm^{-2} during the INDOEX experiment (*Satheesh et al.*, 2002). Therefore the impact of aerosols on the radiative balance in the local atmosphere of Cape Town can lead to local atmospheric heating. This would have potential implications on atmospheric stability and photochemistry on the local scale.

5.6.5 Sensitivity studies

In reported studies cited, single scattering albedoes were calculated from several techniques namely: from combining corrected absorption coefficients measured by aethalometer or PSAP (Particle/Soot Absorption Photometer) and scattering coefficients measured with the nephelometer; from sun-sky irradiance retrievals; from Lidar-sun photometers measurements; and from defining a best-fit ω_0 of particle size distributions measured by PCASP/FSSP which would account for flux changes measured by pyranometers. In this study, optical parameters were derived from particle size distributions measured by the PCASP and refractive indices determined from chemical apportionments of aerosols by single particle analyses. A Cimel sun/sky photometer stationed at Cape Town (18°E, 33°S) as part of the global AERONET program (*Holben et al.*, 2001) malfunctioned throughout CTBH II campaign (B. Holben, *per. comm.*). So there is limited information about optical properties of aerosol particles in this study area. Clearly, comparisons of optical properties have been made from locations with different emission factors and strengths, and meteorological influences - variability that might influence aerosol formation and evolution and hence optical properties of particles (*Dubovik et al.*, 2002). Despite such shortcomings, the value of ω_0 in this study is considerably lower compared with magnitudes of single scattering albedo in literature. There are several possible explanations to these differences.

Firstly, given fractional contributions of soot particles were overestimated, because volatile particles were lost or other particles were not fully accounted for in the SEM analyses, optical parameters were computed with 10% and 20% less soot on all samples. The mean scattering albedo increased only from 0.72 to 0.74 and 0.75, respectively, indicating that absorption coefficients were not significantly sensitive to overestimations within 20%, an acceptable experimental error margin in SEM analysis.

There are limitations in defining particle size with the PCASP due to effects of aerosol refractive indices as has been quantified in Section 5.6.2. Without this correction, light scattering coefficients derived from the PCASP size distributions are systematically lower than those measured by nephelometers (*Liu and Daum*, 2000). These corrections were not carried out here because size resolved relative abundances of particle groups are unknown.

When distributions of the 2D equivalent surface diameters of soot particles were compared with those of all particles on Samples #1 and #4 in Section 5.5, soot particles contributed to the largest particle sizes (Figure 5.13). Given similar trends on other samples,

it is likely that absorption components were overestimated by including absorbing particles with diameter less $d_p = 0.2$ μm into the Mie calculations.

The PCASP does not detect particles outside of the size range of $0.09 < d_p < 3.45$ μm. Depending on size distributions, significant amount of particle volume might have been excluded due to the PCASP size truncation (*Haywood et al.*, 2003b). Considering size distributions of samples with a prominent coarse mode in Figure 5.27 and 5.28, size truncation underestimates total volume of particles responsible for light extinction. To include all particles, optical parameters were determined from lognormal fits to the PCASP size distributions. Using lognormal distributions on Samples #1, #4 and #12 in Figure 5.28, σ_{ep} increased from 164 Mm^{-1}, 369 Mm^{-1} and 62 Mm^{-1} to 249 Mm^{-1}, 457 Mm^{-1} and 153 Mm^{-1} while ω_0 increases from 0.65, 0.87 and 0.72 to 0.68, 0.88 and 0.78, respectively. The significance of the coarse mode is also indicated by the increase in asymmetry parameter, g_0, from 0.62, 0.60 and 0.71 to 0.66, 0.62 and 0.77 on the same samples. Undetected particles outside the range likely containing mineral dust and sea-salt particles, contributed to an increase in extinction coefficients by factors between 1.5 and 2.5. Extinction coefficients and ω_0 might therefore be significantly underestimated due to size truncation by the PCASP. However, due to low concentrations of particles in the coarse mode, there are large uncertainties in the PCASP counts due to low sensitivity of the instrument at low concentrations (see Section 5.2.3.2). Coupling the PCASP number-size measurements with more sensitive particle sizing instruments at large diameters was needed to include the coarse mode aerosol mass.

There were no coupling measurements of particle chemical composition and independent aerosol optical properties. Such measurements were necessary to constrain SEM observations, e.g., in defining chemical composition and refractive index of particles not resolved (and hence identified only as 'others'). Optical parameters are sensitive to the refractive index assigned to aerosol species 'others', particularly on Flights 13, parts of Flight 14 and 16 when the specie contributed to over 50% of fractional number concentrations. The main absorbing particles were taken to be soot and mineral dust particles. If soot particles or iron oxides were incorporated into 'others', ω_0 and σ_{ap} might be lower than has been computed. Conversely, if 'others' contained more scattering aerosol, extinction coefficients and ω_0 calculated here might be underestimated.

The approach of determining complex refractive indices from SEM analysis is only applicable to dry aerosols because water and other volatiles are lost in the SEM vacuum. The PCASP sizes were measured at less than 40% relative humidity, and below the deliquescence relative humidity (DRH) of most particle groups identified. To represent ambient aerosols,

particularly hygroscopic sulphates, an attempt to correct for hygroscopic growth was made in Section 5.6.3.1 using relative humidity profiles from the Cape Town International Airport. On Flight 14, extinction coefficients increased by 79 to 94% on Samples #8 and Sample #10, and ω_0 increased from 0.80 and 0.86 to 0.88 and 0.92, respectively, while being negligible on the rest of the ABS samples. Considering all samples, the mean ω_0 on the same flight increased from 0.79 ± 0.10 to 0.82 ± 0.09, a small change compared to the deviation of ω_0. By assuming internally mixtures and incorporating soot aggregates into these hygroscopic particles, both σ_{sp} and σ_{ap} would increase, without necessarily increasing ω_0 (*Chýlek et al.*, 1988).

Despite uncertainties in PCASP size distributions and SEM analyses identified above, lower ω_0 observed here might also indicate the apparent differences in emission control regulations of vehicles and industry between Europe/USA and South Africa. Diesel vehicles were observed to be the largest contributor of particulate matter in the Cape Town Brown Haze Study 1 (*Wicking-Baird et al.*, 1997). Up to 41% of the emitted particulate matter in diesel engines is in the form of aggregated soot (*Kittelson*, 1998). It is therefore reasonable to conclude that soot particles contribute to a large light absorption component in Cape Town and aerosol single scattering albedo would be lower than observed in Europe/USA.

5.7 Conclusion

As part of the Cape Town Brown Haze II study, microphysical, chemical and optical properties and spatial distribution of aerosol particles were investigated over the metropolitan city. Airborne measurements were made during an intensive field campaign in August 2003. Spatial and temporal resolved particle samples were collected with an ABS sampler, while in-situ particle size distributions were measured with the PCASP over the size range of 0.1 to 3.5 μm. Filters samples collected over four flights were investigated with a high resolution SEM to characterise aerosol chemical compositions, mixing states and relative abundance. A total of 6704 particles were identified and categorised into seven particle groups of: aggregated soot particles, mineral dust, sulphate (SO_4^{2-}), sea-salt, tar balls/fly ash, rod-shaped particles (some were associated with soot agglomerates) and those that could not be attributed to any of these groups were labelled as 'others'.

Apportionments of chemical species were highly variable both spatially and temporally. As expected, high concentrations of soot particles were enhanced around localised

sources within the Cape Town area, like the central business district, CBD, and Khayelitsha, areas with large contributions of soot from mobile sources, industrial and domestic fuel burning. The aggregated soot particles occurred in fractional number concentrations of between $12\% - 46\%$. Soot particles were externally mixed and typical of freshly emitted particulate. On one flight (August 6, afternoon), combustion generated particles (soot aggregates, fly ash, tar balls) dominated aerosol number concentrations with fractional concentrations of between 65% and 80%.

Sulphate particles were found in fractional concentrations of $0 - 82\%$, and from trajectory analysis, high sulphate concentrations were associated with air masses that had recirculated over Cape Town. Sulphates might be due to photochemically processed pollutants from Cape Town. Production of sulphates is suppressed on most days due to prevailing dry conditions during intense haze episodes.

Under the conditions samples were collected, Cape Town was not subjected to aged or fresh marine air masses with high sea-salt particle loadings. Fractional number concentrations of sea-salt particles were $0 - 1.4\%$, and rather low for a coastal location. Other combustion generated particles observed were tar balls/fly ash with $0 - 63\%$, and rod-shaped particles with $0 - 12\%$ of the fractional number concentrations. The latter were sometimes associated with soot aggregates as well. Mineral dust particles occurred in small fractional number concentrations of up to 2%. The majority of dust particles were aluminosilicates sometimes with calcium carbonate, and iron oxides mixed with silicates of several oxides/hydroxides from Na to Zn on the periodic table.

Particle size distributions were complex with 3 to 4 multimodes as follows: $0.07 - 0.09$ μm in the Aitken mode; two peaks in the accumulation mode at $0.14 - 0.22$ μm and $0.5 - 0.90$ μm; and the coarse mode of $d_p > 2$ μm. In the lower free troposphere, particle size distributions were bimodal with the accumulation mode of $0.12 - 0.14$ μm and a coarse mode > 2 μm. The free troposphere modes were shifted to larger sizes, possibly by ageing as particles had stayed longer in the atmosphere.

Vertical distributions of aerosol were influenced strongly by the diurnal development of the boundary layer and atmospheric stability. Aerosol loading were also influenced by location of point sources, variability in source strength and air mass transport. In the mornings ($0500 - 0930$ UTC), high number concentrations of particles were confined to the lower 400 m. These high particles concentrations are due to the accumulation of overnight and morning domestic combustion emissions and vehicle emissions in morning rush hours. In the late mornings to afternoon the boundary layer was mixed with number concentra-

tions of up to 30 000 cm^{-3}. Background concentrations of below 100 cm^{-3} were observed in the lower free troposphere between 1400 and 2000 m. Particle number concentrations and total volumes were 1 to 3 orders of magnitude higher in the boundary layer than in the free troposphere. The decrease of aerosol concentrations with altitude suggest most of the particles had been emitted locally and at low elevations. There was no indication of vertical mixing into the free troposphere. Mixing was inhibited by the persistent temperature inversions capping the top of the boundary layer.

Complex refractive index of aerosols were computed from the abundance of the seven particle groups identified in the SEM analyses and combined with the PCASP size distributions to quantify optical properties of aerosols. From the in-situ number concentrations that were considered as pollution episodes, the ranges light extinction and absorption coefficients by particles were $\sigma_{ep} = 194 \pm 195$ Mm^{-1} and $\sigma_{ap} = 41 \pm 25$ Mm^{-1}, respectively. Large variations in the extensive parameters are due to the variability in the aerosol loadings and variations in chemical compositions of particles. While the extinction coefficients are higher than observed in European and US mega cities, the magnitudes are lower than recent figures from Asian cities (*Bergin et al.*, 2001; *Carrico et al.*, 2003; *Mallet et al.*, 2005).

For externally mixed aerosols, the single scattering albedo varied from 0.61 to 0.94, with a mean value of $\omega_0 = 0.72 \pm 0.08$. Compared to most literature figures where $\omega_0 > 0.80$ (*Bundke et al.*, 2002; *Eck et al.*, 2005; *Russell et al.*, 2002), magnitudes computed here are lower, largely due to high concentrations of absorbing soot particles observed in the SEM analyses. It is possible that contributions of soot particles were overestimated because soot aggregates were more stable under the electron beam. However, reducing soot contributions to within an experimental error margin of 20% only increased the mean ω_0 to 0.75 ± 0.09. Given that transportation, industries and domestic fuel burning are the largest contributors of particulate matter in Cape Town, the lower ω_0 and higher extinctions coefficients observed here indicate strong emissions of soot and other particles in the haze. Vehicles emissions, particularly diesel vehicles, were observed to contribute up to 60% of the PM2.5 apportionment in Cape Town (*Wicking-Baird et al.*, 1997). Up to 41% of the emitted particulate matter in diesel engines is in the form of highly absorbing soot particles (*Kittelson*, 1998). It is therefore reasonable to conclude that soot particles contribute to a large light absorption component in Cape Town and aerosol single scattering albedo are expected to be lower than observed in Europe/USA. The lower ω_0 also demonstrate apparent differences in emission control regulations between Europe/USA and South Africa. These two parameters σ_{ep} and ω_0 clearly demonstrate and explain quantitatively the visibility reduction due to particles in the Cape Town atmosphere, reduction observed as the brown

haze phenomenon.

Evidence presented in this thesis show that soot particles play a critical role in light extinction in the haze as evidenced by the low single scattering albedo determined from the Mie calculations. However, in environments polluted with combustion generated aerosols, both organic carbon and nitrate particles can play significant roles in light scattering and absorption as well (*Hegg et al.*, 1997; *Mayol-Bracero et al.*, 2002; *ten Brink et al.*, 1996). Such particles could not be distinguished from morphological structures in the SEM only, and hence the question remains open. As emission inventories of Cape Town listed significant emissions of organic carbon and nitrate precursors, future studies need to address more closely the role of these species in the Cape Town brown haze.

The visibility range L_v due to extinction of light by dry particles was between 10 and 125 km with a mean of 37 ± 32 km, while inside a particular industrial plume L_v reduced considerably to 5.1 km. Other derived optical parameters are: mean Ångstrom exponents $\alpha_{(450-550)} = 1.20 \pm 0.35$ and $\alpha_{(550-700)} = 1.26 \pm 0.36$ and; asymmetry parameter $g_0 = 0.59 \pm 0.06$. Both parameters are consistent with previous studies on urban aerosols, where particles in the submicrometer range dominate light extinction (*Hignett et al.*, 1999; *Horvath*, 1996; *Mallet et al.*, 2003).

Based on calculated optical properties, aerosols have a TOA radiative forcing ranging from -12 Wm^{-2} to $+10$ Wm^{-2} over land, and a more cooling effect of $\Delta F = -33$ Wm^{-2} to -10 Wm^{-2} over sea. Compared to modelled global radiative forcing by anthropogenic aerosols (*Charlson et al.*, 1992; *IPCC*, 2001), the forcing in Cape Town are several factors larger than the global mean, and therefore likely to have an impact on the local atmospheric stability and photochemistry. In addition to the obvious visibility reduction, particles have the potential to perturb the local climate.

In the second part of the objectives of this study, particle size distributions and number concentrations were compared between the PCASP and the SEM. Small particles were clearly under represented in the SEM possibly due to low deposition efficiencies of small particles because of diffusion losses. Small particles were under counted on substrates, because they had slipped through filter holes during sampling, or they were not detected in the SEM images due to limited resolution. Size distributions from the SEM are biased toward large diameters because of the resting positions of the particles, which will expose the largest surface area for imaging. Number concentrations of aerosol particles computed from microscopy methods were systematically lower by a factor of four compared to simultaneous measurements defined from conventional optical particle counters (in this case the PCASP,

Section 5.5). Such biases limit the use of microscopy techniques in describing aerosol number concentrations quantitatively, hence the need to couple the technique with other aerosol measurements. Finally, a theoretical approach for correcting particle size distributions measured by the OPC was applied to study effects of different refractive indices on particle size distributions. It was shown that the PCASP significantly underestimates the sizes of absorbing aerosols. Effects of refractive index on the PCASP size distributions need to be considered in urban environments and biomass burning plumes where high concentrations of highly absorbing particles are found.

Wicking-Baird et al. (1997) projected an increase in anthropogenic emissions in Cape Town. For a 'business as usual' scenario, PM2.5 emissions were estimated to increase by 48% between 1997 and 2007. Given the role of aerosol in visibility reduction and potential role in regional climate forcing, there is need for further research to reduce uncertainties in aerosol parameterisation. Uncertainties identified here were due to instrumental and analytical limitations in determining aerosol parameters, namely: size and number concentration determined from microscopy techniques; effects of refractive indices on PCASP sizes; and size truncation by the PCASP. For future studies, it will be worthwhile to use a combination of techniques in closure experiments in order to constrain aerosol parameters (e.g., including light scattering and absorption measuring techniques, making use of the available AERONET sun photometer). Closure studies have been successfully employed in larger scale aerosol investigations, e.g., LACE (*Ansmann et al.*, 2002), INDOEX (*Ramanathan et al.*, 2001a) and SAFARI 2000 (*Swap et al.*, 2003).

Emissions from transport, industrial and domestic combustion processes are major sources of the brown haze particulate matter. Using microphysical analyses on highly resolved aircraft measurements, this study has characterised quantitatively contributions of highly absorbing soot particles to visibility reduction and the observed brown haze phenomenon in Cape Town.

5.8 Recommendations

Limitations and challenges were also recognised, and the following recommendations should be considered for future research. Firstly, filter preparations for SEM analysis are critical to maximise image quality. In Section 4.2, filters were coated with gold to enhance image contrast and achieve high resolutions. However, in Section 5.2.3, substrate coating would have interfered with analytical investigations, and subsequently images were not of high

quality. One possibility to improve on ABS sampling would be to replace the polycarbonate ABS substrates with conductive or pre-coat filters.

The high-vacuum SEM used in this study is prone to significant loss of water adsorbed on particles (Chapter 3). Sulphate particles were also difficult to fully characterise in the high-vacuum because they were highly volatile and were damaged by the electron beam (Chapter 5). High resolution low-temperature SEM techniques might have solved some of these analytical uncertainties and need to be considered in future research.

There were no relative humidity measurements during flights. To calculate optical properties of ambient aerosols, knowledge of aerosol hygroscopic properties and ambient RH is crucial because relative humidity affects particle sizes and hence their optical properties. An attempt to correct for hygroscopic growth was made in Section 5.6.3.1 using relative humidity profiles from the Cape Town International Airport. These assumed RH profiles might not represent accurately ambient conditions over the entire domain, considering the complex meteorological zones of Cape Town (*Wicking-Baird et al.*, 1997). For this reason, ambient (wet) scattering coefficients and ω_0 are subjective on days with high sulphate loadings.

The ABS sampling technique combined with microscopy methods offers promising powerful capabilities to understanding high spatially and temporally variability of aerosol particles from aircraft measurements. To our knowledge, existing off-line particulate sampling devices with similar capabilities are used only for ground sampling, e.g., PIXE aerosol particle sampling device provides sampling intervals over 1 second to 99 hours[12]. Three concerns have to be addressed regarding the ABS-microscopy technique: (i) Some samples were excluded for analyses because of low aerosol particle loadings. For this reason, no ABS samples from clean background locations could be characterised for comparison with polluted locations. While maintaining isokinetic sampling, there is need to increase the volume sampled and/or reduce the surface area of the ABS deposition spot in order to increase aerosol loadings; (ii) ABS-microscopy results have to be validated with coupled optical and chemical measurements to constrain chemical information (hence refractive indices) of unresolved aerosol components, which were only defined as 'others' in this study; (iii) like any 'off-line' analytical method of particulate matter, the SEM technique is prone to analytical artefacts. A particularly challenging application for airborne measurements would be to couple aerosol chemical composition from the ABS-microscopy technique with 'on-line' time-resolved aircraft single particle analysis techniques like aerosol mass spectroscopy (*Trimborn et al.*, 2002).

[12]http://www.pixeintl.com/Streaker.asp

Chapter 6

Conclusions

High resolution field emission Scanning Electron Microscope (SEM) and an Atomic Force Microscope (AFM) were employed to investigate several properties of atmospheric aerosol particles and to compliment properties parameterised with conventional techniques. Aerosol particles were collected in three field campaigns - the LBA-EUSTACH (1999) and SMOCC (2002) campaigns in the Amazonia, the Cape Town Brown Haze II (2003) and a laboratory study of biomass combustion emissions carried out at the MPI, Mainz. Aerosol particle properties of interest were: particle size and size distribution (Chapter 3); fractal and dynamic properties of soot aggregates from wood combustion (Chapter 4); chemical composition, mixing state and optical properties of urban aerosol particles (Chapter 5). Major findings of this study, concluding discussions, limitations and outlooks are highlighted in subsequent sections.

6.1 Comparisons of particle size distributions

The first objective of this study was to compare particle size distributions as measured by microscopy techniques and conventional sizing instruments (cascade impactor and optical particle counter). In Chapter 3, particle sizes were measured on four stages of a MOUDI impactor with microscopes and verified against known kernel functions of impactor stages as defined by *Winklmayr et al.* (1990). Measurements were conducted on two samples collected in the Amazonia during the wet and dry seasons. In defining particle sizes from microscope projected images, particle sizes were found to depended on: definition of 'size' in the projected image, i.e., sizes defined from projected volume in 3D or surface area in 2D; and sampling conditions under which particles were collected.

Particle volume distributions derived from microscopy measurements did not adequately reproduce size distributions on expected individual impactor stages. Due to changes in relative humidity between sampling and microscope analysis times, significant losses of mass were observed on particles, particularly those particles that were collected in higher

humidity conditions. Large particles lost more volume of mass per dry particle, consistent with dependence of humidity growth on the size of dry particles. Losses could not be accounted for by taking into consideration humidity growth factors and particle density as had been measured on these particles elsewhere (*Guyon et al.*, 2003; *Rissler et al.*, 2005; *Roberts et al.*, 2002).

Findings suggest that there are inherent problems in defining particle sizes with different sizing techniques, despite accounting for humidity growth and particle density. The physical sizes are subject to the aerosol particle history after deposition. For collected particles, there are mass losses on individual particles, as opposed to particle losses to walls during sampling. These losses are high, suggesting losses of other adsorbed volatile compounds as well. Such losses bias observed mass distribution and hence number-size distributions derived from collected particles. Since this effect could not be generalised in this study, it would be worthwhile to conduct closure experiments to validate and quantify such effects in future studies. One such a procedure could be the measurement of aerosol properties with particle number counters in parallel with an impactor operating at varying humidity conditions. Plausible uncertainties need to be addressed since particle mass distributions and hence number-size distributions are widely derived in the aerosol community from collected and stored samples.

Adsorbed water on particles also affected morphologies of particles deposited on impactor substrates. While this effect might not be true for other sampling devices, particles in impactors experience high jet velocities which flatten and deform particles on deposition. Results are evident on 3D projection of particles in the AFM, rather than the 2D SEM projections. Ratios of lateral diameters to particle heights were between 3 and 13, ratios that indicate significant deformities for particles that had been collected as droplets with a ratio of approximately unity. Because of these deformations, diameters derived from 2D projected surfaces tend to overestimate particle sizes [while this is also true for particles that tend to orient on substrates like fibres and flat dust particles (*J.S Reid et al.*, 2003b)]. Certainly, morphological parameters (aspect ratio, circularity) determined from 2D projections of deformed particles do not represent geometrical properties of original particles.

Particle size distributions and number concentrations were also compared as characterised by SEM technique and an optical particle counter, the PCASP (Passive Cavity Aerosol Spectrometer Probe) in Chapter 5. Large differences were found in the comparisons. The SEM size distributions were biased toward large diameters because of the resting positions of particles, which exposed the largest surface area for imaging. Small particles were under-represented in the SEM possibly due to low deposition efficiencies of small par-

ticles because of diffusion losses. For particle number concentrations, SEM magnitudes were found to be systematically lower than those measured by the PCASP by a factor of 4.3 ± 0.3. The SEM number concentrations were underestimated despite the good correlation found when relative number concentrations were compared. Due to particle losses and deposition inhomogeneities on substrates, microscopy techniques can only be used for morphology characterisation and need to be coupled with conventional instruments to fully characterise aerosol particles.

In conclusion, the definition of particle 'size' in 2D microscopy images and hence morphological parameters (aspect ratio, circularity) depend largely on particle shapes, deposition postures in images as well as ambient sampling conditions. In Chapter 3, AFM and SEM size distributions were smaller than expected due to mass losses on individual particles after deposition on substrates. However, in Chapter 5, SEM particle sizes were larger than expected because particles had deposited flat on substrates. Factors contributing to discrepancies in size distributions derived by different sizing techniques were established and quantified from these comparisons. Such differences in microscopy size distributions make particle sizing from 2D projected images inconsistent, ambiguous and subjective. Microscopy measurements have to be coupled with other sizing techniques to constrain particle sizing uncertainties.

6.2 Morphological and dynamic properties of soot particles

Investigations on smoke particles were focused on understanding three properties of soot particles: formation mechanism (indirectly); morphology, i.e., geometry, fractal dimension, specific surface area; and dynamic properties. In order to generate predominately soot particles, dry wood sticks were combusted in a highly flaming and controlled combustion experiment with combustion efficiency $\Delta CO/\Delta CO_2 < 2\%$. Particles were selected for monodisperse size distributions using a differential mobility analyzer and investigated with the SEM. To characterise the geometry of aggregates, a procedure to describe diffusion limited cluster-cluster aggregates from projected SEM images was used (*Brasil et al.*, 1999). The procedure is widely accepted and has been validated on both laboratory and computer simulated aggregates by several researchers (*Brasil et al.*, 1999; *Forrest and Witten*, 1979; *Julien and Botet*, 1987; *Köylü et al.*, 1995b; *Rogak et al.*, 1993; *Samson et al.*, 1987; *Wentzel et al.*, 2003).

Combustion processes produce ultrafine soot particles from a complex growth

process involving nucleation, surface growth, and coagulation. The smoke particles were found to be principally soot aggregates, formed from irregular chains and branches of small primary spherical particles of nearly the same size. Size distribution of primary particles could be described by a Gaussian distribution of mean radius $a_p = 25.5 \pm 3.5$ nm and standard deviation $\sigma = 1.27 \pm 0.09$, a distribution consistent with soot particles generated from biomass combustion. About 5% of the aggregates contained large spheres, possibly tar balls of diameter up to 200 nm, embedded in soot aggregates during coagulation process in the cooling smoke.

Soot particles were described as being fractal. Aggregate fractal dimensions were derived from three techniques: 2D fractal dimension $D_{f,2} = 1.84 \pm 0.05$ from an asymptotic $D_{f,2}$, corrected for resolution in the projected surfaces of 205 aggregates; 3D fractal dimension $D_f = 1.83 \pm 0.05$ from aggregate mass and radius of gyration relationship; and $D_f = 1.80 \pm 0.13$ from the mobility and mass relationship in the DMA. In spite of limitations associated with each technique, there is good agreement between the three approaches used, with an average $D_f = 1.82$ consistent with aggregation theory.

The $D_{f,2}$ determined from particle projections was found to be a function of image resolution. Previous studies have shown that fractal dimensions of 3D particles determined from 2D projected surfaces were underestimated by $10 - 15\%$, and this correction was therefore applied to 2D $D_{f,2}$ to determine 3D D_f (*Rogak et al.*, 1993; *Samson et al.*, 1987). In this study, it was found that this underestimation was minor compared to uncertainty in determining fractal dimension from images obtained at coarse resolutions. By imaging several aggregates over a range of resolutions, the fractal dimension from 2D projection surfaces increased asymptotically with resolution, possibly approaching a value of 3D D_f. Without the capacity to increase resolution, the dependence of $D_{f,2}$ on resolution presents limitations to SEM analysis of larger aggregates since entire particles need to be imaged, as opposed to certain internal regions, because of lack of asymmetry.

Due to the fractal geometry, aggregates posses a large surface area compared to compact particles, and this geometry has to be taken into account in photochemical models and atmospheric observations on uptake of soot particles (*Ammann et al.*, 1998; *Smith et al.*, 1989). Surface area to mass ratio was found to be 70 ± 10 m^2g^{-1}, an increase of a factor of seven compared to that of compact spherical particles with the same mass and volume. This parameter can be used directly in modelling uptake on freshly formed soot particles from biomass combustion. As indicated before, the specific surface area represents the lower limit since primary particle surfaces were assumed to be smooth and non-fractal.

Dynamic shape factors of aggregates with mobility diameter between 200 and about 800 nm were determined to be $1.5 < \chi < 2.5$, and increasing with particle mass. The χ can be used directly in the Stokes drag law to account for particle shape in aerosol sampling devices where particle size is derived from particle motion. Dynamic properties of soot aggregates were compared with theoretical predictions of the drag on fractal particles in the continuum regime (*Wang and Sorensen*, 2001). An important dynamic parameter, β, which relates the mechanical mobility diameter d_{mob} to the radius of gyration R_g where $\beta = d_{mob}/2R_g$ was derived. The value itself is not without controversy (see comments on *Wiltzius*, 1987). However, following characterisation described by *Wang and Sorensen* (2001), the value of β was found to be 0.81 ± 0.07 and constant in the continuum regime, a kinetic regime parameterised by the Knudsen number $Kn = 2\lambda/d_{mob}$ where $0.2 < Kn < 0.7$ and λ is the mean free path in air = 66.5 nm. In future studies, it would be interesting to extend investigations to aggregates with Knudsen numbers larger than 0.7 (or $d_{mob} < 200$ nm, into the limit of $N \rightarrow 1$) in order to verify the behaviour of β, as has been interpolated in Figure 4.9.

In conclusion, fractal dimensions of soot aggregates from flaming wood combustion were determined using three independent methods. There is good agreement between the three methods used, and results are consistent with theoretical and experimental observations. Fractal dimension is a useful parameter for characterising soot particle morphology, their dynamic properties, the exposed surface area that takes part in heterogeneous reactions. Conditions needed to extract reliable fractal dimensions from SEM analysis were established. Image resolution is critical in characterising particle morphologies, particularly for particles like soot aggregates due to their fractal geometry. While effects of describing 3D particles from 2D projections have been observed to result in the underestimation of 3D fractal dimension of soot aggregates (*Rogak et al.*, 1993; *Samson et al.*, 1987), it was established in this study that choice of appropriate image resolution can constrain the uncertainties.

6.3 Characterisation of aerosol particles collected over Cape Town in winter haze episodes

An intensive airborne experiment was initiated in August 2003 to investigate brown haze episodes in Cape Town metropolitan area. As part of this experiment, the objectives of this study were to characterise aerosol particles in the brown haze by: describing chemical composition, size distribution, mixing states and morphology; identifying contributions of

different aerosol particle sources; describing aerosol spatial distribution; and quantifying optical properties and radiative effects of aerosol particles. Chemical composition, abundance and morphology of particles were determined from spatial and temporal resolved aerosol samples collected on-board the aircraft. Microscopy results were complemented with conventional techniques of measuring particle number-size distributions to quantify optical properties and radiative forcings of particles in the haze.

The ABS (Air Borne Streaker) aerosol sampling technique offered the possibility to characterise highly heterogeneous aerosols over a polluted urban environment with high spatial and temporal resolutions. Chemical compositions of aerosols also showed strong day-to-day variability. Considering aerosol sources are local, similar sources with diurnal patterns (transport, industrial and domestic emissions), these variations indicated that mixing in the boundary layer by horizontal advection was relatively poor.

Aggregated soot particles occurred in fractional number concentrations of between $11\% - 46\%$. The particles were externally mixed, suggesting either recent emissions or particles that had not been processed by aging. This is in agreement with several studies of urban environments where external mixed soot dominated light absorbing component of urban aerosols (*Hasegawa and Ohta*, 2002; *Jacobson*, 2001; *Mallet et al.*, 2004). Variations in soot fractional contributions were attributed to major diffuse source categories within the Cape Town area. As expected, locations with high traffic densities like the Central Business District, Goodwood and Pinelands and low socio-economic suburbs like Khayelitsha showed highest soot concentrations emitted largely from vehicles and domestic combustion processes.

Sulphate particles were found in fractional concentrations of $0 - 82\%$. From trajectory analysis, high sulphate concentrations were associated with air masses that had recirculated over Cape Town. The contributions were highest on one of the four days investigated, and for a polluted location like Cape Town with high SO_2 source strengths (*Wicking-Baird et al.*, 1997), meteorological factors might be influencing secondary production of sulphates. Correlations between sulphate/soot loadings and relative humidity need further investigations considering the strong contributions of combustion emissions to the haze formation in Cape Town.

Calm days associated with haze episodes in Cape Town are associated with low contributions of sea-salt and mineral dust aerosols. Fractional number concentrations of both fresh and aged sea-salt were $0 - 1.4\%$ and mineral dust particles were $0 - 2\%$. Majority of mineral dust particles were aluminosilicates, sometimes with calcium carbonate, and iron

oxides mixed with silicates of several oxides/hydroxides from Na to Zn on the periodic table.

Aerosol vertical distributions were controlled by the stability of the atmosphere. In the mornings, high number concentrations of particles were confined to the lower 400 m asl, and decreased sharply into the residual layer. By convection and turbulences, the boundary layer was mixed in the afternoon, although continuously decoupled from the free troposphere by temperature inversion at the top of the boundary layer. This decoupling suppressed vertical mixing such that particle number and total volume concentrations decreased by up to 3 orders of magnitude between the boundary layer and the free troposphere. These observations indicate that most particles were locally produced and at low elevations. Regional background air in the boundary layer has relatively clean air, as shown by control measurements over Cape Point, a location not influenced by the urban emissions.

Aerosol refractive indices were determined from particle chemical composition and abundance identified in SEM analyses. Together with simultaneous measurements of aerosol number concentrations measured by the PCASP, optical properties of particles - scattering and absorption coefficients (σ_{sp}, σ_{ap}), single scattering albedo (ω_0), Ångstrom exponents (α) were computed from the Mie scattering theory. Maximum number concentrations measured by the PCASP were treated as pollution episodes (excluding measurements made directly in visible industrial plumes). From maximum number concentrations, magnitudes of extinction and absorption coefficients ranged between 19 to 755 Mm^{-1} (mean of 194 ± 195 Mm^{-1}) and 7 to 103 Mm^{-1} (41 ± 25 Mm^{-1}), respectively. The visibility range L_v due to extinction of light by dry particles was between 10 and 125 km with a mean of 37 ± 32 km, while inside an industrial plume $L_v = 5.1$ km. Due to the lack of homogeneity in the haze, there is large variability in aerosol loadings and chemical composition between locations, hence the wide range of extensive optical parameters. The extinction coefficients are higher than observed in European and US mega cities, and lower than recent figures from Asian cities (*Bergin et al.*, 2001; *Carrico et al.*, 2003; *Mallet et al.*, 2005).

The single scattering albedo varied between 0.61 and 0.94, with a mean of $\omega_0 = 0.72 \pm 0.08$. The mean ω_0 is generally lower than observed in most urban influenced environments where $\omega_0 > 0.8$ (*Bundke et al.*, 2002; *Eck et al.*, 2005; *Russell et al.*, 2002). The low ω_0 is largely due to high concentrations of absorbing soot particles observed in the SEM analyses. High contributions of soot particles indicates apparent differences in emission control regulations between Europe/USA and South Africa, considering that vehicles, domestic and industrial emissions are the largest contributors of particulate matter in Cape Town.

Mean Ångstrom exponents were $\alpha_{(450-550)} = 1.20 \pm 0.35$ and $\alpha_{(550-700)} = 1.26 \pm 0.36$ and asymmetry parameter $g_0 = 0.59 \pm 0.06$. Both parameters are consistent with previous studies on urban environments dominated by the fine mode aerosol.

Dry particles have a direct top of the atmosphere radiative forcing ranging from -12 Wm^{-2} to $+10$ Wm^{-2} over land, and a more cooling effect of $\Delta F = -33$ Wm^{-2} to -10 Wm^{-2} over sea. The wide range in the forcings is due to strong variability in both aerosol loadings, aerosol chemical composition between locations, and differences in surface reflectance between land and sea. However, focusing on direct effects alone might not be adequately capturing the local radiative impacts of particles in the Cape Town brown haze. The haze is highly absorbing, and absorbing aerosols in dark hazes were observed to enhance scarcity of cumulus clouds in INDOEX experiment (*Ackerman et al.*, 2000; *Johnson et al.*, 2004). Although Cape Town and surrounding areas are rather small compared to mega cities, the relative location at the southern tip of Africa could provide opportunity for studies of influences of an urban pollution plume on clean background marine air. Further investigations, e.g., using satellite observations could be carried out to understand impacts of Cape Town urban plume, e.g., *Rosenfeld* (2000).

Detailed chemical composition, mixing states, size distributions, lateral and vertical distributions of particles in the Cape Town brown haze were established by analysing spatially resolved aerosol samples. It was found that soot particles are an important component of the aerosol in the haze and contribute to a large absorbing component. Refractive indices of particles, one of the least understood properties of aerosol particles, were determined for dry aerosol particles in the haze. By combining single particle analysis with in-situ measurements, optical properties of aerosols in a complex urban environment were quantified from the Mie scattering theory. While the technique of determining refractive indices of aerosols from SEM analysis is not unique (*Ebert et al.*, 2002a, 2004), complementing the technique with conventional techniques is an approach applied for the first time in this study. The optical parameters demonstrated the role of soot particles in visibility reduction and also as a factor in planetary radiative forcing.

In conclusion, this study combined microscopy and conventional techniques to better characterise aerosol particles and derive fundamental parameters that are usually not directly measured or readily available. Improvements were made in experimental and analytical techniques, and in combining theoretical and interpretive techniques. The critical role of microscopy methods in retrieving properties of aerosol particles required as inputs into numerical models is thus further enhanced.

Bibliography

Ackerman, A. S., O. B. Toon, D. E. Stevens, A. J. Heymsfield, V. Ramanathan and E. J. Welton (2000), Reduction of tropical cloudiness by soot, *Science*, *288*, 1042–1047.

Ackerman, T. P. and O. B. Toon (1981), Absorption of visible radiation in the atmosphere containing mixtures of absorbing and nonabsorbing particles, *Appl. Opt.*, *20*, 3661–3667.

Adams, P. J., J. H. Seinfeld, D. Koch, L. Mickley and D. Jacob (2001), General circulation model assessment of direct radiative forcing by the sulfate-nitrate-ammonium-water inorganic aerosol system, *J. Geophys. Res.*, *106*, 1 097–1 111.

Ammann, M., M. Kalberer, D. T. Jost, L. Tobler, E. Rössler, D. Piguet, H. W. Gäggeler and U. Baltensperger (1998), Heterogeneous production of nitrous acid on soot in polluted airmasses, *Nature*, *395*, 157–160.

Andreae, M. O. and P. J. Crutzen (1997), Atmospheric aerosols: Biogeochemical sources and role in atmospheric chemistry, *Science*, *276*, 1052–1058.

Andreae, M. O. and P. Merlet (2001), Emission of trace gases and aerosols from biomass burning, *Global Biochem. Cycles*, *15*, 955–966.

Andreae, M. O., B. E. Anderson, D. R. Blake, J. D. Bradshaw, J. E. Collins, G. L. Gregory, G. W. Sachse and M. C. Shipham (1994), Influence of plumes from biomass burning on the atmospheric chemistry over the equatorial and tropical South Atlantic during CITE 3, *J. Geophys. Res.*, *99*, 12 793–12 808.

Andreae, M. O., P. Artaxo, C. Brandao, F. E. Carswell, P. Ciccioli, A. L. d. Costa, A. D. Culf, J. L. Esteves, J. H. C. Gash, J. Grace, P. Kabat, J. Lelieveld, Y. Malhi, A. O. Manzi, F. X. Meixner, A. D. Nobre, C. Nobre, M. d. L. P. Ruivo, M. A. Silva-Dias, R. V. P. Stefani, J. v. Jouanne and M. J. Waterloo (2002), Biogeochemical cycling of carbon, water, energy, trace gases, and aerosols in Amazonia: The LBA-EUSTACH experiments, *J. Geophys. Res.*, *107*, 8066, doi: 10.1029/2001JD000524.

Andreae, M. O., D. Rosenfeld, P. Artaxo, A. A. Costa, G. P. Frank, K. M. Longo and M. A. F. Silva-Dias (2004), Smoking rain clouds over the Amazon, *Science*, *303*, 1337–1342.

Annegarn, H. J., M. Flanz, T. Kenntner, M. A. Kneen, G. Helas and S. J. Piketh (1996), Airborne streaker sampling for PIXE analysis, *Nucl. Instr. and Meth. B*, *109/110*, 548–550.

Ansmann, A., U. Wandinger, A. Wiedensohler and U. Leiterer (2002), Lindenberg Aerosol Characterisation Experiment 1998 (LACE 98) Overview, *J. Geophys. Res.*, *107*, doi:1029/2000JD000233.

Artaxo, P., J. V. Martins, M. A. Yamasoe, A. S. Procópio, T. M. Pauliquevis, M. O. Andreae, P. Guyon, L. V. Gatti and A. M. C. Leal (2002), Physical and chemical properties of aerosols in the wet and dry seasons in Rondônia, Amazonia, *J. Geophys. Res.*, *107*, 8081, doi: 10.1029/2001JD000666.

Ballard-Tremeer, G. (1997), Emissions of Rural Wood-Burning Cooking Devices, PhD Thesis, University of the Witwatersrand.

Baltensperger, U., E. Weingartner, H. Burtscher and J. Keskinen (2001), Dynamic Mass and Surface Area Measurements, in *Aerosol Measurements: Principles, Techniques, and Applications*, edited by P. A. Baron and K. Willeke, 2nd ed., pp. 387–418, Wiley-InterScience, New York.

Baron, P. A. and K. Willeke (Eds.) (2001a), *Aerosol Measurement: Principles, Techniques, and Applications*, 2nd ed., 1160 pp., Wiley-InterScience, New York.

Baron, P. A. and K. Willeke (2001b), Aerosol Fundamentals, in *Aerosol Measurement: Principles, Techniques, and Applications*, edited by P. A. Baron and K. Willeke, 2nd ed., pp. 45–60, Wiley-InterScience, New York.

Baron, P. A. and K. Willeke (2001c), Gas and Particle Motion, in *Aerosol Measurement: Principles, Techniques, and Applications*, edited by P. A. Baron and K. Willeke, 2nd ed., pp. 61–82, Wiley-InterScience, New York.

Baron, P. A., C. M. Sorensen and J. E. Brockmann (2001), Nonspherical Particle Measurements: Shape Factors, Fractals, and Fibres, in *Aerosol Measurement: Principles, Techniques, and Applications*, edited by P. A. Baron and K. Willeke, 2nd ed., pp. 705–749, Wiley-InterScience, New York.

Baumbach, G. (1996), *Air quality control*, 490 pp., Springer-Verlag, Berlin, Heidelberg.

Baumgardner, D., G. B. Raga, G. Kok, J. Ogren, I. Rosas, A. Báez and T. Novakov (2000), On the evolution of aerosol properties at a mountain site above Mexico City, *J. Geophys. Res.*, *105*, 22 243–22 253.

Bekki, S., C. David, K. Law, D. M. Smith, D. Coelho, J.-F. Thovert and P. M. Adler (2000), Uptake on fractal particles 2. Applications, *J. Geophys. Res.*, *105*, 3917–3928.

Bell, M. L. and D. L. Davis (2001), Reassessment of the Lethal London Fog of 1952: Novel indicators of acute and chronic consequences of acute exposure to air pollution, *Environ. Health Perspect.*, *109*(Supp. 3), 389–394.

Bergin, M. H., G. R. Cass, J. Xu, C. Fang, L. M. Zeng, T. Yu, L. G. Salmon, C. S. Kiang, X. Y. Tang, Y. H. Zhang and W. L. Chameides (2001), Aerosol radiative, physical, and chemical properties in Beijing during June 1999, *J. Geophys. Res.*, *106*, 17 969–17 980.

Bérubé, D. and M. Jébrak (1999), High precision boundary fractal analysis for shape characterization, *Comput. Geosci.*, *25*, 1059–1071.

Binnig, G., C. F. Quate and C. Gerber (1986), Atomic force microscope, *Phys. Rev. Lett.*, *56*, 930–933.

Birmili, W., F. Stratmann and A. Wiedensohler (1999), Technical Note: Design of a DMA-based size spectrometer for large particle size range and stable operation, *J. Aerosol Sci.*, *30*, 549–553.

Bohren, C. F. and D. R. Huffman (1983), *Absorption and Scattering of Light by Small Particles*, 530 pp., Wiley-InterScience, New York.

Boucher, O., S. E. Schwartz, T. P. Ackerman, T. L. Anderson, B. Bergstrom, B. Bonnel, P. Chýlek, A. Dahlback, Y. Fouquart, Q. Fu, R. N. Halthore, J. M. Haywood, T. Iversen, S. Kato, S.Kinne, A. Kirkevag, K. R. Knapp, A. Lacis, I. Laszlo, M. I. Mishchenko, S. Nemesure, V. Ramaswamy, D. L. Roberts, P. Russell, M. E. Schlesinger, G. L. Stephens, R. Wagener, M. Wang, J. Wong and F. Yang (1998), Intercomparison of models representing direct shortwave radiation forcing by sulfate aerosols, *J. Geophys. Res.*, *103*, 16 979–16 998.

Boy, M. and M. Kulmala (2001), Nucleation events in the continental boundary layer: Influence of physical and meteorological parameters, *Atmos. Chem. Phys. Discuss.*, *1*, 239–276.

Brasil, A. M., T. L. Farias and M. G. Carvalho (1999), A recipe for image characterization of fractal-like aggregates, *J. Aerosol Sci.*, *30*, 1379–1389.

Bundke, U., G. Hänel, H. Horvath, W. Kaller, S. Seidl, H. Wex, A. Wiedensohler, M. Wiegner and V. Freudenthaler (2002), Aerosol optical properties during the Lindenberg Aerosol Characterization Experiment (LACE 98), *J. Geophys. Res.*, *107*, 8123, doi:10.1029/2000JD000188.

Burtscher, H., S. Künzel and C. Hüglin (1995), Structure of particles in combustion engine exhaust, *J. Aerosol Sci.*, *26*, 129–130.

Buseck, P. R. and M. Pósfai (1999), Airborne minerals and related aerosol particles: Effects on climate and the environment, *Proc. Natl. Acad. Sci. USA*, *96*, 3372–3379.

Cachier, H. (1998), Carbonaceous Combustion Aerosols, in *Atmospheric Particles*, edited by R. M. Harrison and R. E. van Grieken, pp. 295–348, Wiley-InterScience, New York.

Cai, J., N. Lu and C. M. Sorensen (1993), Comparison of size and morphology of soot aggregates as determined by light scattering and electron microscope analysis, *Langmuir*, *9*, 2861–2867.

Cai, J., N. Lu and C. M. Sorensen (1995), Analysis of fractal cluster morphology parameters: Structural coefficient and density autocorrelation function cutoff, *J. Colloid Interface Sci.*, *171*, 470–473.

Carrico, C. M., M. H. Bergin and J. Xu (2003), Urban aerosol radiative properties: Measurements during the 1999 Atlanta Supersite Experiment, *J. Geophys. Res.*, *108*, D8422, doi: 10.1029/2001JD001222.

Charlson, R. J., S. E. Schwartz, J. M. Hales, R. D. Cess, J. J. A. Coakley, J. E. Hansen and D. J. Hofmann (1992), Climate forcing by anthropogenic aerosols, *Science*, *255*, 423–430.

Chen, Y., S. M. Kreidenweis, L. M. McInnes, D. C. Rogers and P. J. DeMott (1998), Single particles analyses of ice nucleating aerosols in the upper troposphere and lower stratosphere, *Geophys. Res. Lett.*, *25*, 1391–1394.

Chen, Z.-Y., P. Meakin and J. M. Deutch (1987), Comments on "Hydrodynamic behavoir of fractal aggregates", *Phys. Rev. Lett.*, *59*, 2121.

Chiloane, K. E. (2005), Volatile Organic Compounds (VOCs) Analysis from Cape Town Brown Haze II Study, Msc thesis, University of the Witwatersrand.

Chýlek, P., V. Srivastava, R. G. Pinnick and R. T. Wang (1988), Scattering of electromagnetic waves by composite spherical particles: experiment and effective medium approximations, *Appl. Opt.*, *27*, 2396–2404.

Coetti, A. (1984), Light scattering by non-spherical particles: a laboratory study, *Aerosol Sci. Technol.*, *3*, 39–52.

Colbeck, I., B. Atkinson and Y. Johar (1997), The morphology and optical properties of soot produced by different fuels, *J. Aerosol Sci.*, *28*, 715–723.

Crutzen, P. J. and M. O. Andreae (1990), Biomass burning in the tropics: Impact on atmospheric chemistry and biogeochemical cycles, *Science*, *250*, 1669–1678.

d'Almeida, G., P. Koepke and E. Shettle (1991), *Atmospheric Aerosols. Global Climatology and Radiative Characteristics*, 561 pp., A. Deepak, Hampton.

de Reus, M., P. Formenti, J. Ström, R. Krejci, D. Müller, M. O. Andreae and J. Lelieveld (2002), Airborne observations of dry particle absorption and scattering properties over the northern Indian Ocean, *J. Geophys. Res.*, *107*, 8002, doi:10.1029/2002JD002304.

DeCarlo, P. F., J. G. Slowik, D. R. Worsnop, P. Davidovits and J. L. Jimenez (2004), Particle morphology and density characterization by combined mobility and aerodynamic diameter measurements. Part 1: Theory, *Aerosol Sci. Technol.*, *38*, doi:10.1080/027868290903907, 1138–1205.

Dentener, F. J., G. R. Carmichael, Y. Zhang, J. Lelieveld and P. J. Crutzen (1996), Role of mineral aerosol as a reactive surface in the global atmosphere, *J. Geophys. Res.*, *101*, 22 869–22 889.

di Stasio, S. (2001), Electron microscopy evidence of aggregation under three different size scales for soot nanoparticles in flame, *Carbon*, *39*, 109–118.

Dong, Y., M. D. Hays, N. D. Smith and J. S. Kinsey (2004), Inverting cascade impactor data for size-resolved characterization of fine particulate source emissions, *J. Aerosol Sci.*, *35*, 1497–1512.

Dongmo, S., M. Troyon, P. Vautrot, E. Delain and N. Bonnet (1996), Blind restoration method of scanning tunneling and atomic force microscopy images, *J. Vac. Sci. Technol. B*, *14*, 1552–1556.

Dubovik, O., B. Holben, M. A. Yamasoe, A. Smirnov, D. Tanré and I. Slutsker (1998), Single-scattering albedo of smoke retrieved from the sky radiance and solar transmittance measured from ground, *J. Geophys. Res.*, *103*, 31 903–31 923.

Dubovik, O., B. Holben, T. F. Eck, A. Smirnov, Y. J. Kaufman, M. D. King, D. Tanré and I. Slutsker (2002), Variability of absorption and optical properties of key aerosol types observed in worldwide locations, *J. Atmos. Sci.*, *59*, 590–608.

Dzubay, T. G. and H. Hasan (1990), Fitting multimodal lognormal size distributions to cascade impactor data, *Aerosol Sci. Technol.*, *13*, 144–150.

Dzubay, T. G., R. K. Stevens, C. W. Lewis, D. H. Hern, W. J. Courtney, J. W. Tesch and M. A. Mason (1982), Visibility and aerosol composition in Houston, Texas, *Environ. Sci Technol.*, *16*, 514–525.

Ebert, M., M. Inerle-Hof and S. Weinbruch (2002a), Environmental scanning electron microscopy as a new technique to determine the hygroscopic behaviour of individual aerosol particles, *Atmos. Environ.*, *36*, 5909–5919.

Ebert, M., S. Weinbruch, A. Rausch, G. Gorzawski, P. Hoffmann, H. Wex and G. Helas (2002b), Complex refractive index of aerosols during LACE 98 as derived from the analysis of individual particles, *J. Geophys. Res.*, *107*, 8121, doi:10.1029/2000JD000195.

Ebert, M., S. Weinbruch, P. Hoffmann and H. M. Ortner (2004), The chemical composition and complex refractive index of rural and urban influenced aerosols determined by individual particle analysis, *Atmos. Environ.*, *38*, 6531–6545.

Eck, T. F., B. N. Holben, O. Dubovik, A. Smirnov, P. Goloub, H. B. Chen, B. Chatenet, L. Gomes, X.-Y. Zhang, S.-C. Tsay, Q. Ji, D. Giles and I. Slutsker (2005), Columnar aerosol optical properties at AERONET sites in central eastern Asia and aerosol transport to the tropical mid-Pacific, *J. Geophys. Res.*, *110*, D06202, doi:10.1029/2004JD005274.

Edwards, J. B. (1974), *Combustion: Formation and Emission of Trace Species*, 229 pp., Technomic, Lancaster.

Falkovich, A. H., G. Schkolnik, E. Ganor and Y. Rudich (2004), Adsorption of organic compounds pertinent to urban environments onto mineral dust particles, *J. Geophys. Res.*, *109*, doi:10.1029/2003JD003919.

Finlayson-Pitts, B. J. and J. N. J. Pitts (2000), *Chemistry of the Upper and Lower Atmosphere; Theory, Experiments, and Applications*, 969 pp., Academic Press, San Diego.

Flagan, R. C. (2001), Electrical Techniques, in *Aerosol Measurement: Principles, Techniques, and Applications*, edited by P. A. Baron and K. Willeke, 2nd ed., pp. 537–568, Wiley-InterScience, New York.

Fletcher, R. A., J. A. Small and J. H. J. Scott (2001), Analysis of Individual Collected Particles, in *Aerosol Measurement, Principles, Techniques, and Applications*, edited by P. A. Baron and W. Willeke, 2nd ed., pp. 295–363, Wiley-InterScience, New York.

Formenti, P., O. Boucher, T. Reiner, D. Sprung, M. O. Andreae, M. Wendisch, H. Wex, D. Kindred, M. Tzortziou, A. Vasaras and C. Zerefos (2002a), STAAARTE-MED 1998 summer airborne measurements over the Aegean Sea 2. Aerosol scattering and absorption, and radiative calculations, *J. Geophys. Res.*, *107*, 4451, doi:10.1029/2001JD001536.

Formenti, P., H. Winkler, P. Fourie, S. Piketh, B. Makgopa, G. Helas and M. O. Andreae (2002b), Aerosol optical depth over a remote semi-arid region of South Africa from spectral measurements of the daytime solar extinction and the nighttime stellar extinction, *Atmos. Res.*, *62*, 11–32.

Forrest, S. R. and T. A. Witten (1979), Long range correlations in smoke-particle aggregates, *J. Phys. A: Mat. Gen.*, *12*, 109–117.

Freiman, M. T., M. R. Jury and S. Medcalf (2002), The state of the atmosphere over South Africa during the Southern African Regional Initiative (SAFARI 2000), *S.Afri. J. Sci.*, *98*, 91–96.

Friedbacher, G., M. Grasserbauer, Y. Mesimani, N. Klaus and M. J. Higatsberger (1995), Investigation of environmental aerosol by atomic force microscope, *Anal. Chem.*, *67*, 1749–1754.

Garratt, J. R. (1992), *The Atmospheric Boundary Layer*, 316 pp., Cambridge University Press, New York.

Garrette, T. J., P. V. Hobbs and L. F. Radke (2002), High Aitken nucleus concentrations above cloud tops in the Arctic, *J. Atmos. Sci.*, *59*, 779–783.

Garstang, M., P. D. Tyson, R. Swap, M. Edwards, P. Kallberg and J. A. Lindesay (1996), Horizontal and vertical transport of air over southern Africa, *J. Geophys. Res.*, *101*, 23721–23736.

Gebhart, J. (2001), Optical Detect-Reading Techniques: Light Intensity Systems, in *Aerosol Measurements: Principle, Techniques and Applications*, edited by P. A. Baron and K. Willeke, 2nd ed., pp. 419–454, Wiley-InterScience, New York.

Goldstein, J. I., D. E. Newbury, P. E. Echlin, D. C. Joy, A. D. Romig, C. E. Lyman, C. Fiori and E. Lifshin (1992), *Scanning Electron Microscopy and X-ray Microanalysis, A Text for Biologists, Material Scientists, and Geologist*, 820 pp., Plenum Press, New York and London.

Guyon, P. (2002), Chemical and Physical Properties of the Amazonian Aerosol Particles, PhD Thesis, Johannes Gutenberg University, Mainz.

Guyon, P., B. Graham, G. C. Roberts, O. L. Mayol-Bracero, W. Maenhaut, P. Artaxo and M. O. Andreae (2003), In-canopy gradients, composition, sources, and optical properties of aerosol over the Amazon forest, *J. Geophys. Res.*, *108*, 4591, doi:10.1029/2003JD003465.

Gwaze, P., O. Schmid, H. J. Annegarn, M. O. Andreae, J. Huth and G. Helas (2005), Comparison of three methods of fractal analysis applied to soot aggregates from wood combustion, *J. Aerosol Sci.*, doi:10.1016/j.jaerosci.2005.06.007.

Gwaze, P., H. J. Annegarn, J. Huth and G. Helas (submitted, a), Comparison of particle sizes determined with impactor, DMPS-APS, AFM, and SEM, *Atmos. Res.*

Gwaze, P., G. Helas, H. J. Annegarn, J. Huth and S. J. Piketh (submitted, b), Physical, chemical, and optical properties of aerosol particles collected over Cape Town during winter haze episodes, *S.Afri. J. Sci.*

Hara, K., S. Yamagata, T. Yamanouchi, K. Sato, A. Herber, Y. Iwasaka, M. Nagatani and H. Nakata (2003), Mixing states of individual aerosol particles in spring Arctic troposphere during ASTAR 2000 campaign, *J. Geophys. Res.*, *108*, doi:10.1029/2002JD002513.

Hara, K., K. Osada, M. Kido, M. Hayashi, K. Matsunaga, Y. Iwasaka, T. Yamanouchi, G. Hashida and T. Fukatsu (2004), Chemistry of sea-salt particles and inorganic halogen species in Antarctic regions: Compositional differences between coastal and inland stations, *J. Geophys. Res.*, *109*, doi:10.1029/2004JD004713.

Hasegawa, S. and S. Ohta (2002), Some measurements of the mixing state of soot-containing particles at urban and non-urban sites, *Atmos. Environ.*, *36*, 3899–3908.

Haywood, J., P. Francis, O. Dubovik, M. Glew and B. Holben (2003a), Comparison of aerosol size distributions, radiative properties, and optical depths determined by aircraft observations and Sun photometers during SAFARI 2000, *J. Geophys. Res.*, *108*, doi:10.1029/2002JD002250.

Haywood, J. M. and O. Boucher (2000), Estimates of the direct and indirect radiative forcing due to troposphere aerosols: A review, *Rev. Geophys.*, *38*, 513–543.

Haywood, J. M. and K. P. Shine (1995), The effect of anthropogenic sulfate and soot aerosol on the clear sky planetary radiation budget, *Geophys. Res. Lett.*, *22*, 603–606.

Haywood, J. M., S. R. Osborne, P. N. Francis, A. Keil, P. Formenti, M. O. Andreae and P. H. Kaye (2003b), The mean physical and optical properties of regional haze dominated by biomass burning aerosol measured from the C-130 aircraft during SAFARI 2000, *J. Geophys. Res.*, *108*, doi:10.1029/2002JD002226.

Hegg, D. A., J. Livingston, P. V. Hobbs, T. Novakov and P. Russell (1997), Chemical apportionment of aerosol column optical depth off the mid-Atlantic coast of the Unites States, *J. Geophys. Res.*, *102*, 25 293–25 303.

Hignett, P., J. P. Taylor, P. N. Francis and M. D. Glew (1999), Comparison of observed and modeled direct aerosol forcing during TARFOX, *J. Geophys. Res.*, *104*, 2279–2287.

Hinds, W. C. (1999), *Aerosol Technology: Properties, Behaviour and Measurements of Airborne Particles*, 2nd ed., 483 pp., Wiley-InterScience, New York.

Hobbs, P. V. and L. F. Radke (1969), Cloud condensation nuclei from a simulated forest fire, *Science*, *163*, 279–280.

Holben, B. N., D. Tanre, A. Smirnov, T. F. Eck, I. Slutsker, N. Abuhassan, W. W. Newcomb, J. S. Schafer, B. Chatenet, F. Lavenu, Y. J. Kaufman, J. V. Castle, A. Setzer, B. Markham, D. Clark, R. Frouin, R. Halthore, A. Karneli, N. T. ONeill, Pietras, R. T. Pinker, K. Voss and G. Zibordi (2001), An emerging ground-based aerosol climatology: Aerosol optical depth from AERONET, *J. Geophys. Res.*, *106*, 12 067–12 097.

Horvath, H. (1993), Atmospheric Light absorption - a review, *Atmos. Environ.*, *27A*, 293–317.

Horvath, H. (1996), Spectral extinction coefficients of rural aerosol in southern Italy - case study of cause and effect of variability of atmospheric aerosol, *J. Aerosol Sci.*, *3*, 437–453.

Horvath, H. (1998), Influence of Atmospheric Aerosols upon the Global Radiation Balance, in *Atmospheric Particles*, vol. 5, edited by R. M. Harrison and R. E. van Grieken, pp. 543–596, Wiley-InterScience, New York.

Huang, P.-F. and B. Turpin (1996), Reduction of sampling and analytical errors for electron microscopic analysis of atmospheric aerosols, *Atmos. Environ.*, *30*, 4137–4148,.

Ikegami, M., K. Okada, Y. Zaizen, Y. Tsutsumi, Y. Makino, J. B. Jensen and J. L. Gras (2004), The composition of aerosol particles in the middle troposphere over the western Pacific Ocean: aircraft observations from Australia to Japan, January 1994, *Atmos. Environ.*, *38*, 5945–5956.

IPCC (2001), in *Climate Change 2001: The Scientific Basis. Contribution of Working Group I to the Third Assessment Report of the Intergovernmental Panel on Climate Change*, edited by J. T. Houghton, Y. Ding, D. J. Griggs, M. Noguer, P. J. van der Linden, X. Dai, K. Maskell, and C. A. Johnson, p. 881, Cambridge University Press, Cambridge, United Kingdom and New York, NY, USA.

Jacobson, M. Z. (2001), Strong radiative heating due to the mixing state of black carbon in atmospheric aerosols, *Nature*, *409*, 695–697.

Jennings, S. G. (1998), Wet processes affecting atmospheric aerosols, in *Atmospheric Particles*, *IUPAC Series on Analytical and Physical Chemistry of the Environmental Systems*, vol. 5, edited by R. M. Harrison and R. E. van Grieken, pp. 475–507, Wiley-InterScience, New York.

Johnson, B. T., K. P. Shine and P. M. Forster (2004), The semi-direct aerosol effect: Impact of absorbing aerosols on marine stratocumulus, *Q. J. Roy. Meteor. Soc.*, *130*, 1407–1422.

Julien, R. and R. Botet (1987), *Aggregation and Fractal Aggregates*, 120 pp., World Scientific Publishing, Singapore.

Jury, M., A. Tegen, E. Ngeleza and M. Dutoit (1990), Winter air pollution episodes over Cape Town, *Boundary-Layer Meteorology*, *53*, 1–20.

Kandlikar, M. and G. Ramachandran (1999), Inversion methods for analysing aerosol spectrometer measurements: A critical review, *J. Aerosol Sci.*, *30*, 413–437.

Kasper, G. (1982), Dynamics and measurement of smokes. II The aerodynamic diameter of chain aggregates in the transition regime, *Aerosol Sci. Technol.*, *1*, 201–215.

Katrinak, K. A., P. Rez, P. R. Perkes and P. R. Buseck (1993), Fractal geometry of carbonaceous aggregates from an urban aerosol, *Environ. Sci Technol.*, *27*, 539–547.

Kinney, P. D., D. Y. H. Pui, G. W. Mulholland and N. P. Bryner (1991), Use of the electrostatic classification method to size 0.1 μm SRM particles - A feasibility study, *J. Res. Natl. Inst. Stand. Technol.*, *96*, 147–176.

Kittelson, D., J. Johnson, W. Watts, Q. Wei, M. Drayton, D. Paulsen and N. Bukowiecki (2000), Diesel aerosol sampling in the atmosphere, SAE Technical Paper Series, Warrendale PA.

Kittelson, D. B. (1998), Engine and nanoparticles: A review, *J. Aerosol Sci.*, *29*, 575–588.

Knutson, E. O. and K. T. Whitby (1975), Aerosol classification by electric mobility: Apparatus, theory, and applications, *J. Aerosol Sci.*, *6*, 443–451.

Kojima, T., P. R. Buseck, J. C. Wilson, J. M. Reeves and M. J. Mahoney (2004), Aerosol particles from tropical convective systems: Cloud tops and cirrus anvils, *J. Geophys. Res.*, *109*, D12201, doi:10.1029/2003JD004504.

Köllensperger, G., G. Friedbacher, R. Kotzick, R. Niessner and M. Grasserbauer (1999), In-situ atomic force microscopy investigation of aerosols exposed to different humidities, *Fresenius J. Anal. Chem.*, *364*, 296–304.

Köylü, U. O., G. M. Faeth, T. L. Farias and M. G. Carvalho (1995a), Fractal and projected structure properties of soot aggregates, *Combust. Flame*, *100*, 621–633.

Köylü, U. O., Y. Xing and D. E. Rosner (1995b), Fractal morphology analysis of combustion-generated aggregates using angular light scattering and electron microscope images, *Langmuir*, *11*, 4848–4854.

Krestinin, A. V. (2000), Detailed modeling of soot formation in hydrocarbon pyrolysis, *Combust. Flame*, *121*, 513–524.

Kulmala, M., H. Vehkamäki, T. Petäjä, M. D. Maso, A. Lauri, V.-M. Kerminen, W. Birmili and P. H. McMurry (2004), Formation and growth rates of ultrafine atmospheric particles: a review of observations, *J. Aerosol Sci.*, *35*, 143–176, doi:10.1016/j.jaerosci.2003.10.003.

Laskin, A. and J. P. Cowin (2001), Automated single-particle SEM/EDX Analysis of submicrometer particles down to 0.1 m, *Anal. Chem.*, *73*, 1023–1029.

Li, J., J. R. Anderson and P. R. Buseck (2003a), TEM study of aerosol particles from clean and polluted marine boundary layers over the North Atlantic, *J. Geophys. Res.*, *108*, 8484, doi: 10.1029/2002JD002106.

Li, J., M. Pósfai, P. V. Hobbs and P. R. Buseck (2003b), Individual aerosol particles from biomass burning in southern Africa: 2. Composition and aging of inorganic particles, *J. Geophys. Res.*, *108*, 8484, doi:10.1029/2002JD002310.

Lippmann, M., M. Frampton, J. Schwartz, D. Dockery, R. Schlesinger, P. Koutrakis, J. Froines, A. Nel, J. Finkelstein, J. Godleski, J. Kaufman, J. Koenig, T. Larson, D. Luchtel, L.-J. S. Liu, G. Oberdörster, A. Peters, J. Sarnat, C. Sioutas, H. Suh, J. Sullivan, M. Utell, E. Wichmann and J. Zelikoff (2003), The U.S. Environmental Protection Agency Particulate Matter Health Effects Research Centers Program: A Midcourse Report of Status, Progress, and Plans, *Environ. Health Perspect.*, *111*, 1074–1092.

Liu, P. S., W. R. Leaitch, J. W. Strapp and M. A. Wasey (1992), Response of Particle Measuring Systems airborne ASASP and PCASP to NaCl and latex particles, *Aerosol Sci. Technol.*, *16*, 83–95.

Liu, Y. and P. H. Daum (2000), The effect of refractive index on the size distributions and light scattering coefficients derived from optical particle counters, *J. Aerosol Sci.*, *31*, 945–957.

Lobert, J. M. and J. Warnatz (1993), Emissions from the Combustion Process in Vegetation, in *Fire in the Environment: The Ecological, Atmospheric, and Climatic Importance of Vegetation Fires*, edited by P. J. Crutzen and J. G. Goldammer, pp. 15–37, John Wiley & Sons, Chichester.

Lobert, J. M., D. H. Scharffe, W.-M. Hao, T. A. Kuhlbusch, R. Seuwen, P. Warneck and P. J. Crutzen (1991), Experimental evaluation of biomass burning emission: Nitrogen and carbon containing compounds, in *Global Biomass Burning: Atmospheric, Climatic, and Biospheric Implications*, edited by J. S. Levine, pp. 289–304.

Mallet, M., J. C. Roger, S. Despiau, O. Dubovik and J. P. Putaud (2003), Microphysical and optical properties of aerosol particles in urban zone during ESCOMPTE, *Atmos. Res.*, *69*, 73–97.

Mallet, M., J. C. Roger, S. Despiau, J. P. Putaud and O. Dubovik (2004), A study of the mixing state of black carbon in urban zone, *J. Geophys. Res.*, *109*, D04202, doi:10.1029/2003JD003940.

Mallet, M., R. V. Dingenen, J. C. Roger, S. Despiau and H. Cachier (2005), In situ airborne measurements of aerosol optical properties during photochemical pollution events, *J. Geophys. Res.*, *110*, D03205, doi:10.1029/2004JD005139.

Malm, W. C. and D. E. Day (2001), Estimates of aerosol species scattering characteristics as a function of relative humidity, *Atmos. Environ.*, *35*, 2845–2860.

Malm, W. C., J. F. Sisler, D. Huffman, R. A. Eldred and T. A. Cahill (1994), Spatial and seasonal trends in particle concentration and optical extinction in the United Sates, *J. Geophys. Res.*, *99*, 1347–1370.

Marple, V. A., K. L. Rubow and S. M. Behm (1991), A Microorifice Uniform Deposit Impactor (MOUDI): Description, calibration, and use, *Aerosol Sci. Technol.*, *14*, 434–446.

Marple, V. A., B. A. Olson and K. L. Rubow (2001), Inertial, Gravitational, Centrifugal, and Thermal Collection Techniques, in *Aerosol Measurement: Principles, Techniques, and Applications*, edited by P. A. Baron and K. Willeke, 2nd ed., pp. 229–260, Wiley-InterScience, New York.

Mayol-Bracero, O. L., P. Guyon, B. Graham, G. Roberts, M. O. Andreae, S. Decesari, M. C. Facchini, S. Fuzzi and P. Artaxo (2002), Water-soluble organic compounds in biomass burning aerosols over Amazonia 2. Apportionment of the chemical composition and importance of the polyacidic fraction, *J. Geophys. Res.*, *107*, 8091, doi:10.1029/2001JD000522.

McInnes, L. M., D. S. Covert, P. K. Quinn and M. S. Germani (1994), Measurements of chloride depletion and sulfur enrichment in individual sea-salt particles collected from the remote marine boundary layer, *J. Geophys. Res.*, *99*, 8257–8268.

Meakin, P. (1983), Formation of fractal clusters and networks by irreversible diffusion-limited aggregation, *Phys. Rev. Lett.*, *51*, 1119–1122.

Meakin, P. (1989), Simulations of aggregation processes, in *The Fractal Approach to Heterogeneous Chemistry*, edited by D. Avnir, pp. 131–160, John Wiley & Sons, New York.

Meakin, P., B. Donn and G. W. Mulholland (1989), Collisions between point masses and fractal aggregates, *Langmuir*, *5*, 510–518.

Mishchenko, M. I., J. W. Hovenier and L. D. Travis (2000), *Light Scattering by Nonspherical Particles Theory, Measurements, and Applications*, 690 pp., Academic Press, San Diego.

Myhre, G., F. Stordal, M. Johnsrud, D. J. Diner, I. V. Geogdzhayev, J. M. Haywood, B. Holben, T. Holzer-Popp, A. Ignatov, R. Kahn, Y. J. Kaufman, N. Loeb, J. Martonchik, M. I. Mishchenko, N. R. Nalli, L. A. Remer, M. Schroedter-Homscheidt, D. Tanré, O. Torres and M. Wang (2004), Intercomparison of satellite retrieved aerosol optical depth over ocean during the period September 1997 to December 2000, *Atmos. Chem. Phys. Discuss.*, *4*, 8201–8244.

Neimark, A. V., O. U. Köylü and D. E. Rosner (1996), Extended characterization of combustion-generated aggregates: Self-affinity and lacunarities, *J. Colloid Interface Sci.*, *180*, 590–597.

Nel, A. (2005), Air pollution related illness: Effects of particles, *Science*, *308*, 804–806.

Nemery, B., P. H. M. Hoet and A. Nemmar (2001), The Meuse Valley fog of 1930: an air pollution disaster, *Lancet*, *357*, 704–708.

Nemmar, A., P. H. M. Hoet, D. Dinsdale, J. Vermylen, M. F. Hoylaerts and B. Nemery (2003), Diesel exhaust particles in lung acutely enhance experimental peripheral thrombosis, *Circulation*, *107*, 1202–1208.

Neusüß, C., H. Wex, W. Birmili, A. Wiedensohler, C. Koziar, B. Busch, E. Brüggemann, T. Gnauk, M. Ebert and D. S. Covert (2002), Characterization and parameterization of atmospheric particle number-, mass-, and chemical-size distributions in central Europe during LACE 98 and MINT, *J. Geophys. Res.*, *107*, 8127, doi:10.1029/2001JD000514.

Norman, A.-L., W. Belzer and L. Barrie (2004), Insights into the biogenic contribution to total sulphate in aerosol and precipitation in the Fraser Valley afforded by isotopes of sulphur and oxygen, *J. Geophys. Res.*, *109*, D05311, doi:10.1029/2002JD003072.

Nyeki, S. and I. Colbeck (1994), The measurement of the fractal dimension of individual in situ soot agglomerates using a modified Millikan cell technique, *J. Aerosol Sci.*, *25*, 75–90.

Oh, C. and C. M. Sorensen (1997), The effect of overlap between monomers on the determination of fractal cluster morphology, *J. Colloid Interface Sci.*, *193*, 17–25.

Okada, K. and R. M. Hitzenberger (2001), Mixing properties of individual submicrometer aerosol particles in Vienna, *Atmos. Environ.*, *35*, 5617–5628.

Oke, T. R. (1993), *Boundary Layer Climates*, 2nd ed., 435 pp., Routlegde, London.

Park, K., D. B. Kittelson and P. H. McMurry (2004), Structural properties of diesel exhaust particles measured by Transmission Electron Microscopy (TEM): Relationships to particle mass and mobility, *Aerosol Sci. Technol.*, *38*, 881–889.

Piketh, S. J., H. J. Annegarn and P. D. Tyson (1999), Lower troposphere aerosol loadings over South Africa, the contribution of aeolian dust, industrial emissions and biomass burning, *J. Geophys. Res.*, *104*, 1597–1607.

Piketh, S. J., L. B. Otter, R. P. Burger, N. Walton, M. A. van Nierop, T. Bigala, K. E. Chiloane and P. Gwaze (2004), Cape Town Brown Haze II Report, Climatology Research Group, University of Witwatersrand, p. 84.

Pilinis, C. and X. Li (1998), Particle shape and internal inhomogeneity effects on the optical properties of tropospheric aerosols of relevance to climate forcing, *J. Geophys. Res.*, *103*, 3789–3800.

Pineda, C. A. and M. G. de Villiers (1995), Air pollution study in the Cape Town area by proton-induced X-ray emission spectroscopy, *S.Afri. J. Chem.*, *48*, 90–93.

Pope, C. A., R. T. Burnett, M. J. Thun, E. E. Calle, D. Krewski, K. Ito and G. D. Thurston (2002), Lung cancer, cardipulmonary mortality and long term exposure to fine particulate air pollution, *JAMA*, *287*, 1132–1141.

Pósfai, M., J. R. Anderson, P. R. Buseck and H. Sievering (1995), Compositional variation of sea-salt-mode aerosol particles from the North Atlantic, *J. Geophys. Res.*, *100*, 23 063–23 074.

Pósfai, M., H. Xu, J. R. Anderson and P. R. Buseck (1998), Wet and dry sizes of atmospheric aerosol particles: An AFM -TEM study, *Geophys. Res. Lett.*, *25*, 1907–1910.

Pósfai, M., R. Simonics, J. Li, P. V. Hobbs and P. R. Buseck (2003), Individual aerosol particles from biomass burning in southern Africa: 1. Compositions and size distributions of carbonaceous particles, *J. Geophys. Res.*, *108*, 8483, doi:10.1029/2002JD002291.

Pósfai, M., A. Gelencsér, R. Simonics, K. Arató, J. Li, P. V. Hobbs and P. R. Buseck (2004), Atmospheric tar balls: Particles from biomass and biofuel burning, *J. Geophys. Res.*, *109*, 8483, doi:10.1029/2003JD004169.

Quinn, P. K., T. Anderson, T. Bates, R. Dlugi, J. Heintzenberg, W. von Hoyningen-Huene, M. Kulmala, P. B. Russell and E. Swietlicki (1996), Closure in tropospheric aerosol-climate research: A review and future needs for addressing aerosol direct shortwave radiative forcing, *Contrib. Atmos. Phys./Beitr. Phys. Atmosph.*, *69*, 547–577.

Ramanathan, V., P. J. Crutzen, J. T. Kiehl and D. Rosenfeld (2001a), Aerosols, climate, and the hydrological cycle, *Science*, *294*, 2119–2124.

Ramanathan, V., P. J. Crutzen, J. Lelieveld, A. P. Mitra, D. Althausen, J. Anderson, M. O. Andreae, W. Cantrell, G. R. Cass, C. E. Chung, A. D. Clarke, J. A. Coakley, W. D. Collins, W. C. Conant, F. Dulac, J. Heintzenberg, A. J. Heymsfield, B. Holben, S. Howell, J. Hudson, A. Jayaraman, J. T. Kiehl, T. N. Krishnamurti, D. Lubin, G. McFarquhar, T. Novakov, J. A. Ogren, I. A.

Podgorny, K. Prather, K. Priestley, J. M. Prospero, P. K. Quinn, K. Rajeev, P. Rasch, S. Rupert, R. Sadourny, S. K. Satheesh, G. E. Shaw, P. Sheridan and F. P. J. Valero (2001b), Indian Ocean Experiment: An integrated analysis of the climate forcing and effects of the great Indo-Asian haze, *J. Geophys. Res.*, *106*, 28 371–28 398.

Reid, E. A., J. S. Reid, M. M. Meier, M. R. Dunlap, S. S. Cliff, A. Broumas, K. Perry and H. Maring (2003a), Characterization of African dust transported to Puerto Rico by individual particle and size segregated bulk analysis, *J. Geophys. Res.*, *108*, 8591, doi:10.1029/2002JD002935.

Reid, J. S., P. V. Hobbs, R. J. Ferek, D. R. Blake, J. V. Martins, M. R. Dunlap and C. Liousse (1998), Physical, chemical, and optical properties of regional hazes dominated by smoke in Brazil, *J. Geophys. Res.*, *103*, 32 059–32 080.

Reid, J. S., T. F. Eck, S. A. Christopher, P. V. Hobbs and B. Holben (1999), Use of the Ångstrom exponent to estimate variability of optical and physical properties of aging smoke particles in Brazil, *J. Geophys. Res.*, *104*, 27 473–27 489.

Reid, J. S., H. H. Jonsson, H. B. Maring, A. Smirnov, D. L. Savoie, S. S. Cliff, E. A. Reid, J. M. Livingston, M. M. Meier, O. Dubovik and S.-C. Tsay (2003b), Comparison of size and morphological measurements of coarse mode dust particles from Africa, *J. Geophys. Res.*, *108*, 8593, doi:10.1029/2002JD002485.

Reimer, L. (1998), *Scanning Electron Microscopy: Physics of Image Formation and Microanalysis*, vol. 45, 2nd ed., 527 pp., Springer-Verlag, Berlin.

Rissler, J., E. Swietlicki, J. Zhou, G. Roberts, M. O. Andreae, L. V. Gatti and P. Artaxo (2004), Physical properties of the sub-micrometer aerosol over the Amazon rain forest during the wet-to-dry season transition comparison of modeled and measured CCN concentrations, *Atmos. Chem. Phys. Discuss.*, *4*, 3159–3225.

Rissler, J., A. Vestin, E. Swietlicki, G. Fisch, J. Zhou, P. Artaxo and M. O. Andreae (2005), Size distribution and hygroscopic properties of aerosol particles from dry-season biomass burning in Amazonia, *Atmos. Chem. Phys. Discuss.*, *5*, 8149–8207.

Roberts, G. C., P. Artaxo, J. Zhou, E. Swietlicki and M. O. Andreae (2002), Sensitivity of CCN spectra on chemical and physical properties of aerosol: A case study from the Amazon Basin, *J. Geophys. Res.*, *107*, 8070, doi:10.1029/2001JD000583.

Roe, G., L. McDonnell and A. Ghanem (2004), A method for measuring the size distribution of latex particles by scanning force microscopy, *Ultramicroscopy*, *100*, 319–329.

Rogak, S. N., R. C. Flagan and H. V. Nguyen (1993), The mobility and structure of aerosol agglomerates, *Aerosol Sci. Technol.*, *18*, 25–47.

Rogge, W. F., L. M. Hildemann, M. A. Mazurek, G. R. Cass and B. R. T. Simoneit (1993), Sources of fine aerosol. 2. Noncatalyst and catalyst-equipped automobiles and heavy-duty diesel trucks, *Environ. Sci. Technol.*, *27*, 636–651.

Rosenfeld, D. (2000), Suppression of rain and snow by urban and industrial air pollution, *Science*, *287*, 1793–1796.

Russell, P. B., J. Redemann, B. Schmid, R. W. Bergstrom, J. M. Livingston, D. M. McIntosh, S. A. Ramirez, S. Hartley, P. V. Hobbs, P. K. Quinn, C. M. Carrico, M. J. Rood, E. Ostrom, K. J. Noone, von W. Hoyningen-Huene and L. Remer (2002), Comparison of aerosol single scattering albedos derived by diverse techniques in the two North Atlantic experiments, *J. Atmos. Sci.*, *59*, 609–619.

Samson, R. J., G. W. Mulholland and J. W. Gentry (1987), Structural analysis of soot agglomerates, *Langmuir*, *3*, 272–281.

Satheesh, S. K., V. Ramanathan, B. N. Holben, K. K. Moorthy, N. G. Loeb, H. Maring, J. M. Prospero and D. Savoie (2002), Chemical, microphysical, and radiative effects of Indian Ocean aerosols, *J. Geophys. Res.*, *107*, 4725, doi:10.1029/2002JD002463.

Schmid, O., G. Helas, D. Chand, U. Dusek, G. Frank, Y. Iinuma, K. Zeromskiene, H. Herrmann, A. M. ling, R. S. Parmar, M. Welling, A. Wiedensohler and M. O. Andreae (2004), Methodology for experimental characterization of aerosol emissions from biomass burning, in *8th Intl. Conf. on Carbonaceous Particles in the Atmosphere (ICCPA)*, Vienna.

Schmidt-Ott, A. (1988), In situ measurement of the fractal dimensionality of ultrafine aerosol particles, *Appl. Phys. Lett.*, *52*, 954–956.

Seinfeld, J. H. and S. N. Pandis (1998), *Atmospheric Chemistry and Physics, from Air Pollution to Climate Change*, 1326 pp., Wiley-InterScience, New York.

Senaratne, I. and D. Shooter (2004), Elemental composition in source identification of brown haze in Auckland, New Zealand, *Atmos. Environ.*, *39*, 3049–3059.

Sievering, H., E. Gorman, Y. Kim, T. Ley, W. Seid and J. Boatman (1994), Heterogeneous conversion contribution to the sulfate observed over Lake Michigan, *Atmos. Environ.*, *28*, 367–370.

Simonics, R. and M. Pósfai (2004), Properties of aerosol particles measured using atomic force microscopy, in *European Aerosol Conference*, pp. 351–352, Budapest, Hungary.

Slowik, J. G., K. Stainken, P. Davidovits, L. R. Williams, J. T. Jayne, C. E. Kolb, D. R. Worsnop, Y. Rudich, P. F. DeCarlo and J. L. Jimenez (2004), Particle morphology and density characterization by combined mobility and aerodynamic diameter measurements. Part 2: Application to combustion-generated soot aerosols as a function of fuel equivalence ratio, *Aerosol Sci. Technol.*, *38*, 1206–1222.

Smith, D. M., M. S. Akhter, J. A. Jassim, C. A. Sergides, W. F. Welch and A. R. Chughtai (1989), Studies of the structure and reactivity of soot, *Aerosol Sci. Technol.*, *10*, 311–325.

Solomon, P. A., G. Norris, M. Landis and M. Tolocka (2001), Chemical Analysis Methods for Atmospheric Aerosol Components, in *Aerosol Measurements: Principles, Techniques, and Applications*, edited by P. A. Baron and K. Willeke, 2nd ed., pp. 261–293, Wiley-InterScience, New York.

Sorensen, C. M. and G. C. Roberts (1997), The prefactor of fractal aggregates, *J. Colloid Interface Sci.*, *186*, 447–452.

South African Weather Service (2003), *Daily Weather Bulletin August 2003*, ISSN 0011-5517.

Statistics South Africa (2001), *http://www.statssa.gov.za/census01*, South Africa Census 2001.

Strawa, A. W., K. Drdla, G. V. Ferry, S. Verma, R. F. Pueschel, M. Yasuda, R. J. Salawitch, R. S. Gao, S. D. Howard, P. T. Bui, M. Loewenstein, J. W. Elkins, K. K. Perkins and R. Cohen (1999), Carbonaceous aerosol (soot) measured in the lower stratosphere during POLARIS and its role in the stratospheric photochemistry, *J. Geophys. Res.*, *104*, 26 753–26 766.

Stull, R. B. (1999), *An Introduction to Boundary Layer Meteorology*, 670 pp., Kluwer Academic, Dordrecht, The Netherlands.

Swap, R. J., H. A. Annegarn, J. T. Suttle, M. D. King, S. Platnick, J. L. Privette and R. J. Scholes (2003), Africa burning: A thematic of the Southern African Regional Science Initiative (SAFARI 2000), *J. Geophys. Res.*, doi:10.1029/2003JD003747.

Tang, I. N. (1996), Chemical and size effects of hygroscopic aerosols on light scattering coefficients, *J. Geophys. Res.*, *101*, 19 245–19 250.

Tegen, I., A. A. Lacis and I. Fung (1996), The influence on climate forcing of mineral aerosol from disturbed soils, *Nature*, *380*, 419–422.

ten Brink, H. M., J. P. Veefkind, A. Waijers-Ijpelaan and J. C. van der Hage (1996), Aerosol light-scattering in The Netherlands, *Atmos. Environ.*, *30*(24), 4251–4261.

Tence, M., J. P. Chevalier and R. Jullien (1989), On the measurement of the fractal dimension of aggregated particles by electron microscopy: experimental method, corrections and comparison with numerical models, *J. Physique*, *47*, 1989–1998.

Todd, B. A. and S. J. Eppell (2001), A method to improve the quantitative analysis of SFM images at the nanoscale, *Surf. Sci.*, *000*, 1–11.

Trebs, I., F. X. Meixner, J. Slanina, R. Otjes, P. Jongejan and M. O. Andreae (2004), Real-time measurements of ammonia, acidic trace gases and water-soluble inorganic aerosol species at a rural site in the Amazon Basin, *Atmos. Chem. Phys.*, *4*, 967–987.

Trimborn, A., K.-P. Hinz and B. Spengler (2002), Online analysis of atmospheric particles with a transportable laser mass spectrometer during LACE 98, *J. Geophys. Res.*, *107*, 8132, doi: 10.1029/2001JD000590.

Tulloch, G. S. and J. E. Shapiro (1954), Brochosomes and leafhoppers, *Science*, *120*, 232.

Twomey, S. (1975), Comparison of constrained linear inversion and an iterative nonlinear algorithm applied to the indirect estimation of particle size distributions, *J. Comput. Phys*, *18*, 188–200.

Tyson, P. D. and P. C. D'Abreton (1998), Transport and recirculation of aerosols off southern Africa-macroscale plume structure, *Atmos. Environ.*, *32*, 1511–1524.

Usher, C. R., A. E. Michel and V. H. Grassian (2003), Reactions on mineral dust, *Chem. Rev.*, *103*, 4883–4939.

Väkevä, M., K. Hämeri, T. Puhakka, E. D. Nilsson, H. Hohti and J. M. Mäkelä (2000), Effects of meteorological processes on aerosol particle size distribution in an urban background area, *J. Geophys. Res.*, *105*, 9807–9821.

van de Hulst, H. C. (1957), *Light Scattering by Small Particles*, 470 pp., Wiley-InterScience, New York.

Vetter, T. (2004), Berechnung der Mie-Streufunktionen zur Kalibrierung optischer Partikelzahler, Diplomarbeit, Johannes Gutenberg-Universitat and Max Planck Institut fur Chemie.

Villarrubia, J. S. (1997), Algorithms for scanned probe microscope image simulation, surface reconstruction and tip estimation, *J. Res. Natl. Inst. Stand. Technol.*, *102*, 425–454.

Walton, N. M. (2005), Characterisation of Cape Town Brown Haze, Msc thesis, University of Witwatersrand.

Wang, G. M. and C. M. Sorensen (1999), Diffusive mobility of fractal aggregates over the entire knudsen number range, *Phys. Rev. E*, *60*, 3036–3044.

Wang, G. M. and C. M. Sorensen (2001), Aggregation kernel homogeneity for fractal aggregate aerosols in the slip regime, *Aerosol Sci. Technol.*, *34*, 297–306.

Wayne, R. P. (1991), *Chemistry of Atmospheres*, 2nd ed., 447 pp., Oxford University Press, New York.

Weingartner, E., H. Burtscher and U. Baltensperger (1997), Hygroscopic properties of carbon and diesel soot particles, *Atmos. Environ.*, *31*, 2311–2327.

Wen, H. Y. and G. Kasper (1984), Dynamics and measurement of smokes III-Drag and orientation of chain aggregates in an Electric Mobility Spectrometer, *Aerosol Sci. Technol.*, *3*, 397–403.

Wendling, P., A. Stifter, B. Mayer, M. Fiebig, C. Kiemle, H. Flentje, M. Wendisch, W. Armbruster, U. Leiterer, von W. Hoyningen-Huene and A. Petzold (2002), Aerosol-radiation interaction in the cloudless atmosphere during LACE 98 2: Aerosol-induced solar irradiance changes determined from airborne pyranometer measurements and calculations, *J. Geophys. Res.*, *107*, 8131, doi: 10.1029/2000JD000288.

Wentzel, M., H. J. Annegarn, G. Helas, S. Weinbruch, A. G. Balogh and J. S. Sithole (1999), Giant dendritic carbonaceous particles in Soweto aerosols, *S. Afri. J. Sci.*, *95*, 141–146.

Wentzel, M., H. Gorzawski, K.-H. Naumann, H. Saathoff and S. Weinbruch (2003), Transmission electron microscopical and aerosol dynamical characterization of soot aerosols, *J. Aerosol Sci.*, *34*, 1347–1370.

Wernli, H. and H. C. Davies (1997), A Lagrangian-based analysis of extratropical cyclones. I: The method and some applications, *Q. J. R. Meteorol. Soc.*, *123*, 467–489.

Wicking-Baird, M. C., M. G. V. de and R. K. Dutkiewicz (1997), Cape Town Brown Haze Study, Report No. Gen 182, Energy Research Institute, University of Cape Town, p. 80.

Wiedensohler, A. (1988), Technical note: An approximation of the bipolar charge distribution for particles in the submicron size range, *J. Aerosol Sci.*, *19*, 387–389.

Wilkins, E. T. (1954), Air pollution and the London fog of December, 1952, *J. Royal Sanitary Institute*, *74*, 1–21.

Williams, P. M., K. M. Shakesheff, M. C. Davies, D. E. Jackson, C. J. Roberts and S. J. B. Tendler (1996), Blind reconstruction of scanning probe image data, *J. Vac. Sci. Technol. B*, *B14*, 1557–1562.

Wilson, J. C. and B. Y. H. Liu (1980), Aerodynamic particle size measurements by laser-Doppler velocimetry, *J. Aerosol Sci.*, *11*, 139–150.

Wiltzius, P. (1987), Hydrodynamic behavior of fractal aggregates, *Phys. Rev. Lett.*, *58*, 710–713.

Winkler, P. (1988), The growth of atmospheric aerosols particles with relative humidity, *Physica Scripta*, *37*, 223–230.

Winklmayr, W., H.-C. Wang and W. John (1990), Adaptation of the Twomey algorithm to the inversion of cascade impactor data, *Aerosol Sci. Technol.*, *13*, 322–331.

Wiscombe, W. J. (1980), Improved Mie scattering algorithms, *Appl. Opt.*, *19*, 1505–1509.

Woolf, D. K. and E. C. Monahan (1988), Laboratory Investigations on the Influence on Marine Aerosol Production of the Interaction Oceanic Whitecaps and Surface-active Material, in *Aerosols and Climates*, edited by P. V. Hobbs and M. P. McCormick, pp. 1–18, A. Deepak, Hampton.

World Bank Report (1998), World Development Indicators, 1998, New Ideas in Pollution Regulation, World Bank Group, pp. 162–163.

Wu, M. K. and S. K. Friedlander (1993), Note on the power law equation for fractal-like aerosol agglomerates, *J. Colloid Interface Sci.*, *159*, 246–248.

Wurzler, S., H. Herrmann, C. Neusüß, F. Stratmann, A. Wiedensohler, M. Wilck, T. Trautmann, M. O. Andreae, G. Helas, J. Trentmann, B. Langmann, H. Graf and C. Textor (2001), Impact of vegetation fires on the composition and circulation of the atmosphere: Introduction of the research project EFEU, *J. Aerosol Sci.*, *32*, S199–S200.

Yokelson, R. J., D. W. T. Griffith and D. E. Ward (1996), Open-path Fourier transform infrared studies of large-scale laboratory biomass fires, *J. Geophys. Res.*, *101*, 21 067–21 080.

Zhang, X. and P. H. McMurry (1992), Evaporative losses of fine particulate nitrates during sampling, *Atmos. Environ.*, *26A*, 3305–3312.

Zhou, J., E. Swietlicki, H. C. Hanson and P. Artaxo (2002), Submicrometer aerosol particle size distribution and hygroscopic growth measured in the Amazon rain forest during the wet season, *J. Geophys. Res.*, *107*, 8055, doi:10.1029/2000JD000203.

Zunckel, M., J. John and M. Naidoo (2006), The National Air Quality Management Programme (NAQMP), Output c.1., Air Quality Information Review. A Report for Directorate Environmental Information and Reporting, Environmental Quality and Protection Chief Directorate: Air Quality Management & Climate Change, CSIR-Environmentek.

Appendices

Appendix A: Publications and conference proceedings

Articles 1, 2 and 3 were extracted and modified from Chapters 4, 3 and 5 of this thesis, respectively. Articles 4 and 5 were presented by first author as conference proceedings at the European Aerosol Conference, Budapest, Hungary, 6 to 10 September 2004. Article 6 (authors in alphabetical order) is a chapter of notes produces after attending the 1^{st} French-German Summer School of Aerosol, Heterogeneous Chemistry and Climate, Ile d'Oleron, France, September 19 to October 2004, as part of the International Max Planck Research School (IMPRS) initiatives. Articles 7, 8, 9 and 11 were collaborative research activities carried out with colleagues at the Max Planck Institute for Chemistry, Mainz. Article 10 is a report collaborated with the Climatology Research Group, University of Witwatersrand.

1. **Gwaze, P.**, O. Schmid, H. J. Annegarn, M. O. Andreae, J. Huth and G. Helas (2005), Comparison of three methods of fractal analysis applied to soot aggregates from wood combustion, J. Aerosol Sci., doi:10.1016/j.jaerosci.2005.06.007.

2. **Gwaze, P.**, H. J. Annegarn, J. Huth and G. Helas (submitted), Comparison of particle sizes determined with impactor, DMPS-APS, AFM, and SEM, *Atmos. Res.*

3. **Gwaze, P.**, G. Helas, H. J. Annegarn, J. Huth and S. J. Piketh (submitted), Physical, chemical, and optical properties of aerosol particles collected over Cape Town during winter haze episodes, *S.Afri. J. Sci.*

4. **Gwaze, P.**, H. J. Annegarn, J. Huth and G. Helas (2004), Measurements of atmospheric aerosol particle sizes with impactor, AFM and SEM, in European Aerosol Conference, EAC, pp. 659-660, Elsevier, Budapest, Hungary, September 6-10.

5. **Gwaze, P.**, O. Schmid, H. J. Annegarn, J. Huth and G. Helas (2004), Characterisation of soot aggregates from the combustion of wood, in European Aerosol Conference, EAC, Elsevier, Budapest, Hungary, September 6-10.

6. Bartenbach, S., L. Chiappini and **P. Gwaze** (2004), Secondary Organic Aerosols Formation: Process Studies and Mechanisms, in *Aerosol, Heterogeneous Chemistry and Climate; Notes from the 1st French-German Summer School*, edited by G. Moorgat, pp. 38-42.

7. Chand, D., O. Schmid, **P. Gwaze,** R. S. Parmar, G. Helas, K. Zeromskiene, A. Wiedensohler, A. Massling and M. O. Andreae (2005), Laboratory measurements of smoke optical properties from the burning of Indonesian peat and other types of biomass, *Geophys. Res. Lett.*, 32, L12819, doi:10.1029/2005GL022678.

8. Dusek, U., G. P. Frank, G. Helas, Y. Iinuma, K. Zeromskiene, **P. Gwaze,** T. Hennig, A. Massling, O. Schmid, H. Herrmann, A. Wiedensohler and M. O. Andreae (2005), 'Missing' cloud condensation nuclei in peat smoke, *Geophys. Res. Lett.*, 32, L11802, doi:10.1029/2005GL022473.

9. Eremets, M.I., I.A. Trojan, **P. Gwaze,** J. Huth, V.D. Blank and R. Boehler (2005), The strength of diamond, *Appl. Phys. Lett.,* 87, 141902, doi: 10.1063/1.2061853.

10. Piketh, S.J., L.B. Otter, R.P. Burger, N. Walton, M.A. van Nierop, T. Bigala, K.E. Chiloane and **P. Gwaze,** (2004), Cape Town Brown Haze II Report, University of Witwatersrand, Johannesburg.

11. Schneider., J., S. Weimer, F. Drewnick, N. Hock, S. Borrmann, G. Helas, G. Frank, **P. Gwaze,** O. Schmid, M.O. Andreae, and U. Kirchner (submitted), Mass spectrometric analysis and aerodynamic properties of various combustion derived aerosol particles, *Aerosol Sci. Technol.*

Appendix B: Analytical expressions

This section of the Appendix lists of some analytical expressions used in this thesis. The expressions were adapted from *Baron and Willeke* (2001a); *Hinds* (1999); *Seinfeld and Pandis* (1998).

1. **Particle morphological properties**

   - Radius of gyration R_g: For a rigid particle consisting of mass elements of mass m_i, each located at a distance r_i from the centre of mass, the radius of gyration, R_g, is defined as the square root of the mass-average of r_i^2 for all the mass elements such that

   $$R_g = \left[\frac{\sum_i m_i r_i^2}{\sum_i m_i}\right]^{1/2}$$

   - Fractal dimension: The fractal dimension is defined as D_f

   $$n(\in) \propto \in^{D_f}$$

   where $n(\in)$ is the minimum number of open sets of diameter $\in$ needed to cover the set.

2. **Particle number-size distributions**

   - The absolute number of particles per cm^3, N, is given by the aerosol distribution $n_N(d_p)$ such that

   $$n_N(d_p) = \frac{dN}{dp}$$

   where $n_N(d_p)d_p$ (μm^{-1} cm^3) is the number of particles having diameters in the range d_p to $d_p + dd_p$.

   For $\partial d_p \rightarrow 0$, then

   $$N = \int_0^\infty n_N(d_p) dd_p$$

- The total aerosol volume per cm^3 of air V_{tot} (μm^3 cm^3) is

$$V_{tot} = \frac{\pi}{6} \int_0^{\infty} d_p^3 n_N(d_p) dd_p$$

- For a distribution based on log d_p, the number of particles is expressed as functions of log d_p such that

$$\frac{dN}{d\,log\,d_p} = 2.303\; d_p n_N(d_p)$$

$$\frac{dV}{d\,log\,d_p} = \frac{2.303\pi\; d_p^4}{6}\; n_N(d_p)$$

- The number concentration N is log-normally distributed when

$$\frac{dN}{d\,log\,d_p} = \frac{1}{\sqrt{2\pi}\;\sigma_g}\; exp\left[-\frac{(log\;d_p - log\;d_g)^2}{2(log\;\sigma_g)^2}\right]$$

where d_g is the the geometric mean diameter and σ_g is the geometric standard deviation.

3. **Aerosol optical parameters**

- The scattering σ_{sp}, absorption σ_{ap} and extinction coefficients σ_{ep} for a particle ensemble with number size distribution $n_N(d_p)$ is given by

$$\sigma_{ep,ap,sp} = \int_0^{d_p^{max}} \frac{\pi d_p^2}{4}\; Q_{ep,ap,sp}(m,\alpha)\; n_N(d_p)\; dd_p$$

where $Q_{ep,ap,sp}(m,\alpha)$ are the respective extinction efficiencies.

- The optical depth τ is

$$\tau(\lambda) = \int_{z_1}^{z_2} \sigma_{ep}(\lambda, z) dz$$

where z is the height above ground.

Appendix C: Other tables and figures

This section of the Appendix provides tables of the haze measurement station locations discussed in Section 5.2, coefficients of polynomial fits to PCASP response functions derived in Section 5.6.1; and vertical distribution of aerosol number concentrations described in detail in Section 5.4.1.

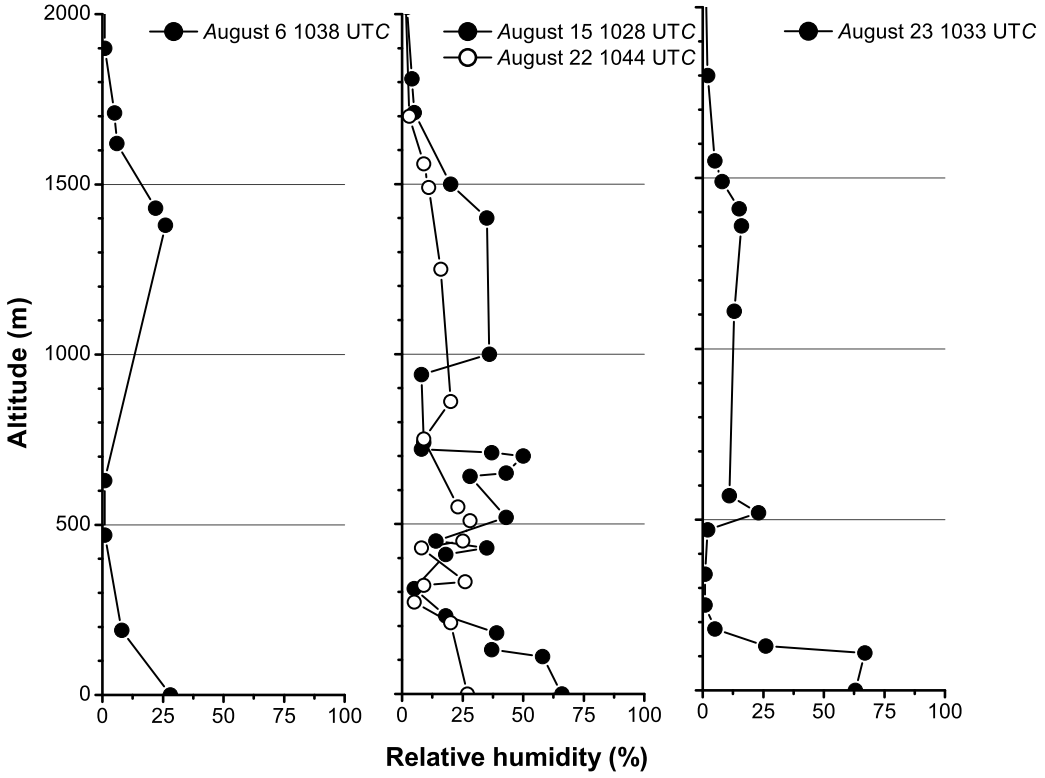


Figure 1: Vertical profiles of relative humidity on August 6, 15, 22 , and 23 (for Flights 9, 13, 14 and 16, respectively) at Cape Town International Airport weather station as provided by the South African Weather Services. Flights 9 and 13 were conducted within 2 hours after these soundings, and Flights 14 and 16 were made 3 to 4 hours prior to the soundings.

Table 1: Coordinates of Cape Town brown haze measurement stations

Site location	**Latitude (° South)**	**Longitude (° East)**
Ysterplaat	-33.91	18.48
Woodstock	-33.94	18.45
Pinelands	-33.94	18.51
Hanover Park	-33.99	18.54
Belville	-33.89	18.63
Belhar	-33.94	18.61
Mfuleni	-34.00	18.68
Wynberg	-34.00	18.46
Mannenburg	-34.00	18.55
Camps Bay	-33.94	18.38
Hout Bay	-34.05	18.34
Fishoek	-34.14	18.42
Khayelitsha	-34.02	18.67
Mitchell's Plain	-34.04	18.60
Grassy Park	-34.04	18.50
Tableview	-33.82	18.51
Edgemead	-33.87	18.55
Goodwood	-33.90	18.56
Bothasig	-33.86	18.52
Plattekloof	-33.87	18.58
Labiance	-33.91	18.66
Cape Town	-33.93	18.42
Athlone	-33.95	18.51
Oranjezicht	-33.94	18.41
Drill Hall	-33.93	18.42
Killarney	-33.83	18.53
Wallacedene	-33.86	18.73

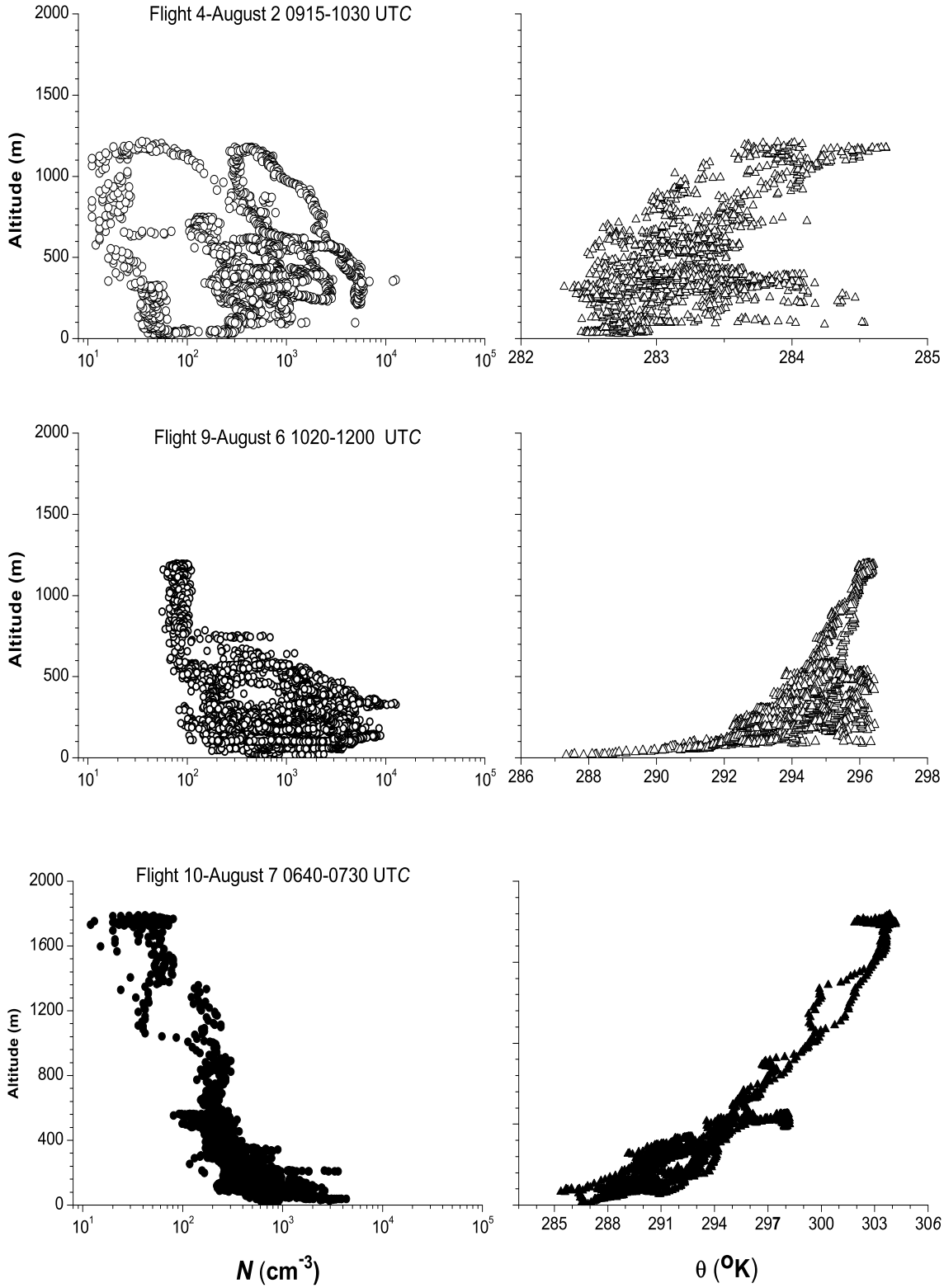


Figure 2: Vertical distributions of particle concentrations N and θ. In the mornings, before 0900 UTC (solid circles), high number concentrations are confined to a more stable layer below 400 m asl. As day time progresses, particle concentrations are mixed by turbulence in the growing convective boundary layer to about 1200 m asl (open circles).

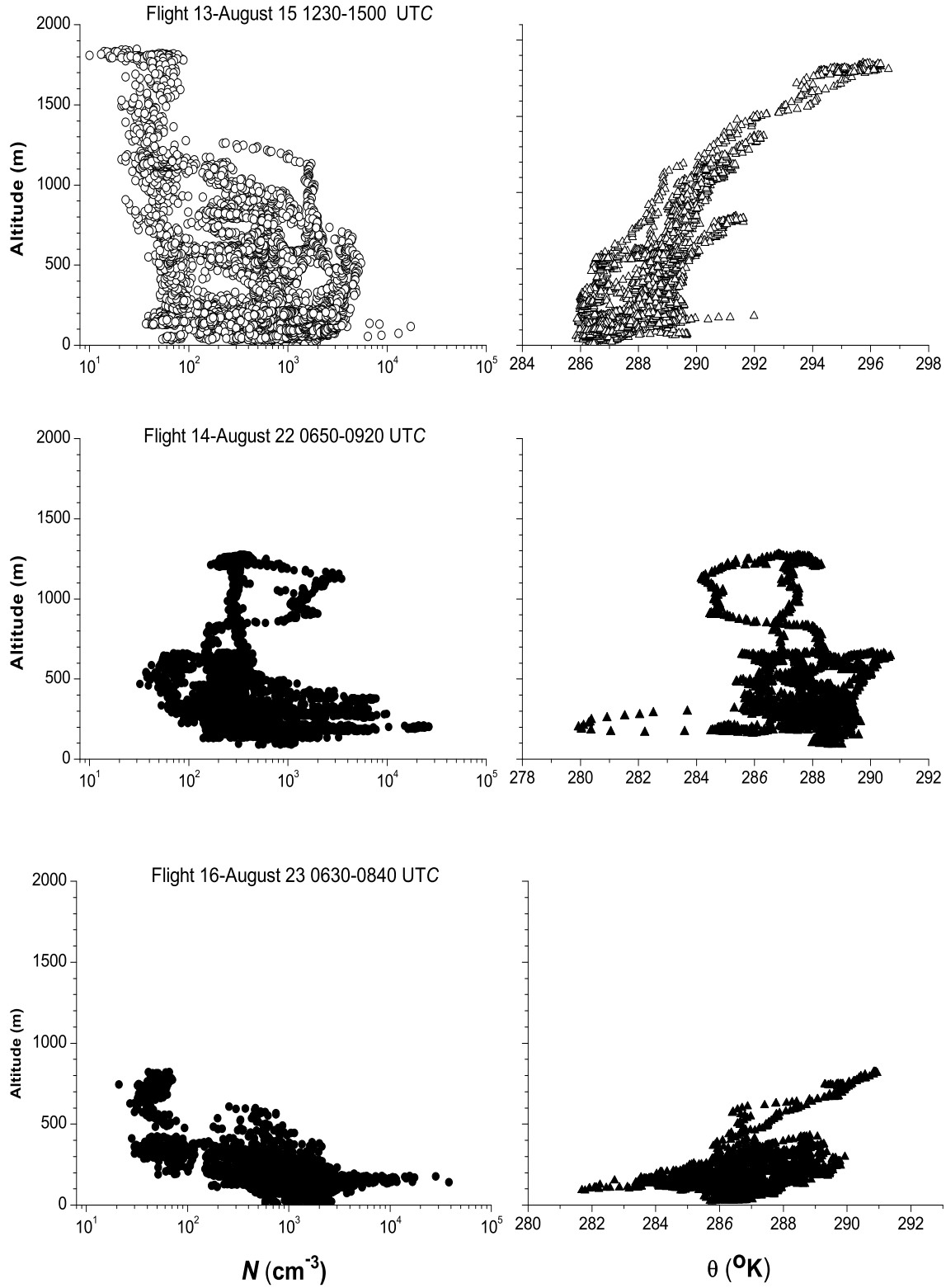


Figure 3: Vertical distributions of particle concentrations N and θ. In the mornings, before 0900 UTC (solid circles), high number concentrations are confined to a more stable layer below 400 m asl. As day time progresses, particle concentrations are mixed by turbulence in the growing convective boundary layer to about 1200 m asl (open circles).

Table 2: Coefficients of 8-order polynomial functions fitted to the response functions of the PCASP at refractive index of PSL spheres $m = 1.585 - 0.0i$ and ambient particles with $m = n_j - k_j$ for particle groups $j = 1$ to 7 identified in the SEM analyses.

Polynomial	**PSL spheres**	**Soot aggregates**	**Mineral dust**	**Rod-shaped particles (ass. with soot)**	**Sulphates (as sulphuric acid)**	**Sea-salt**	**Tar balls fly ash & others**	**Test particles**
coefficients	$1.583 - 0.0i$	$1.75 - 0.44i$	$1.56 - 0.006i$	$1.50 - 0.0i$	$1.43 - 0.00i$	$1.54 - 0.00i$	$1.50 - 0.0i$	$1.33 - 0.0i$
C_0	2.4487	2.4400	2.3576	2.4400	2.4324	2.4436	2.4400	2.3729
C_1	0.8332	0.7593	0.7098	0.7593	0.7282	0.7917	0.7593	0.9046
C_2	0.2424	0.2210	0.2112	0.2210	0.1305	0.2442	0.2210	-0.2279
C_3	-0.1142	0.0267	-0.0842	0.0267	0.1075	-0.0372	0.0267	-0.0761
C_4	-0.1450	-0.1622	-0.1703	-0.1622	-0.1225	-0.1649	-0.1622	0.0952
C_5	0.0934	0.0288	0.0689	0.0288	0.0006	0.0558	0.0288	0.1171
C_6	0.0269	0.0269	0.0299	0.0269	0.0175	0.0292	0.0269	-0.0148
C_7	-0.0126	-0.0020	-0.0079	-0.0020	0.0004	-0.0058	-0.0020	-0.0258
C_8	-0.0032	-0.0013	-0.0025	-0.0013	-0.0006	-0.0021	-0.0013	-0.0043
R^2	0.9988	0.9989	0.9987	0.9988	0.9988	0.9988	0.9988	0.9980